^{16}N Calibration and Background Studies for SNO+

BY

POUYA KHAGHANI

THESIS SUBMITTED IN PARTIAL FULFILLMENT
OF THE REQUIREMENTS FOR THE DEGREE OF
PhD IN MATERIALS SCIENCE

THE FACULTY OF GRADUATE STUDIES
LAURENTIAN UNIVERSITY
SUDBURY, ONTARIO, CANADA

THESIS DEFENCE COMMITTEE/COMITÉ DE SOUTENANCE DE THÈSE
Laurentian Université/Université Laurentienne
Office of Graduate Studies/Bureau des études supérieures

Title of Thesis
Titre de la thèse ^{16}N Calibration and Background Studies for SNO+

Name of Candidate
Nom du candidat   Khaghani, Pouya

Degree
Diplôme   Doctor of Philosophy

Department/Program   Date of Defence
Département/Programme   Materials Science   Date de la soutenance December 15, 2022

APPROVED/APPROUVÉ

Thesis Examiners/Examinateurs de thèse:

Dr. Christine Kraus
(Supervisor/Directeur(trice) de thèse)

Dr. Aleksandra Bialek
(Committee member/Membre du comité)

Dr. Caio Licciardo
(Committee member/Membre du comité)

                                    Approved for the Office of Graduate Studies
                                    Approuvé pour le Bureau des études supérieures
                                    Tammy Eger, PhD
                                    Vice-President Research (Office of Graduate Studies)
Dr. Marcin Kuzniak   Vice-rectrice à la recherche (Bureau des études supérieures)
(External Examiner/Examinateur externe)   Laurentian University / Université Laurentienne

Dr. Nelson Belzile
(Internal Examiner/Examinateur interne)

ACCESSIBILITY CLAUSE AND PERMISSION TO USE

Abstract

SNO+ is a multipurpose scintillator based neutrino experiment which is located 2km underground at SNOLAB, Creighton mine, Sudbury. The primary physics goal of the experiment is the search for the elusive process of neutrino-less double beta decay with ^{130}Te loaded into the liquid scintillator cocktail. In addition, SNO+ will be able to detect low energy solar neutrinos, geo- and reactor-antineutrinos, as well as supernova neutrinos. SNO+ has completed its water phase in 2019. During the water phase SNO+ made measurements of ^{8}B neutrinos, and improved the limits on the lifetime of nucleon decay. Aside from the physics goals, the optical and energy calibration of the detector was accomplished in water phase. SNO+ has finished filling the detector in May 2022, and preparing for the ^{130}Te phase.

This thesis consists of author's major contributions to the experiment: i) calibration analysis described in chapter 7, and ii) the background analyses discussed in chapter 6 and chapter 7.

Chapter 5 focuses on the calibration of SNO+ detector using ^{16}N calibration source. The tagged 6.1 MeV γ's from ^{16}N provided the primary energy calibration data in the water phase. Furthermore, the source was deployed externally throughout the scintillator filling process, and the data was used for various calibration purposes such as studying the scintillation light yield, verifying the reconstruction algorithms, characterizing the scintillation timing, and studying the Cherenkov signal in liquid scintillator.

The second part of my analysis focuses on background analyses in SNO+. Chapter 6 describes a model that I have used to estimate the effective attenuation length of the detector in scintillator phase. The model was used to fit the tagged ^{214}Po events in scintillator phase, and estimate the effective attenuation length. The result is consistent with other studies.

Moreover, chapter 7 focuses on the external backgrounds. A set of timing and angular classifiers have been developed, and originally optimised to distinguish the external backgrounds from $0\nu\beta\beta$ signal. I have utilised these classifiers to investigate their performance for the detectable solar ν signals. The classifiers found effective, however it is demonstrated that the performance can be significantly improved by taking advantage of supervised learning methods. `ROOT TMVA` was used for this classification study. Furthermore, I have used the partial-fill scintillator data to estimate the level of the external backgrounds. The 2.6 MeV γ signal from the external ^{208}Tl is identified in partial-fill. Furthermore, the level of external ^{208}Tl γ's from the hold-down ropes are estimated by taking advantage of their angular symmetry. The estimated result is consistent with previous measurements taken in water phase.

Moreover, I have used the vertical displacements of the AV to estimate the creep rate of the hold-down rope system during the partial-fill period. This analysis is described in appendix A. Furthermore, the long-term stability tests of the Tensylon fibres are described in the second part of appendix A. Finally, the leaching model is briefly described in appendix B. I have developed this model as part of my MSc. research. During my first year of Ph.D, I had the chance to complete the model and develop a simple `python` tool to estimate the surface activity, and the level of leached isotopes for different filling scenarios.

Acknowledgments

There are many people without whom this work would not have been possible. First of all, I would like to thank my supervisor, Christine Kraus for her continual support of my research, for her guidance, patience and her remarkable perseverance. Her supervision has given me the freedom to become independent in my work.

I had the pleasure of sharing an office at Laurentian with many wonderful friends: Jamie Grove, Adil Hussain, Pooja Woosaree, Ingrida Semenec, Matt Depatie. Thanks for all the chats, coffees, potlucks, Friday workshops, and the weekly challenges throughout Covid.

I would also like to thank Ryan Bayes for all the helpful discussions. Your witty sense of humor made the calibration shifts much more fun.

I would also like to thank all the SNO+ members and the SNOLAB crew for all the good times working underground, and for all the karaokes.

I would also like to thank my committee members, Aleksandra Bialek, Caio Licciardi, Marcin Kuzniak and Nelson Belzile. This work would not have been possible without your support.

I would like to thank my beloved family for their continual support throughout my studies. I would also like to thank Jess Blaauw, Mike Schwendener, Jen Davidson, Carrie Regenstreif, Doug Giblin, Kristina Donato and Niranga Munasingh for being my best friends in Sudbury. Finally, I would like to thank everyone who went out of their ways to give me a lift for early SNOLAB cages.

Table of Contents

List of Tables

List of Figures

xii

List of Acronyms

ADC: Analog to digital converter

AV: Acrylic vessel

CNO: Carbon, nitrogen, and oxygen (neutrinos), a fusion path within the Sun that has not yet been well measured, but produces a measurable flux of neutrinos

DT generator: Deuterium-Tritium generator. A commercial accelerator that produces fast neutrons that can be used to activate nuclei and produce radioactive calibration sources.

DAQ: Data Acquisition System

ELLIE: External LED/Laser Light Injection Entity

FEC: Front-end card

FPGA: Field-programmable gate array.

FV: Fiducial Volume

GT: Global trigger.

HD ropes: Hold Down Ropes.

HU ropes: Hold Up Ropes.

HTiO: Hydrous Titanium Oxide

LAB: Linear alkylbenzene

ITR: In time ratio.

MC: Monte Carlo.

MTC/A: Master Trigger Card/Analog

MTCD: Master Trigger Card/Digital.

Nhits: Number of fired PMTs (triggering a hit) within the triggering time window.

NSRS: Neck Sense Rope System.

PDF: Probability Density Function

PMT: Photo-multiplier Tube

PMTIC: PMT interface cards.

PMNS Matrix: Pontecorvo-Maki-Nakagawa-Sakata Matrix.

PSUP: Photo-multiplier Tube Structure Support.

SNU: equal to a flux that produces 10^{-36} captures per second per target atom.

SM: The standard model of particle physics.

SSM: The Solar standard model.

TAC: Time to Analog Converter.

TMVA: Toolkit for Multivariate Data Analysis

UI: Universal Interface.

UPW: Ultra-pure water.

URM: Umbilical retrieval mechanism.

β_{14}: $\beta_1 + 4\beta_4$, a classifier based on PMT hit patterns expressed in terms of Legendre polynomials.

Chapter 1: Physics of Neutrinos

1.1 Introduction

Neutrinos are the least understood of the known elementary particles, and perhaps can give insight into some of the most fundamental questions in physics such as the matter anti-matter asymmetry in the universe. Furthermore, the fact that neutrinos rarely interact, and they can easily travel across galaxies and give insights into the fundamental properties of matter from very distant objects such as supernovae, makes the neutrino experiments the frontier of the particle physics. The discovery of neutrino oscillations by Super-Kamiokande and Sudbury Neutrino Observatory (SNO) which confirmed that neutrinos have non-zero mass has provided the only strong direct evidence for the physics beyond the standard model to date [1, 2]. Despite all the progress that has been made by the neutrino experiments in past 25 years, many fundamental questions still remain unanswered. The nature of neutrinos, the absolute mass of neutrinos and their mass states hierarchy, and the role of neutrinos in the early universe are amongst the most fundamental neutrino physics questions yet to be probed.

This chapter gives an overview of the physics of neutrino, describes some of the milestones, and discusses the role of neutrino measurements in developing the beyond the standard model theories.

1.2 The Birth of Neutrinos

The neutrino was predicted by Wolfgang Pauli, and proposed in a letter to a conference in radioactivity in 1930 [3]. Pauli proposed neutrino to save the irrefragable energy conservation law in the β decay process. β decay was modeled as a two body process, in which the energy of the recoiling nucleus and the emitted β should be constrained, however many observations showed a continuous energy spectrum for β particles starting from zero to a maximum value known as the end point [4]. Neutrino was introduced as the third particle coming out of the process, taking away the missing energy. Pauli described neutrino as an electrically neutral, low-mass, spin-1/2 particle that cannot be detected.

Inspired by Pauli's work, Enrico Fermi developed the first theory of weak interactions, and incorporated neutrino in his model to explain the β-decay process [5]. However, it took until 1956 that the first experimental observation of neutrinos was made by Cowan and Reines [6]. They detected neutrinos through the delayed coincidence signal from anti-neutrinos generated in a nuclear reactor [6], demonstrated in equation 1.1.

$$\bar{\nu}_e + p \rightarrow n + e^+ \tag{1.1}$$

This interaction is known as inverse β decay. The positron would annihilate almost instantly and produce two γs, as the prompt signal. The neutron thermalizes and gets captured in about 5μs, and would emit a delayed γ.

Followed by this experiment, Ray Davis used dry cleaning fluid[1]to perform an experiment to detect neutrinos through the neutrino capture interaction described below [7]:

$$\nu_e + {}^{37}\text{Cl} \rightarrow \text{e}^- + {}^{37}\text{Ar} \tag{1.2}$$

Davis developed a technique to extract the Argon atoms and count them [7]. However, he did not observe any increase in the number of counted ^{37}Ar when the reactor

---

[1]The dry cleaning fluid is rich in chlorine.

was operating. This result suggested that neutrinos are different than anti-neutrinos produced in β-decays. An electron neutrino is usually accompanied by an electron, the associated lepton, and an electron anti-neutrino is produced with a positron. This could be explained by the lepton number conservation law proposed by Konopinski and Mahmoud in 1953 [8].

The muon neutrinos, ν_μ are discovered by studying the decay of cosmic muons [9]. In 1962, Lederman, Schwartz and Steinberger conducted an experiment in Brookhaven National Laboratory [10], and confirmed that ν_μ are different than ν_e. They showed that unlike electron neutrinos, muon neutrinos do not participate in interactions such as inverse β-decay.

The third generation of neutrinos, ν_τ was proposed after discovery of τ leptons, and was not detected until 2000 by the DONUT collaboration [11].

1.3   Neutrinos in Standard Model of Particle Physics

Fermi's theory of weak-interactions could successfully explain most of the phenomena involving weak interactions up until 50s. In 1956, Chien-Shiung Wu conducted an experiment to test the parity transformation in the β decay of ^{60}Co$\rightarrow^{60}$Ni, questioning what most physicists had considered to be a trivial law of nature; the laws of physics should remain invariant under the parity transformation. She cooled the cobalt atoms down to 0.001K, and used a magnetic field to align the spin of their nuclei, then measured the orientation of the electrons produced in β-decay process [12]. The result was quite surprising, and demonstrated that the electrons are preferentially emitted anti-parallel to the original nuclei spin, in other words, the parity was maximally violated. Moreover, Garwin and Lederman showed that parity is violated in the decay of μ [13]. The results suggested that weak interactions only engage left-handed electrons/neutrinos and right-handed positrons/anti-neutrinos, in other words, the neutrinos/anti-neutrinos are always left/right handed. This required a new algebraic

model for weak interactions.

After Wu's experiment, Feynman and Gellmann developed a model for weak interactions known as V-A (vector, axial-vector) theory [14]. They formulated the weak interactions so they would maximally violate parity. This theory is one of the preliminary blocks of the electro-weak model developed by S. Weinberg [15], and later incorporated in what is known as the standard model of particle physics.

The standard model of particle physics (SM) is a brilliant theory developed by several generations of physicists in 50s, 60s and 70s [14, 15, 16, 17]. SM formulates the strong nuclear and electro-weak interactions using algebraic groups, and has successfully explained most of the experimental data to date. Three generations of neutrinos are incorporated into the SM as mass-less, spin 1/2, left-handed particles till the observations of neutrino flavour transformation in the 90s required the introduction of non-zero mass for neutrinos [2, 1], the only direct observation for beyond the standard model. The next sections focus on the neutrino mass and its implications.

1.4 Neutrino Mass and Beyond the Standard Model

The discovery that neutrinos have non-zero mass came from two main observations; i) the observed deficit in measured ν_e solar neutrinos, known as the solar neutrino problem, and ii) the observed deficit in atmospheric neutrinos. Inspired by Kaon oscillations, a model was developed for neutrino flavour oscillations that could explain the observed deficit, which necessitated non-zero mass states for neutrinos. The neutrino flavour oscillations was confirmed by the solid measurements from SNO and Super-Kamiokande, leading into the 2015 Nobel prize in physics for Arthur McDonald and Takaaki Kajita. This section gives an overview of the evidences for neutrino oscillations, discusses the neutrino oscillations model, and explains what is known, and what is yet to be determined about neutrino masses.

1.4.1 Solar Neutrino Problem

The standard solar model (SSM) explains the energy generation mechanisms in the sun. The model was developed by Bachall et. al. [18] by 1960s, and describes that the solar energy is produced through two main thermo-nuclear fusion chains: i) *pp* and *pep* chain which is the dominant contributor shown in figure 1.1, and ii) the CNO cycle shown in figure 1.2. The model could also predict the flux of solar neutrinos at the surface of earth from different interactions on those cycles. Figure 1.3 shows the flux of solar neutrinos versus their energies.
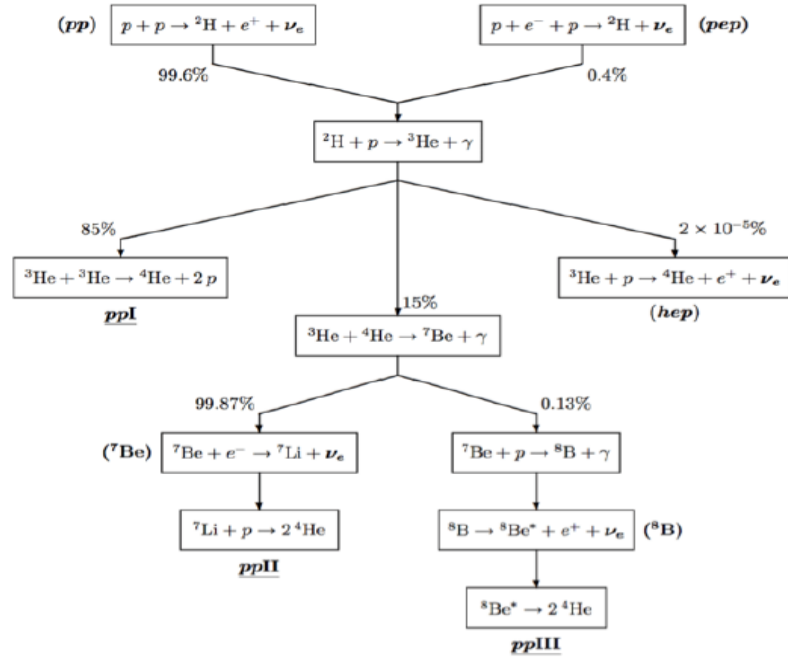
Figure 1.1: *pp* and *pep* solar fusion cycles from SSM. The figure is taken from [19].

In 60s, Davis proposed an experiment to measure the solar neutrinos, and verify the SSM [20]. Using dry cleaning fluid, the experiment detected solar neutrinos upon their capture on chlorine, demonstrated previously in equation 1.2. This interaction has the threshold of 0.8 MeV, which made the experiment sensitive to *pep*, CNO and ^{8}B neutrinos. He also improved the technique that he had developed to extract ^{37}Ar back in 50s [20]. They measured the capture rate of solar neutrinos of 3 SNU, where 1 SNU is equivalent to a flux that produces 10^{-36} captures per second per target
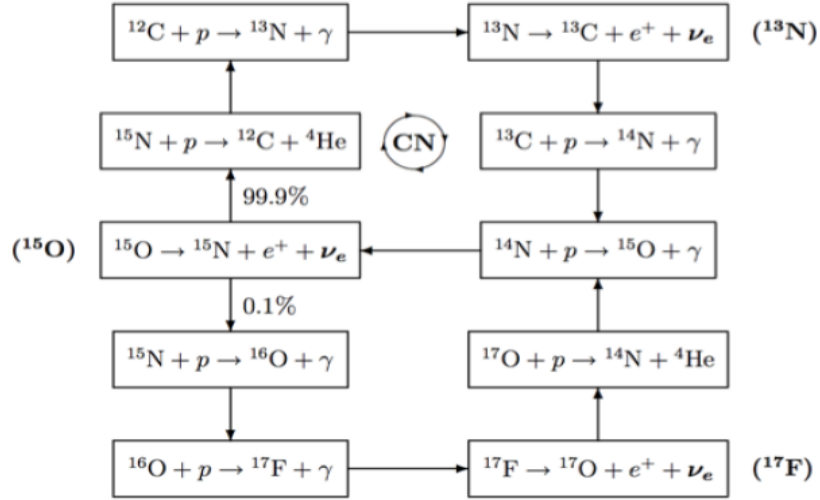
Figure 1.2: The CNO solar fusion cycles from SSM. The figure is taken from [19].

atom. They published their results in a paper in 1968 [7]. Their result confirmed the thermonuclear fusion origin of sun's energy, and also ruled out the CNO as the dominant cycle since they would have produced a flux of neutrinos up to 35 SNU [21]. However, the measured flux was not quite consistent with the SSM prediction of 6 SNU from pp cycle. The discrepancy only grew larger when the large Cherenkov detectors made measurements of ^{8}B solar neutrinos in 80s. Kamiokande detector measured the solar neutrinos over 8 years, and the flux was found to be less than 50% of what SSM predicted [22]. Furthermore, in 1998, Super-Kamiokande experiment measured the ^{8}B solar neutrinos to be $0.358^{+0.009}_{-0.008}(stat)^{+0.014}_{-0.010}(syst)$ of the SSM prediction [1]. Moreover, the other experiments such as GALLEX and SAGE with lower energy threshold measured pp solar neutrinos to be about 50% of what is predicted by SSM [23, 24]. This discrepancy known as the solar neutrino problem, became very controversial in physics community for years.

1.4.2 Atmospheric Neutrinos

The atmospheric neutrinos are created when high energy cosmic rays hit the atmosphere and create hadronic showers. The $\pi^\pm$ created in the atmosphere decays into $\mu^\pm$ and $\bar\nu_\mu/\nu_\mu$. The produced $\mu^\pm$ have a half-life of 1.56 μs and decays into $e^\pm$ and a
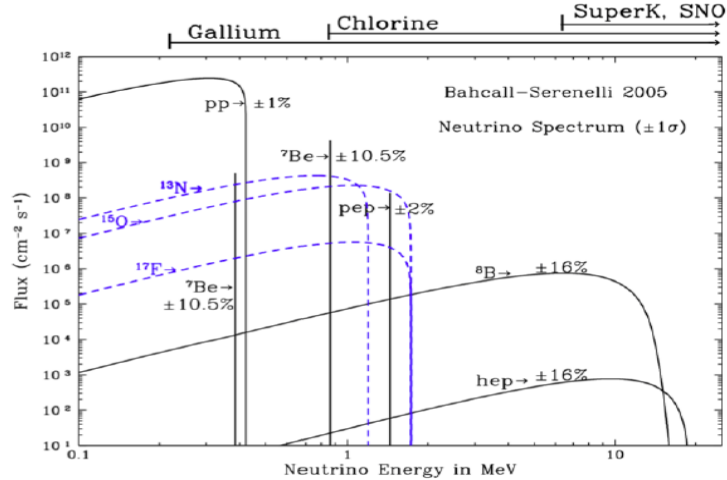
Figure 1.3: The flux of solar neutrinos at the surface of earth. The annotations above the plot show the energy ranges of neutrinos that could be detected in the detectors, taken from [19].

$\bar{\nu}_\mu/\nu_\mu$ and a $\nu_e/\bar{\nu}_e$. The following shows the decay process of atmospheric $\pi^\pm$:

$$\pi^\pm \rightarrow \bar{\nu}_\mu/\nu_\mu + \mu^\pm \rightarrow e^\pm + \bar{\nu}_\mu/\nu_\mu + \nu_e/\bar{\nu}_e \qquad (1.3)$$

It can be seen from equation 1.3, there would be 2 ν_μ created for every atmospheric ν_e, $R_{atm} = \frac{\Phi(\nu_\mu)}{\Phi(\nu_e)} = 2$. The Kamiokande and IBM experiment measured the atmospheric neutrinos through elastic-scattering off an electron (ES), and charge current (CC) interactions, and found the ratio to be significantly less than 2 [25, 26]. Furthermore, Super-Kamiokande experiment observed the same significant deficit of atmospheric ν_μ [27]. This discrepancy became known as the atmospheric neutrino anomaly.

1.4.3 Neutrino Oscillations

In order to explain the controversial solar- and atmospheric-ν deficits observed by several neutrino detectors, an extension to SM was necessary. The most successful solution is known as the neutrino flavour oscillations, a model that had been developed from the work of several theoretical physicists in 60s, 70s, and 80s [28, 29, 30, 31, 32]. Perhaps, Pontecorvo was the first who proposed $\nu \leftrightarrow \bar{\nu}$ oscillations inspired by kaon oscillations [28]. Inspired by Pontecorvo's work, Maki, Nakagawa and Sakata de-

veloped a model for neutrino flavour oscillations [30]. Furthermore, the model was completed by Blineky, Pontecorvo, Eliezer and Swift in 70s [31, 29]. In addition, Wolfenstein, Mikheev and Smirnov extended the model to incorporate the neutrino oscillations in matter [32]. The neutrino oscillations model relies on the argument that neutrinos have non-zero mass, and their three mass eigen-states $|\nu_{k=1,2,3}\rangle$ are mis-aligned with their three flavour states $|\nu_{\alpha=e,\mu,\nu}\rangle$. The mass and the flavour eigen-states are both complete sets of basis of the space, and therefore there is a unitary operator U that can transform the flavour eigen-states into the mass eigen-states. The matrix representation of this operator U_{kj} is known as Pontecorvo-Maki-Nakagawa-Sakata (PMNS) matrix which is discussed later. Neutrinos participate in weak interactions in their flavour states but propagate in space in their mass states. For instance, the flavour state of a neutrino created in an electron flavour state, $|\nu_e\rangle$ will evolve over time as it propagates, and the time evolution can be described by a time evolution operator $T_{flavour}$ as follows:

$$|\nu(t)\rangle = T\,|\nu_e\rangle \tag{1.4}$$

where $\nu(t)$ can be written as a linear combination of three flavour states. For instance, the probability of detecting this neutrino in the μ flavour state after time t would be:

$$P_{e\to\mu} = |\langle\nu_\mu|\,T\,|\nu_e\rangle|^2 \tag{1.5}$$

Since T is not diagonal in flavour basis, the probability is non-zero. However, T is diagonal if written in mass basis.

$$T_{mass} = \begin{pmatrix} e^{-iE_1 t} & 0 & 0 \\ 0 & e^{-iE_2 t} & 0 \\ 0 & 0 & e^{-iE_3 t} \end{pmatrix} \tag{1.6}$$

where T in flavour basis would be $UT_{mass}U^\dagger$, and E_i is the energy of the ith mass state. In the case of two flavour oscillations, as it is often the case, the unitary matrix U would become a 2×2 unitary matrix, hence can be presented in terms of a single angle θ, and written as follows:

$$
\begin{pmatrix}
\cos\theta & \sin\theta \\
-\sin\theta & \cos\theta
\end{pmatrix}
\tag{1.7}
$$

Therefore, the probability of $P_{e\to\mu}$ can be calculates as follows:

$$
Pe \to \mu = \sin^2 2\theta \sin^2\left(\frac{\Delta E_{12}t}{2}\right)
\tag{1.8}
$$

Neutrinos are relativistic particles so their energy should be calculated accordingly:

$$
E_i = \sqrt{p^2 + m_i^2} \sim p + \frac{m_i^2}{2p}
\tag{1.9}
$$

Moreover, experiments usually care about the probability of detecting a certain flavour neutrino which propagated over a certain distance L, known as baseline. Therefore, the probability can be written in terms of L, assuming $t = \frac{L}{c}$ and $E \sim p$. Therefore, the probability for a two flavour neutrino oscillations can be written as:

$$
P_{e\to\mu} = \sin^2 2\theta \sin^2\left(1.27\frac{\Delta m_{21}^2[eV^2.km]}{E[GeV]}\right)
\tag{1.10}
$$

It can be seen from equation 1.10 that the probability is a function of the baseline L, the energy E, the squared mass difference $\Delta m_{21}^2 = m_2^2 - m_1^2$, and the value of mixing angle θ. Therefore, the the mixing angle and Δm_{21}^2 can be determined by measuring the neutrino flux over different baselines and looking at various energies.

In the case of three flavour oscillations, the PMNS unitary matrix can be written in terms of three mixing angles ($\theta_{21}, \theta{13}, \theta_{23}$), and a CP-violation phase. Furthermore, there would be three squared mass differences, Δm_{21}^2, Δm_{31}^2 and Δm_{32}^2, which two of

them are independent.

1.4.4 Confirmation of the Neutrino flavour Oscillations; The Results from the SNO and Super-K.

The results from SNO and Super-Kamiokande confirmed the neutrino flavour oscillations as the best explanation to the solar neutrino problem and the atmospheric neutrino anomaly. The SNO was a large Cherenkov detector filled with about 1kT of heavy water. Taking advantage of heavy water, SNO could detect neutrinos through neutral current interactions via breaking up of the deuterium nuclei as follows:

$$\nu_\alpha + D \rightarrow n + p + \nu_\alpha \tag{1.11}$$

The neutral current interaction are mediated by Z bosons, hence they are equally sensitive to all flavours of neutrinos. The produced free neutron captured on hydrogen nucleus, and produced a γ which is the key signature to identify this interaction [33]. Furthermore, SNO could detect neutrinos through two other interactions. The charged current interactions mediated by charged W bosons which are only sensitive to electron type neutrinos

$$\nu_e + n \rightarrow p + e^- \tag{1.12}$$

In addition, the elastic scattering (ES) interactions mediated by Z bosons for all type of neutrinos. However, electron type neutrinos can participate in ES also by exchanging W bosons, therefore ES has a larger cross section for ν_e than ν_μ and ν_τ [34][2]. Through these three interactions, SNO could estimate the flux of electron type solar neutrinos and the total neutrino flux. Figure 1.4 summarizes the measured solar neutrino flux by SNO. The collaboration published their results from the first phase of the experiment in 2002 [2], and the measured fluxes were as follows:

---

[2]The cross-section of ES for ν_e is about 6 times larger than $\nu_{\mu,e}$.

$$\Phi_e = 1.76^{+0.05}_{-0.05}(\text{stat})^{+0.09}_{-0.09}(\text{syst}) \times 10^{-6} \text{cm}^{-2} \text{sec}^{-1} \tag{1.13}$$

$$\Phi_{\mu,\tau} = 3.41^{+0.45}_{-0.45}(\text{stat})^{+0.48}_{-0.45}(\text{syst}) \times 10^{-6} \text{cm}^{-2} \text{sec}^{-1} \tag{1.14}$$
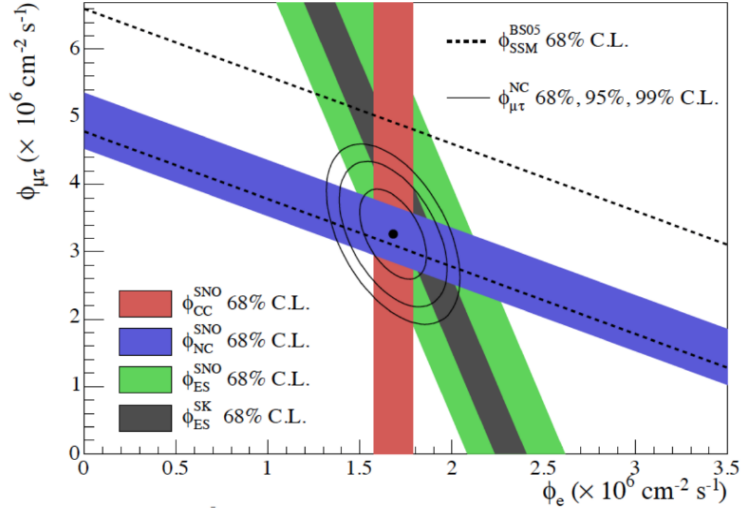
Figure 1.4: The electron type neutrino flux along with $\nu_{\mu,\tau}$ flux measured in SNO and Super-Kamiokande, taken from [2].

The results from the SNO are shown in figure 1.4. The total neutrino flux was consistent with what is predicted in SSM, and the electron type neutrino flux was found to be around 1/3 of the total neutrino flux, which was consistent with previous measurements. The result from the SNO confirmed the solar neutrino flavour transformation. Furthermore, Super-Kamiokade measured the flux of atmospheric ν_μ as a function of L/E, and confirmed the neutrino flavour oscillations. Figure 1.5 shows the measured flux by Super-Kamiokande along with the neutrino oscillations model and two other alternative models fit to the data.

The three flavour oscillations model has several free parameters to be determined: the three mixing angles θ_{ij} and the CP-violation phase δ_{cp} are the free parameters incorporated in PMNS matrix as shown in equation 1.15, and the squared-mass differences
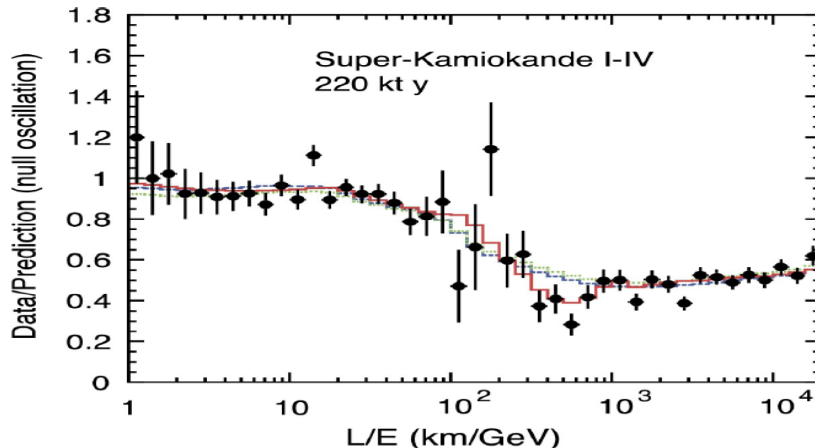
Figure 1.5: The ratio between the observed and the predicted flux of atmospheric ν_μ vs. L/E measured by Super-Kamiokande. the best fit found to be the neutrino oscillations model (red). The neutrino decoherence model (dotted line), and the neutrino decay model (dashed line) are also shown [27].

Δm_{ij}.

$$
U_{\alpha k} = \begin{pmatrix} 1 & 0 & 0 \\ 0 & c_{23} & s_{23} \\ 0 & -s_{23} & c_{23} \end{pmatrix} \times \begin{pmatrix} c_{13} & 0 & s_{13}e^{-i\delta} \\ 0 & 1 & 0 \\ -s_{13}e^{i\delta} & 0 & c_{13} \end{pmatrix} \times \begin{pmatrix} c_{12} & s_{12} & 0 \\ -s_{12} & c_{12} & 0 \\ 0 & 0 & 1 \end{pmatrix} \tag{1.15}
$$

where $c_{ij} = \cos\theta_{ij}$, and $s_{ij} = \sin\theta_{ij}$. These parameters should be constrained using the experimental data. In the case of Solar neutrinos, the flavour oscillations are mostly described by Δm_{21}^2 and θ_{21} since ν_e is the only type of neutrino produced in sun. Furthermore, atmospheric neutrinos are governed by Δm_{23} and θ_{23}. Combining the results from the solar neutrino and the reactor neutrino experiments Δm_{21}^2 found to be $7.53\pm0.18 \times 10^{-5}$ eV^2, and the best fit for the mixing angle found to be $\theta_{12} = 34.5^{\circ+1.2}_{-1.0}$ [35]. Δm_{32}^2 is determined from atmospheric neutrino and long baseline neutrino beams from accelerators such as T2K. However, in this case only the absolute value of squared-mass difference can be determined and the sign is unknown. The best fit for $|\Delta m_{32}^2| = 2.50 \pm 0.03$ [35]. This ambiguity leads into two different mass hierarchies for the neutrinos. Normal hierarchy (NH) which corresponds to m_3 mass

normal hierarchy (NH)　　　　inverted hierarchy (IH)
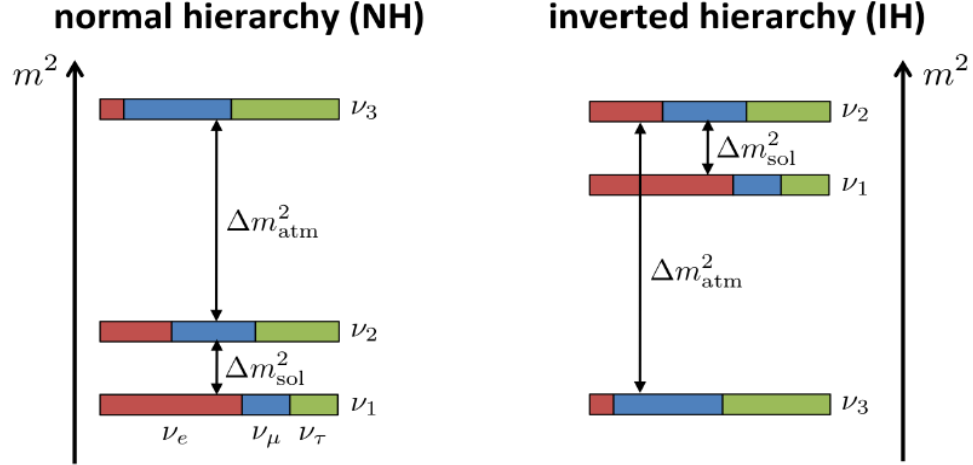
Figure 1.6: Two arrangements of neutrino mass states, normal hierarchy (NH) on the left, and inverted hierarchy (IH) on the right.

state being heavier than m_1 and m_2, and the inverted mass hierarchy (IH) in which m_3 is the lightest mass state. Figure 1.6 demonstrates two possible arrangements for the neutrino mass states. The future generation of accelerators can potentially probe longer baselines, and therefore can detect the flavour oscillations in matter and determine the sign of Δm_{32}^2.

The other parameter that needs to be determined is δ_{cp} which represents the CP-violation in flavour oscillations (e.g. $P(\nu_e \rightarrow \nu_m u) \neq P(\bar{\nu}_e \rightarrow \bar{\nu}_\mu)$). This parameter can be constrained using accelerator experiments which can produce both ν and $\bar{\nu}$ [36].

1.4.5 Neutrino Absolute Mass and Neutrino Mass Mechanism

The other unknown is the neutrino absolute mass and its origin. The upper limits on the neutrino mass comes from the direct neutrino experiment by kinematic studies of β decay. In β decay, the end point of the electron energy spectrum is altered by the value of neutrino mass. KATRIN experiment studies the β decay of tritium, and has set the lowest upper limit of $m_\nu < 0.7$eV at 90% confidence level [37]. Furthermore, indirect measurements of total neutrino mass comes from cosmological measurements. The results from *Planck* places an upper limit of $\sum_i m_i < 0.45$eV for

the sum of neutrino masses [38].

Fermions such as electrons gain their mass through Higgs mechanism in SM [39]. Treating neutrinos as Dirac particles, one can write the Lagrangian of Higgs field interacting with the right-handed and left-handed components of neutrino as follows:

$$\mathcal{L}_{\text{mass}}^D = -\frac{gv}{\sqrt{2}}(\bar{\psi}_R\psi_L + \bar{\psi}_L\psi_R) \tag{1.16}$$

where g is the coupling of the neutrino field to the Higgs field, v is the vacuum expectation value of the Higgs field, and $\psi_{R/L}$ is the left-handed/right-handed components of the neutrino field, and the bar denotes the adjoint component of the Dirac neutrino. In this case, the mass of the Dirac neutrino is estimated to be:

$$m_D = \frac{gv}{\sqrt{2}} \tag{1.17}$$

In order to gain mass through this mechanism, the neutrino should be a Dirac particle, in other words, neutrino and anti-neutrino should be two distinct particles. Furthermore, both right-handed and left-handed components should exist for neutrinos. Since the weak field only couples to the left-handed leptons, the right-handed neutrino known as sterile neutrino should be incorporated in this model as a particle that only interacts with gravity.

There is an alternative mechanism that was postulated by Majorana [40]. Majorana suggested that some neutral particles can be their own anti-particles[3], in other words $\psi^C \sim \psi$, where ψ^C is the charge conjugate of ψ. These particles became known as Majorana particles. As the only neutral fermions, neutrinos seem to be good candidates to be their own anti-particles. The Lagrangian of Majorana neutrino mass can be incorporated in SM as follows:

$$\mathcal{L}_{\text{mass}}^L = -m_L(\bar{\psi}_L^C\psi_L + \bar{\psi}_L\psi_L^C) \tag{1.18}$$

---

[3]$\bar{\psi} = i\gamma^2\psi^*$ to satisfy Dirac equation.

where m_L is the Majorana mass of left-handed neutrino, which formulates the direct coupling between the neutrino and anti-neutrino field.

The most general mass Lagrangian contains both the Dirac mass term and the Majorana mass term, so that the neutrino would gain mass through both coupling to the Higgs field as well as coupling to the anti-neutrino fields. This mechanism also requires a heavy right-handed neutrino which is not the same as the light sterile neutrino mentioned earlier.

1.5 Neutrino-less Double Beta Decay

This section describes a process known as neutrino-less double beta decay ($0\nu\beta\beta$) which can be used to probe the Majorana nature of neutrinos. First, the double beta decay is discussed, and then $0\nu\beta\beta$ is described, and some of the experiments searching for this process are outlines.

1.5.1 Double Beta Decay

In 1935, M. Goeppert-Mayer proposed a decay process for unstable nuclei known as double beta decay ($2\nu\beta\beta$) [41]. The nucleus undergoes two simultaneous β decays in this process, which results in an increase of a charge Z by 2, and emission of two electrons and two anti-neutrinos, demonstrated as follows:

$$(A, Z) \rightarrow (A, Z + 2) + e^- + 2\bar{\nu}_e + 2e^- \tag{1.19}$$

Figure 1.7a shows the Feynman diagram for this process. $2\nu\beta\beta$ is proposed for unstable nuclei in which the single β-decay is forbidden due to the higher binding energy of the daughter nucleus $(A, Z + 1)$ compared to (A, Z). Figure 1.7b demonstrates the binding energy of nuclei vs. their atomic number Z. There are 35 known naturally occurring isotopes that can undergo $2\nu\beta\beta$ decay, and the process has been observed for 20 isotopes to date [42]. $2\nu\beta\beta$ is a second order weak process, hence has a long half-life (10^{18}-10^{21} years).
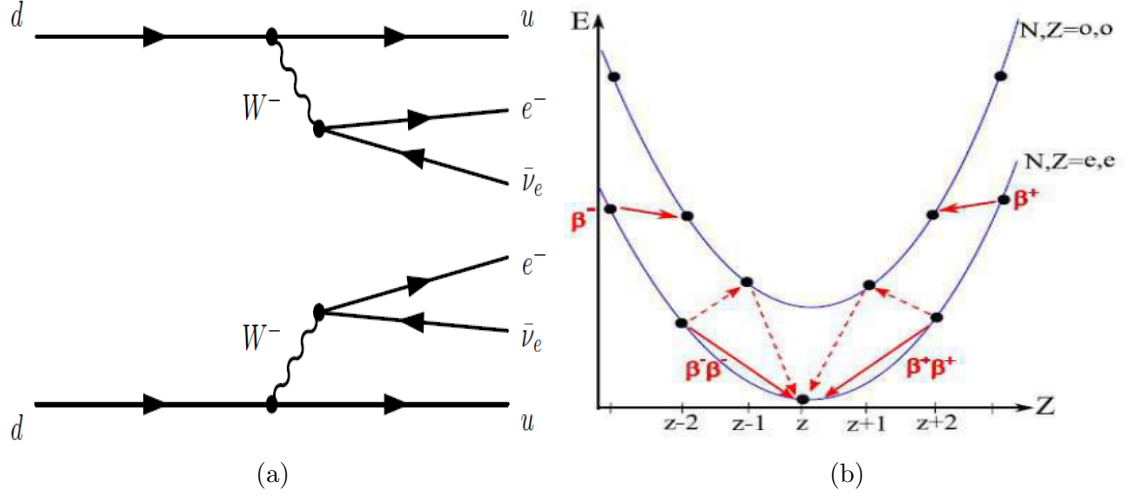
Figure 1.7: (a) The Feynman diagram of double beta decay process. (b) The β decay and $2\nu\beta\beta$ decay for nuclei versus atomic number (Z). As it can be seen for some nuclei the β decay is energetically forbidden but $2\nu\beta\beta$ is allowed, taken from [43].

1.5.2 Neutrino-less Double Beta Decay

Neutrino-less double beta decay ($0\nu\beta\beta$) is a hypothetical process as follows:

$$(Z, A) \rightarrow (Z + 2, A) + 2e^- \tag{1.20}$$

Unlike $2\nu\beta\beta$ which is allowed in SM and has been observed, $0\nu\beta\beta$ has never been observed to date. Furthermore, this process violates the lepton number conservation by two units. As it can be seen from figure 1.8, no anti-neutrinos are emitted in this process. The process can be thought of as an anti-neutrino is created at one vertex and a neutrino is absorbed at the other one. This requires neutrino to be a Majorana particle. Moreover, the anti-neutrino needs to flip helicity between two vertices. This helicity evolution (flip) is only possible if neutrino has a non-zero mass.

The rate of $0\nu\beta\beta$ decay can be written as a product of the phase space of the decay $G^{0\nu}$, the nuclear matrix element $M^{0\nu}$, the effective Majorana mass $m_{\beta\beta}$ normalized
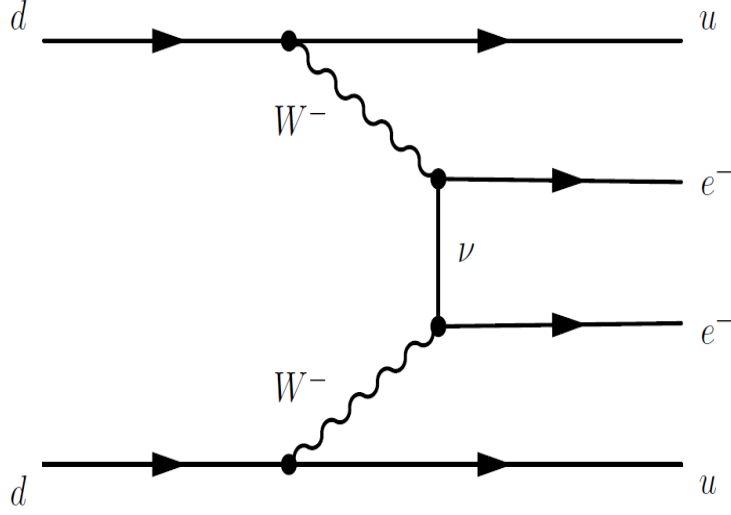
Figure 1.8: Feynman diagram of neutrino-less double beta decay.

by the mass of electron m_e:

$$\frac{1}{T^{0\nu}_{1/2}} = G^{0\nu}|M^{0\nu}|^2 \left(\frac{|m_{\beta\beta}|^2}{m_e}\right) \qquad (1.21)$$

$G^{0\nu}$ depends on the nucleus, more specifically, depends on the $Q_{\beta\beta}$ value of the decay. The nuclear matrix element, $M^{0\nu}$ is the biggest source of uncertainty in the calculation of $0\nu\beta\beta$ rate since it highly depends on the chosen nuclear model [44]. The effective Majorana mass depends on the three neutrino mass eigen-values and the PMNS matrix parameters, and can be calculated as follows:

$$m_{\beta\beta} = \sum_{k=0}^{3} U^2_{\alpha k} m_k \qquad (1.22)$$

Lower m_i would lead into lower rate for the process, in other words, there will be lower chance of helicity flip for the neutrino for lower masses. Figure 1.9 shows the effective Majorana mass versus the lightest neutrino mass eigen-value along with the observation limits [45]. As it can be seen a major portion of the shaded region is yet to be probed.
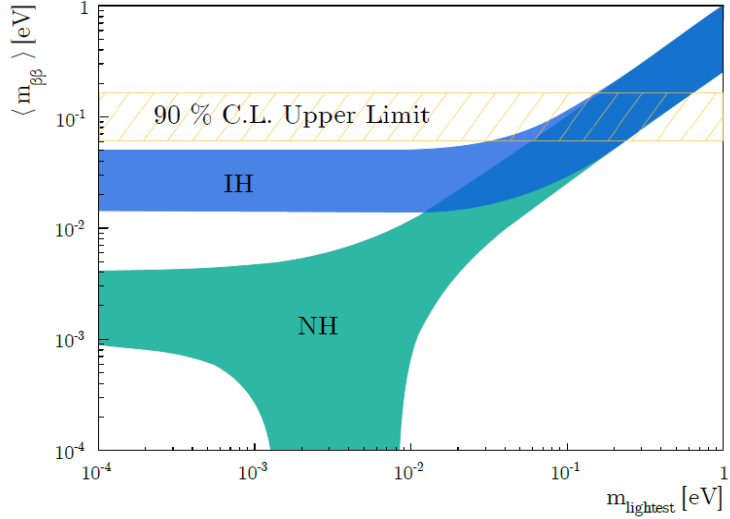
Figure 1.9: The effective Majorana mass versus the lowest neutrino mass eigen state for two mass-state hierarchies along with the best observation limit from KamLAND-Zen [45].

1.5.3 $0\nu\beta\beta$ Experiments

Detecting $0\nu\beta\beta$ decay will confirm the Majorana nature of neutrinos, and furthermore can potentially give insight into the true hierarchy of the neutrino mass states. In addition, cosmological observations suggest an excess amount of quarks over anti-quarks to be 1 part 10^9 in the early universe. The origin if this broken symmetry and the interactions involved are still unknown. However, the discovery of heavy Majorana neutrino can provide an explanation for the matter/anti-matter asymmetry in the universe through a process known as leptogenesis. The asymmetry between leptons and anti-leptons could be transferred to the baryon sector [46].

Since no neutrinos are produced in $0\nu\beta\beta$, almost the entire energy of the decay is carried away by the electrons. Therefore in a detector with a perfect energy resolution, the energy spectrum of $0\nu\beta\beta$ would be a delta function about the end point of the $2\nu\beta\beta$ spectrum. Thus, in order to detect the 0ν signal, it is crucial to have a good energy resolution. Furthermore, the rate of $0\nu\beta\beta$ is orders of magnitude smaller than $2\nu\beta\beta$ decay. Figure 1.10 illustrates the $0\nu\beta\beta$ and $2\nu\beta\beta$ energy spectra.

A simplified model of a $0\nu\beta\beta$ experiment using N nuclei of the $\beta\beta$ isotope can be obtained to estimate the half-life sensitivity at the confidence level ($C.L.$). Assuming
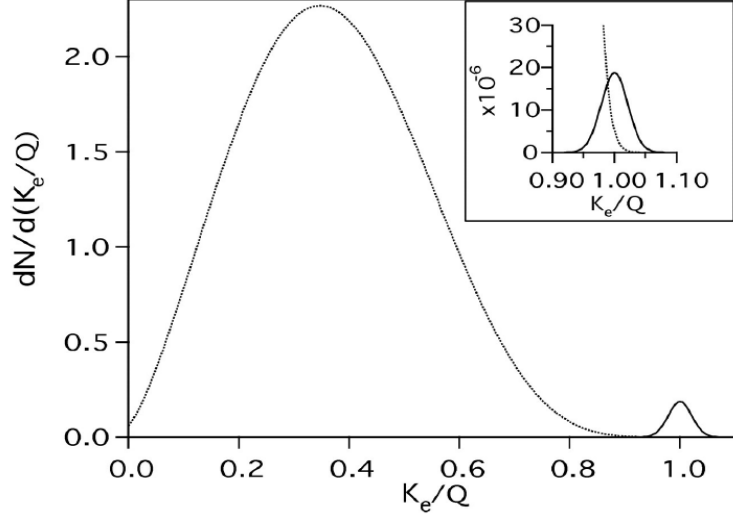
Figure 1.10: Schematic of $2\nu\beta\beta$-decay and $0\nu\beta\beta$ energy spectra. The kinetic energy of two electrons is normalized to the end point energy $Q_{\beta\beta}$. The rate of 0ν is scaled to $10^{-2}/10^{-6}$ of the $2\nu\beta\beta$ rate for the main spectra and the one on the top right respectively, taken from [47].

the background rate of r_B[4] within the energy region of interest, the live-time t, and the detection efficiency ϵ for the experiment, the half-life sensitivity can be estimated as follows:

$$T_{1/2}^{C.L.} = \frac{\ln(2)}{C\sqrt{r_B}}.\epsilon.\sqrt{t}.N \qquad (1.23)$$

Therefore, in addition to the good energy resolution discussed earlier, a large quantity of the isotope, low background level, long live-time, and good detection efficiency are required for the $0\nu\beta\beta$ experiments.

Choices of $0\nu\beta\beta$ Isotope

The choice of isotope is another important factor in the experiments searching for $0\nu\beta\beta$ decays. The followings should be taken into account in choosing the isotope:

- Natural abundance: higher natural abundance of the isotope leads into greater $N_{\beta\beta}$ avoiding the cost and engineering challenges for enriching the isotope.

---

[4]A Poisson distribution is assumed for the background within the region of interest.

Isotope	Experiment	$Q_{\beta\beta}$ [MeV]	Technology	Latest limits (years) 90% C.L.
^{130}Te	CUORE	2.53	Crystal Bolometer	2.2×10^{25} [48]
^{76}Ge	MAJORANA	2.04	Germanium Detector	8.3×10^{25} [40]
^{136}Xe	EXO-200	2.46	Time projection chamber	4.3×10^{24} [49]
^{100}Mo	NEMO-3	3.04	Tracking Calorimeter	6.93×10^{18} [50]
^{82}Se	NEMO-3	2.00	Tracking Calorimeter	2.3×10^{22}
^{116}Cd	NEMO-3	2.81	Tracking Calorimeter	1.0×10^{23} [51]
^{150}Nd	NEMO-3	3.37	Tracking Calorimeter	2.0×10^{22} [52]
^{96}Zr	NEMO-3	3.35	Tracking Calorimeter	9.210^{21} [53]
^{48}Ca	NEMO-3	4.27	Tracking Calorimeter	2.0×10^{22} [54]

Table 1.1: The best current limits on $0\nu\beta\beta$ half-lives of different isotopes along with their $Q_{\beta\beta}$ values.

- The nuclear physics of the isotope: the nuclear structure of the isotope determines the size of the $0\nu\beta\beta$ signal ($|M^{0\nu}|$). Furthermore it determines the rate of $2\nu\beta\beta$ ($|M^{2\nu}|$ which is the major background for the signal. Therefore, lower $2\nu\beta\beta$ rate is desirable for 0ν experiments

- The position of $Q_{\beta\beta}$: larger $Q_{\beta\beta}$ makes it easier to detect 0ν signal with higher efficiencies. The signal would be easier to discriminate if the end point lies further away from natural radioactive signals.

Table 1.1 summarizes some of the 0ν experiments together with their chosen isotopes and their best measured upper limits.

The SNO+ experiment is aiming to search for $0\nu\beta\beta$ decay using ^{130}Te loaded into about 1kT liquid scintillator [55]. ^{130}Te has the highest natural abundance ($\sim$34%) amongst all the $\beta\beta$ isotopes, and has the second best expected ratio of $2\nu\beta\beta$ to $0\nu\beta\beta$ signal after ^{136}Xe [56]. Furthermore, ^{130}Te has good optical properties which allows SNO+ to increase the loading of ^{130}Te until the $2\nu\beta\beta$ signal is dominant. The $Q_{\beta\beta}$ value of ^{130}Te is 2.53 MeV. The major radioactive background in this region is $^{212/214}$BiPo, which can be tagged and rejected using delayed coincidence technique. The SNO+ experiment is described in detail in the next chapter.

Chapter 2: SNO+ Experiment

SNO+ is a multipurpose kilo-tonne scale neutrino experiment, located 2 km underground at SNOLAB in an active nickel mine in Sudbury, Canada. The experiment has a diverse physics program, however the main goal of the experiment is the search for elusive $0\nu\beta\beta$ decay with ^{130}Te loaded into the liquid scintillator cocktail. This chapter describes the SNO+ experiment, provides an overview of the detector, describes different operational phases of the experiment and the associated physics goals. Furthermore, the optics, Data AcQuisition system (DAQ), calibration, and the analysis tools are described in this chapter.

2.1 Detector

SNO+ reuses the Nobel prize winning SNO detector, replacing the heavy water target with the liquid scintillator cocktail. A schematic of the SNO+ detector is shown in figure 2.1. The detector consists of a 12m diameter acrylic vessel (AV) which is suspended in a 6263 m^3 cylindrical shape chamber, known as the cavity [57]. The AV is supported by 10 pairs of Tensylon hold-up (HU) ropes from a platform known as the SNO+ deck. In order to detect the scintillation/Cherenkov photons, the AV is surrounded by $\sim$9300 photomultilier tubes known as PMTs. The PMTs are mounted facing radially inward on a 18m diameter stainless steel structure, known as the PSUP which is held by 15 stainless steel cables from the deck. The cavity volume is filled with about 7000 tonnes of ultra pure water (UPW) which shields the detector against the external background such as γ's from the walls. Furthermore, 91 outward looking PMTs view the cavity volume and can be used to identify and reject cosmic muons.

The next section summarizes the detector upgrades to facilitate the transitioning from SNO to SNO+.
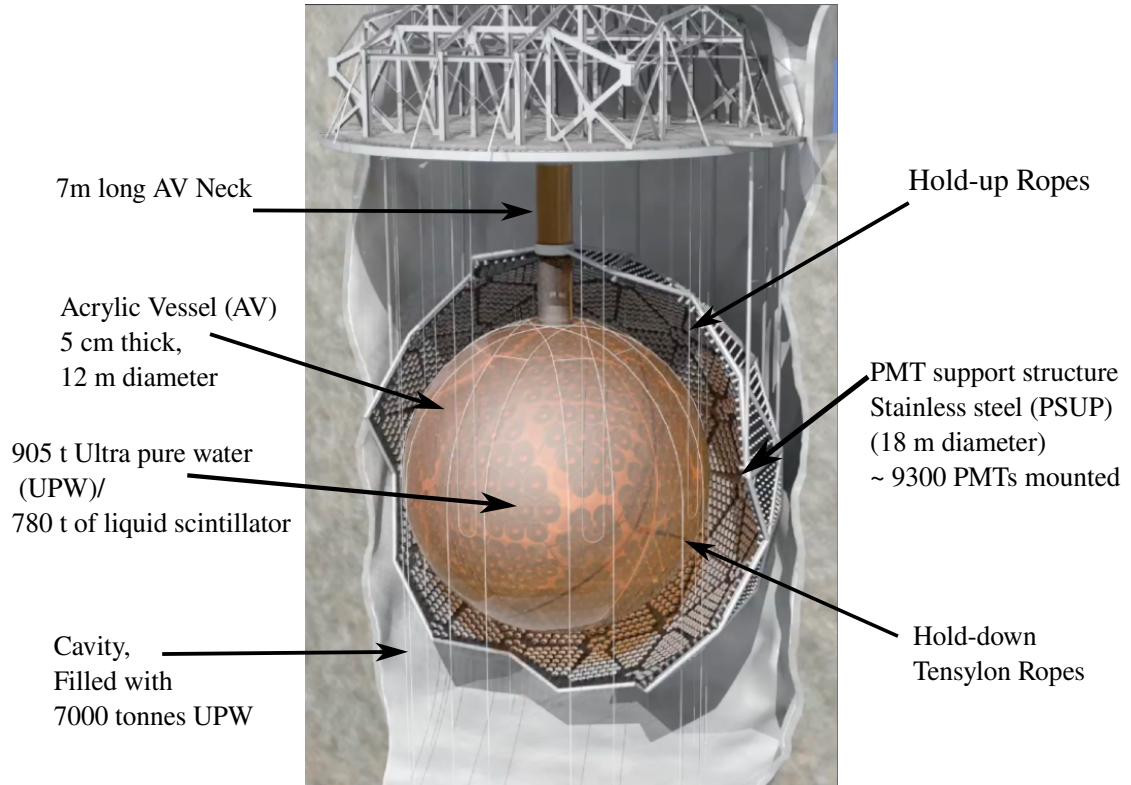
Figure 2.1: Schematic of SNO+ detector, taken from [58].

2.1.1 Detector Upgrades

The SNO+ liquid scintillator is composed of Linear Alkyl Benzene known as LAB loaded with 2,5-diphenyloxazole (PPO) as the primary fluor dissolved in a concentration of about 2g/L[1]. The liquid scintillator cocktail has a much higher light yield ($\sim$50$\times$) compared to the UPW/heavy water Cherenkov signal, therefore SNO+ has a lower energy threshold to sub-MeV energies, and furthermore can achieve much lower energy resolutions of a few $\%\sqrt{E/MeV}$ [59]. LAB has good optical properties and high purity levels directly from the manufacturer. In addition, since LAB is a non-polar compound, it can be purified to about 3 orders of magnitude smaller

---

[1]The PPO concentration can vary in different phases.

concentrations of radio-isotopes than water [60]. In order to achieve the target purity level of roughly 10^{-17}g/g of ^{238}U and ^{232}Th in LAB, a new scintillator purification plant was designed, installed, and commissioned underground at SNOLAB.

The liquid scintillator has a lower density (ρ=0.86g/cm^3) than the surrounding UPW. In order to compensate for the buoyancy force, the hold-down rope system was designed and installed. The hold-down ropes system (HD) consists of 20 high purity polyethylene fiber (Tensylon) ropes, and were laid over the AV around the neck, and on the other end were anchored to the bottom of the cavity [61](see figure 2.1). The HD ropes system is discussed in detail in section A.1. In addition to the HD ropes, the old hold-up rope system (HU) has been replaced with the new Tensylon ropes of 20mm diameter to improve the radio-purity.

There is a significant level of ^{222}Rn in the lab air (= 131$\pm$6.7 Bq/m^3 [62]) which can ingress into the scintillator and increase the background level, therefore the detector must be air-tight. This was accomplished in the SNO experiment by replacing the air volume with boil-off N$_2$ from a liquid nitrogen dewar. Since the old system is not a sealed cover-gas system it does not meet the radio-purity constraints for SNO+, therefore a new system is designed for SNO+. This system consists of three flexible bags ($\sim$240 L), fail-safe pressure relief device (U-tube system) and electro-polished stainless steel tubing [63]. The radon-tight buffer bags are filled with high purity N$_2$ and connected to the detector volume. They isolate the detector from the lab air while balancing out the air pressure difference between the lab environment and the detector volume. The system is expected to reduce the radon ingress by a factor of 10^5 [63].

Furthermore, the Data Acquisition System (DAQ) has been upgraded for the increased light yield, and to handle higher event rates. Section 2.2 describes SNO+ DAQ system.

2.1.2 PMTs

The light detection unit of SNO+ detector is the 8" Hamamatsu R1408 Photomulti-plier Tube (PMT) shown in figure 2.2. A PMT consists of a vacuumed round glass. The photo-electrons (p.e.) are created via photo-electric effect on a thin caesium bial-kali film inside the glass [64]. This thin film is known as photo-cathode. The cathode is held at ground potential, whereas the anode at the base is held at about 2000V, forming a strong electric field inside the PMT. The photo-electrons are accelerated in this electric field, and multiplied by a cascade of secondary emissions in a stack of 9 parallel plates known as dynodes. Finally, the photo-electrons are collected on the anode in the base and the signal (charge) is sent up through a cable. The efficiency of a PMT is defined as the probability of creating p.e in cathode, and furthermore collecting those electrons in anode. The efficiency found to be wavelength dependant, and the average efficiency is measured to be about 13.5% at 440nm.
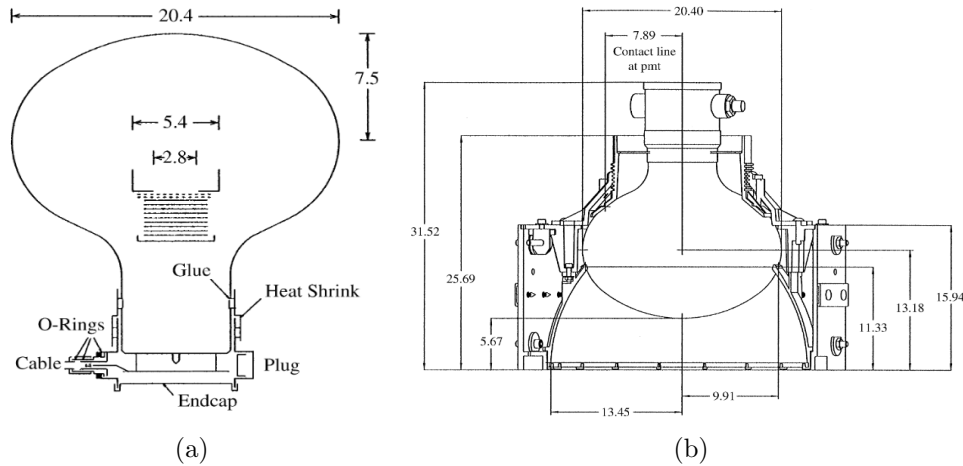
Figure 2.2: (a) shows the 8" R1408 Hamamatsu PMT. The sizes are in cm. (b) shows a cross section of a PMT fitted with a concentrator, taken from [64].

Concentrators

In order to increase the coverage of photo-cathodes, each PMT is equipped with a 27 cm outer diameter reflector buckets known as *concentrators* shown in figure 2.2 (b) [65]. The concentrators increase the PMTs coverage from 31% to about 50% [55].
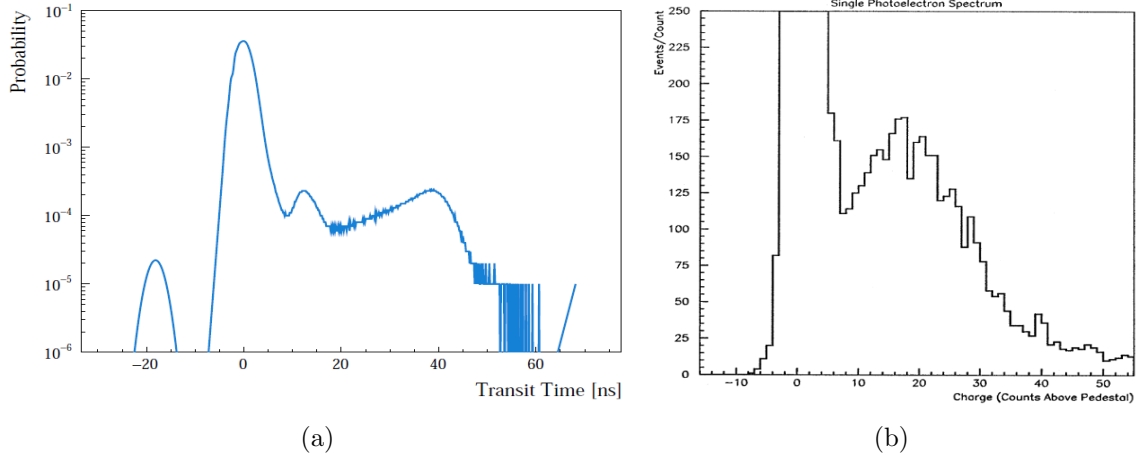
Figure 2.3: (a) shows the transit time probability distribution for a R1408 PMT from RAT. (b) shows the signal from a single p.e. in a PMT along with the dark noise, taken from [64]. The count for the dark noise peak goes up to about 2000 counts.

Timing

The time between the incident photon arriving at photo-cathode and the resulting p.e signal reaching its maximum is known as the PMT transit time. The transit time is determined by the path of p.e inside the PMT. The PMT transit time spread (TTS) needs to be well understood and taken into account in modeling the timing (see 5.4.4). Figure 2.3a shows the probability distribution of a R1408 PMT from a RAT simulation, originally measured by P. Skensved at SNO. The width of the dominant peak found to be about FWHM~3.7ns. The early peak is known as pre-pulsing, and is formed by the photons passing through the photo-cathode, and creating p.e on the dynodes. Furthermore, the late peaks are created by p.e scattering off dynodes back towards the photo-cathode, and creating secondary electrons that are eventually captured on the anode.

Charge

The PMTs always produce a current (charge) at their base without any exposure to light. This current is known as the *Dark Noise*. Figure 2.3b shows the spectra from a single p.e. generated in a R1408 PMT from an in-situ measurement in SNO [64].

The dominant peak about 0 shows the dark noise. The threshold is set at about 1/4 of the average deposited charge by a single photo electron. A PMT is considered *hit* or triggered when this threshold is crossed. The PMTs charge and time are handled via the DAQ system which is discussed in the next section.

2.2   Data Acquisition System (DAQ)

SNO+ DAQ is essentially responsible for reading out the charge and time from the fired PMTs, and grouping them into events. This is achieved by constantly buffering through the collected analog data (charge) by PMTs. Once a global trigger (GT) is issued, the collected charge from PMTs are processed, digitised, and saved, otherwise the data are discarded every 400ns [55].

The GT is issued upon the coincidence of several PMT hits, when the sum of trigger signals issued by each PMT crosses the threshold. Each PMT has a coaxial cable which supplies the high voltage and carries the charge from the PMT anode to a channel on PMT interface card (PMTIC). One PMTIC has a capacity for 32 PMTs (channels). Overall 9728 channels are divided into groups of 512, each hosted by one of the 19 crates located on the SNO+ deck. The PMTICs control the high voltage supply to the PMTs through 4 relays, one relay per 8 PMTs. Furthermore, the PMTICs collect the signal from PMTs, and pass them onto the front end cards (FEC).

The FEC has a discriminator to distinguish the physics signal from the electronic dark noise. The threshold for this discriminator is set to be roughly 1/4 of the charge generated by a single photo-electron as dicussed previously. Then the discriminator signal is summed up at each crate and passed to 7 MTC/A (Master Trigger Card/Analog) boards. Each MTC/A is devoted to a particular type of physics, and would sum the analog signal from crates if that sum crosses the pre-determined threshold. The most important MTC/A trigger for the physics analysis is NHIT100 which is proportional

to the number of hit PMTs within 100ns.

The signal from thr MTC/A is sent to Master Trigger Card/Digital (MTC/D). MTC/D would either ignore or acknowledge the received signal based upon the masked in trigger types. If the trigger pulse is masked in, GT is issued, and the MTC/D would sent back a signal to the FECs. Once the GT is issued, all the channels data are collected and grouped from a period of 180 ns before the GT to 220 ns after the GT. This period is know as the triggering time window. In fact, one event is the PMTs data collected within a single triggering window.

The timing information is measured through a 50 MHz clock, and processed through time-to-analogue-converter (TAC). If the signal crosses channel's threshold, a TAC inside the channel's CMOS chip starts. Upon arriving a GT signal, the TAC stops, and the charge and timing readouts are integrated and saved. If no GT is issued within 410ns, the data are discarded, and the TAC resets automatically.

Aside from the recorded TAC for each channel, there are three charge related parameters which would be integrated and saved upon issuing a GT. QHS: high gain with short integration time interval, QHL: high gain with long integration, and QHX which is a low gain with short integration charge. The short and long integration time intervals are 60 and 390ns, respectively.

2.3   SNO+ Phases
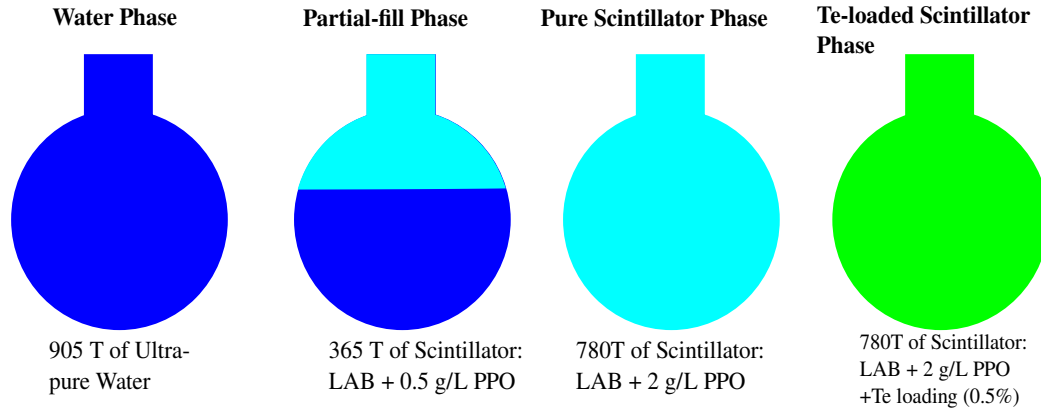
Figure 2.4: 4 different phases of the SNO+ experiment.

The various stages of the experiment is defined based upon the target medium in the AV as illustrated in figure 2.4. The analyses presented in this work mostly include the data from water phase, the partial-fill, and the scintillator phase.

Water Phase

The detector was filled with 905 tonnes of ultra-pure water. The water phase started in May 2017, and ended in July 2019. An extensive energy and optics calibration of the detector was performed within this period. Furthermore, SNO+ made measurements of internal background levels and the external γ's in water phase. SNO+ reached a very low background levels of 4.2×10^{-15}gU/gH$_2$O, and 3×10^{-16}gTh/gH$_2$O in water, and set new upper limits on five modes of nucleon decay [66], and measured the ^{8}B solar neutrinos [67].

Partial-fill

The second phase of SNO+ is known as the partial-fill period. The scintillator filling process was interrupted in March 2020, and paused for about 7 months due to the COVID-19 pandemic. Within this period, the scintillator/water interface was sitting at about 0.75 m with 365 tonnes of LAB sitting on top of ultra-pure water. The $in-$

situ measurement shows the PPO concentration of 0.57g/L $\pm$ 0.05 in this period [68]. Figure 2.5 shows the AV within this period, where the scintillator/water interface is evident. Relatively stable detector condition during this time period provided us with a set of data that was used to understand the detector response for scintillator events. Some of the analyses carried out on partial-fill data is discussed in chapter 5 and chapter 7.
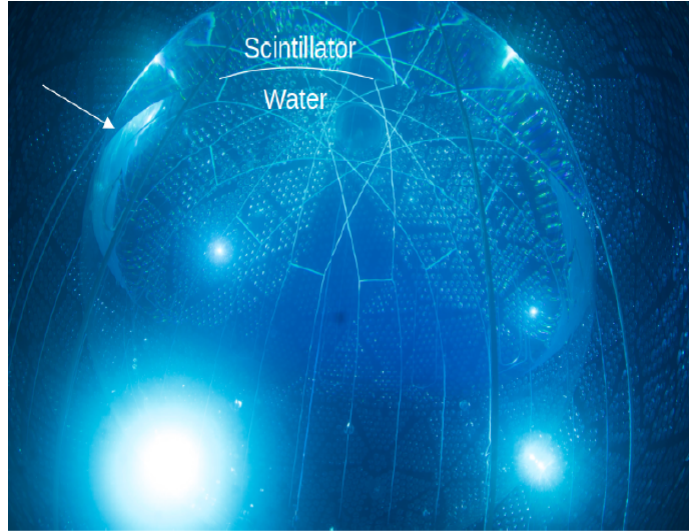
Figure 2.5: A picture of SNO+ AV and scintillator/water interface during partial-fill, taken from one of the bottom cameras.

Scintillator Phase

The pure scintillator phase has started in May 2022 while the detector was filled with 780 tonnes of scintillator, and the PPO concentration was increased to about 2g/L. The data were used to learn the timing profile of the scintillator cocktail [69]. Furthermore, some analyses have been carried out to understand the light yield, the level of backgrounds, and verify the reconstruction algorithms. Chapter 6 describes my analysis carried out on this data that was used to determine the attenuation length. Furthermore, the scintillator data can be used to make measurements of solar neutrinos, geo- and atmospheric-antineutrinos, and furthermore capture the neutrinos from a possible supernova event.

Te-loaded Scintillator Phase

The primary phase of the experiment that involves loading ^{130}Te into the scintillator cocktail for $0\nu\beta\beta$ search. The initial loading target is 0.5% of Tellurium into LAB + 2g/L PPO + 15 mg/L bisMSB[2]. The cocktail is described further in section 2.4.

2.4 Optics

SNO+ essentially registers physics events in form of the photons. Therefore it is crucial to understand the interactions and the processes generating the photons at MeV scale energies in the detection volume. This section describes the main two processes generating light in the detector; i) the Cherenkov mechanism in water and scintillator, and ii) the scintillation processes in scintillator.

2.4.1 Cherenkov Radiation

Cherenkov radiation is emitted when a charged particle is travelling through a dielectric medium with a speed faster than the phase velocity of light in that medium (c/n). A charged particle travelling through a dielectric medium can polarise the molecules around its path. The polarisation field would have enough time to compensate, and remain symmetric about the particle's trajectory when the particle is moving slowly. However, when the particle is moving faster than the local velocity of light, the polarisation field cannot fully compensate, and therefore forms a non-zero net polarisation (dipole) along the particle's trajectory. As an oscillating dipole would radiate, the molecules along the fast charged particle's path get polarised and depolarised, and emit photons. The Cherenkov photons are emitted in form of a cone along the trajectory, known as the Cherenkov cone, shown in figure 2.6. The angle between the trajectory and the emitted Cherenkov photons, θ_c can be expressed as follows:

---

[2]C_24H_22, a fluorescent compound with an excitation peak at 347 nm, and an emission peak at 423 nm [70]
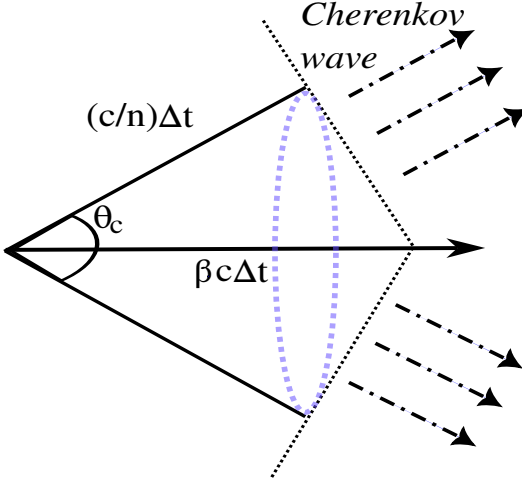
Figure 2.6: Schematic of Cherenkov mechanism when a charged particle is passing through a dielectric material.

$$\cos\theta_c = \frac{1}{n(\lambda)\beta} \tag{2.1}$$

where n is the refractive index of the medium, and $\beta = c/v$. For instance, as $v \to c$ the opening angle, $\theta_c \sim \cos^{-1}(\frac{1}{n})$, which would give an opening angle of $\theta_c \sim 40.5°$ in LAB. The angular distribution of fired PMTs is the key to identify and isolate the Cherenkov signal in scintillator which is discussed in section 5.4.5. The Cherenkov photons are emitted within a very short time window, ~ 100 ps for MeV scale electrons, which is instantaneous compared to the scintillation process. The number of emitted Cherenkov photons per unit length can be calculated by Frank-Tamm formula [71], as follows:

$$\frac{d^2N}{dxdE} = \frac{2\pi\alpha Z^2}{\lambda^2}\left(1 - \frac{1}{\beta^2 n(\lambda)^2}\right) \tag{2.2}$$

where α is the fine-structure constant $\alpha \sim \frac{1}{137}$, and Z is the charge of the particle. The total number of emitted photons within visible range can be estimated by integrating over the particle's track.

2.4.2 Scintillation

A charged particle travelling through a liquid scintillator can excite the electrons. The electrons eventually de-excite after a short relaxation period (∼ps), and fall back to the ground state and emit photons. The scintillation photons are emitted through two main processes: i) the fluorescence which takes place over a short time period of (ns-μs), and ii) the phosphorescence that can be distinguished from fluorescence with their much longer decay time, on the order of ms to a few seconds. The organic liquid scintillators contain aromatic rings[3] which form π-bonds. The π electrons are highly de-localized, and their excited energy states are separated by a few eV. Figure 2.7 shows an example of the energy states of these π electrons in an organic liquid scintillator along with their possible transitions.
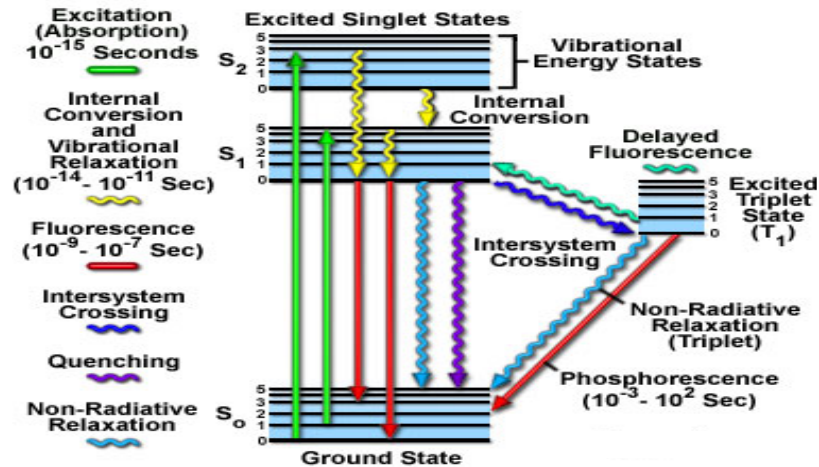
Figure 2.7: The energy states of π electrons in an organic liquid scintillator along with their possible transitions, taken from [72].

A charged particle passing through scintillator can excite the π electrons, either directly through elastic scattering, or indirectly through ionization and then recombination, forming an excited state. In the case of elastic scattering, the electrons always transition up to singlet excited states ($S_{1,2,...}$), since the spin selection law makes it forbidden for transitioning to triplet states. The excited singlet electrons de-excite almost instantly (∼ps) via vibrational relaxation or internal conversion to the lowest

---

[3]In the case of LAB, the aromatic ring is a benzene ring.

excited state, S_{10}. Subsequently, the excited electrons de-excite to the ground state $(S_{10} \rightarrow S_{0x})$ within a few ns, and emit scintillation photons.

In some cases, the excited electron can de-excite to one of ground states vibrational modes without emitting any scintillation photons. This transition is known as *non-radiative* de-excitation. The ratio between the radiative and non-radiative transitions determines the fluorescence quantum efficiency of the scintillator.

The electrons can transition to the triplet excited states through ionisation and re-combination which would produce triplets excited electrons in 75% of the cases. The excited triplet electron de-excites to T_0, the lowest triplet state. The triplet state electrons are more stable due to the spin selection rules, and cannot de-excite to the ground state unless stimulated externally. Therefore, the phosphorescence decay might take up to a minute. Moreover, the excited triplet electrons can transition to the excited singlet states, and then de-excite to the ground state and produce fluorescence photons. This transition is known as the delayed fluorescence, identical to the prompt fluorescence however their decay time constant is longer ($\sim$100 ns). The timing profile of scintillation photons has multiple decay components due to the several different transitions involved. Massive particles such as αs generate more delayed-fluorescence photons since they make more ionisation-recombination excited states. This leads to a longer emission tail on their timing profile. The scintillation timing is discussed in detail in 5.4.4.

The scintillation light can be suppressed due to high ionization density along the particle's trajectory. This phenomena is known as quenching and can be described through Birks' law:

$$\frac{dL}{dx} = S_0 \frac{dE/dx}{1 + k_B dE/dx} \tag{2.3}$$

where L is the light yield, x represents the particle's path, S is the scintillation efficiency, E is the energy, and K_B is Birks' constant which depends on type of the particle. The heavy ionizing particles experience higher quenching, and therefore have

greater Birks' constants.

One of the important characteristics of scintillators is their significant Stokes shift. Stokes shift is the difference between the emission and absorption spectra in a material. In order to avoid self-absorption, the energy of the emitted scintillation photon must be too low to re-excite the π electrons. In the case of an organic liquid scintillator, the Stokes shift is conformed by the vibrational modes . As it is demonstrated in figure 2.7, the absorbed photons have the minimum energy of $S_{10} - S_{00}$, the difference between the lowest excited state and the ground state, whereas the emitted photons have the maximum energy of $S_{10} - S_{00}$.

Fluor

Performance of the scintillator can be improved by adding dopants, known as fluor in concentrations of g/L. The excited scintillator molecule most likely encounters a dopant molecule, and transfer the excitation before it has a chance to fluorescence. The dopants are usually chosen to have a different emission spectrum than the scintillator, therefore they can improve the Stokes shift and reduce the self-absorption. Furthermore, the dopant might have a better net fluorescence quantum efficiency than the primary scintillator, taking into account the transferring efficiency.

As discussed previously LAB is chosen as the SNO+ primary scintillator. SNO+ utilizes 2,5-Diphenyloxazole (PPO) as the primary fluor in expected concentration of 2g/L. The excited LAB molecules transfer their excitation non-radiatively to PPO before they scintillate. The emission and absorption spectra for the PPO is shown in figure 2.8.

Furthermore, 1,4-bis(2-methylstyryl) benzene known as bisMSB will be added to the liquid scintillator to improve the light yield in Te-loaded phase [73]. This secondary fluor will be added in concentration of about 15 mg/L, and can enhance the Stokes shift, and furthermore act as a wavelength shifter, improving the overlap between the emission spectrum and the desirable optical range of PMTs, demonstrated in
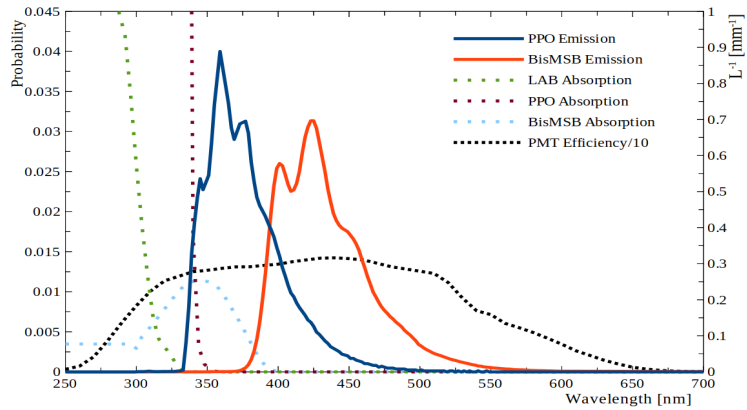
Figure 2.8: The absorption and Emission spectra for various components in the SNO+ scintillator cocktail. The right y axis shows the absorption constant for dashed lines in units of mm^{-1}. Furthermore, the black dashed line shows the R1408 PMTs detection efficiency, scaled down by the factor $\times 10$ to fit on the graph, taken from [74].

figure 2.8.

Figure 2.8 also shows the absorption length for various components in the scintillator cocktail. The attenuation length of LAB is on the order of 10m [75], whereas UPW has a much higher attenuation length of 100m in the optical range. Chapter 6 discusses a method that is used to determine the effective attenuation length of the detector in scintillator phase using tagged ^{214}Po events.

2.5 Calibration

A proper understanding of the light production, propagation, and detection is necessary in order to understand the response of the detector to neutrinos, muons and radioactive backgrounds. SNO+ uses a detailed Monte Carlo (MC) modeling of the detector along with extensive optical and energy calibration data to achieve this goal. Furthermore, the PMT hit patterns in time and space are utilized to reconstruct the event position and time vertex. The SNO+ reconstruction algorithm is discussed in detail in section 3.3. This section focuses on the optical and the radioactive calibration sources, and furthermore describes the calibration hardware in SNO+. Moreover, SNO+ performs electronic calibration frequently which is not discussed in this section. The electronic calibration is used to understand the time and charge response of each channel using forced firing and forced global triggering.

The calibration data was used for two main purposes; i) to determine the free parameters in the detector models, and ii) furthermore to verify the reconstruction algorithms and determine the associated systematic uncertainties. The following are some of the main quantities that are measured or constrained using the calibration data:

- **The light yield:** the number of scintillation photons emitted for various particles with different energies. Understanding the light yield is crucial for energy reconstruction. Studying light yield is also necessary to model the scintillation mechanism, to determine the Birks' constants, and understand the quenching in scintillator.

- **Emission timing of scintillator:** understanding the time response of the scintillator is important for reconstruction. The calibration data was used to characterize the emission timing and determine the scintillation decay constants. Furthermore, the timing profile can be used for particle identification as the

shape of the signal depends on the particle type.

- **The optics:** understanding the detector's optics is crucial. The optical properties of the detector is incorporated in `RAT`, and the absorption length, scattering, and the refractive properties of different components of the detector is determined for various wavelengths [76]. The optical calibration sources are discussed in 2.5.1.

- **Detector collection efficiency:** in order to determine the probability of detecting a single photon of a given wavelength in SNO+, the collection efficiency needs to be determined through the detector model. The global collection efficiency depends on the quantum efficiency of the PMTs as well as the channel efficiencies due to the discriminator threshold on FEC.

- **PMTs timing offsets**: there is an offset of each PMT time due to the cable delay. This time offset needs to be determined and corrected for each channel. In addition, the discriminator crossing time in FEC is charge dependent, which needs to be well calibrated.

- **PMT angular response and the concentrators reflectivity:** the probability of a PMT getting hit is a function of the photons incident angle. This dependency is incorporated in the optics model, and was measured using the optical sources. Furthermore, the reflectivity of the PMT concentrators can be degraded over time. The reflectivity is measured and monitored through in-situ measurements in SNO+ [77, 76].

- **Reconstructions:** the calibration data were used to verify the reconstruction algorithm, and furthermore determine the associated resolutions and systematic uncertainties.

2.5.1 Optical Calibration

The optical calibration sources are used two main analyses: i) understanding the optical properties of the detector, and ii) determining the timing offset on the PMTs. SNO+ utilises two main optical calibration sources to model the optics of the detector. The laserball is deployed into the detector volume, whereas ELLIE (External LED/Laser Light Injection Entity) consists of optical fibres that are mounted on PSUP.

Laserball

The laserball is a light diffusing quartz sphere with a diameter of 10.9cm which contains a 50μm hollow glass beads suspended in soft silicone gel [78, 79]. The laser is produced by a nitrogen laser on SNO+ deck and transferred down to the sphere through an optical fibre. The light is reflected and scattered inside the sphere through the beads, and eventually comes out isotropically. The 337 nm laser can be shifted to five wavelengths of 369, 385, 420, 505 and 619 nm, using the laser dyes. The laserball system is inherited from SNO, and upgraded to meet the cleanliness requirements for scintillator phase. The laserball can be deployed into the detector volume as well as the volume between the PSUP and the AV (external). A complete set of laserball scan was performed during the water phase, and the data were used to calibrate the optical model; determine wave-length dependent attenuation and understand the PMTs angular responses [76].

ELLIE

The Embedded LED/Laser Light Injection Entity (ELLIE) is a system designed for SNO+ to allow optical calibration of the detector without the contamination risk of deploying a source in scintillator. The system consists of a set of optical fibres mounted on the PSUP, and can shine light across the detector, demonstrated in figure 2.9. ELLIE consists of 3 modules for different calibration purposes.

- **TELLIE**: the module for timing calibration which consists of 92 fibres and LED drivers. This module can asynchronously trigger the detector, and the data can be used to calibrate the timing offset of the PMTs.

- **SMELLIE**: the scattering module which consists of 15 fibres that transfer the laser at 5 different wavelengths and shine across the detector. The data were used to determine the Rayleigh scattering length for different wavelengths.

- **AMELLIE**: the module to measure the attenuation for different wavelengths.
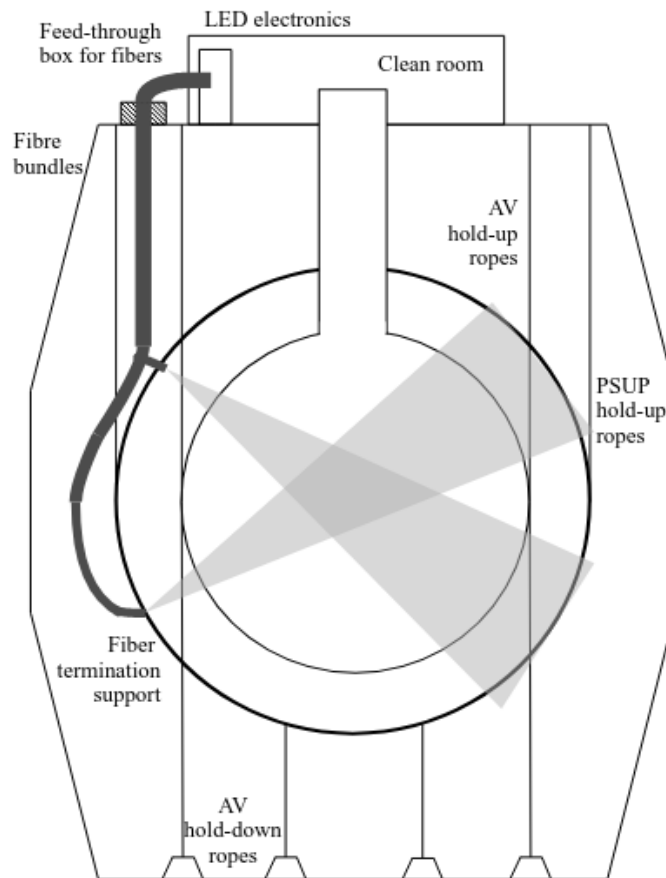
Figure 2.9: An overview of ELLIE system, taken from [80]

2.5.2 Radioactive Sources

In addition to the optical calibration, the radioactive sources can be deployed inside the detector to calibrate the detector response to primary particle interactions with

Isotope/source	Particle	Energy [MeV]	Calibration goal
^{16}N (tagged source)	β (tagging) γ	6.1 MeV (66%) 7.1 MeV (6%)	Primary source in water, external source in LS, energy and reconstruction
AmBe	n, γ	2.2 + 4.4 MeV	Neutron capture response (water), external source in LS, Light yield and energy & reconstruction
^{8}Li	optical photons	—————-	Cherenkov Light
^{46}Sc*	γ ($\times 2$)	1.1 + 1.3 MeV	Energy scale & reconstruction
^{57}Co*	γ	0.14 MeV	Energy & reconstruction
^{48}Sc*	γ ($\times 3$)	1.0 + 1.1 + 1.3 MeV	Energy scale & reconstruction

Table 2.1: Radioactive sources in SNO+. The sources marked with * are in preparation for scintillator phase. The plus signs indicate the coincident signals [58].

different energies. The calibration data can be used to obtain the energy scale, the systematic uncertainties and offset values associated with the reconstructed position and energy, and the resolutions. Table 2.1 shows the main radioactive sources in SNO+. ^{48}Sc, ^{137}Cs and ^{57}Co are three γ sources in preparation [58]. They are designed to calibrate the energy scale in scintillator phase. While some sources are being commissioned, the calibration data from the ^{16}N and AmBe source are used for several analyses discussed in the following chapters.

^{16}N Source

Inherited from SNO, the ^{16}N source was the main energy calibration source in water phase in SNO+ [81]. The ^{16}N undergoes β-decay and produce an excited ^{16}O*. The β particle is captured within the decay chamber, and used to tag the calibration events. The excited ^{16}O nuclei de-excites by emitting a 6.1 MeV (7.12 MeV) γ with the branching ratio of 66.2% (5%). The ^{16}N water data were used to verify the reconstruction algorithms and determine the associated uncertainties and resolutions [82, 83, 84]. Furthermore, the ^{16}N data were used to verify the optics. The ^{16}N hardware design does not meet the radio-purity requirements to be de-

ployed into the scintillator volume, however the source has been deployed externally throughout the scintillator filling process, and the tagged data were used for various scintillator analysis such as light yield studies, reconstruction verification, and scintillation timing studies. Chapter 5 describes the ^{16}N source in detail, and discusses my calibration analyses.

AmBe Source

Inherited from SNO, SNO+ has used Americium beryllium (AmBe) calibration source for energy calibration in water phase and scintillator phase [85]. The source is a mixture of powdered long-lived ^{241}Am ($\tau_{1/2}$=432y) and ^{9}Be contained within a stainless steel capsule that can be temporarily deployed into the detector. The ^{241}Am undergoes α decay with Q_α=4.9 MeV. The αs are absorbed by the ^{9}Be nuclei with an efficiency of $\sim 10^{-4}$ [86]. Upon capturing the α, the following interaction takes place with branching ratio of 60%:

$$^9\text{Be}(\alpha, \text{n})^{*12}\text{C} \rightarrow^{12}\text{C} + \gamma(4.4\text{MeV}) \tag{2.4}$$

The 4.4 MeV γ is the prompt signal from AmBe. The produced fast neutron thermalizes within $\sim 200\mu$s in scintillator/water, and most likely would be captured by a hydrogen nucleus, emitting a 2.2 MeV γ. The calibration events can be identified taking advantage of the delayed coincident γ's. Furthermore, the coincident γ's make a similar signal as the antineutrino signal, hence the AmBe data were used to determine the detection efficiency of the neutron, and the neutron capture time constant in water [87].

The source capsule is not upgraded to be deployed into the scintillator volume, however AmBe has been deployed externally into the volume between the PSUP and the AV several times [88]. Along with the ^{16}N calibration data, the AmBe data were used to study scintillators energy response, to model the light yield, and estimate the Birks' parameters in scintillator.

2.5.3 Calibration Hardware

The calibration hardware consists of different mechanisms and tools that enable deploying, and safely positioning the source in the detector. Figure 2.10 gives an overview of the SNO+ calibration hardware. The following describes the main components of calibration hardware.

Universal Interface

Universal interface (UI) is an air-tight stainless steel structure that sits on top of the neck inside SNO+ deck clean room (DCR), and hosts 3 gate valves, the pipes which transfer liquids, 4 motor boxes shown in figure 2.10, the glove ports, and the neck PMTs. Figure 2.11a shows an overview of UI without the motor boxes. The deployed sources are lowered through one of the gate-valves on the UI inside the detector volume.

URM

Umbilical retrieval mechanism consists of a set of pulleys, a load cell, a motor and a gas connection. URM enables deploying and moving the source. Prior to lowering the source, the URM source tube is connected to one of the gate valves. The load on the source is constantly monitored using the load cell. In addition, the source umbilical runs through the URM down to the source. The source umbilical is a Tygothane tube filled with a silicon gel that contains 4 wires, a coaxial cable, and optical fibre [58]. In order to meet the radio-purity requirements and mitigate radon ingress in scintillator, a new cover-gas system is being designed for the scintillator URMs.

The side ropes and motor boxes

The source is moved through the rope system shown in figure 2.10. The ropes are manipulated through 4 motor boxes on top of the UI. Furthermore, there is a set of side ropes that enables moving the source off the vertical axis in the detector. The

load on the ropes are monitored through the load-cells.

Guide Tubes

There source can be deployed vertically into the volume between the AV and PSUP through the guide tubes. There are 6 guide tubes on the SNO+ deck as shown in figure 2.11c.

MANIP

MANIP is the calibration software used by the calibration operator to control the motors, and move the source around the detector. Furthermore, the source position and the loads can be monitored through MANIP. The system needs to be sanity checked and calibrated prior to deploying a source.

2.6   RAT Simulation

SNO+ uses a simulation and analysis package called RAT (Reactor Analysis Tools) originally written for Braidwood collaboration. RAT contains Geant4 toolkit which is utilised to simulate the detector in detail taking into account the detector's geometry, electronics, optics, the physics of scintillation and Cherenkov radiation, and the relevant electroweak and hadronic physics in MeV scale. The optics model and the reconstruction algorithms are calibrated and verified using calibration sources. A run-by-run RAT simulation enables meaningful comparison between the data and the models by taking into account the detail information of the detector state such as the on-line channels/crates, the triggering conditions, the AV offset and the LAB interface level. RAT uses ROOT as the main data analysis package, which is a C++ object-oriented software developed by CERN [90]. The processed (generated) data (MC) were written to disk as ROOT files for physics analysis.
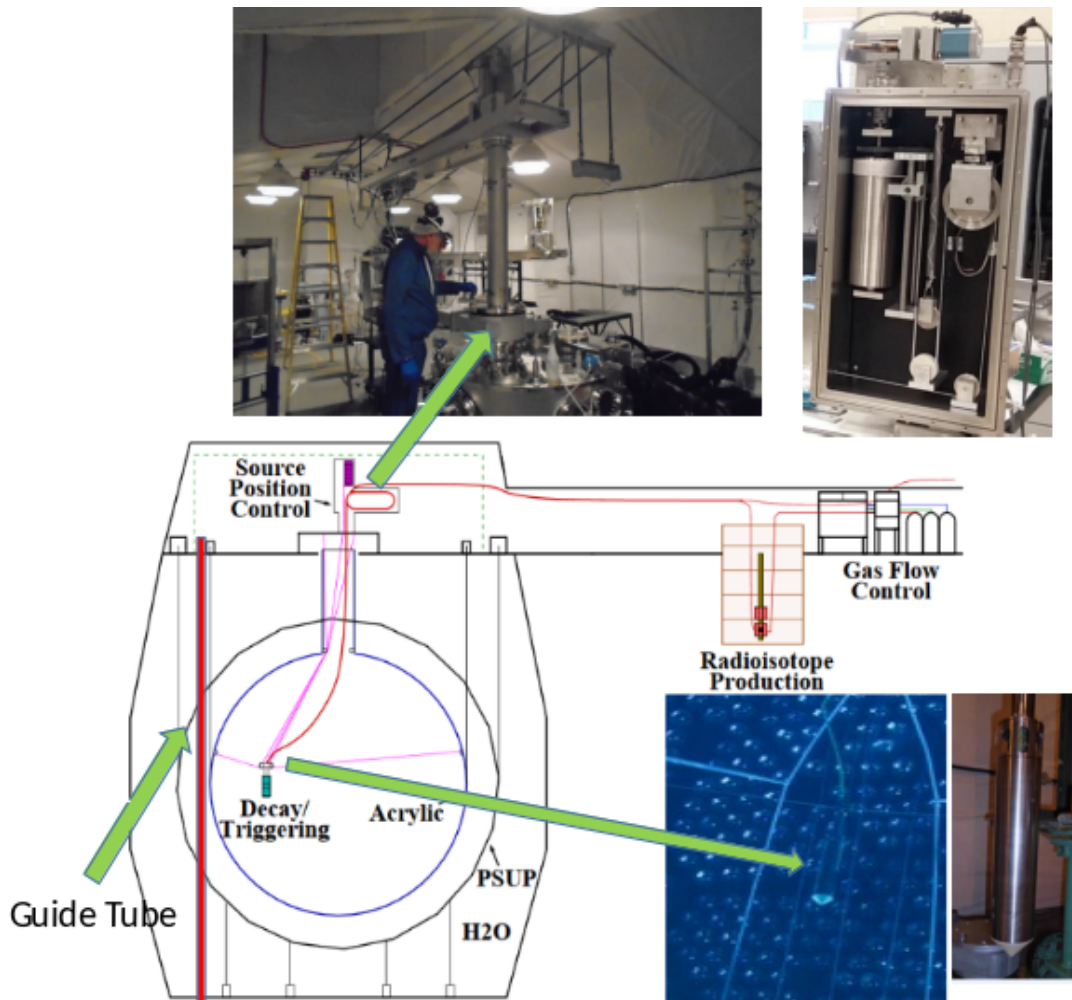
Figure 2.10: The diagram shows part of the SNO+ calibration hardware used to deploy the calibration source through the UI (top left) and moce the source across the detector using the side rope system and the motor boxes shown on the upper right. The decay chamber is shown in bottom right and one of the guide tubes (4) is highlighted and shown in red.
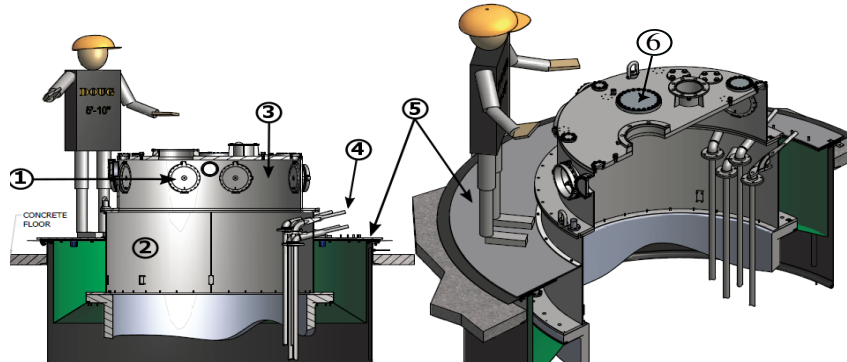
(a) Overview of the SNO+ UI; 1) Glove ports. 2) The lower UI. 3) The upper UI. 4)The pipes that transfer the liquid in and out of the AV. 5) The Sliding floor. 6) one of the gate valves. Figure is taken from [89].
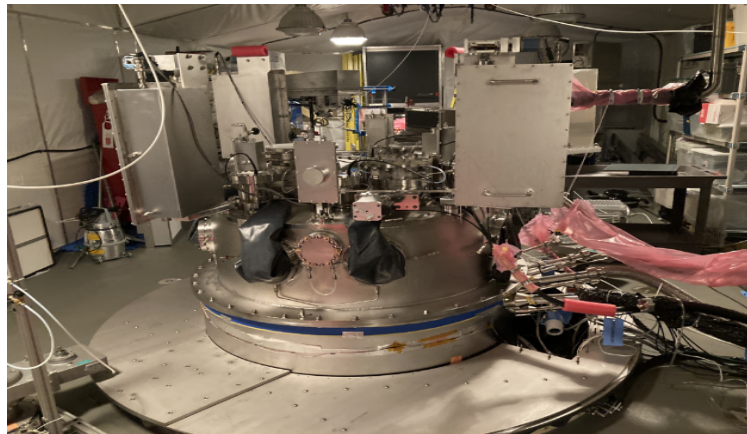
(b) SNO+ UI.
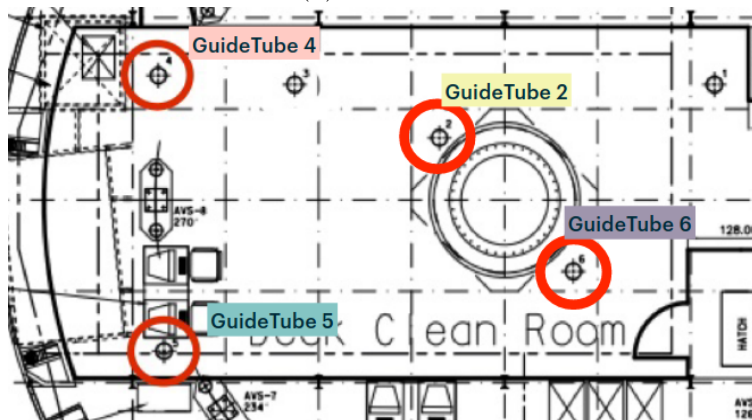
(c) The top view of 6 guide tubes in SNO+ Deck Clean Room (DCR).

Figure 2.11

45

Chapter 3: Event Reconstruction in SNO+

3.1   Introduction

Event reconstruction is a process of inferring the key physics parameters from the raw read outs in every event in the detector. SNO+ uses a set of reconstruction algorithms known as `scintFitter` in scintillator phase, and `waterFitter` in water phase[1]. The basis of both algorithms is very similar as they both use the PMT hit times/patterns within an event to estimate the time, position, energy, and the direction. This chapter describes various types of expected events in SNO+, discusses the reconstruction algorithms, and furthermore introduces a set of timing and topological event classifiers. This chapter is mostly a description of other's work [91, 92, 93], however, crucial to discuss since the reconstructed vertex and time residuals are often used throughout the analyses in chapters 5 and 6, and the timing and angular classifiers are used as the basis of some analysis in chapter 7.

3.2   Events in SNO+

The passage of charged particles through water or the scintillator cocktail can produce both Cherenkov and scintillation photons. However, the number of Cherenkov photons is much less ($< 3\%$) than scintillation photons. The events generating light in the detector can be divided into the following categories:

---

[1]In addition, **partialFitter** was developed to reconstruct the event's vertex in partial-fill period, taking into account the optics and the geometry of water and scintillator in the AV.

Electrons (β^-)

Fast electrons generate photons in scintillator through I) the scintillation mechanism, and II) through Cherenkov radiation, both discussed in section 2.4, however the scintillation signal is dominant. In addition, electrons with kinetic energies greater than 0.78 MeV can potentially generate Cherenkov photons in water. The fast electrons are produced through various interactions such as single β decays of radioisotopes in the detector, the $2\nu\beta\beta$ decays, the $0\nu\beta\beta$ decays, and the neutrino interactions such as ES.

α particles

α particles are mainly emitted through α decays of various radioactive nuclei (e.g. ^{210}Po) in the detector, and via the same mechanisms as the electrons, they can generate photons in scintillator. However their energy loss per unit length $\left(\frac{dE}{dx}\right)$ is much higher than electrons. The higher ionisation density for αs leads to smaller scintillation light compared to an electron with the same kinetic energy, in other words the scintillation light is quenched down for α particles. The quenching can be characterised through Birks' equation (see equation 2.3), discussed in section 2.4. In addition, the higher ionisation density affects the emission time for αs, which provides a basis for pulse shape discrimination between αs and βs [94].

γ particles

γ particles cannot produce light directly since they are neutral. However, they produce light through making secondary fast electrons as they undergo Compton scattering and pair production in scintillator and water. Unlike electrons and αs, γ's have much longer mean free path in the detection medium ($\sim$30cm in scintillator), and most likely go through multiple Compton scatterings. The longer mean free path leads to a more smeared emission time for γ's, demonstrated in section 5.5. The main sources of γ's in the detector are the γ emitter nuclei in the external components of

the detector (e.g. ropes).

Neutrons

Free neutrons are mainly produced through cosmic muon spallations discussed in section 4.7, inverse beta decays, and α-n interactions discussed in section 4.6. Free neutrons scatter off protons as they slow down, causing the protons to produce scintillation light. Once cooled down, the neutron most likely captures on a hydrogen nucleus, which de-excites and and emits a 2.2 MeV γ.

Muons (μ^-)

SNO+ expects about 3 muons per hour in within the PSUP volume [95]. Most of the muons enter from one side of the detector, deposit part of their energy along their trajectory, produce a large number of photons, and exit from the other side. They can activate the nuclei along their path and produce cosmogenic backgrounds. There are a set of outward looking PMTs that can be used to identify and veto the muons.

Positrons (β^+)

Positrons generate scintillation light in the detector in the same way as electrons. However, at end of their trajectory, they annihilate and produce two γ's. As a result, the total deposited energy of a positron is a bout 1 MeV higher compared to an electron with the same kinetic energy.

3.3   Reconstruction

The reconstruction algorithms calculate the time, position, and the energy of an event assuming that they are fast electrons. As demonstrated earlier, electrons deposit all their energy within a few millimeters in the detector, therefore thy can be assumed as point-like photon sources. The energy is determined through the number of hit (fired) PMTs within an event, known as *Nhits*. Higher energy particles generate more

photons in the detector, and therefore fire more PMTs. The energy reconstruction is discussed in section 3.4. The time, position, and direction (water) of events are reconstructed based upon the fired PMT hit times along with the PMT positions, discussed below.

3.3.1 Hit Time Residuals

Hit time residuals provide the key distribution to reconstruct the position and the time of an event. For a given event and associated fired PMTs, time residuals can be written as follows:

$$t_{res}^i(\vec{r}_{evt}, t_{evt}) = t_{PMT}^i - t_{t.o.f}^i - t_{evt} \tag{3.1}$$

where t_{PMT}^i is the hit time of the ith PMT, $\vec{r}_{evt}$ is a vector pointing to the position of the event, $t_{t.o.f}$ is the time of flight, the time that takes for a photon to travel from the event position to the ith PMT, and t_{evt} is the time of the event. The time of flight is calculated for a given PMT assuming a straight line for light through different mediums. The light path is determined using `LightPathCalculator`, which is a function in a class implemented in `RAT`. Having the paths and the effective speeds of photons in each medium, time of flight in water/scintillator can be obtained as follows:

$$t_{t.o.f} = \frac{d_{w/s}}{c_{w/s}^{eff}} + \frac{d_{av}}{c_{av}^{eff}} + \frac{d_{exw}}{c_{exw}^{eff}} \tag{3.2}$$

where d_i and c_i^{eff} are the light path and the effective speed of photons in medium i[2] respectively. The hit time residuals is a rough estimate of the photons emission time.

3.3.2 Position and Time Reconstruction

The position of the events is expressed in the AV coordinate system in which the center of the AV is the origin. The reconstruction algorithms are developed by P.

---

[2] w/s stands for water/scintillator, and exw stands for the external water.

Jones, I. Coulter, and many others [91, 92]. The method works as a two step process; I) `QuadFitter` gives a rough estimate of event vertex (position and time), and II) the results from `QuadFitter` is used as a seed for a likelihood fit through which the event vertex is obtained. For a point-like instantaneous event in an isotropic detector the event vertex can be obtained from 4 PMT hits, as shown in equation 3.3.

$$|\vec{r}_{pmt} - \vec{r}_{evt}| = c(t_{pmt} - t_{evt}) \tag{3.3}$$

4 PMT hits provide 4 equations, which are sufficient to estimate 4 unknowns, x_{evt}, y_{evt}, z_{evt}, t_{evt}. `QuadFitter` uses several sets of 4 PMTs, and calculates a set of event vertices, and then selects the median as the final estimate of event vertex to pass onto the `PositionTimeLikelihood`. Furthermore, `PositionTimeLikelihood` models the hit time residual distribution using the results from `QuadFitter`, correcting for different light speeds in different mediums, and also taking into account the modelled emission time PDF for scintillator/water. The best fit vertex is obtained to maximise the agreement with this distribution through the method of maximum likelihood. The log-likelihood can be written as:

$$\log \mathcal{L}(\vec{r}_{evt}, t_{evt}|h_{\vec{r},t}^i) = \sum_{i=0}^{Nhits} \log p(t_{res}^i(\vec{r}_{evt}, t_{evt})) \tag{3.4}$$

where $p(t_{res})$ is the PDF of the expected time residuals, and the most probable $\vec{r}_{evt}$ and t_{evt} would maximise the likelihood. The fits that do not converge are flagged as invalid with `Fitter==false`. The shape of the time residuals distribution depends on the vertex resolution, and the light path in the detector. For instance, figure 3.1 shows simulated time residuals distribution for different reconstructed radii ranges. The events are simulated for a 2.5 MeV electrons in 2 g/L PPO scintillator. The photons are more likely to take straight paths further from the center of the detector, in other words less likely to get scattered or absorbed. This explains the more strongly peaked time residuals at the higher radii up until $R \sim 5$ m. As it can be seen, the distribution

becomes more smeared beyond 5 m, which can be explained by the dominant internal reflection off the boundary between the acrylic and water.
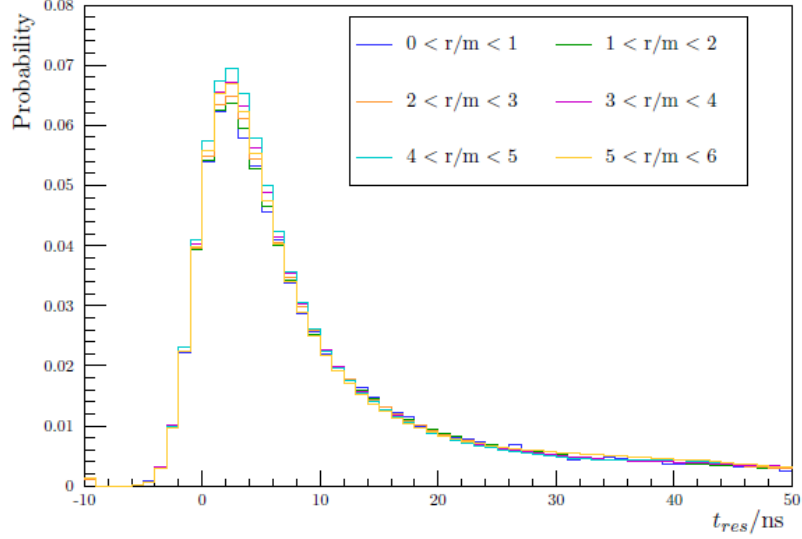
Figure 3.1: The simulated time residuals of a 2.5 MeV electron in liquid scintillator for different reconstructed radius.

3.3.3 Direction Reconstruction

Direction of an event is described in form of a normalized vector $\vec{d}$ satisfying the following equation:

$$\cos\theta = \vec{d}.(\vec{r}_{pmt} - \vec{r}_{evt}) \tag{3.5}$$

where $\cos\theta$ is the Cherenkov angle, the angle between event's direction and the triggered PMT, demonstrated in figure 3.2 (right). $\cos\theta$ as a distribution would peak around 41.4° in water. The direction is obtained by fitting $\cos\theta$ distribution with a PDF for Cherenkov angles distribution demonstrated in figure 3.2. Furthermore, Cherenkov cone can be generated in scintillator cocktails. There has been successful studies demonstrating the possibility of separating Cherenkov signal from scintillation signal for low PPO concentration scintillator cocktails by looking at the very early PMT hits [96, 97, 98, 99]. In addition, the Cherenkov signal is identified in liquid

51
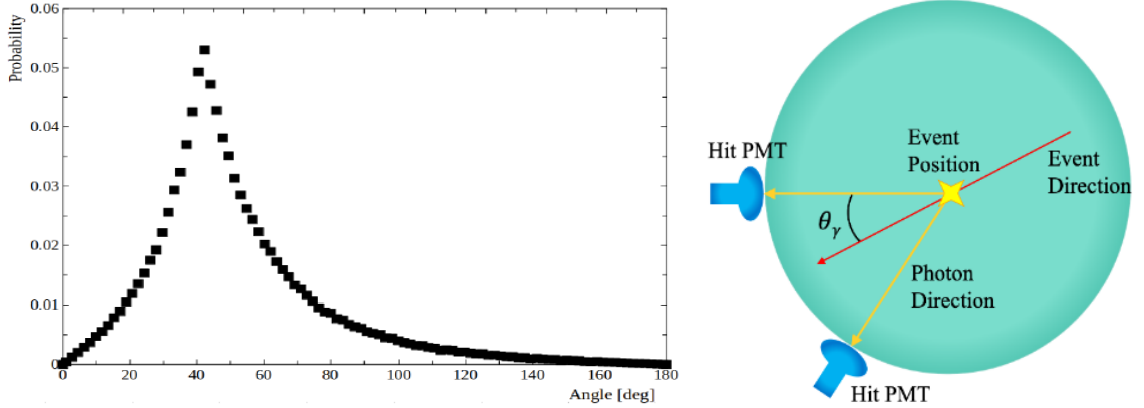
Figure 3.2: *Left*: The PDF used to determine the event direction in water through likelihood fit, taken from [74]. *Right*: The Cherenkov angle.

scintillator using ^{16}N calibration data, which is discussed in section 5.4.5 [99].

3.4 Energy and Light Yield

Energy reconstruction in SNO+ is carried out through `scintFitter/waterFitter`, assuming that the light is generated by 3 MeV electrons. The deposited energy in the detector is proportional to the (quenched) number of generated photons ($N_{p.e.} \propto E^Q_{dep}$). The number of collected photons are not the same as the number of generated photons, however they can be linked through Poisson statistics as follows:

$$N_{\text{detected}} \sim \text{Poi}(N_{\text{p.e.}}) \tag{3.6}$$

For a large number of photons, the number of detected photons can be assumed as a Gaussian distribution with the width of $\sigma/E = 1/\sqrt{N_{p.e.}(E)}$. This would enforce a lower limit on the achievable energy resolution regardless of the reconstruction algorithm, known as the Poisson limit. SNO+ expects about 1000 *p.e.* around ^{130}Te Q value in scintillator, which would give a Poisson limit of $\sim$3% ($\sim$70keV) [100].

In practice SNO+ measures the number of fired PMTs (Nhits), not the number of collected photons, $N_{p.e.}$. The photons can get lost due to the pile-up of multiple hits on a single PMT, which leads to a relatively smaller `Nhits`. The multi-hit corrections

is modeled by J. Dungar [93]. Furthermore, Nhits can be suppressed due to other factors such as the absorption, PMT angular response, and PMT coverage, which are carried out in `scintFitter/waterFitter` reconstruction algorithms. Finally the energy reconstruction algorithm is verified using calibration sources such as ^{16}N, and the energy resolution and the associated uncertainties are determined, discussed in chapter 5.

3.5 Event Classifiers

A set of timing and topological event classifiers are developed that can be utilized to distinguish the signal of interest from the backgrounds, and reject the background events. The following section describes some of these classifiers that are frequently used in my analyses in the following chapters.

3.5.1 ITR

In Time Ratio (ITR) is a timing classifier which shows the ratio between the number of prompt hits and the total number of hits (Nhits).

$$ITR = \frac{Nhits(-2.5ns, 5ns)}{Nhits} \tag{3.7}$$

The prompt Nhits are defined as the number of fired PMTs within the time residuals window of (-2.5, 5)ns. As discussed before, Cherenkov signal is a relatively sharp and peaked signal, in other words, most of the hits take place within the prompt window, therefore has ITR values closer to 1. The ITR classifier can be used to distinguish valid water events from the instrumental background in water phase. Furthermore, since the scintillator emission time is smeared out over a longer time span, ITR classifier can assist discriminating scintillator-like events from water-like events in partial-fill phase.

3.5.2 β_{14}

The PMT hits patterns can be characterized through distributions based upon θ_{ij}, the angles between the fired PMTs. The simplest angular classifier that SNO+ uses is the average of the angles between PMT hits within one event, defined as follows:

$$\langle\theta_{ij}\rangle = \frac{2}{N(N-1)}\Big[\sum_{i=1}^{N-1}\sum_{j=i+1}^{N}\theta_{ij}\Big] \tag{3.8}$$

This classifier has been used to separate the external γ's from the signal in the SNO analyses [101, 102]. Furthermore, another topological classifier was developed based on spherical harmonics, known as β_{14}. Any distribution of PMT hits on a surface of a sphere can be written as a linear combination of orthogonal harmonic oscillators as follows:

$$f(\theta,\phi) = \sum_{l=0}^{\infty}\sum_{m=-l}^{l}\alpha_{lm}Y_{lm}^*(\theta,\phi) \tag{3.9}$$

where the orthonormality of $Y_{lm}(\theta,\phi)$ dictates:

$$\alpha_{lm} = \int f(\theta,\phi)Y_{lm}(\theta,\phi)d\Omega \tag{3.10}$$

In other words, the expansion parameter (α_{lm} is the average value of Y_{lm} over the distribution $f(\theta,\phi)$. In the case of PMT hits, equation 3.10 can be written as a sum over N individual hits.

$$\alpha_{lm} = \frac{1}{N}\sum_{i=1}^{N}Y_{lm}(\theta_i,\phi_i) \tag{3.11}$$

A class of rotational invariants can be defined as:

$$\beta_l = \sum_m\big|\alpha_{lm}\big|^2 \tag{3.12}$$

Using the spherical harmonic addition theorem, these invariants can be written in terms of θ_{ij}, the angles between PMT hits. Furthermore, corrections can be applied to avoid double summation, and also exclude the angles between the hit PMT and

itself. The final form of β_l can be written as:

$$\beta_l = \frac{2}{N(N-1)}\left[\sum_{i=1}^{N-1}\sum_{j=i+1}^{N} P_l(\cos\theta_{ij})\right] \tag{3.13}$$

where $P_l(x)$ represents Legendre polynomials. As it can be seen β_1 is closely related to $\langle\theta_{ij}\rangle$. A set of analysis was done through various linear combinations of β_ls, and it was demonstrated that $\beta_{14} = \beta_1 + 4\beta_4$ gives the best separation between the neutral current events (NC) and charge current events (CC) in SNO [102]. Unlike the Cherenkov signal in water, the generated scintillation light is isotropic which would lead into $\beta_{14} \sim 0$, therefore β_{14} can be used to distinguish the water events from scintillator events in partial fill, as demonstrated in chapter 5.

3.5.3 External Timing Classifiers

As described previously, the position reconstruction algorithm treats every event as an electron with a single vertex. Furthermore, the fitted vertex is used to determine the hit time residuals. However, as demonstrated in section 3.2, γ's can deposit their energy over a longer trajectory in scintillator ($\sim$ 30cm), and most likely go through multiple Compton scatterings. Figure 3.3 shows the track length for a simulated 1 MeV electron versus γ's on the left, and the associated time residuals on the right [100].
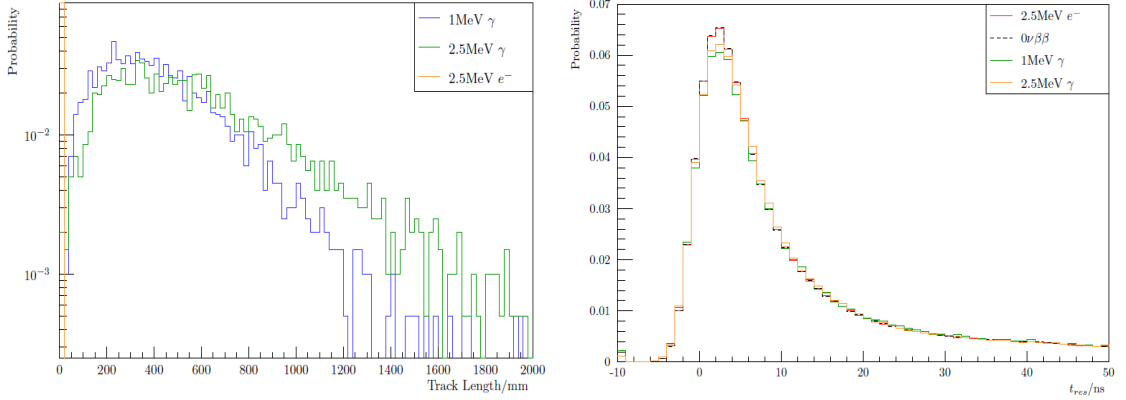
Figure 3.3: The track length of an electron and γ's from MC simulation on the left, and the associated time residuals along with the time residuals from $0\nu\beta\beta$ decay shown on the right [100]. As it can be seen the time residuals from $0\nu\beta\beta$ and e are very similar.

The spread out energy deposition of γ's leads to the broader time residuals, which is the basis of developing timing classifiers for identifying and rejecting external γ's. Aside from broadening of the time residuals distribution, more early PMT hits are expected for γ's since they are reconstructed far away from their first Compton scattering. The timing classifiers use the hit time residuals to assign a discriminant value (D) to every event. The discriminant is defined as follows:

$$D = \vec{w}.\vec{T} \tag{3.14}$$

where $\vec{T}$ is the vector consists of bin contents from time residuals, and $\vec{w}$ is the weight vector assign to every bin. $\vec{w}$ can be determined from MC simulations for different signals. The weights can be obtained from:

$$w^i = \log\left(\frac{\mu_{sig}}{\mu_{bg}^i}\right) \tag{3.15}$$

where w^i is the weight assigned to the ith bin, μ_{sig}^i/μ_{bg}^i are the probability of a PMT hit in the ith bin of time residuals of the signal and the background respectively.

Therefore the discriminant can be written as a log-likelihood ratio as follows:

$$D = \sum_{i=0}^{N_{bins}} \log \frac{\mu^i_{sig}}{\mu^i_{bg}} \qquad (3.16)$$

A set of timing classifiers is developed, re-coordinated, and the weights are obtained for $0\nu\beta\beta$ signal versus different external γ sources.

For instance, `ext0NuTimeTl208AVNaive` is one of the timing classifiers optimized for ^{208}Tl external γ's from the AV versus the 0ν signal, which is used frequently in my analysis in chapter 7.

3.5.4   External Topological Classifiers

Aside from the timing classifiers, the PMT hits patterns (topology) of the external γ's are different from electron-like events from the 0ν or the solar ν signals, and therefore are used to develop a set of classifiers. The external γ's reaching the the scintillator volume are most likely travelling towards the center of the AV. That being the case, PMTs that most likely to fire earlier are the ones along the vector pointing to the reconstructed position from the center of the AV. The angular distribution ($\cos\theta$) of the early PMT hits from simulated external ^{208}Tl γ's is shown in figure 3.4 along with simulated $0\nu\beta\beta$ signal. The PMT hits with time residuals within -2 ns and 20 ns are selected as the early hits, and $\cos\theta$ is defined as the angle between the PMT vector, averaged over the prompt fired PMTs position vectors, and the reconstructed position vector. As it can be seen, the early hits from the external sources are significantly peaked towards $\cos\theta \sim 1$, whereas the angular distribution from $0\nu\beta\beta$ is relatively flat with a gentle negative slope which is due to optical effects. The topological classifiers have the same form as the timing classifiers, however, the $\cos\theta$ is the key distribution instead of the hit time residuals. Therefore, a topological discriminant value can be defined in form of a log-likelihood as follows:

$$D = \vec{w_\theta}.\vec{\Theta} = \sum_{i=0}^{N_{bins}} \log\left(\frac{\lambda^i_{sig}}{\lambda^i_{bg}}\right) \qquad (3.17)$$
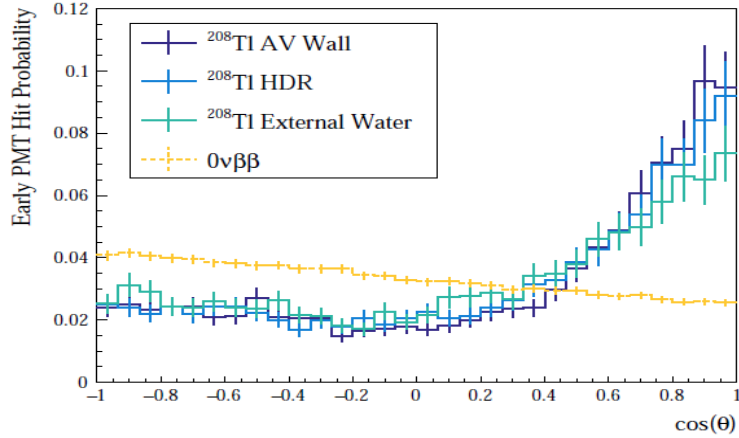
Figure 3.4: $\cos\theta$ distribution of early PMT hits from simulated external γ's in scintillator along with the distribution from simulated 0ν signal, taken from [100].

where $\vec{\Theta}$ is the vector that consists of the bin contents of $\cos\theta$ hit distribution, and $\vec{w}_\theta$ is the associated topological weight vector that can be obtained from MC for different signals. $\lambda^i_{sig/bg}$ is the probability of a hit in the ith bin in $\cos\theta$ distribution of the signal and the background respectively. A set of topological classifiers are developed, and the angular weights are obtained for different sources of external γ's versus $0\nu\beta\beta$ signal. For instance, `ext0NuAngleTl208AV` is one of the many topological classifiers that is used in my analysis in chapter 7 in order to investigate the separation power of the solar ν signal from the external γ's.

Chapter 4: Backgrounds in SNO+

4.1 Introduction

In SNO+ anything that triggers the detector resulting in an event that could be mistaken as the signal is considered as a background. Searching for rare events requires very stringent background limits in the energy region of interest of the signals. Therefore, it is crucial to understand the nature of potential background events and their rates, and reject or constrain them as much as possible. Furthermore, certain background events can be used for calibration purposes, demonstrated in chapter 6. This chapter reviews the major backgrounds in SNO+, their origin, their expected rates, and some of the methods that can be used to constrain and reject them. Certain background events such as ^{214}BiPo and ^{208}Tl are the main focus of the analyses discussed in chapter 6 and chapter 7 respectively.

4.2 Double Beta Decay

One of the major backgrounds for $0\nu\beta\beta$ signal comes from $2\nu\beta\beta$ decays. As a consequence of finite energy resolution of the detector, events from the falling tail of $2\nu\beta\beta$ decay spectrum can fall into the region of interest for the signal. The half-life of $2\nu\beta\beta$ of ^{130}Te is well understood by CUORE collaboration, and measured to be $[7.9 \pm 0.1(stat) \pm 0.2(syst)] \times 10^{20}$ year [103]. The half-life of $2\nu\beta\beta$ and the shape of the signal along with good understanding of the reconstructed energy can help to constrain the expected number of events within the energy region of interest of 0ν signal.

4.3 Radioactive Backgrounds

Radioactive decays are on of the major backgrounds in SNO+. They are classified into two categories based upon their source of origin, the internal and external. The internal radioactive backgrounds originate inside the AV volume ($R <$6m), whereas the external backgrounds are created outside of the AV volume (e.g. ropes, external water, and the acrylic), but can propagate into the detector. Regardless of the origin, a detailed analysis and measurement of radioactive backgrounds is crucial for an accurate measurement of low energy solar neutrinos and $0\nu\beta\beta$ decay signal. The level of background from different isotopes can be continuously monitored and measured through *in-situ* measurements. Furthermore, *in-situ* analyses of certain radioisotopes can be used for calibration purposes, for instance, ^{214}Bi and ^{214}Po events are used to study the timing profile of scintillation throughout filling [69, 74].

The following sections reviews the major internal and external radioactive backgrounds, and describes their origin and characteristics.

4.3.1 Internal Backgrounds

The most important radioisotope backgrounds come from the decay chain of ^{238}U and ^{232}Th as shown in figure 4.1. In addition, there are other radioisotopes such as ^{40}K and ^{14}C that can contribute to the background.

^{238}U decay chain

^{238}U is a naturally occurring radioisotope with a half-life of 4.47×10^9 years. ^{238}U can produce several αs, βs, and γ's in its decay chain as demonstrated in figure 4.1 (top). The most problematic isotopes are the short-lived isotopes towards the end of the decay chain. ^{214}Bi decays by β and γ emissions with $Q_\beta \sim 3.27$MeV which makes them a serious background for $0\nu\beta\beta$. The dominated decay branch of ^{214}Bi is the 18% direct transition to the ground state of ^{214}Po. The Polonium has a half-life of 164.3 μs and undergoes an α decay.The 7.8 MeV αs from ^{214}Po would quench down

to 0.75 MeV in electron equivalent energy [93], and can be backgrounds for CNO and *pep* solar neutrinos. Fortunately, the delayed coincidence between ^{214}Bi and ^{214}Po decays can be used to tag these events with high efficiencies. Chapter 6 describes the tagging technique in detail.

The most significant disequilibrium in ^{238}U chain comes from ^{222}Rn gas which naturally exists in the lab air. The average concentration of ^{222}Rn in the lab air is measured to be 131 ± 6.7Bq/m^3 [62]. Therefore, it is crucial to keep the detector isolated from the lab air. In order to achieve that, an extensive leak checking is done on various parts of the UI such as the gate-valves. In addition, SNO+ uses 3 radon tight buffer bags filled with high purity nitrogen gas, known as cover gas system, described in chapter 2. This system is designed to reduce radon contamination by a factor of 10^5 [55]. In addition, SNO+ utilises a radon monitoring system that is connected to the UI. In order to determine the level of radon, the system has a proportional counter that detects αs from ^{222}Rn daughters such as ^{214}Po [104]. ^{222}Rn has a half-life of 3.8 days, and decays via several short lived daughter nuclei to ^{210}Pb which has a relatively long half-life of 22.3 years. ^{210}Pb eventually β-decays to ^{210}Bi which decays by β emission to ^{210}Po. These isotopes are one of the main concerns for solar neutrino studies. Aside from radon ingress, there is a significant ^{210}Pb contamination (~ 1.5 Bq/m^2 in 2021) on the acrylic surface, which can leach into the liquid scintillator and increase the background. This class of background is discussed in section 4.5.

^{232}Th decay chain

Another class of radioisotopes comes from the decay chain of ^{232}Th shown in figure 4.1. The most problematic isotopes are ^{212}Bi, ^{212}Po, and ^{208}Tl.
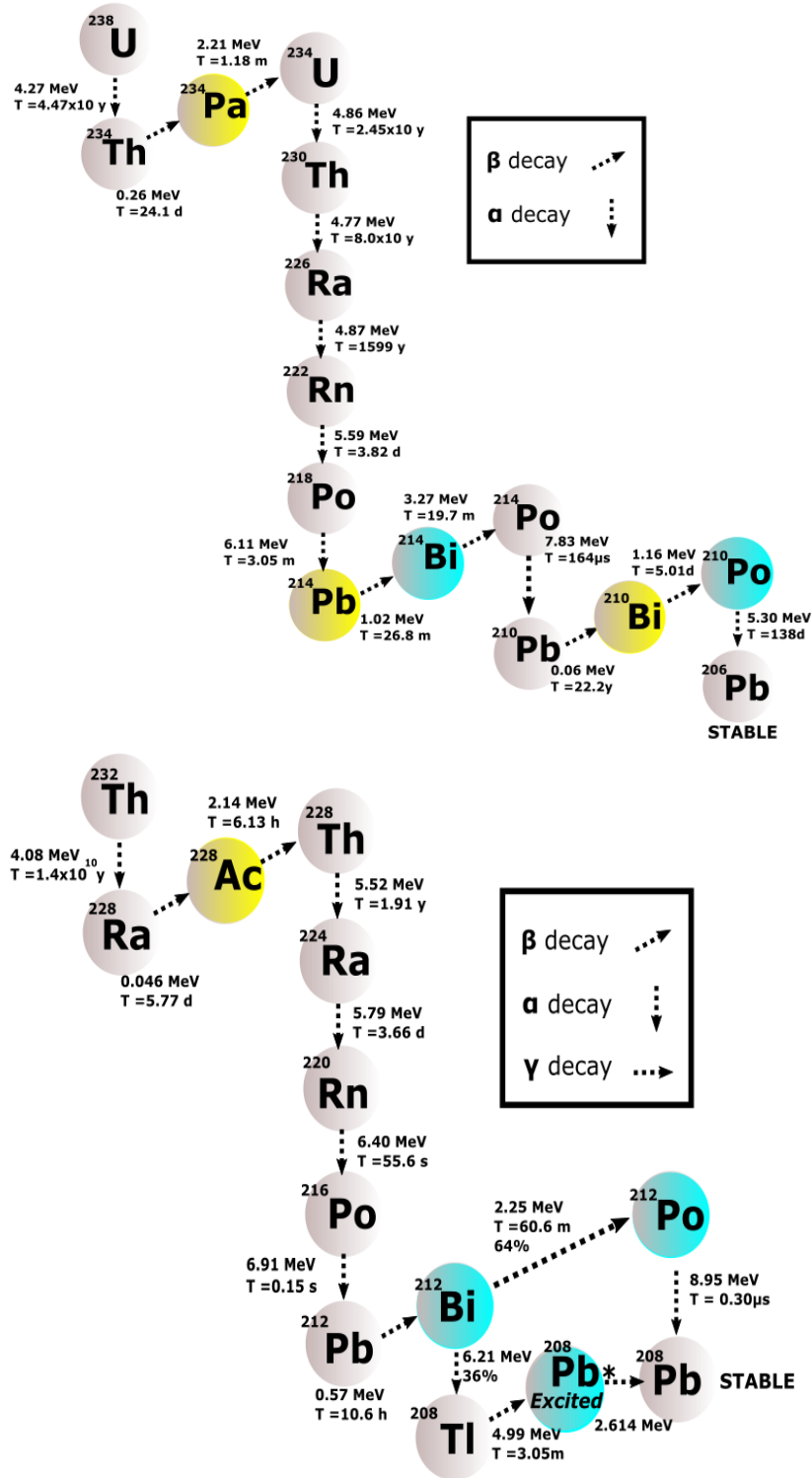
Figure 4.1: The decay chains of ^{238}U (top) and ^{232}Th (bottom).

^{212}Bi β decays with an endpoint of 2.225 MeV, followed by ^{212}Po α decays with a half-life of $\sim 0.3 \mu$s. The α decay has a Q-value of 8.95 MeV which is quenched down

to 0.9 MeV in electron equivalent energy. The delayed coincidence tagging efficiency of ^{212}BiPo pairs are not as good as ^{214}BiPo due to the branching ratio, and very short half-life of ^{212}Po, and therefore they can be potential backgrounds for solar neutrino measurements and $0\nu\beta\beta$ search, however their rate is orders of magnitude lower than ^{214}BiPo events. Furthermore, the bismuth and polonium decays can take place withing a single triggering window and cause pile-up events with higher energies.

One of the other concerning radioisotopes is ^{208}Tl which comes from α decays of ^{212}Bi with branching ratio of 36%. ^{208}Tl undergoes β decay with Q_β=4.99 MeV, and produces excited states of ^{208}Pb which decays by emitting several γ's, and subsequently decays to the ground state by emission of a 2.61 MeV γ [105]. These γ's can be a serious background for the $0\nu\beta\beta$ signal, and they are discussed in chapter 7.

^{40}K

Potassium 40 is a naturally occurring radioisotope with a natural abundance of 0.0117%. ^{40}K is a unique nuclide that undergoes two types of decays: I) β decays to ^{40}Ca with Q_β =1.31 MeV and branching ratio of 89.3%, and II) in about 11% of events, it decays to ^{40}Ar via electron capture, and the emission of 1.46 MeV γ.
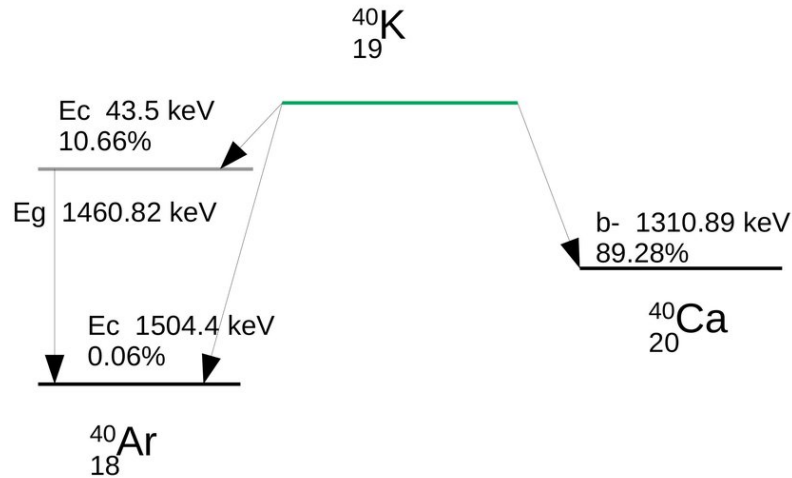
Figure 4.2: Decay schematic of ^{40}K, taken from [106]

The decay schematics of ^{40}K is shown in figure 4.2. These events are backgrounds for

pep solar neutrino measurements. The β portion of the decay can be estimated and modeled by identifying the γ peak from the data.

Removing and Rejecting the Internal Backgrounds

The primary strategy to remove the internal radioactive background is purification of the scintillator and Diol through the purification plants [107]. The target LAB impurity levels for SNO+ are equal to those measured by Borexino [55, 108]. Aside from purification, further data analysis techniques should be used to suppress the background. The delayed coincidence between $^{212/214}$Bi and $^{212/214}$Po is used to efficiently tag these events. This technique is discussed in chapter 6. Furthermore, the tagged $^{212/214}$BiPo events can be used to estimate other backgrounds from $^{232/238}$Th/U decay chain under the assumption of equilibrium within the decay chain. Moreover, the rate of pile-up events is estimated [19], and furthermore they can be rejected using the double pulse structure of their hit time residuals [109].

4.3.2   External Backgrounds

One class of radioactive backgrounds are created outside of the AV but can propagate into the detector. The most concerning radioisotopes are the γ emitters such as ^{214}Bi, ^{208}Tl, and ^{40}K. They emit γ's with energies greater than 1 MeV that can penetrate into the detection volume. These γ emitters have various sources such as the acrylic, external water, the rope systems, the inner/outer dust on the AV, and the PMTs. The sources of external γ's along with their expected rates are summarized in tables 7.1 & 7.2. Figure 4.3 shows the reconstructed energy spectrum of the external γ's from ^{208}Tl and ^{214}Bi in the detector for one year of data taking in Tellurium phase, the rates are taken from [110]. The 2.61 MeV γ peak from the external ^{208}Tl is very close to $Q_{\beta\beta}$ of ^{130}Te, and can be a serious background for $0\nu\beta\beta$ studies. Furthermore, high rates of various γ's from ^{214}Bi and ^{40}K can mask any signal at the higher radii.
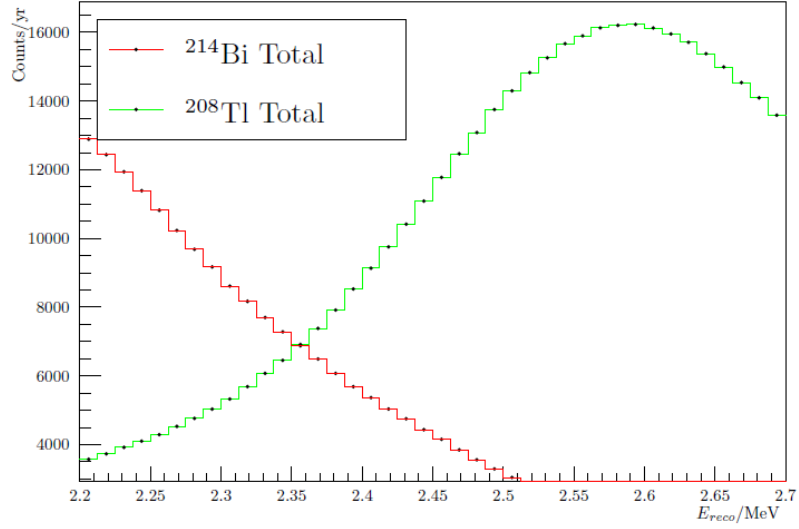
Figure 4.3: Reconstructed energy of simulated external γ's from ^{208}Tl and ^{214}Bi.
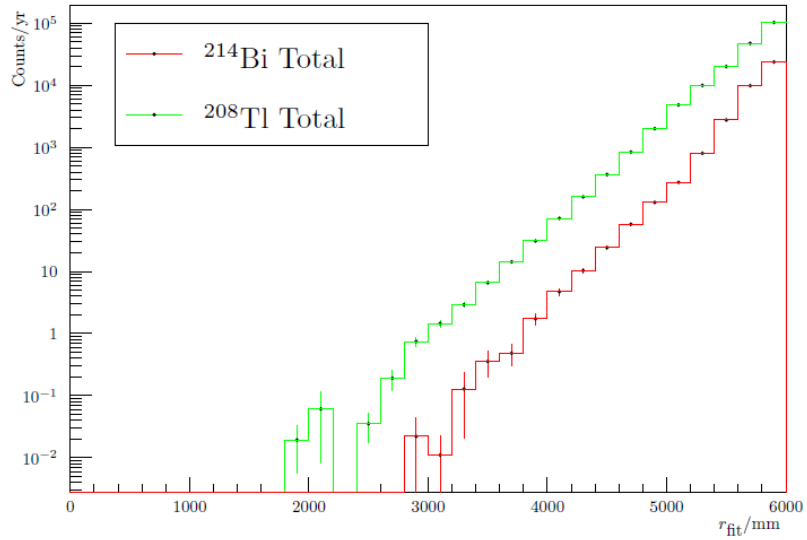
Figure 4.4: Reconstructed radius of simulated external γ's from ^{208}Tl and ^{214}Bi. The rates are scaled to match the expected number of events from [110].

Rejecting the External Backgrounds

The most primary strategy to reject external γ's is fiducialising the inner regions of the detector. However, optimizing the fiducial volume is a compromise between sacrificing data and rejecting the background [92]. Figure 4.4 shows the rate of these γ's within a year of data taking versus the reconstructed radius from a set of sim-

65

ulated data. Despite of fiducialising, a small fraction of the γ's can travel far into the center of detector, as it can be seen from figure 4.4. The time residuals of these events are more smeared due to multiple Compton scatterings, which can be used to discriminate them from the internal α/β decays. As described in section 3.5, a set of timing and topological classifiers are developed and optimised. The efficiency of some of these classifiers are investigated in chapter 7. Furthermore, the rate of external γ's from the AV, external water, and hold-down ropes are measured through two independent analyses during the water phase [82, 74].

Furthermore, SNO+ uses different assay techniques such as HTiO technique to measure ^{238}U and ^{232}Th daughters such as $^{226/224}$Ra in external water, and study the disequilibrium within the decay chain [111, 112].

4.4   Pile-up Events

A pile-up event occurs when two or more decays take place within a single trigger time window ($\sim$ 400ns). The detector would register the pile-up events as a single event with the energy equal to the sum of the pile-up events energies. Therefore, low energy events can pile up, and fall into the energy region of interest of the signal. The probability of such events can be described by Poisson statistics as follows:

$$N_{PU} = N_A N_B e^{-N_B} \tag{4.1}$$

where N_{PU}, N_A, and N_B are the number of pile-up events, the number of events from source A, and the number of events from source B within the same triggering window, respectively. As it can be seen from equation 4.1, the pile-up become concerning when the rates of the contributing events are high, on the order of a few hundred Hz. ^{14}C, ^{210}Po, ^{210}Bi, and $2\nu\beta\beta$ decays are some of the signals that can potentially pile-up due to their high rates. Fortunately, the timing of the pile-up events is distorted, and is used to identify and reject them [19].

4.5 Surface Contamination and Leaching of ^{222}Rn Progeny

During transitioning from SNO to SNO+ the detector was empty and exposed to the lab air. As a result some level of ^{222}Rn has diffused into the acrylic surface. ^{222}Rn eventually decays into ^{210}Pb which has a relatively longer half-life of 22.3 years [113], and can build up on the acrylic surface. Therefore, ^{210}Pb is out of equilibrium with its parents isotopes in the decay chain, however it can be considered in equilibrium with its daughters. As shown in figure 4.1, ^{210}Pb decays to ^{210}Bi with $Q_\beta \sim 0.06$ MeV. Subsequently, ^{210}Bi β-decays to ^{210}Po with end point of 1.6 MeV that can be a direct background for CNO and *pep* solar neutrinos. Moreover, ^{210}Po is a source of 5.3 MeV αs. The quenched α peak in scintillator found to appear at about 0.4 MeV in electron equivalent energy [114]. In addition, α-particles can go through (α, n) interactions and produce free neutrons. These interactions are discussed in the next section. In order to determine the surface activity of ^{222}Rn daughters, several *in-situ* measurements have been performed on different spots of the AV [115, 116], and the average surface activity found to be 2.4 ± 0.8Bq/m^2 in 2013. This is a bigger concern since the radon progeny can leach into the detection volume (e.g. liquid scintillator) and increase the background level and suppress the fiducial volume. Figure 4.5 demonstrates the leaching mechanism of the ^{222}Rn progeny. As part of my M.Sc. research I have developed a model that can be used to determine the surface activities over time, and furthermore estimate the level of backgrounds from the leaching process [117]. The model is described in Appendix B.

Furthermore, the rates of ^{210}Bi and ^{210}Po are relatively higher, $O(100)$Hz [110], and they make the major portion of the events below 1 MeV in scintillator. These events can pile-up within the triggering time window and fall into the energy region of interests for $0\nu\beta\beta$ signal. The probability of pile-up of the surface events with ^{16}N calibration data was discussed in section 5.4.3.
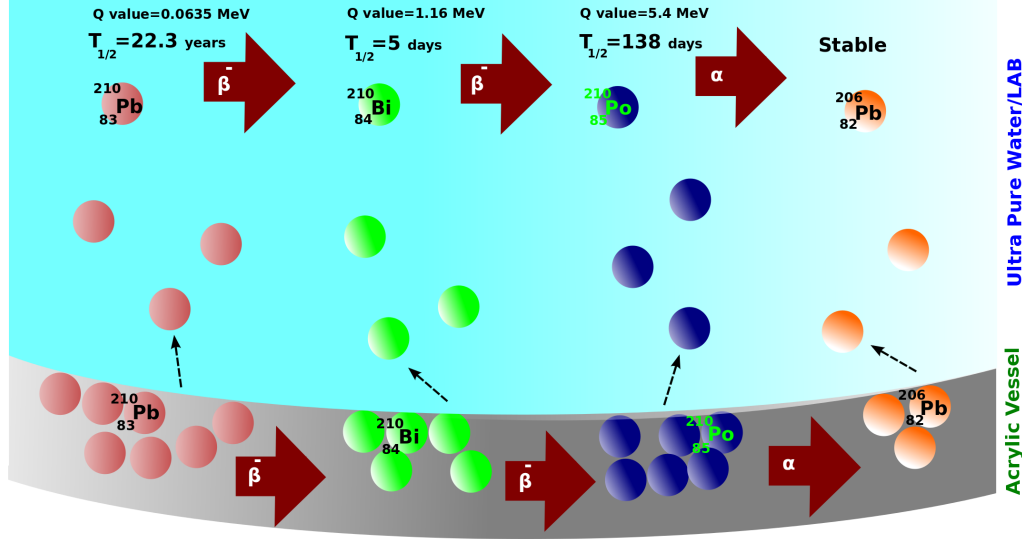
Figure 4.5: Figure demonstrates acrylic surface contamination of ^{222}Rn progeny and the leaching process. A set of differential equation was used as a basis of a model to estimate the rate of each isotope over time.

4.6 α-n Interactions

The α-n interaction occur when a high energy α particle get absorbed by a nucleus, causing the nucleus to emit a neutron. The most dominant source of high energy αs in the detector is the surface ^{210}Po. In addition, other isotopes of polonium are also α emitters such as ^{214}Po and ^{212}Po. Such events can make three different scintillation signals: I) the α can produce quenched scintillation light, II) the fast neutron can scatter off protons while thermalizing and cause the protons to make scintillation light, and III) the neutron eventually captures on a nucleus once thermalized, and possibly causes the nucleus to emit γ's. The most common neutron absorber in the detector is hydrogen, and once captured a neutron would emit a 2.2 MeV γ. This signal can be reconstructed close to the energy region of interest for $0\nu\beta\beta$. In addition, the delayed neutron capture signals can form serious backgrounds for anti-neutrino studies since they have the same characteristics.

The rate of such events is estimated based upon leaching models. Furthermore, the fast neutron has a thermalisation time of $\sim$220 μs, and average path length of 49 cm in

scintillator [55]. Therefore, the α-n events can be tagged through delayed coincidence tagging.

4.7 Cosmogenics

Cosmic rays have the potential to interact with stable elements in scintillator or on Tellurium, and produce radioisotopes that do not naturally exist in the detector. The most concerning isotopes that can be produced through muon interactions in scintillator are as follow; ^{16}N ($\tau_{1/2}$ =7.13 s), ^{11}C (20 min), ^{10}C (19.3 s), ^{11}Be (13.8 s), and ^{7}Be (53.3 days) [110]. Fortunately, less than 3 cosmic muons per hour are expected in the detector at the depth of SNOLAB. Furthermore, removing the events within a few minute time window of a muon event can reject most of these decays except for ^{7}Be. Additionally, position cuts along the muon trajectory can effectively reject these events. However, the bigger concern is the cosmogenic isotopes produced during manufacturing, transportation, and storage on surface. The rate of the cosmogenic isotopes can be estimated based upon the exposure time of LAB or Tellurium on surface. It is estimated that it takes about 3.4 years for ^{7}Be to reach equilibrium with underground production rate [110].

Furthermore, ^{130}Te is a concerning target for production of long-lived cosmogenic radioisotopes. V. Lozza and J. Petzoldta have studied the rate of cosmogenic isotopes produced by spallation of cosmic rays on ^{130}Te [118]. The primary strategy is removing these isotopes through Tellurium purification process. More concerning isotopes are the ones with a half-life comparable with the run time of the experiment, $O(1$ year). The most worrisome isotopes are ^{110}Ag, $^{56/58/60}$Co, ^{22}Na, $^{102/106}$Rh, $^{124/126}$Sb, ^{106}Rh, $^{44/46}$Sc, ^{42}K, and $^{88/90}$Y.

^{14}C

^{14}C is a radioisotope produced through cosmogenic activation of ^{14}N, and is naturally present in liquid scintillator. ^{14}C has a $Q_{\beta} = 0.16$MeV, and half-life of 5730 years.

We expect a ^{12}C/^{14}C ratio of the order of magnitude of $\sim 10^{-18}$, consistent with what Borexino has measured in their test facility [119]. This abundance would translate to a decay rate of about a few hundred Hz in scintillator. The amount of cosmogenic ^{14}C produced throughout transportation and storage is negligible in comparison. ^{14}C can be a potential background for low energy pp solar neutrinos, and furthermore can contribute to the pile-up due to the high rate. Moreover, the endpoint of ^{14}C energy spectrum can be characterised, and used for calibration purposes at lower energies [120].

4.8   Summary

This chapter reviews the most concerning backgrounds for SNO+, their nature, their expected rates, and some of the techniques that can be used to remove or identify and reject the background events. The target levels of backgrounds can be found in [110]. It is noteworthy that one class of backgrounds known as the instrumental backgrounds produced by the electronic system is not discussed in this chapter. This chapter is a prerequisite for my background analyses discussed in chapter 6 and chapter 7.

Chapter 5: SNO+ Calibration with ^{16}N Source

5.1 Introduction

In order to understand the response of the detector to different types of events, SNO+ uses MC modelings of the detector along with an extensive optical and energy calibration program. Calibration is achieved by utilising various deployed and embedded calibration sources discussed in section 2.5. The primary energy calibration source in water phase was a tagged 6.13 MeV γ emitted through de-excitation of ^{16}O*, which is created through β decay of radioactive nitrogen gas, simply known as the ^{16}N source [81]. The source is described in detail in section 5.2. The ^{16}N data was taken for over 90 different source positions during the water phase. The calibration data were used to tune our physics models, verify the position reconstruction algorithms, determine the global efficiency of the detector, determine the energy scale and resolution, determine the systematic uncertainties and offsets, and finally verify the optical model [76]. The ^{16}N water analyses are discussed in section 5.3.

In addition, the source was deployed externally throughout the scintillator filling process, and the data were used to understand the scintillator light yield, and the PPO mixing process. Furthermore, the position reconstruction algorithms are verified at the higher radii, and the position dependency of the light yield has been investigated, presented in section 5.4.3. In addition, I have used the hit time residuals of ^{16}N γ's to characterize the scintillation timing for different PPO concentrations, which is discussed in section 5.4.4. Moreover, the Cherenkov signal in scintillator with low PPO concentrations was identified using the ^{16}N data.

Finally the findings from these analyses are summarized in section 5.5.

5.2 The ^{16}N Source

5.2.1 ^{16}N Production

^{16}N is a short-lived radioactive gas with half-life of 7.13 seconds that undergoes β decay, and most likely produces excited ^{16}O*. Due to the short half-life, the gas needs to be produced locally, and used right away. In order to produce ^{16}N, SNO+ uses a commercial Deuterium-Tritium (DT) generator, the MF Physics model A-320 [121]. DT generator is a small particle accelerator that produces high energy neutrons ($\sim$14 MeV) by accelerating a mixed beam of Deuterium and Tritium into a target of both Deuterium and Tritium which results in the fusion reaction as shown in equation 5.1.

$$d + t \longrightarrow n +^4 He \tag{5.1}$$

This model of DT generator has a relatively large flux of neutrons which is tunable between 2×10^7 and 10^8 neutrons/second. The DT accelerator is a 2.2 m long cylindrical shape with a diameter of 4.3 cm. The convenient size of the accelerator allows us to increase the flux of produced ^{16}N through the production chamber shown in figure 5.1. The DT generator is placed inside a concrete shielding pit that is located about 40m away from the center of the detector. The concrete pit should effectively eliminate the radiation hazard [122]. Figure 5.1 shows a detailed schematic of the DT generator inside the pit.

^{16}N can be produced using the high energy neutrons through ^{16}O(n,p) interactions with $Q = -9.6$MeV and $\sigma = 25$mb as it is demonstrated in equation 5.2. Another alternative interaction that can be used is ^{19}F(n, α) with $Q = -1.5$MeV and $\sigma = 35$mb. The radioisotope transfer was found to be easier using a gas target, therefore CO_2 gas is used as both the target oxygen, and as the carrier to transfer the ^{16}N through a Teflon tubing all the way to the URM, and down into the ^{16}N decay chamber shown
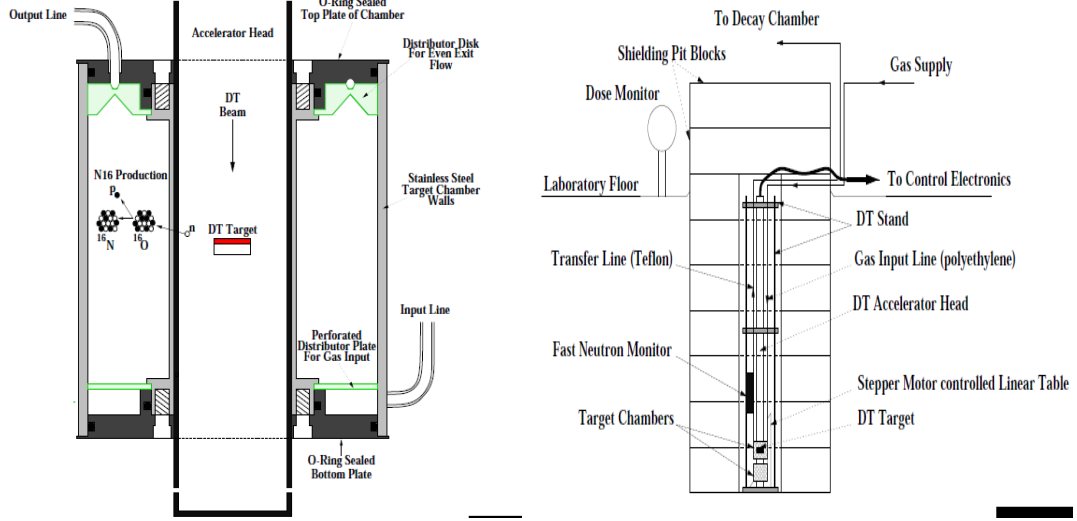
Figure 5.1: Schematic of the target chamber (left). ^{16}N is produced by introducing CO_2 into the target chamber. Schematic of the DT generator (right).

in figure 5.2 [123].

$$n +^{16} O \longrightarrow p +^{16} N \tag{5.2}$$

The target chamber is located at the bottom of the pit which is shown in figure 5.1(left). The design is a compromise between maximizing the ^{16}N production and minimizing the residence time of the gas in the chamber.

5.2.2 The Gas Transfer and The Decay Chamber

The produced ^{16}N is sent through a Teflon tubing from the target chamber to SNO+ deck into the URM, and further sent through the umbilical down into the ^{16}N decay chamber shown in figure 5.2. The return flow is sent up through a line in the umbilical back to the lab exhaust. The flowing ^{16}N undergoes β decay with a half life of 7.13 seconds, and Q_β=10.4 MeV (see eq. 5.3). The β particles within the decay chamber can be captured in the plastic scintillator, and are used to tag the calibration events. The produced ^{16}O* is most likely in an excited state, and can de-excite and emit γ that can penetrate through the decay chamber into the detector volume.

$$^{16}N \longrightarrow^{16} O^* + \beta(tagged) + \bar{\nu}_e \qquad (Q = 10.4 MeV) \tag{5.3}$$

73

Figure 5.2 shows the schematics of the SNO+ ^{16}N decay chamber which consists of a stainless steel casing, the sleeve material, plastic scintillator, and a dedicated PMT to detect the scintillation signal and tag the β particles.
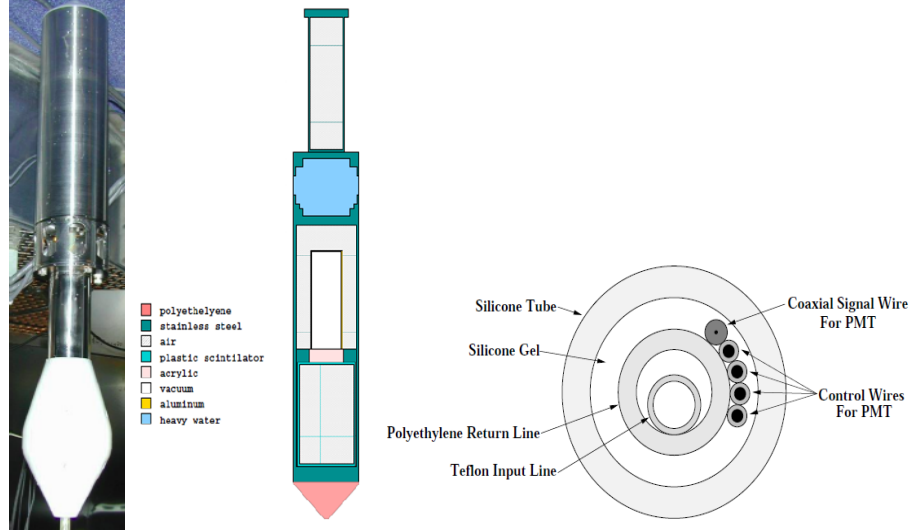
Figure 5.2: The ^{16}N decay chamber (left). A cross section of the umbilical is shown on the right.

The main casing is a cylindrical stainless steel that is about 70 cm long with a diameter of 11 cm [124]. The general design is a compromise between minimizing the γ rays attenuation, and maximizing the β particles containment. The stopping power in steel is about 2 MeV cm^2/g for a 10 MeV β particle. It can be demonstrated that 0.5 cm thickness of the steel along with the sleeve material and the plastic scintillator can effectively capture the emitted β particles. The ^{16}N decays take place in the lower half of the decay chamber within a volume that is enveloped by a 3 mm thick cylindrical plastic scintillator (Bicron BC400 [125]). The upper volume of the decay chamber holds a 5.08 cm diameter PMT (model 9208B [126]) which collects the scintillation light through an optical coupling which is a rigid acrylic window. The high voltage for the PMT as well as the signal are carried through coaxial cables in the umbilical shown in figure 5.2.

5.2.3 γ Emission and The Source Performance

Figure 5.3 demonstrates the ^{16}N decay with the two main γ decay branches of ^{16}O*(dashed vertical lines).
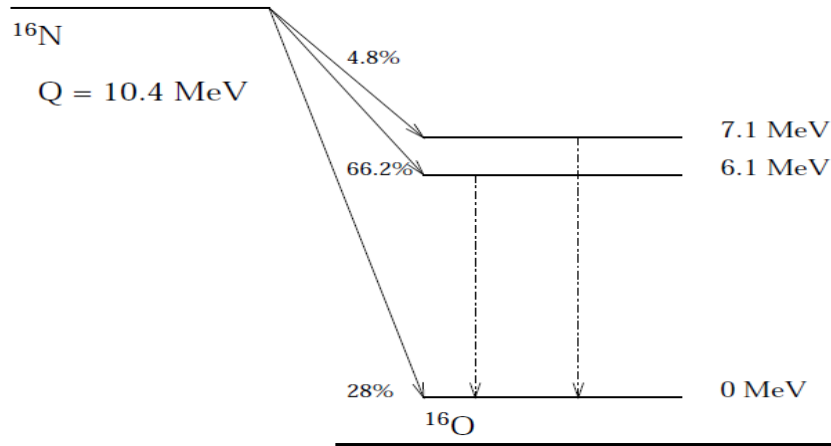
Figure 5.3: Schematic of ^{16}N decay. The diagonal lines represent different β-decay branches. The γ-less β decay has $Q_\beta = 10.4$ MeV. Two main gamma decay branches are represented with vertical dashed lines.

There is a branch ratio of 28% that the ^{16}N nuclei would β-decay to the ground state of ^{16}O without emitting any gammas. However, the β particles from these γ-less decays can fire the ^{16}N PMT and produce invalid calibration tags. This set of invalid tagged events can pile-up with other backgrounds (e.g. ^{210}Po), and should be properly taken into account for the ^{16}N analyses. They are discussed in section 5.4.3. The main decay branch (66.2%) produces a β particle with an end point of 4.3 MeV followed by a 6.13 MeV γ which provides the most important signal for the calibration purposes. Furthermore, there is a branch ratio of 6% that produces 7.1 MeV γ. The peak for 7.1 MeV γ cannot be distinguished from the main peak in water, however it can be clearly identified in scintillator as it is demonstrated in the following sections. Figure 5.4 shows the β-decay spectrum from MC simulated ^{16}N events taking place inside the decay chamber.
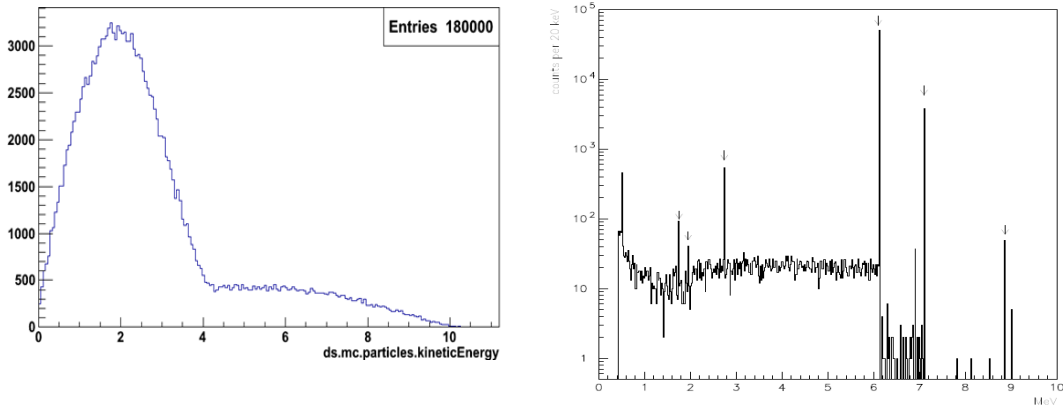
Figure 5.4: The energy spectrum of ^{16}N β decay (left) from MC. The apparent energy spectrum of different γ's from de-excitation of ^{16}O from MC [83, 81].

The emitted γ can interact in steel, and lose a fraction of its energy through Compton scattering. This can introduce a continuum to the detected energy spectrum (Nhits) of ^{16}N γ's that can be clearly seen in scintillator data. The continuum is also shown in the simulated emission spectrum in figure 5.4. Moreover, β particles can interact with the material in decay chamber, and generate secondary γ's through Bremsstrahlung effect[1] [81]. These secondary γ's can also contribute to the continuum, and smear out the signal. However, the rate of Bremsstrahlung γ's has been studied and found to be negligible ($\sim 10^{-3}$/decay).

The tagging efficiency of the source was measured offline using a NaI detector in SNO. The signal was analysed for the energy range between 6-7 MeV and the tagging efficiency found to be 95±2% [127]. The *in-situ* measurements from SNO calibration was also consistent, and shows about 95% tagging efficiency for a central ^{16}N run. As shown in figure 5.5, we have also confirmed the measured tagging efficiency from the scintillator signal for ^{16}N. A comparison between the peak integrals of the tagged and untagged events shows over 93% tagging efficiency for external ^{16}N run in scintillator.

---

[1] $e^- + (Z, A) \longrightarrow e^- + \gamma + (Z, A)$
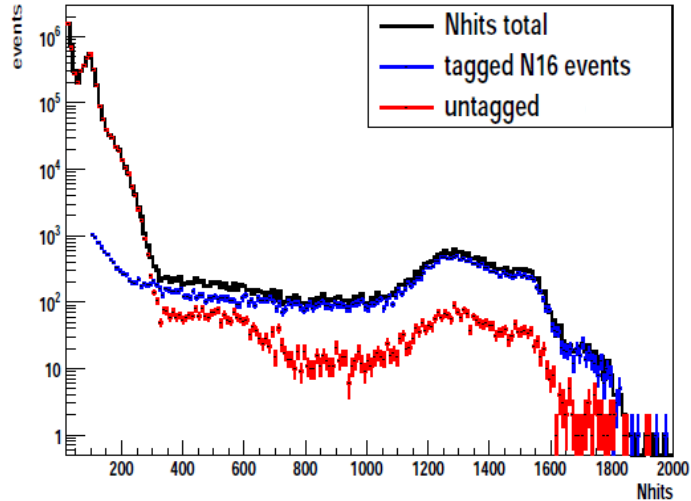
Figure 5.5: Nhits distribution of tagged ^{16}N (blue), untagged events (red) and the total (black) in scintillator. The 6.1 MeV γ peak can be identified about 1300 Nhits. The ratio between the peak integral of the tagged events and the peak integral of untagged ^{16}N shows about 93% tagging efficiency.

5.2.4 ^{16}N Deployment

An overview of SNO+ calibration hardware was given in section 2.5.3. The ^{16}N source was the primary calibration source in the water phase, and was deployed internally through the UI, and externally through the guide tubes. The calibration data were taken for over 80 different source positions inside the detector. A typical calibration run was about 1 hour with a rate of about 40 Hz for tagged calibration events. The water calibration data are discussed in section 5.3. In addition, the summary of ^{16}N calibration program in water can be found in [83].

The ^{16}N hardware is not designed to be deployed into the scintillator since they do not meet the cleanliness requirements. However, the source has been deployed externally 7 times through different guide tubes throughout the scintillator fill. Table 5.2 shows a summary of the scintillator ^{16}N runs.

5.3 ^{16}N in Water

The tagged 6.13 MeV γ's provide a clean calibration sample with energies close to the energy ranges of two physics topics studied during the water phase; i) the ^{8}B solar neutrinos, and ii) the invisible nucleon decay. The first set of ^{16}N calibration was performed in May 2017, and the data were taken with the source placed at 7 different positions along z-axis. The central ^{16}N run was used as a reference to tune the total collection efficiency of the detector, determine the energy scale, and verify the reconstructions. Furthermore, a full volume internal calibration was performed in November 2017. ^{16}N data were taken in a series of runs for 88 different source positions inside the detector. This data set was used to determine the position dependencies of the detector model. Figure 5.6 (left) shows the source positions for the ^{16}N full scan during the water phase. Finally, a set of external calibration data were taken in March 2018. The source was deployed through guide-tube 4 into the volume between the PSUP and AV, and the calibration data were taken for 19 different positions along the vertical axis. The reconstructed position for the full external ^{16}N data set is shown in figure 5.6(right).

5.3.1 Event Selection Criteria

Even though ^{16}N is a tagged source, a set of selection criteria is required to perform standard analyses. The selection cuts might vary depending on the type of analysis. For instance one of the cuts for the water analysis is known as the proximity cut which removes all the events that are reconstructed within 70 cm of the source. The purpose of the proximity cut is to minimize the effect of shadowing from the source itself. The standard event selection criteria for the water phase can be outlined as follow [83]:

- Have a valid `Fitter`; valid time and charge.
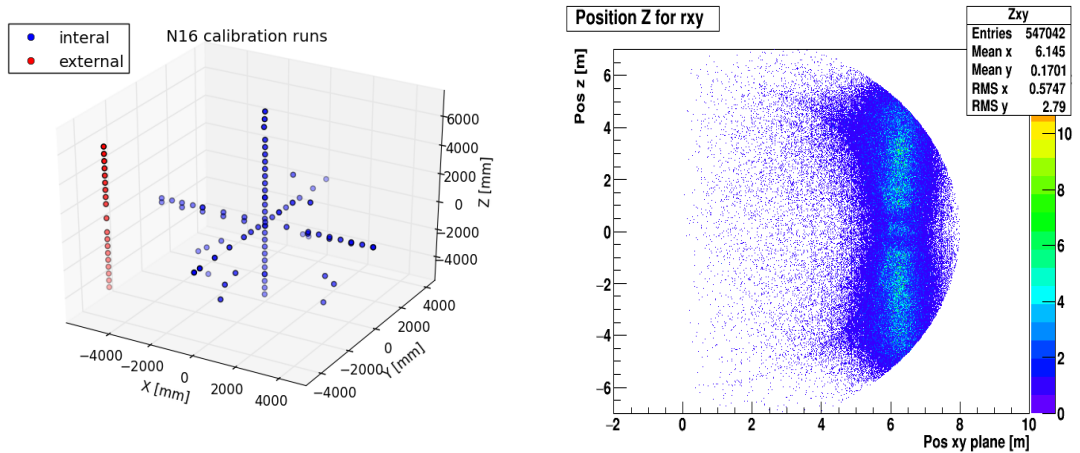
Figure 5.6: The **left** shows the ^{16}N source positions in water phase; 88 points for the full internal scan and 19 points for the external calibration. Reconstructed z[m] vs. reconstructed ρ for the full external scan is shown on the right.

- Have the ^{16}N calibration tag (FECD PMT 9188).

- Hits are not attributed to cross-talk.

- $-0.12 < \beta_{14} < 0.95$.

- $0.55 < $ ITR .

- The proximity and direction cuts:

  - Keep the events that are being reconstructed further than 70 cm from the source.

  - Keep events that are reconstructed within 70 cm of the source if the event direction is within 45° of the vector from the source to event vertex (reconstructed position).

5.3.2   Global efficiency

As described in section 3.3.1, the hit time residuals of the PMTs is the key distribution to reconstruct the event vertex. Figure 5.6 shows an example of the hit time residuals distribution for a ^{16}N run in water. Furthermore, the optical model of the detector

79
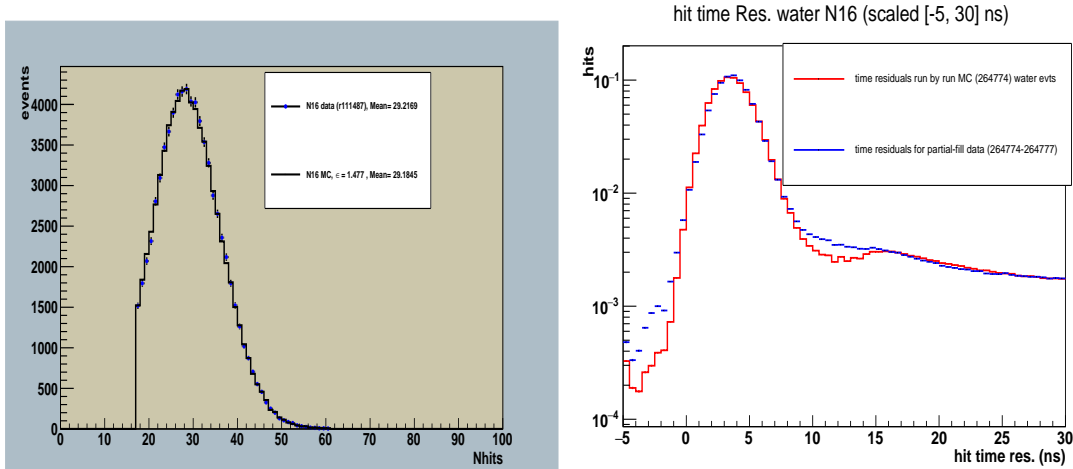
Figure 5.7: The **left** plot shows the prompt Nhit distribution of simulated ^{16}N data matched up to the central calibration data to determine the global trigger efficiency, where the events with nhits>17 are selected. The hit time residuals of ^{16}N in water is shown on the right.

can be calibrated by matching time residuals distribution from MC to the optical calibration data.

The efficiency of capturing light in the detector can be described through a parameter ϵ, known as global efficiency. The global efficiency is a relative indicator of light collection in the detector and involves many factors such as the channels efficiency and the detector coverage. The prompt Nhits distribution of the central ^{16}N run was used to determine ϵ [83], and furthermore determine the energy response of the detector. In this case, the prompt Nhits is defined as the number of fired PMTs within the hit time residuals window of (-5, 8) ns. The prompt signal is selected to avoid the complications due to optical effects such as the reflection off different components in the detector. In order to determine ϵ, the prompt Nhits distribution from a MC simulation is matched up to the central ^{16}N data as shown in figure 5.7 (left).

5.3.3 Energy Calibration

Energy is reconstructed using the EnergyRSP algorithm [83]. The energy scale and the energy resolution in the water phase was determined using the ^{16}N data. In addition, the associated systematic uncertainties were estimated comparing the energy

scale and resolution in data with the run-by-run MC simulations. The relative energy scale δ_E, and the detector energy resolution σ are incorporated in the model, and estimated by fitting the reconstructed energy spectrum $P(T_{eff})$.

$$P(T_{eff}) \sim \int (P_{source}(T_e) \frac{1}{\sqrt{2\pi}\sigma} \exp(\frac{-((1+\delta_E)T_{eff} - T_e)^2}{2\sigma^2})dT_e) \qquad (5.4)$$

As shown in equation 5.4, $P(T_{eff})$ is described in terms of the apparent energy spectrum of electrons, $P_{source}(T_e)$, convolved with a Gaussian. The apparent energy of electrons is essentially defined as the energy that scattered electrons ultimately deposit in water. The apparent energy of electrons in not a trivial distribution, and in order to be determined, the detailed physics should be taken into account. For instance, a 6.1 MeV γ can deposit a fraction of their energy in the source container on the way out. In addition, the γ's most likely go through multiple Compton scatterings, knock off multiple electrons, and form multiple Cherenkov rings. The physics of scattered electrons is simulated using `RAT-6.5.0`, and their apparent energy distribution is shown in figure 5.8. This distribution is incorporated into equation 5.4 to fit the calibration data.
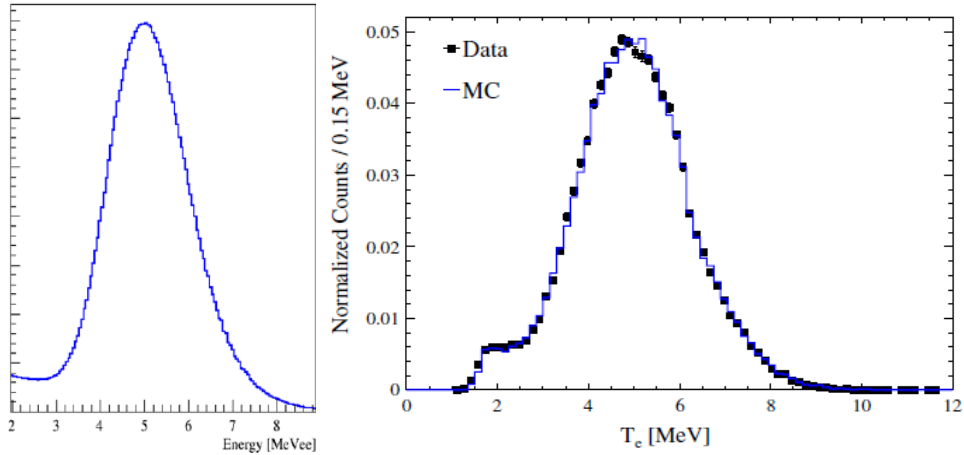
Figure 5.8: The apparent energy of scattered electrons simulated with RAT-6.5.0 shown on the left. The reconstructed energy of ^{16}N data (black) on the right [83] together with the MC simulation (blue), for a central run.

The energy resolution σ is expected to be energy dependent, and can be expressed as $\sigma = b\sqrt{E}$, where b can be estimated from the fit. No energy offset is considered

in this case since it is assumed that there is no significant background contribution to the tagged ^{16}N signal. Figure 5.7 shows the reconstructed energy spectrum for a central ^{16}N run in water together with the one from a run-by-run simulation [82]. Furthermore the position dependency of the energy related parameters are investigated through the full ^{16}N scan [83].

5.3.4 The Reconstructed Position and angular Uncertainties

In order to determine the uncertainties associated with the reconstructed position and direction, the measured ^{16}N data were compared with MC simulations. For the purpose of this analysis, the difference between the tagged ^{16}N events and the source position was used as the key distribution to fit the model, shown in figure 5.9. This distribution was fit with a function representing the position of the first Compton electron generated from MC, convolved with a Gaussian and an exponential tail, see equation 5.5.

$$f(x) = A.\gamma_{first} * \left(e^{-x/\tau} * e^{\frac{-(x-\mu)}{2\sigma^2}}\right) \tag{5.5}$$

where γ_{first} is the distribution representing the position of the first Compton electron, μ is the bias, σ is the resolution, and τ characterises the tail. Furthermore, the systematic uncertainties can be described in terms of the offset between the position of the source and the mean reconstructed position, $x_{data} \rightarrow x_{source} + \delta_i$. Table 5.1 shows a summary of the systematic uncertainties and the resolutions determined using ^{16}N data.
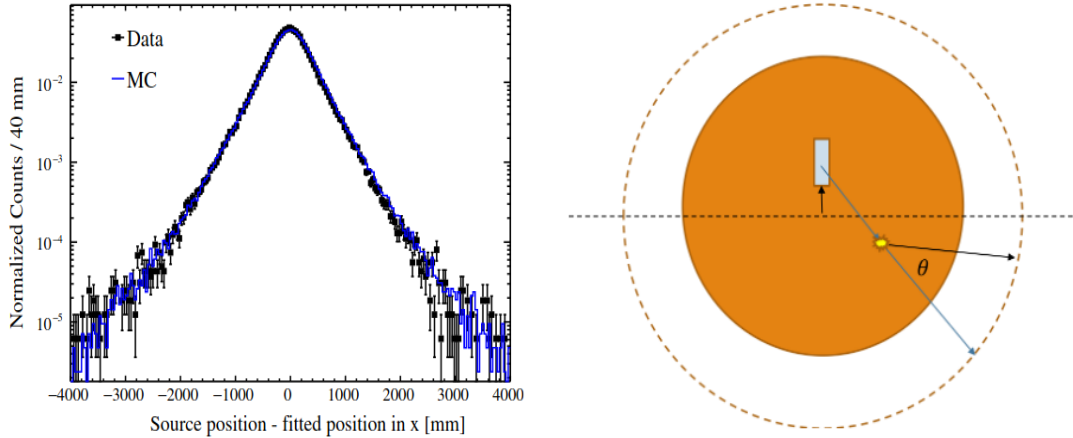
Figure 5.9: The histogram on the left shows the difference between the source position and the reconstructed position of the event, assumed to be the first Compton scattered electron, for a central ^{16}N run [82]. The angle of the Compton scattered electron, θ is demonstrated on the right.

The angular resolution and the uncertainty were determined based upon the colinearity of Compton scattered electrons with the initial γ direction, θ, shown in figure 5.9. The reconstructed position is assumed to be the scattering vertex, however to reduce the effect of position reconstruction uncertainties, only events that are reconstructed further than 1200 mm from the source were selected [82]. The resulting distribution is fit with the following functional form [128] [129]:

$$R(\cos\theta) = \alpha_m\beta_m\frac{e^{\beta_m(\cos\theta-1)}}{1-e^{-\beta_m}} + (1-\alpha_m)\beta_s\frac{e^{\beta_s(\cos\theta-1)}}{1-e^{-\beta_s}} \tag{5.6}$$

where β_m and β_s are two exponential components, and α_m is the fraction of the events following the exponential with slope β_m. β_m represents the electron-like resolution whereas β_s describes the contribution of events with multiple Compton scatterings [66].

5.3.5 β_{14} discrepancy and uncertainty

As described in section 3.5, β_{14} is a powerful topological classifier that can determine the isotropy of the fired PMTs within an event. β_{14} can be used to distinguish the scintillator-like ^{16}N events (isotropic light emission) from the water-like ^{16}N events

Parameter	x offset [mm]	y offset	z offset	x resolution	y resolution	z resolution	Uncert. on angular resolution	β_{14} syst.
uncertainty	+16.4	+22.3	+38.4	104(mm)	98(mm)	106(mm)	+0.08	0.031±0.004
resolution	-18.2	-19.2	-16.7				-0.13	

Table 5.1: Summary of systematic uncertainties for reconstructed position and direction during water phase based on ^{16}N data, the values are taken from [82, 66].

(Cherenkov ring) when the source is deployed in partial-fill, which is discussed in section 5.4. We have observed about 9% discrepancy between the $\beta_1 4$ from ^{16}N central
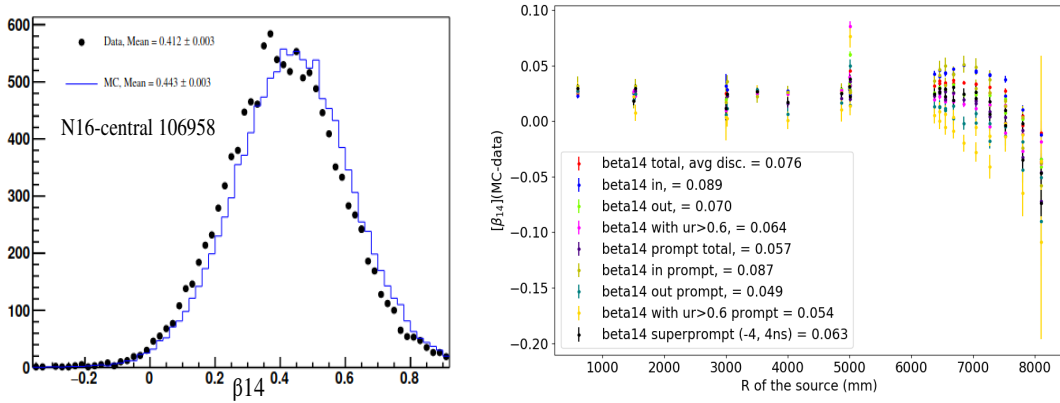
Figure 5.10: β_{14} distribution of a central ^{16}N in water, data (black) and MC (blue). The plot on the right shows the β_{14} discrepancy (MC-data) vs. the radial position of the source. Different colors represent different directionality and timing cuts.

run and the associated MC shown in figure 5.10. In addition, the calibration data from the AmBe source confirmed the discrepancy. In order to understand the nature of the discrepancy, a set of directionality, and timing analysis was performed on the full ^{16}N data. It was demonstrated that looking at outward-going events ($\vec{u}.\vec{r} > 0$) can reduce the discrepancy by about 40%. $\vec{u}$ is the vector representing the direction of event, and $\vec{r}$ is the vector pointing to the event vertex from the center of the detector. Furthermore, selecting the events with higher `ITR` (prompt) seems to slightly reduce the discrepancy. Figure 5.10 shows the summary of different analysis cuts used to understand the β_{14} discrepancy. Finally, the observed discrepancy was implemented into the model as the systematic uncertainty of β_{14}. The systematic uncertainty for β_{14} was found to be 0.031±0.004 [82].

5.3.6 The PMT angular response and the optical calibration in water

As mentioned previously, the laser-ball is the main calibration source to calibrate the optical model and the angular response of PMTs during the water phase [76]. Furthermore, the model was verified using ^{16}N data [77, 76].

The angular response of PMTs should be well understood for the physics analyses. SNO+ is mostly concerned with the incident angles smaller than 50°. The angular response determines the probability of a photon entering a PMT with the incident angle θ to generate a photo-electron, and can be expressed as:

$$f(\theta) = N_{pe}/N_\gamma(\theta) \tag{5.7}$$

The PMT angular response was measured for 5 different wavelengths using the laser-ball source [76]. The ^{16}N complete calibration data were also used to confirm this measurement [77].

Laser-ball was used to determine various optical parameters such as the effective attenuation lengths, and build a comprehensive optical model for the detector. After optical calibration, the model was verified by comparing the prompt Nhits from ^{16}N data with MC at different positions across the detector [79]. Figure 5.11 shows the mean prompt Nhits value (fit value for the peak) along three different axes inside the detector, together with run-by-run simulations (blue). It can be seen that as the calibration source moves away from the center more prompt light is collected.
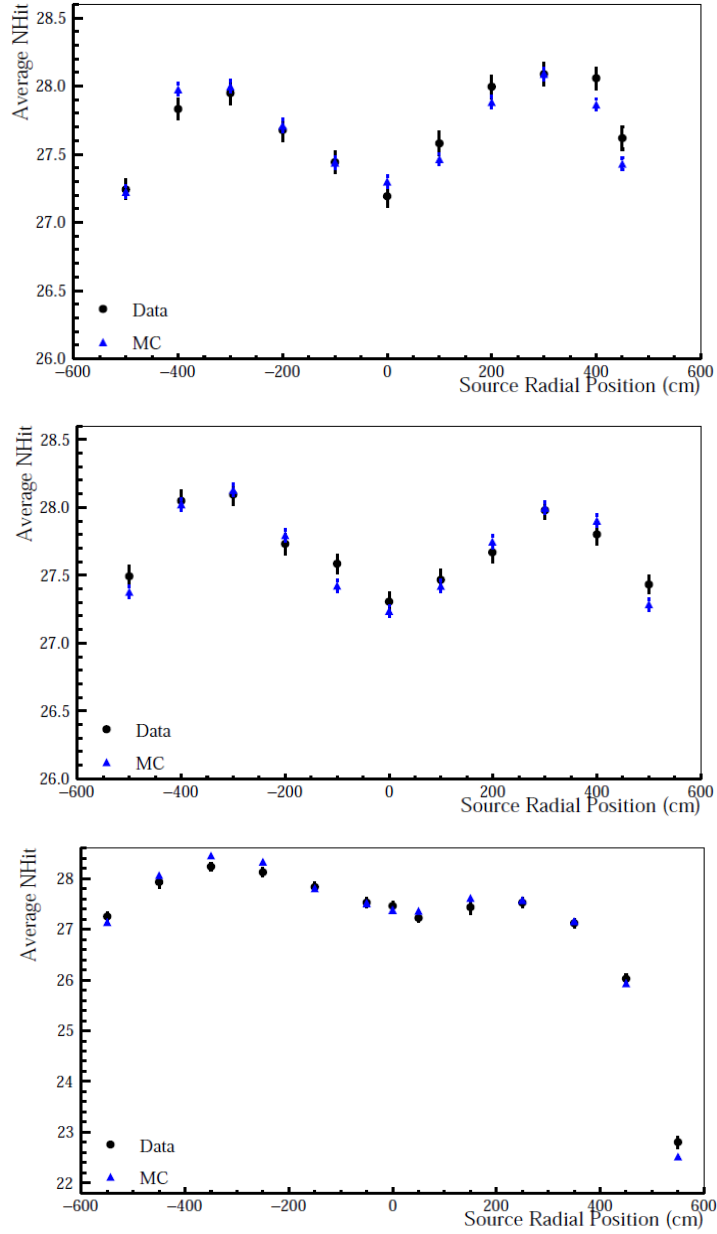
Figure 5.11: ^{16}N prompt mean Nhits from data (black) and MC (blue) as a function of axial position where x-axis is the top, y-axis is the middle, and z-axis is the bottom plot [76].

However, at the higher radii closer to the AV, the average number of hits decreases due to the non-trivial optical properties of the AV (e.g. internal reflection).

5.3.7 External ^{16}N in water

The external calibration data were used to verify the reconstruction algorithms for the events at higher radii, for instance the external data can be used to verify the angular response of PMTs at higher angles. The directionality information of the external events in water can be utilised for various analyses, for instance making comparison between the events going through the AV, and the ones that are out-ward going.
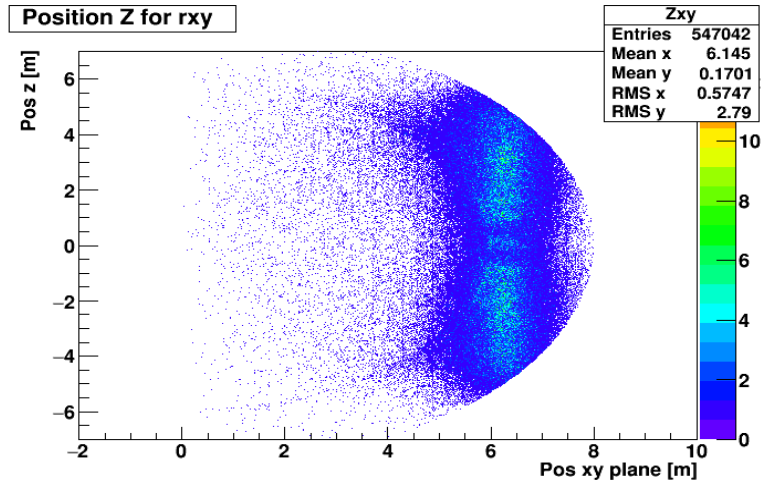
Figure 5.12: The reconstructed position of external ^{16}N scan during water phase.

The outward- inward-going events are defined as events with $\vec{u}.\vec{r} > 0$, $\vec{u}.\vec{r} < 0$ respectively, where $\vec{u}$ is the direction of the event, and $\vec{r}$ is the vector pointing to the event vertex from the center of the detector. The outward-going external events can be selected for particular analyses to exclude the optical effects of the AV, for example the light yield (Nhits) of the outward-going events can be a relative indicator of the global collection efficiency of the detector over time. In addition, since ^{16}N is a tagged source, the external data can be used to examine timing and topological classifiers to identify and reject external γ's. A few examples of these classifiers are discussed in the following sections.

In March 2018 the ^{16}N source was deployed externally through guide tube 4 which is located at $x = -5.86$ m and $y = -2.52$ m with respect to the center of the AV. The calibration data were collected for 19 different positions along the vertical axis.

Figure 5.12 shows the reconstructed z versus reconstructed ρ^2 of the full external scan in water. A significant position reconstruction offset was observed in data, comparing the mean of the reconstructed positions with the source position. Moreover, we demonstrated that the position reconstruction offset can be significantly reduced by selecting the outward-going events shown in red in figure 5.13.
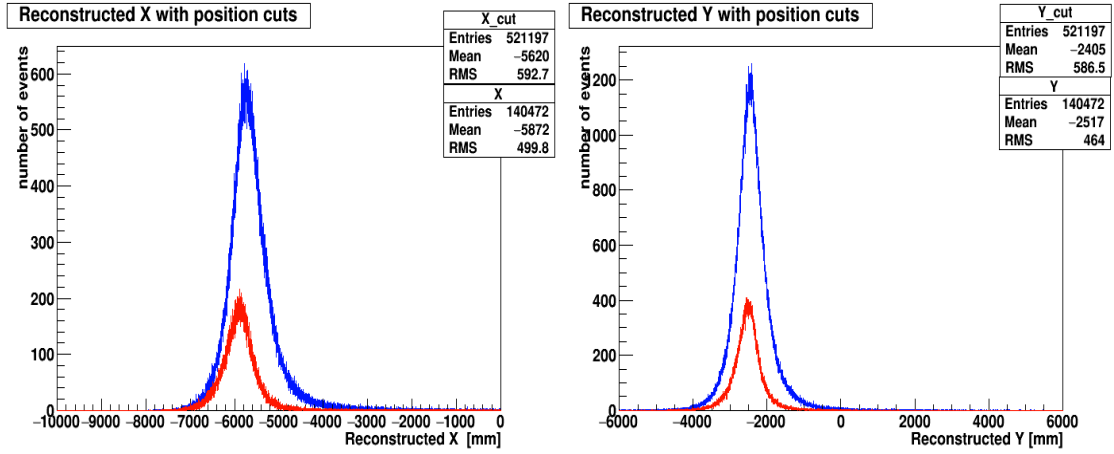
Figure 5.13: Reconstructed positions x[mm] (left) and y[mm] (right) for the external ^{16}N scan in water. The blue shows the total events with mean values of x_{mean} =-5620 mm and y_{mean} =-2405 mm, and the red shows only the outward-going events with x_{mean} =-5872 mm and y_{mean} =-2517 mm. The source is at $x = -5860$ m and $y = -2520$ mm.

$^2\rho = \sqrt{x^2 + y^2}$

5.4 ^{16}N in Scintillator

The ^{16}N calibration hardware is not designed to be deployed into the scintillator cocktail, and does not meet the radio-purity requirements, however the source can be deployed externally through the guide-tubes. The ^{16}N and the AmBe source were the main two external calibration sources during the partial-fill, and both have been deployed frequently throughout the filling process. The external calibration data were used to study the light yield, and monitor the PPO mixing process throughout filling. In addition, the light yield is modeled as a function the energy deposition, and the Birk's parameters were determined using the AmBe data together with the ^{16}N tagged γ's. The light yield analyses are discussed in section 5.4.2. Furthermore, the reconstruction algorithms in scintillator were studied at the higher radii $(R > 4m)$, and the radial dependency of the light yield (Nhits) was investigated, discussed in section 5.4.3. The emission spectrum of scintillator cocktail highly depends on the dopant fluor concentrations. The ^{16}N γ's were used to characterize the timing profile of scintillation with different PPO concentrations. The timing studies are described in section 5.4.4. In addition, the timing studies can be used to optimize timing classifiers to identify and reject the external γ's more efficiently, which is briefly discussed in section 5.5. Aside from the scintillation signal, the 6.1 MeV γ's can provide a neat data set to study the Cherenkov radiation in liquid scintillator. The Cherenkov signal extraction and the directionality analysis is discussed in section 5.4.5. These analyses can be used to improve the position reconstruction [98].

5.4.1 ^{16}N Deployment Program and the Selection Criteria in Scintillator

The ^{16}N source was deployed several times externally throughout the filling process. The source was deployed initially through guide tube 2, and later through guide tube 4, and 5. Table 5.2 summarizes the list of ^{16}N runs along with their source positions, the scintillator/water interface level, and the PPO concentrations. For the purpose

of the following analyses, I have used the standard ^{16}N selection criteria in water as previously outlined in section 5.3.1, most importantly the ^{16}N calibration tag. Further cuts are applied for scintillator analysis, for instance, `Nhits`> 100 can be applied to select most of the scintillator-like tagged events. Moreover, β_{14} and `ITR` classifiers can be used to distinguish the water events from the scintillator-like ^{16}N. Two main population of the tagged events can be seen in figure 5.14: i) the scintillation signal (dashed black box) has ITR values close to 0, as the emission is spread out over time, on the other hand, ii) the Cherenkov signal is a sharp signal, and most of the photons are generated within the prompt timing window, and therefore has ITR values closer to 1. Additionally, the isotropic scintillation signal has β_{14} values closer to 0, whereas to the Cherenkov ring has β_{14} values averaged around 0.2. ITR<0.18 and $\beta_{14} < 0.1$ would select most of the scintillator-like events for 0.5 g/L PPO liquid scintillator. A 6.1 MeV γ most likely goes through multiple Compton scatterings.
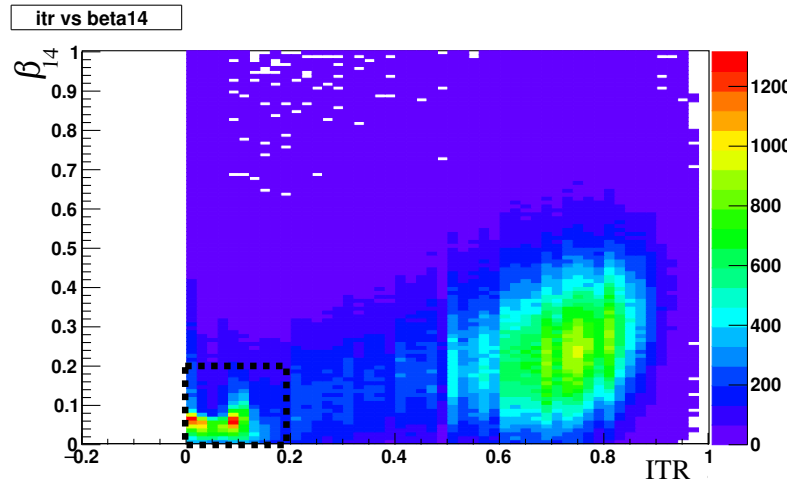
Figure 5.14: **ITR** and β_{14} for the external ^{16}N in partial-fill. The dashed box shows the pure scintillator-like events.

For the external ^{16}N in partial-fill, there is a good chance that the first Compton scattering takes place in water, and the scattered γ deposits the rest of its energy in scintillator. This can explain the population of the tagged events between the main two populations on ITR-β_{14} plane. They have lower Nhits compared to pure scintillator-like events, and manifest themselves as a continuum to the Compton peak

Table 5.2: The table summarizes the external ^{16}N runs through out the scintillator fill.

Date	run numbers	Source Position [mm]	livetime	LAB/UPW Interface [mm]	PPO level [g/L]
2020-01-22	255554 - 255597	(-1121, 1041, 6051)		~ 370	0.18 - 0.33 g/L
2020-11-05	265065	(-5861, -2080, 710)	60 min	$\sim$810	$\sim$0.5
	265068	(-5861, -2080, 2000)	60 min	$\sim$810	$\sim$0.5
2020-10-26**	264774 264775 264776 264777	(-1121, 1041, 6055)	4hrs	810	0.56 [68]
	264780 264786 264788 264789	(-1121, 1042, 6260)	4hrs	810	
2021-02-18	268105 268106	(-5861, 2071, +500)	119 min	-3210	$\sim$0.5 [130]
	268115	(-5861, 2071, -500)	60 min		
	268118 268119	(-5861, 2071, +1000)	96 min		
	268121 268122	(-5861, 2071, -1000)	85 min		
2021-07-07	272396 272398	(-5861, 2071, 0)	105 min	-5300	0.6 [130]
	272401 272429	(-5861, 2071, -500)	98 min		
	272426 272427	(-5861, 2071, 500)	78 min	i	
2021-09-21	275217 275218 275221* 275222*	(-5861, 2071, -0.9)	3hrs/ 28 min	—-	$\sim$1.06 [130]

on the Nhits spectrum of tagged events (see figure 5.22).

5.4.2 Light Yield in Scintillator

The light yield analyses are presented in three sections. The first section focuses on the very preliminary analysis of the ^{16}N data, taken before the partial-fill period. The lower concentrations of PPO in scintillator (0.18 g/L, 0.33 g/L) made this set of runs favorable for Cherenkov analysis. However, these sets of runs are suffering from low statistics and limited source positions, and therefore they are not suitable for position reconstruction studies and stratification analysis of the light yield. The two other sections presents analyses on the data taken after partial-fill period (April 2020). In order to investigate the position dependencies of the light yield, a set of stratification analysis is presented in the second section. Finally, more sophisticated light yield analysis is discussed in the third section.

5.4.2.1 Pre-partialfill Light Yield

The ^{16}N source was deployed through guide-tube 2, two times before the partial-fill period. The source was placed at $z \sim 6.05$m, by the bottom of the neck (see figure 5.15). The first set of ^{16}N was taken while the scintillator interface was at $z \sim 5.2$m, and the PPO concentration was estimated to be about 0.7 g/L. The second set of data were taken while the interface was at 3.8 m, and the PPO level was about 0.18 g/L initially, and increased to about 0.33 g/L throughout the calibration shift. Figure 5.15 shows the reconstructed positions of the tagged scintillator-like events from this calibration session. The Nhits distributions of the scintillator-like ^{16}N γ's are shown in figure 5.16(left) for 3 different PPO concentration levels. Furthermore, the Nhits for the water-like events is shown for the same sets of runs (right), and as expected the light yield of water events remains unchange for different PPO levels. The rates of water-like ^{16}N events from different runs were used to scale up the populations of scintillator-like events.
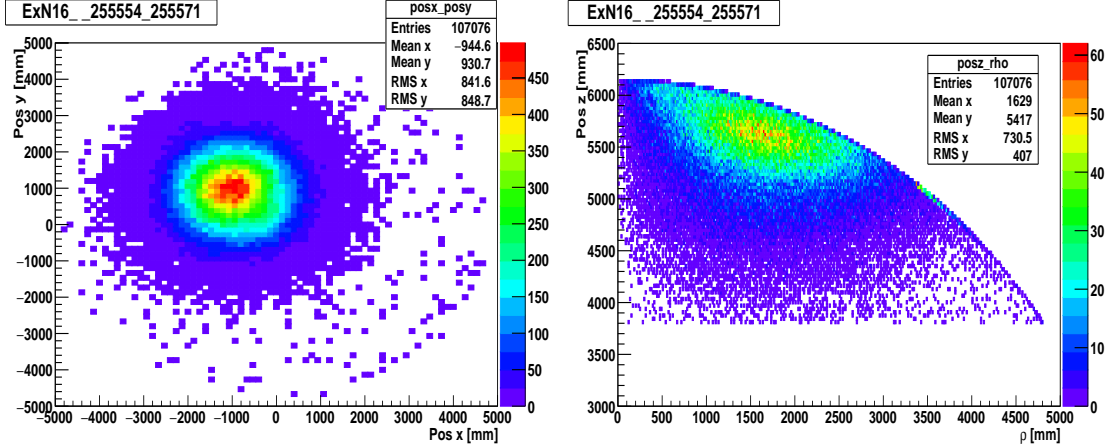
Figure 5.15: The reconstructed x-y for scintillator-like ^{16}N events shown on the left. The reconstructed z versus ρ on the right. The average PPO levels found to be ~ 0.18 g/L for this data set.
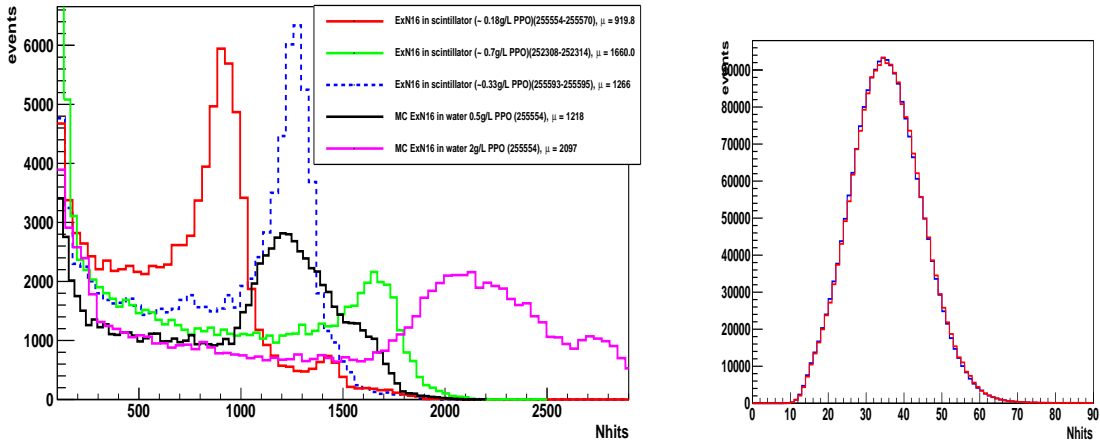
Figure 5.16: The plot on the left shows the Nhits distributions from ^{16}N runs with different PPO concentrations, and 2 sets of simulated data for 0.5 g/L and 2g/L PPO. The plot on the right shows the water-like tagged ^{16}N events for the 3 sets of data were used to scale up the scintillator distribution.

Figure 5.17 (right) shows the mean Nhits from the fits versus the PPO levels for 3 sets of runs. In addition, two sets of MC simulations were generated using RAT-6.17.6 with two available profiles for 0.5 g/L and 2 g/L PPO concentrations. The results from the simulated data were also shown on the plot. In order to understand the light yield as function of PPO concentration, a set of proper $in-situ$ studies was done in 2022 [131], and the results are consistent with the curve from ^{16}N data.
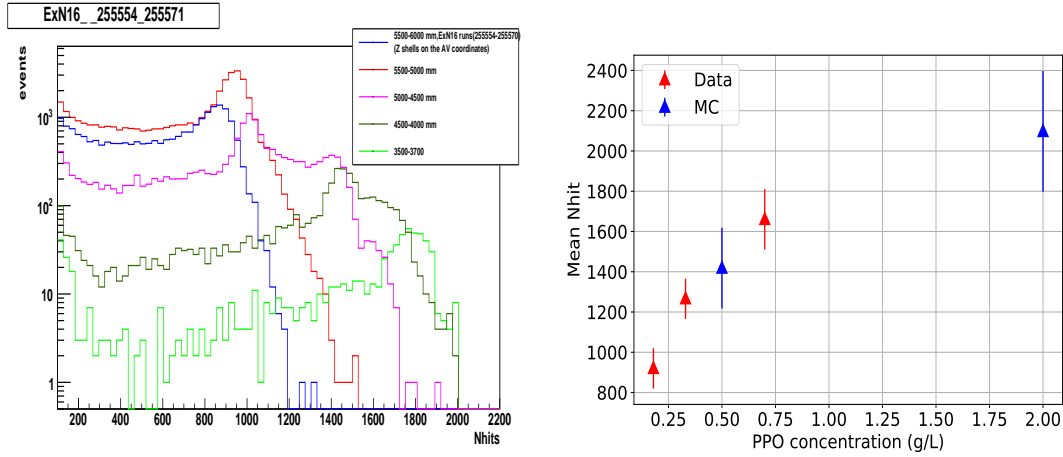
Figure 5.17: The stratification of light yield (Nhits) along z-axis is shown on the left. The plot on the right shows the mean Nhits vs. PPO concentrations for ^{16}N data (red) and MC (blue).

A set of stratification analysis on the preliminary data shows significant position dependencies of the light yield. Figure 5.17 (left) shows Nhits distributions within 50 cm intervals along $z-$axis while the interface was at 3.8 m. It can be seen that the light yield is significantly higher for the events that are being reconstructed closer to the interface, which is due to non-trivial optical effects within this region (e.g. internal reflections off the interface boundary). As expected, the radial dependency studies of the Nhits shows that the mean Nhits decreases significantly at the higher radii ($R > 5$m), which can be explained through several effects such as the internal reflection off the border between acrylic and water, or the photons getting lost due to the pile up of multiple hits on a single PMT as discussed in chapter 3.

5.4.2.2 Position Dependencies of Light Yield

In order to understand the light yield across the detector, and the position dependencies, more sophisticated analysis was performed using the ^{16}N data while the interface was at about -3.2 m and the level of PPO was measured to be 0.50g/L $\pm$ 0.05 g/L [68].

Figure 5.18: The left shows the Nhits of tagged ^{16}N events versus reconstructed radius [mm], two main populations, 6.1 MeV γ (the main one) and 7.1 MeV peak are evident. The right shows the same type of histogram from the AmBe data. Three populations are evident, 2.2 MeV (bottom), 4.4 MeV (middle), and the 6.1 MeV (top).
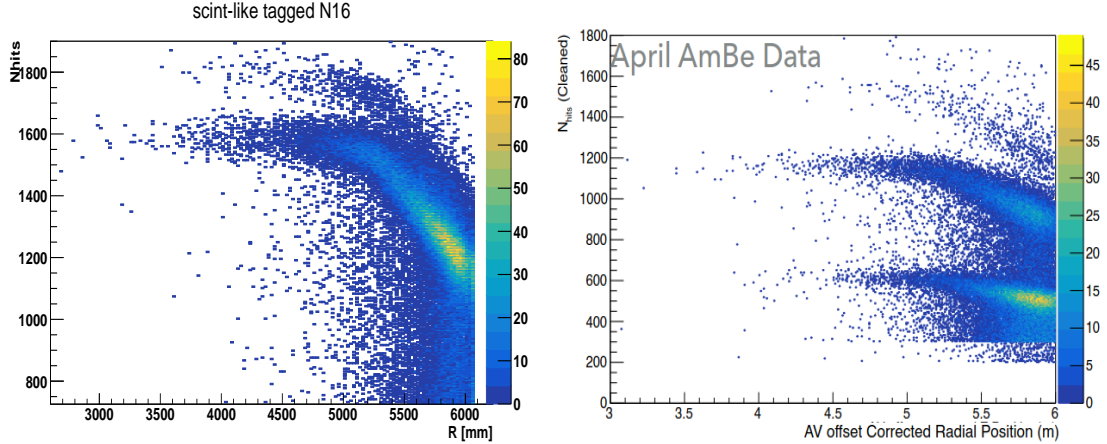
Figure 5.18(left) shows Nhits of the tagged scintillator-like ^{16}N versus the reconstructed radius. Two populations: **I**) the 6.1 MeV which is the dominant branch that plateaus in slightly below 1600 Nhits, and **II**) the smaller population from 7.1 MeV γ's that can be seen on the top. The same type of analysis on AmBe data that were taken within two months of the ^{16}N data were also consistent with ^{16}N, and presented on the right. The light yield drops significantly with radius at the higher radii, beyond $R \sim 5.2$ m. This feature is mainly caused by the total internal reflection off the boundary between the acrylic and external water. The refractive indices of LAB and acrylic at 420 nm are 1.495±0.002 [132] and 1.505±0.001 [133] respectively, and would not cause any significant optical effect. On the other hand, the refractive index of water, $n \sim 1.33$, is significantly lower than acrylic, and would make a critical angle of about $\theta_c \sim 62.5°$, which can explain the cut out of $R \sim 5.2$m. Some other factors such as angular response of PMTs, and the photons getting lost due to the pile up of multiple hits on a single PMT can also suppress the light yield at the higher radii, but their contributions are not as nearly significant. In order to characterize the light yield and its position dependencies, the 6.1 MeV peak was fit with a Gaussian function within different regions along R and z-axis. The radial stratification was

done within the range of 4m to 6m for the intervals of 50cm, and μ (the mean Nhits) and σ (the deviation) from the fit is shown in figure 5.19.
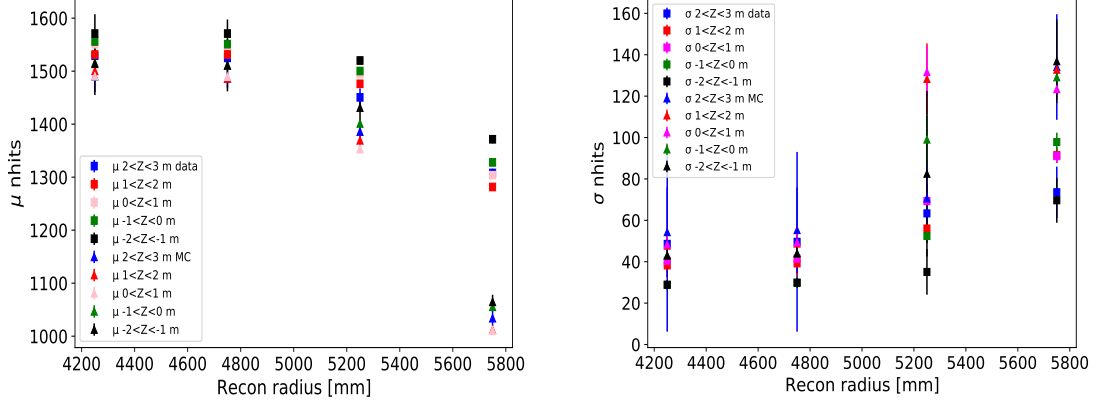
Figure 5.19: The right shows the mean Nhits (μ) versus reconstructed radius within 50 cm segments. The different set of colors represent different regions along z-axis as demonstrated on the legend. The left plot shows the deviation σ from the fits.

Moreover, a set of run-by-run MC simulations was generated using `RAT-7.0.0`, and analysed, and the result was presented on the same histograms. The average Nhits of the data found to be higher than MC, and the discrepancy gets more significant at the higher radii beyond 5.2 m. The MC seems overestimating the light suppression at the higher radii. The same discrepancy has been observed through looking at other sources such as the AmBe and ^{210}Po [134] within the same time period. In addition, a set of stratification along the z-axis was done for the range of -2m< z < 3m, and the result is shown in figure 5.20.

Finally, figure 5.21 summarizes the stratification analyses of the light yield, and shows data/MC for various segments along the reconstructed radius and z-axis. The average Nhits from data found to be about 3% higher than MC for events with $R < 5$ m.
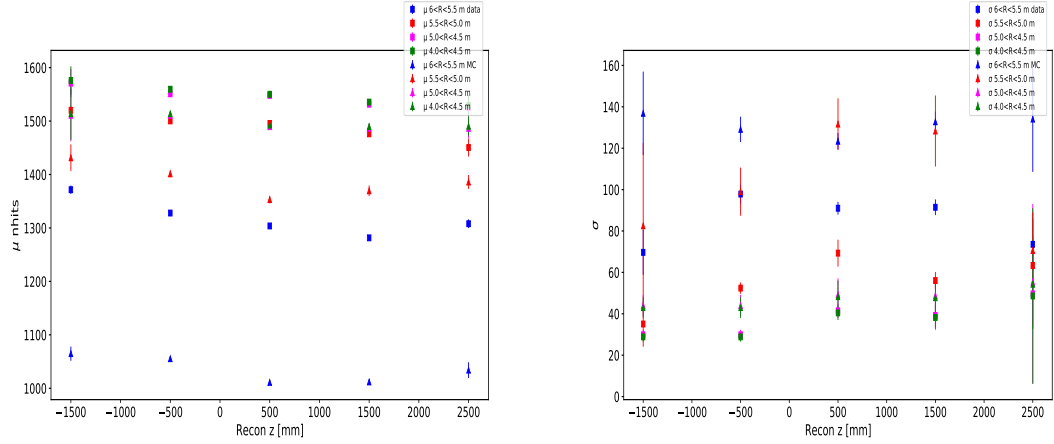
Figure 5.20: The mean Nhits μ and the deviation σ of scintillator like ^{16}N from stratification analysis along z-axis for different radial regions is shown on the left, the deviations from the fit is shown on the right.
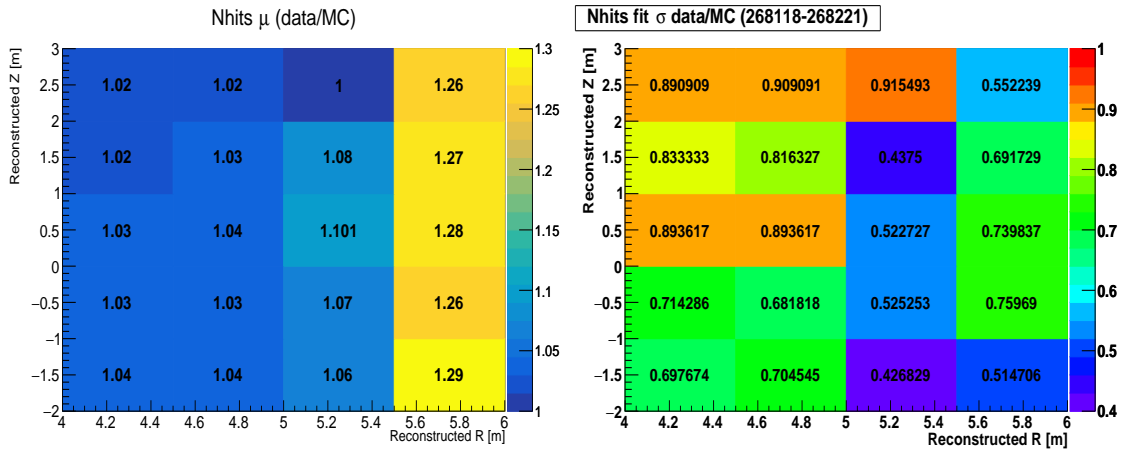
Figure 5.21: The results from a full stratification analysis of the 6.1 MeV ^{16}N peak. The ratio of $\mu(\text{data})/\mu(\text{MC})$ (left) and $\sigma(\text{data})/\sigma(\text{MC})$ (right) are presented for 50cm segments along R and z.

5.4.2.3 Post-partialfill Light Yield

The radial stratification showed that Nhits distribution is relatively more consistent for $R <$5m and $0 < z < 1$m. Therefore, this region is selected as a reference for post partial-fill light yield analysis. Furthermore, higher statistics made it affordable to look into regions with lower radii. The Nhits spectrum within the region of interest for 4 different set of ^{16}N runs are shown in figure 5.22. They have been taken from

97

different periods with different PPO concentrations, see table 5.2.
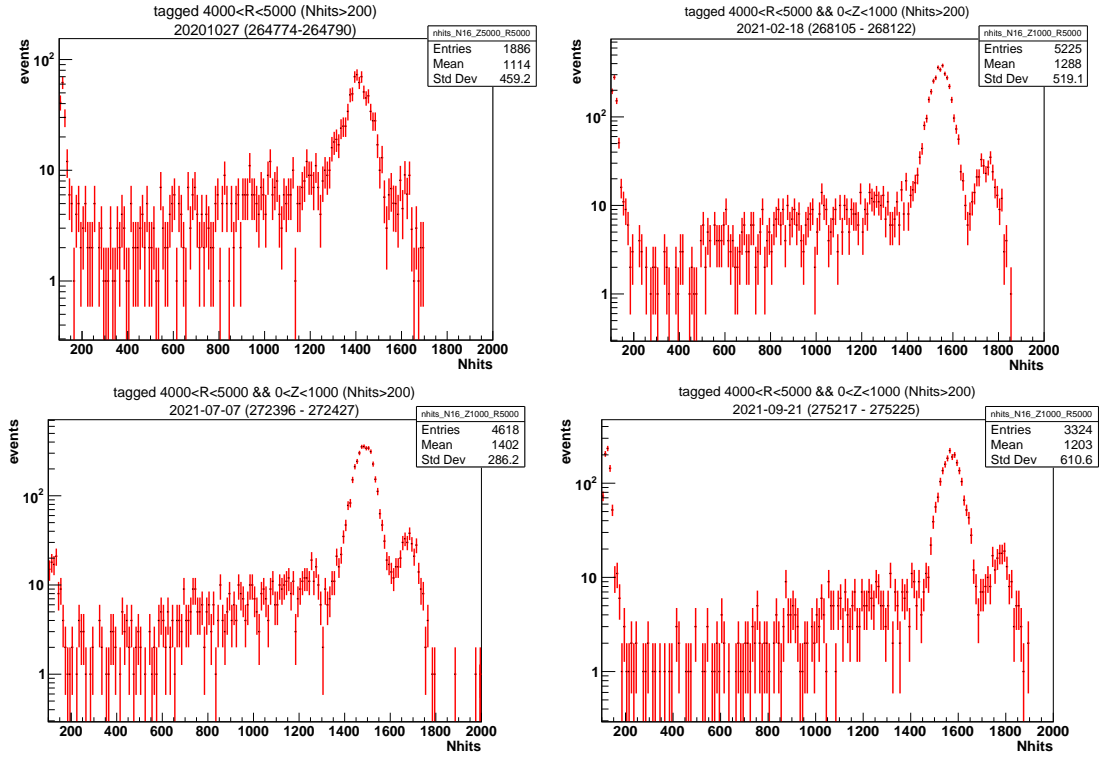
Figure 5.22: Nhits distributions of 4 sets of ^{16}N runs within the region of interest. The associated run numbers and the fit results are presented in the table 5.3.

Date	μ (6.1 MeV)	σ (6.1 MeV)	μ (7.1 MeV)	σ (7.1 MeV)	PPO level g/L
2020-10-26	**1546±5**[3](1413±3)	43 ±4	**1741±23** (1592±21)	78±43	0.56
2020-11-05	1631±2	50±2	1828±9	58±10	0.56
2020-11-05	1589±3	46±3	1756±6	28±8	~0.5
2021-02-18	1546 ±1	37 ±1	1743 ±4	42±4	~0.5
2021-07-06	1485±2	36 ± 1	1678±3	38 ±5	0.598
2021-09-21	1570±1	40±2	1776±5	40 ±7	1.06

Table 5.3: The results from fitting the tagged ^{16}N Nhits within the region of interest. The source positions can be find from table 5.2.

Two distinct peaks can be identified for two main γ branches, 6.1 MeV, and 7.1 MeV. The peaks are fit with a Gaussian and the results are presented in table 5.3. The Nhits from the partial-fill runs are corrected for the off crates by averaging over the hits on the 4 adjacent crates. The mean Nhits for the partial-fill period found to be 1546±5 and 1741±23, for 6.1 and 7.1 MeV γ's respectively. In addition, the ratio between the peak integrals of 6.1 MeV and 7.1 MeV found to be 13.1±0.4 which is consistent with the branching ratio of the decay.

5.4.2.4   Birks' Parameters

As discussed in section 2.4, the scintillation light yield can be parameterized through Birks' law. The Birks' parameters; Birks' constant k_B, and the scintillation efficiency, S, can be estimated by fitting the relative light yield from the three identifiable AmBe peaks (2.2 and 4.4 MeV) together with the 6.1 MeV peak from ^{16}N. Figure 5.23 shows the mean Nhits versus energy for 3 different energies within the region of interest. In

---

[3]The partial-fill mean Nhits value is corrected for the off channels (bold values).

order to fit the data, the energy loss of electrons $(\frac{\Delta E}{\Delta x})$ was treated as a state function, and simulated in RAT-7.0.0 [135].
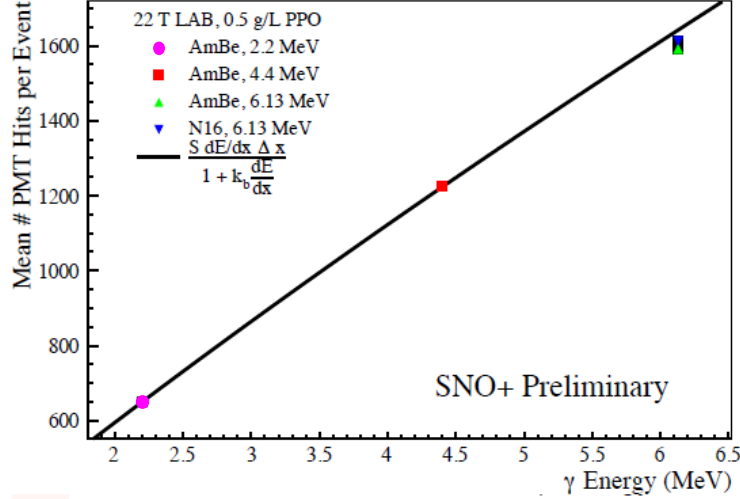
Figure 5.23: Fitting the Nhits from 3 data points from AmBe and ^{16}N to find the Birks' parameters, taken from [135].

The Birks' parameters found to be $S = 6410 \pm 78$ 1/MeV, and $k_B = 0.08 \pm 0.01$ mm/MeV using the AmBe data from April 2021 together with ^{16}N data from February 2021.

5.4.3 The Position Reconstruction and the Far Tagged Events

The position reconstruction of scintillator-like events was investigated using the data as well as a set of generated run-by-run MC. The AV coordinate system is used for this analysis, therefore the position needed to be corrected for z-offset. Figure 5.24 shows the reconstructed z versus reconstructed R for the tagged scintillator-like events in the AV coordinates (blue), as well as the PSUP coordinates (black). The z-offset of the AV with respect to the center of PSUP is estimated through the neck sense rope system (see appendix A), and measured to be 17.4±0.2 cm. The AV z-offset is used to calculate the reconstructed position in the AV coordinates. There is a cut out at 6.05m on the reconstructed R in the AV coordinates, which verifies the incorporated offset. It has been seen from the data and the MC that a fraction of tagged scintillator-like

events (Nhits> 100) are being reconstructed outside of the scintillator volume. These events can be explained through multiple Compton scatterings of γ's, while the first Compton electrons are generated in water, and the scattered γ's deposits the rest of their energy in scintillator.
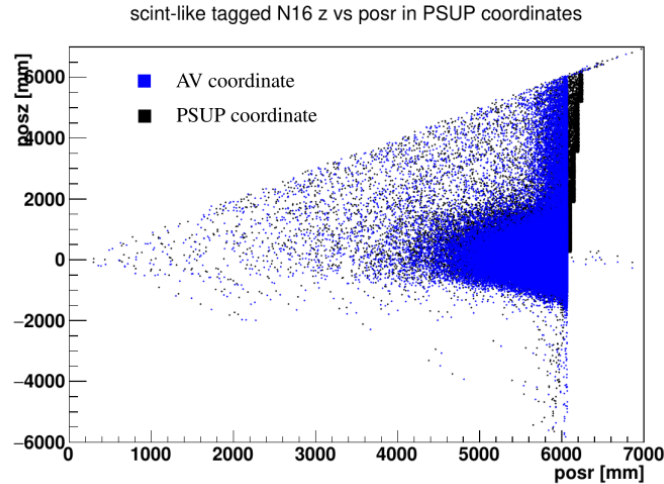
Figure 5.24: Reconstructed z versus R of the tagged scintillator-like ^{16}N events in AV coordinates (blue) and the PSUP coordinates (black). The z-offset was estimated to be 17.4 cm from NSR.

The distance between the reconstructed position of tagged events and the source position (red) and MC (blue) is shown in figure 5.25. There is a significant surplus population of the tagged events that are being reconstructed beyond 6 m from the source in data. These far events are about 5% of the tagged data, and mostly have Nhits below 200. Figure 5.26 shows the reconstructed x and y for three different Nhits regions. As it can be seen, there is a significant population of these far events reconstructed closer to the surface of the AV. In addition, the Nhits distribution of these events is shown in figure 5.27, and part of the spectrum around 100 Nhits has the same characteristics as the surface ^{210}Po signal. Furthermore, timing studies of the far events with respect to FECD time, the tagging time of the source PMT, has given insight into the origin of these events. Figure 5.27 shows the timing of ^{16}N events with respect to the FECD time. As expected for the events with higher Nhits (pink), the distribution peaks around an offset ($\sim$100 ns). However, the timing difference for the
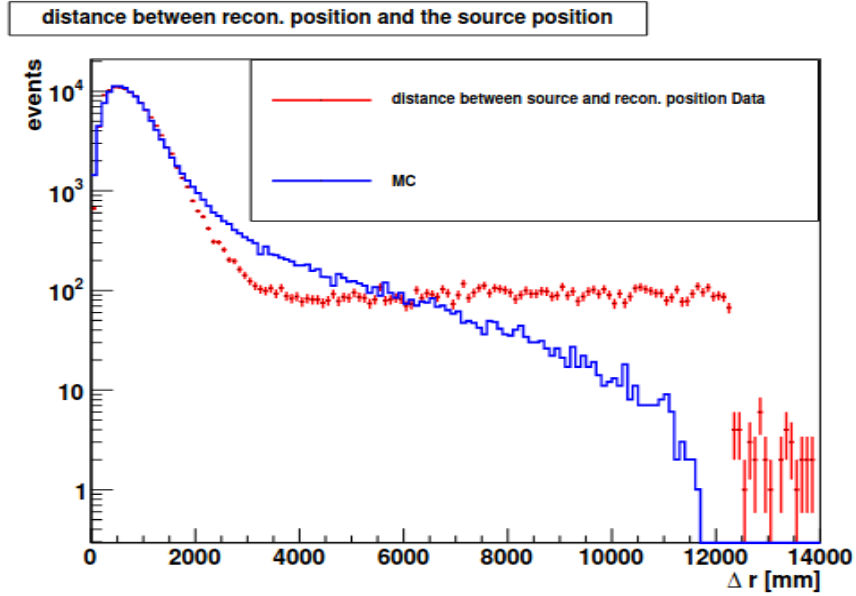
Figure 5.25: The distance between the reconstructed tagged scintillator ^{16}N events and the source position with Nhits> 100 for data (red) and MC (blue).

far events (blue) makes a flat distribution and seems to have absolutely no correlation with the FECD time, in other words, these events take place randomly within the 400 ns window. Therefore, one can suggest that they have a different origin rather than the calibration γ's, and they could be from the pile-up of other events such as the α decays of the surface ^{210}Po with the tagged β decays of ^{16}N.
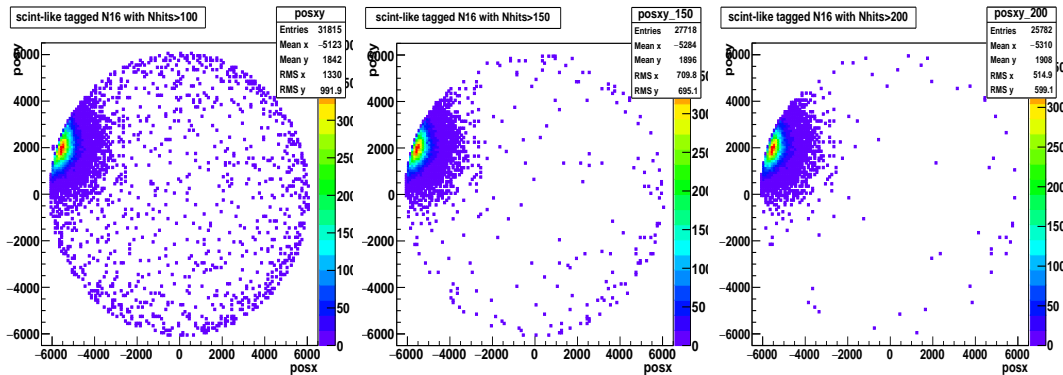
Figure 5.26: Reconstructed position, x-y plane, of the tagged ^{16}N events; 100<Nhits (left), 150<Nhits (middle), 200<Nhits (right).

The rate of such pile-up events within the triggering time window can be described analytically through Poisson statistics. In this case, the pile-up would be between
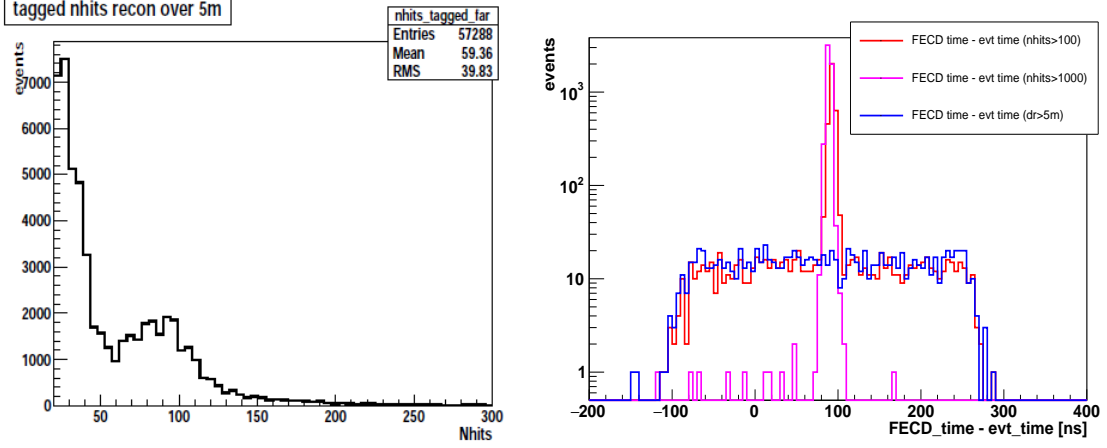
Figure 5.27: The Nhits distribution of the tagged far events on the left, and time(FECD) - time$_{evt}$ distribution for the tagged far events (blue) and high Nhits events (pink).

the tagged β-decays, and all the un-tagged events below 200 Nhits. The pile-up rate would be negligible for events above 200 Nhits. The number of pile-up events within the time window can be described as 5.8.

$$N_{pu} \sim N_1 \times N_2 \times \frac{e^{-N_2}}{1!} \tag{5.8}$$

where N_1 and N_2 are the average number of tagged and untagged events within the time window. The rate of pile-up is estimated to be about $3.8 \times 10^{-8}/400$ ns. The rate of the tagged events, including the γ-less β decays within the decay chamber is assumed to be 60Hz, and the rate of the untagged events is taken from the ^{16}N runs. The estimated rate of pile-up is on the order of the observed rate for the far events, however about 50% lower. For the purpose of position analysis, $\Delta t =$time$_{\text{FECD}}- t_{evt}$) can be a very useful parameter. Most of the far (pileup) events ($> 90\%$) can be removed by selecting events with $\Delta t \in (80, 110)$ns.

5.4.4 Timing Studies

^{16}N events provide a clean sample to study and verify the scintillation timing profile. I have taken two different approaches for the course of this analysis. First, the ^{16}N time residuals were used to characterise the scintillation timing analytically. Furthermore, a set of proper MC runs is generated, and the time residuals were compared with data.

The scintillation intensity of an organic scintillator over time can be characterised through different components as follows [136]:

$$n(t) = \frac{N}{\tau - \tau_r}[\exp(-t/\tau) - \exp(-t/\tau_r)] \tag{5.9}$$

where $n(t)$ is the number of emitted photons as a function of time, N is the total number of emitted photons, τ_r is the time that is required for the intensity to reach the maximum, and τ is the time that characterises the decay of intensity. However, multiple decay components are typically required, which collectively can describe different scintillation mechanisms as discussed in section 2.4. For the purpose of this analysis 3 decay constants are used. Therefore, the intensity of emission in terms of three decay components can be written as:

$$n(t) = \frac{N}{R_1\tau_1 + R_2\tau_2 + R_2\tau_3 - \tau_r}[R_1e^{-t/\tau_1} + R_2e^{-t/\tau_2} + R_3e^{-t/\tau_3} - e^{-t/\tau_r}] \tag{5.10}$$

where τ_is represent various decay components, and R_i is the relative contribution of the ith decay component ($\sum_i R_i = 1$). In reality, the intensity of emitted photons is not quite the same as the intensity of detected photons. The light collected by PMTs have an inherent Gaussian timing resolution due to the transit time spread within the channel, discussed in section 2.1.2. The intensity of detected photons, $n_d(t)$ can be modeled as the intensity of emission photons, $n(t)$, convolved with Gaussian as

shown in equation 5.11.

$$n_d(t) = \int_0^\infty n(t) \cdot \frac{1}{\sigma\sqrt{2}} e^{-t^2/2\sigma^2} dt \tag{5.11}$$

where σ represents the timing resolution of the PMTs. Several bench-top measurements have been performed to determine the timing constants for various scintillator cocktails with different PPO concentrations [94, 137, 138]. In order to fit the detected scintillation intensity, I used the hit time residuals of tagged events from 4 different sets of ^{16}N runs listed in table 5.4. The results from the bench-top measurements were used to set rough ranges on R_is and σ. Figure 5.28 shows the best fits (dashed red curve) for the ^{16}N time residuals. On a side note, a two decay component function found to be a more suitable fit for the time residuals with 1.06 g/L PPO level. The fit parameters are shown in table 5.4, and they seem consistent with the bench-top measurements. However, the function poorly fits the peaks. The obtained timing constants do not reflect the true physical description of the scintillation signal since the optics of the detector is not taken into account in this toy model. For instance the scattering off different components (e.g. AV) can significantly affect the detected light. Furthermore, as demonstrated in section 3.3.1, the time residuals spectrum spread out more at the higher radii. The purpose of this phenomenological analysis was to use a simple toy model to fit the data, and to relatively characterise the time residuals for different PPO concentrations.
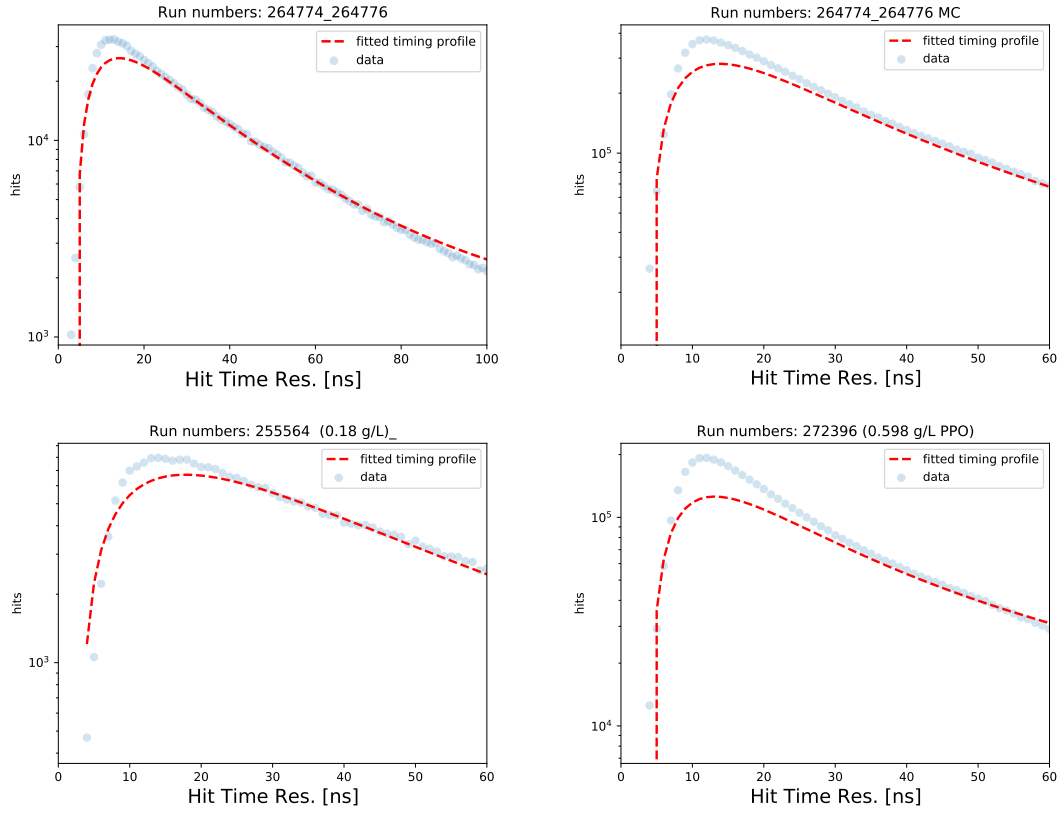
Figure 5.28: The tagged ^{16}N time residuals from 4 different sets of runs (blue) along with the best fit.

Run Numbers	PPO level (g/L)	τ_1 (ns)	τ_2 (ns)	τ_3 (ns)	R_1	R_2	R_3	τ_r (ps)	σ(ns)
255564	0.18	7.3 ±0.4	25.4 ± 0.6	252 ±0.7	65.8±0.8	31.1% ± 0.4		950 ±50	7.9 ± 0.4
264774_264776 MC	0.5**	7.8 ± 0.3	25.2 ± 0.5	203 ± 1.3	68.0% ± 1.3	29.3% ±0.2	2.6% ± 0.2	900± 50	8.7± 0.5
264774_264776 Data	0.56	7.6 ± 1.2	25.1 ± 0.9	189 ± 5.7	67.3% ±2.1	29.1% ±0.1	3.5% ± 0.1	850± 70	8.31 ± 0.5
272396	~0.6	7.9 ± 1.0	25.2 ± 0.7	168 ± 2.0	66.0% ± 4.0	28.9 ± 1.2	5.0% ± 1.0	770± 100	8.80± 0.50
275217	~1.06	6.8 ±0.6	20.7 ± 0.3	—	68.2±2.1	32.8±1.0	—	940±100	8.7±0.5

Table 5.4: Timing constants from fitting ^{16}N time residuals.
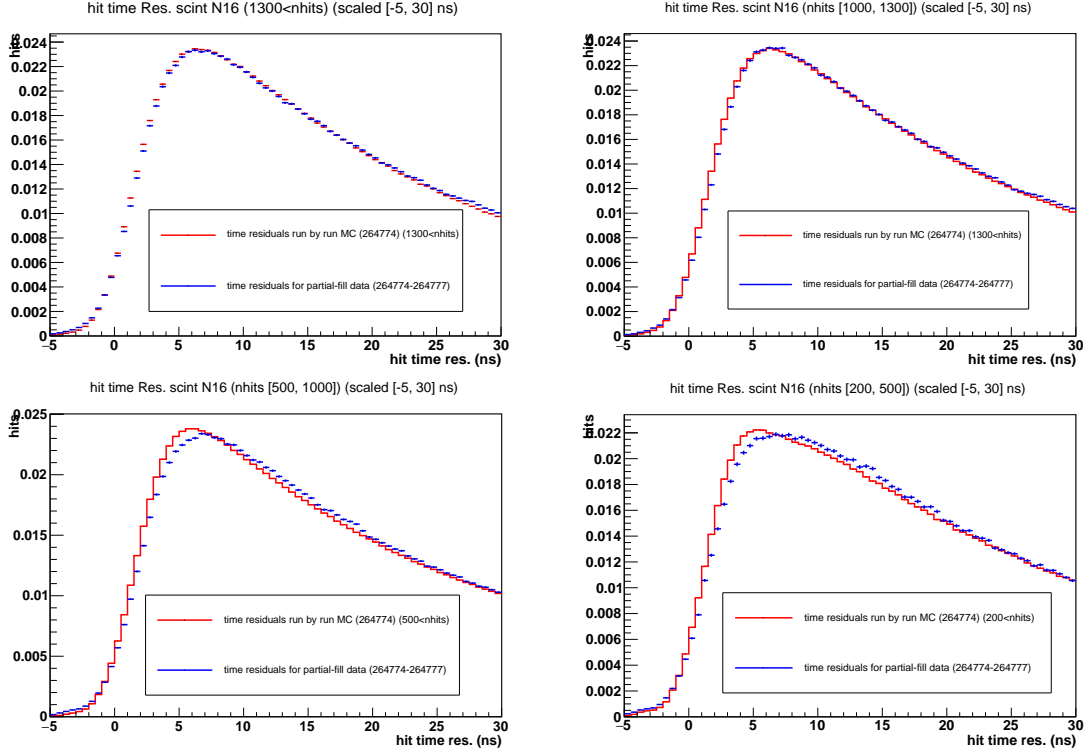
Figure 5.29: Time residuals of the tagged partial-fill ^{16}N and run-by-run MC for 4 different Nhits regions.

More sophisticated timing analysis was done by generating a set of run-by-run ^{16}N events using `RAT-7.0.0`, and furthermore, comparing the time residuals with data. The timing constants of the scintillator cocktails are included in the model from the previous bench-top measurements to match the partial-fill data [94, 138, 137]. In addition, the optical model of the detector for the partial-fill, the physics of scintillation, and the detector response are incorporated in the model. Figure 5.29 shows the time residuals from partial-fill data (PPO$\sim$0.56 g/L$\pm$0.4[68]) as well as the run by run MC for 4 different Nhits ranges. As it can be seen, the time residuals from MC matches remarkably with data above 1000 Nhits. However, below 1000 Nhits, the data seem to have a longer rise time rather than MC, which is also evident from the analyitical fits (see table 5.4).
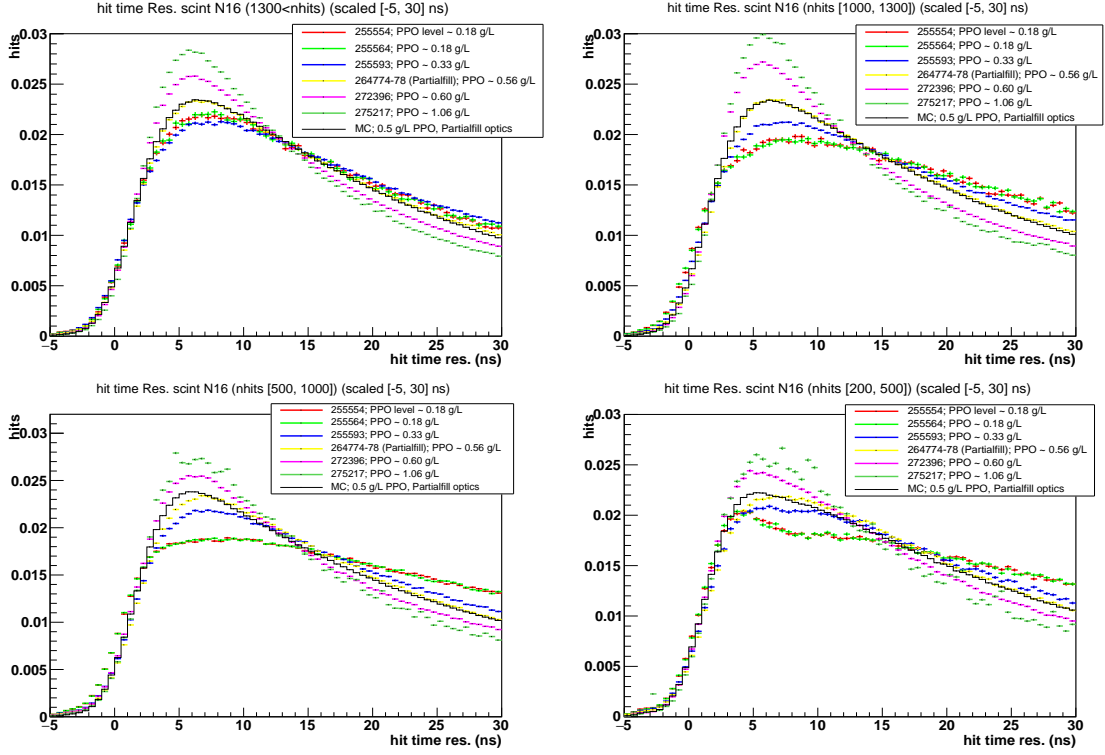
Figure 5.30: Time residuals of scintillator-like tagged events from 5 different sets of runs throughout the scintillator fill for different Nhits regions.

Furthermore, hit time residuals from 5 different set of ^{16}N runs with different PPO concentrations are shown for 4 different Nhits regions in figure 5.30. As expected, we can see that the scintillation rise time gets shorter, and the signal becomes more strongly peaked for higher PPO concentrations. This fact makes the basis of the Cherenkov signal extraction in the following section.

5.4.5   Identifying Cherenkov Signal in the Scintillator using ^{16}N

As briefly discussed section 2.4, Cherenkov radiation is emitted when a charged particle passes through a dielectric medium at a speed higher than the phase velocity of light in that medium ($\beta > 1/n$). For instance there is an energy threshold of ~ 0.8 MeV for electron to emit Cherenkov radiation in water ($n = 1.33$). The Cherenkov radiation propagates in form of a cone in the same direction as the moving charged

particle. The cross section of the Cherenkov cone and the PMT array forms a ring, known as Cherenkov ring. The topological information of the fired channels along with timing information (event vertex) can be used to determine the direction of the charged particle. The emission angle shown in figure 5.31 (left) can be described as follows:

$$\cos\theta = \frac{1}{n\beta} \qquad (5.12)$$

where $\beta = \frac{v_p}{c}$, and n is the refractive index of the medium. For instance the Cherenkov angle in water at 20°C is about 41°. Cherenkov radiation can be emitted by an energetic charged particle in both water and liquid scintillator. However, the major portion of the photons generated in liquid scintillator come from the scintillation processes ($\sim 95\%$). Identifying the Cherenkov signal in scintillator would give us directionality information that can make a powerful tool to classify events with respect to their source, for instance, separating the solar neutrinos versus other backgrounds [67]. The Cherenkov signal is a very sharp signal. In other words, most of the Cherenkov photons are generated within a short time span of ($\sim$100ps). On the other hand, the scintillation photons are generated over a much longer time span and spread out due to the randomness of different scintillation processes. The timing difference between Cherenkov and scintillation timing can be demonstrated through looking at the time residuals of water events and scintillator-like events (see figure 5.36). The difference in timing makes it possible to separate two signals within an event, and extract the directionality information. However, as it was demonstrated in the previous sections, the timing profile of scintillation highly depends on PPO concentration. Higher PPO concentrations make the rise time shorter, and as a result would make it harder to separate the Cherenkov signal from the dominant scintillation signal. As the first step to study Cherenkov signal in scintillator, 1,000,000 ^{8}B solar neutrino events in 0.5 g/L PPO scintillator are simulated by J. Paton [139]. The ^{8}B neutrinos are energetic enough to generate significant Cherenkov signals. In order to find any manifestation of Cherenkov signal, the hit angles distribution, $\cos\theta$, were probed over

the first 10 ns of the hit time residuals, shown in figure 5.31. As it can be seen from
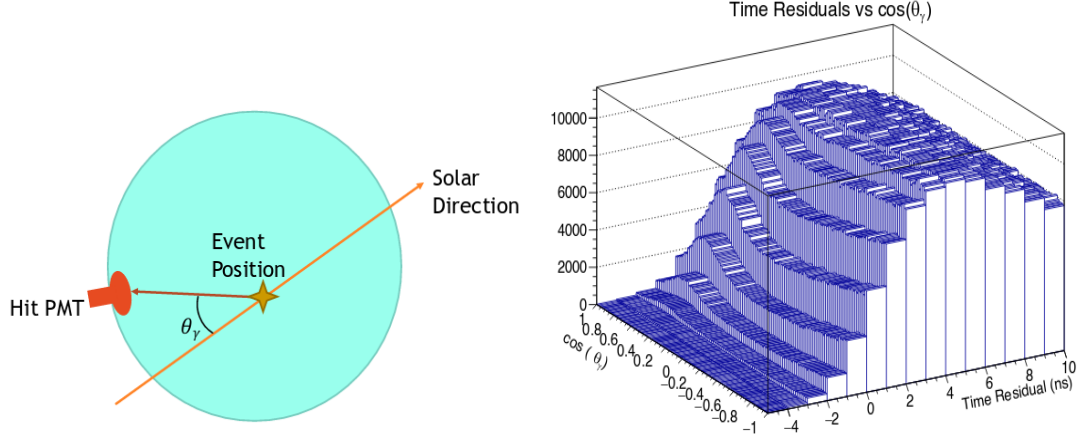
Figure 5.31: The figure on the left demonstrates the emission angle θ. The right plot shows the hit time residuals of simulated ^{8}B neutrinos versus $\cos(\theta)$, taken from [139]

.

figure 5.31, the Cherenkov photons manifest themselves in form of a bump that is peaked about $\cos(\theta) \sim 0.77$ within the prompt hits, (-2, 1) ns of the hit time residuals. The scintillation photons take over passed 2 ns, and the angular distribution seems flat (isotropic). Furthermore, a sum over the early hit vectors, $\hat{r}_{pmts}$ is used to determine $\cos(\phi)$ for every event. $\cos(\phi)$ is a parameter that can be describes as equation 5.13, and is highly correlated with the direction of the source.

$$\cos\phi = \hat{r}_{pmts}.\hat{r}_{evt} \qquad (5.13)$$

where $\hat{r}_{evt}$ is a normalized vector that represents reconstructed position with respect to the source, and $\hat{r}_{pmts}$ is a normalized vector that can be calculated as follows:

$$\hat{r}_{pmts} = \frac{\sum_{hits} \vec{r}_j}{|\sum_{hits} \vec{r}_j|} \qquad (5.14)$$

where $\vec{r}_j$ is a vector pointing to the ith PMT with respect to the reconstructed position. In order to ensure sufficient statistics in this analysis, I selected only the events with more than 4 hits within their early time window.

In order to probe the ^{16}N data in scintillator, two sets of MC simulations have been

generated using `RAT-6.17.6` for 0.5g/L and 2g/L PPO in which the source was set to be at (-1121, 1041, 6108)[mm], and the scintillator interface at 3.8 m. Furthermore, I selected events with energy>4.5 MeV so that I have sufficient Cherenkov photons. The hit time residuals versus the hit angles are shown in figure 5.32. As expected, the Cherenkov emission angular peak is evident for 0.5 g/L PPO, which is peaked around 0.8 within the early time residuals, whereas the early window is populated by the dominant isotropic scintillation hits for 2g/L PPO. As described in
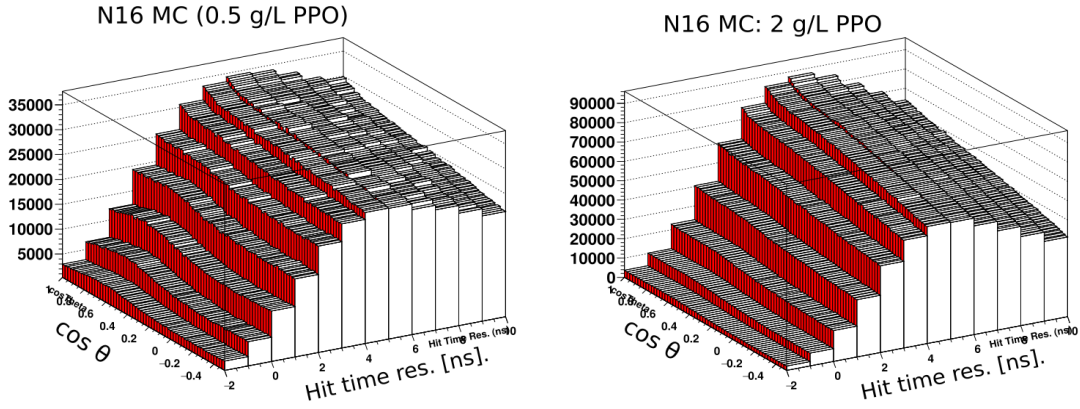
Figure 5.32: The hit time residuals versus the emission angles for simulated ^{16}N scintillator-events with 0.5 g/L PPO (left) and 2g/L PPO (right).

equation 5.13, $\cos\phi$ is calculated for early and delayed hits, and shown in figure 5.33. It is demonstrated clearly that the early hits within the events contain the directionality information as they are strongly peaked towards $\cos\phi \sim 1$, whereas the late hits which are isotropic and show no significant correlations with the vector pointing to the source. The delayed window is defined as hits with time residuals>5 ns. The same approach is taken to identify the Cherenkov signal, and obtain the directionality in ^{16}N data. The average PPO concentration for this data set is measured to be 0.18 g/L and the interface was at 3.8 m. The energy cuts are accomplished using the Nhits curve shown in figure 5.17. The Cherenkov emission angle peak is evident within the early window of the hit time residuals, demonstrated in figure 5.34. Furthermore, $\cos\phi$ is calculated, and a clear directionality towards the ^{16}N source is observed for the early hits.
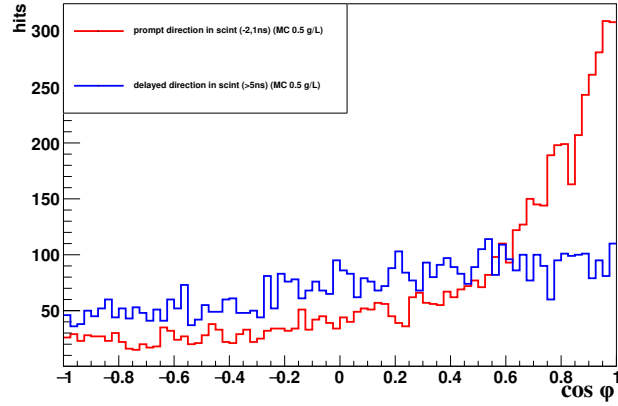
Figure 5.33: The plot shows $\cos\phi$ (direction) 0.5 g/L PPO MC. The red distribution shows the sum over early hits and blue shows the delayed hits.
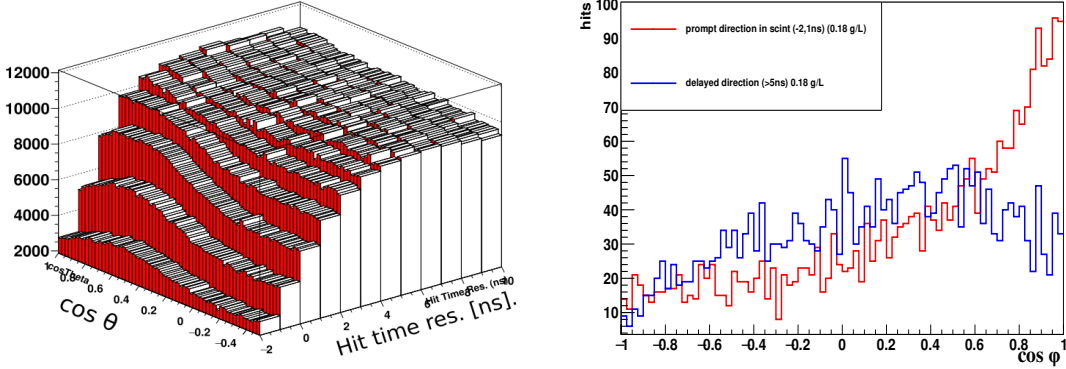
Figure 5.34: The hit time residuals versus the emission angle of ^{16}N data while the average PPO estimated to be 0.18 g/L, shown on the **left** plot. The **right** plot shows the directionality correlation of the early hits (blue), and the late hits (red).

Furthermore, the same analysis was performed on a set of ^{16}N while the level of PPO concentration is estimated to be about 0.33 g/L. The result is shown in figure 5.35. $\cos\phi$ is calculated, and within the early hits (red) the correlation with respect to the source position is demonstrated, in other words the distribution is clearly peaked towards $\cos\theta \sim 1$, however, as expected the directionality correlation is not as strong as the 0.18 g/L PPO data set. As mentioned earlier, the directionality information from Cherenkov signal provides a powerful tool to identify the signals from a known source. In addition, this information can be used to improve the position reconstruction [139].
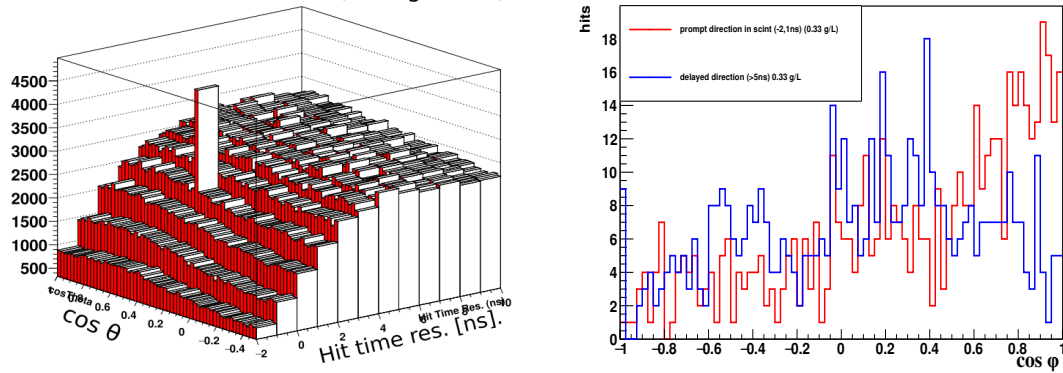
Figure 5.35: The hit time residuals versus the emission angle of ^{16}N data while the average PPO is estimated to be 0.33 g/L, shown on the **left** plot. The **right** plot shows the directionality correlation of the early hits (blue) and the late hits (red).

5.5 Summary and the Prospects

Tagged γ's from the ^{16}N source were used for several calibration analyses. As the primary energy calibration source in water, the 6.1 MeV γ's were used to calibrate energy, verify the reconstruction algorithms, and determine the resolutions and systematic uncertainties, presented in section 5.3.

In addition, the source have been deployed externally throughout the filling process, and the data were used for various scintillator analyses presented in section 5.4.2. The tagged 6.1 MeV and 7.1 MeV γ's were used to study the light yield in scintillator with different PPO concentrations, and furthermore, used to determine the Birks' parameters. Moreover, the position reconstruction algorithms are verified at the higher radii, and the position dependencies of the light yield was investigated. The emission timing of the scintillator cocktail is characterized using the time residuals of ^{16}N, and the timing constants are determined for different PPO concentrations. Finally, the Cherenkov signal in liquid scintillator is identified using the ^{16}N data.
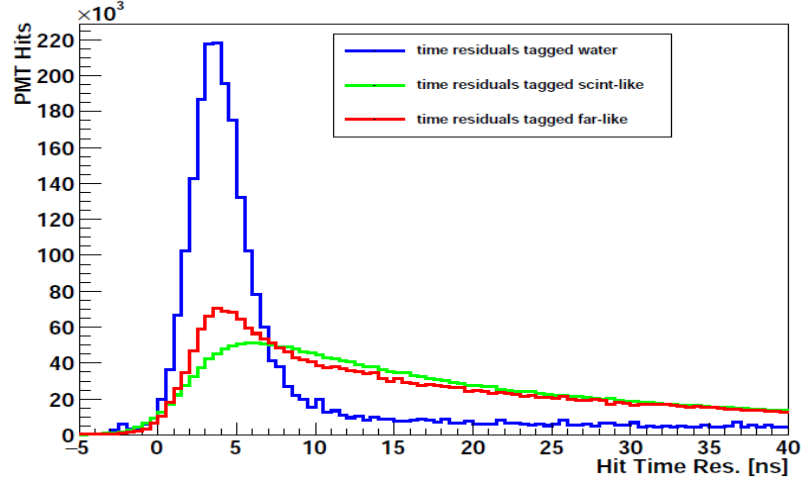
Figure 5.36: Hit time residuals of tagged scintillator-like ^{16}N events (green), the tagged water-like events (blue), and the ^{210}Po-like (far-like) events (red). The hits are normalized.

Furthermore, the time residuals of tagged ^{16}N events along with other population of events (e.g. ^{210}Po) can be used to develop, and optimize timing event classifiers. For instance, figure 5.36 shows the time residuals of tagged scintillator-like and water-like ^{16}N events along with ^{210}Po-like events. As it can be seen, time residuals of the ^{210}Po-like events is sharper and more peaked than the scintillator-like ^{16}N. Multiple Compton scatterings of tagged γ's in scintillator explains the spread out time residuals of these events. One class of timing classifiers are the in-time ratio classifiers. ITR is an example of this class of classifiers, which is defined as the ratio between the number of hits within the prompt window (-2.5, 5) ns and the total number of hits. The prompt window can be optimized to increase the separation power for different classes of events. For instance, figure 5.37 (top) shows in-time ratio classifiers with 3 different prompt window ranges, (-2.5, 5) ns on the left, (-2.5, 8) ns the middle, and (-2.5, 10) ns on the right. 4 class of events are shown, the tagged scintillator-like, and water-like ^{16}N, tagged far events as discussed in section 5.4.3, and ^{210}Po-like events. Furthermore, another class of classifiers are defined as $\frac{Nhits(prompt)-Nhits(delayed)}{Nhits(total)}$, shown on the bottom row.
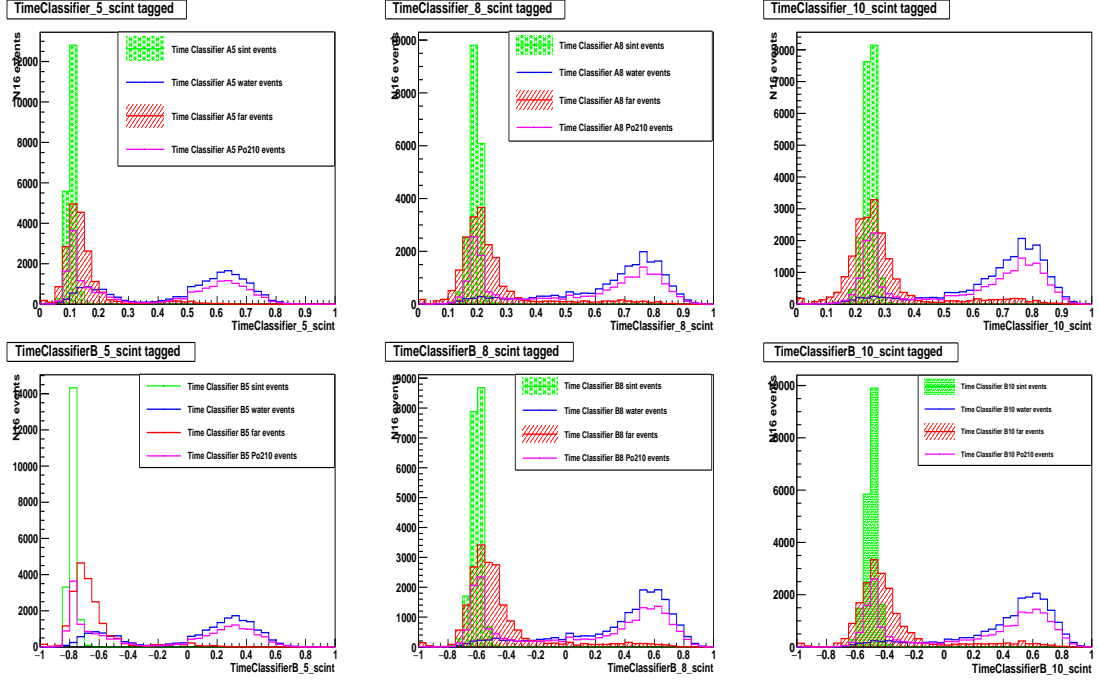
Figure 5.37: The time-ratio type classifiers with different prompt windows are shown on the top. The prompt windows are selected to be (-2.5, 5) ns on the left, (-2.5, 8) ns the middle, and (-2.5, 10) ns on the right. The bottom row shows another class of timing classifiers which is defined as $\frac{Nhits(prompt) - Nhits(delayed)}{Nhits(total)}$, and the same prompt windows are selected. The green shows the tagged water-like ^{16}N, the blue is the tagged scintillator-like ^{16}N, and pink is the ^{210}Po-like events.

The prompt window of (-2.5, 10) ns shows the highest separation power between tagged ^{16}N and ^{210}Po events. However, more sophisticated analysis can be done through a grid search over the prompt windows.

Chapter 6: *In-situ* ^{214}BiPo Measurements and the Effective Attenuation Length

6.1 Introduction

As previously discussed in section 4.3, one of the most problematic backgrounds comes from β-γ decays of ^{214}Bi and ^{212}Bi, with Q_β values of 3.27 and 2.25 MeV respectively. As it can be seen from the decay chain shown in figure 6.1, $^{214/212}$Bi β-decays are followed by $^{214/212}$Po α-decays with half-lives of $\tau_{1/2}(^{214}\text{Po})\sim164.3\mu$s and $\tau_{1/2}(^{212}\text{Po})\sim0.3\mu$s, and Q_α values of 8.95 and 7.8 MeV respectively. The energy of these αs are quenched down to 0.9 MeV for ^{214}Po, and 0.75 MeV for ^{212}Po, in electron equivalent energy [93]. The delayed coincidence between bismuth and polonium decays can be used to effectively tag and constrain these events. Furthermore, the tagged ^{214}BiPo events have been used for various calibration purposes such as energy and position calibration, light yield studies, the scintillation timing studies, and determining the optics of the detector [69, 74]. Moreover, *In-situ* BiPo measurements can be used to monitor ^{222}Rn ingress throughout the filling process, and also estimate the level radioisotopes from ^{238}U and ^{232}Th decay chains. Section 6.2 describes the delayed coincidence tagging technique, and the outlines the analysis selection criteria. The delayed coincidence tagging is used to tag the BiPo events during partial-fill and scintillator phase. The tagging results are presented in section 6.3. Finally, a toy
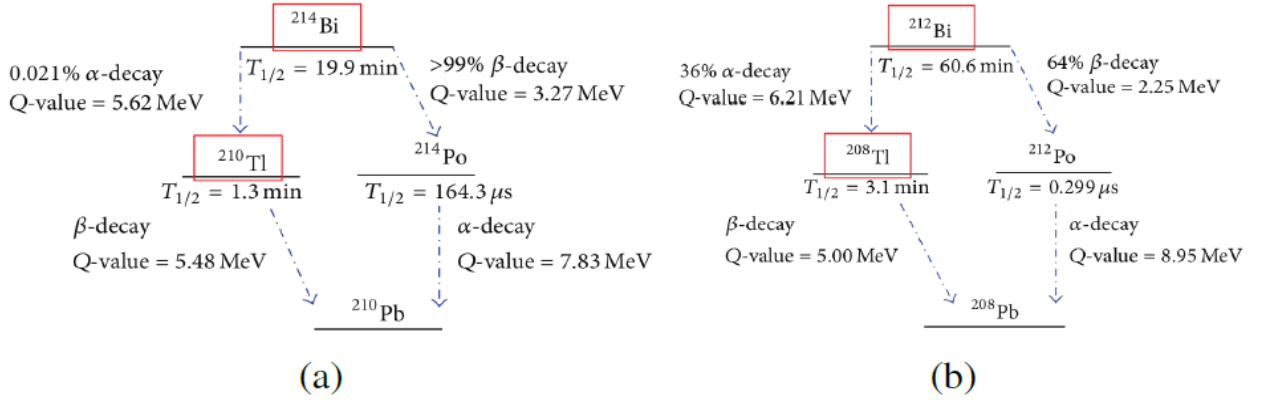
Figure 6.1: The decay chain of ^{214}Bi (left) and ^{212}Bi (right). Red boxes show the potential backgrounds for $0\nu\beta\beta$ signal.

model is developed that can be used to determine the effective attenuation length in scintillator using the tagged ^{214}Po. This toy model is described, and the obtained results are presented in section 6.4.

6.2 Delayed Coincidence Tagging

Figure 6.1 shows the decay chain of $^{214/212}$Bi. As it can be seen, $^{214/212}$Bi undergo β decay with 99% and 64% branching ratio, and produce short-lived $^{214/212}$Po, respectively. In addition, ^{212}Bi nuclei undergo α-decay with a branching ratio of 36%, and produce ^{208}Tl with half-life of 3.1 minutes. ^{208}Tl undergoes various β and γ decays, and eventually produces stable ^{208}Pb by emitting 2.6 MeVγ's. The short half-lives of $^{214/212}$Po allows us to search for the coincidence of bismuth and polonium events within certain Nhits (energy) ranges, occurring close together in time and space. Tagging these coincident events in scintillator provides a clean sample of bismuth and polonium pairs separated from the other backgrounds, which are uncorrelated in time and position. However, the tagging performance is not as efficient in water phase due to the much lower light yield. Table 6.1 summarizes the criteria used to perform coincidence tagging for $^{214/212}$BiPo in scintillator. For the purpose of tagging $^{214/212}$BiPo events in scintillator data, the energy ranges are selected in terms of the `Nhits`. Since

the mean `Nhits` changes with PPO concentration, the tagged $^{214/212}$BiPo events can be used to monitor the light yield across the detector throughout the filling process, and study the PPO mixing process. The presented Nhits ranges are selected for pure scintillator phase (full-fill).

Coincident events	^{214}BiPo	^{212}BiPo
Fitter	scintFitter/partialFitter==True	scintFitter/partialFitter==True
Prompt Nhits	^{214}Bi Nhits $\in$[300, 1050]	^{212}Bi Nhits $\in$[120, 750]
Delayed Nhits	^{214}Po Nhits $\in$ [160, 320]	^{212}Po Nhits $\in$ [230, 380]
Δt [ns]	[4000, 1e6] ns	[400, 800] ns
Δr [mm]	[0, 1000] mm	[0, 1000] mm

Table 6.1: The analysis cuts used for delayed coincidence tagging of $^{214/212}$BiPo events. The Nhits ranges are selected for the pure scintillator period. Δt is the time difference between the bismuth and polonium decays, and ΔR is the difference between the reconstructed positions of the coincident events. In addition, further positional cuts were used depending on the analysis. The cuts are taken from [140].

Δt is the time between the coincident $^{214/212}$BiPo events. In order to maximise the tagging efficiency the width of sequential time window (Δt) is set to be several times ($\sim 7\times$) of polonium half-lives. Furthermore, $\Delta R < 1000$mm is a proximity cut that can remove pile-up coincident events effectively. The presented cuts are used throughout the analysis in this chapter. In addition, further positional cuts are used depending on type of the analysis, for instance, an additional interface cut, 800mm $< z^1$is required for the BiPo tagging in the partial-fill phase.

---

[1]The LAB/UPW interface was at $z \sim$750mm during partial-fill phase.

Tagging Efficiency

The tagging efficiency of ^{214}BiPo events in scintillator is a function of energy, PPO concentration, and the reconstructed positions. The tagging efficiency and its dependencies are investigated using MC simulations, and the average efficiency in partial-fill found to be about $\sim$99% [141]. It was demonstrated that the tagging efficiency drops significantly at the higher radii closer to the AV surface, for instance the efficiency found to be about 95% within $R \in [5.5, 6]$m. This is expected since there is a higher probability for the events (e.g. γ's from bismuth) to escape the scintillator volume at the higher radii. Figure 6.2 shows the tagged and untagged ^{214}BiPo in scintillator as a function of reconstructed radius from a MC simulation. The tagging efficiency of ^{212}BiPo is much lower due to the 36% branching ratio of ^{212}Bi β-decay into ^{208}Tl with a half-life of 3.1 min.
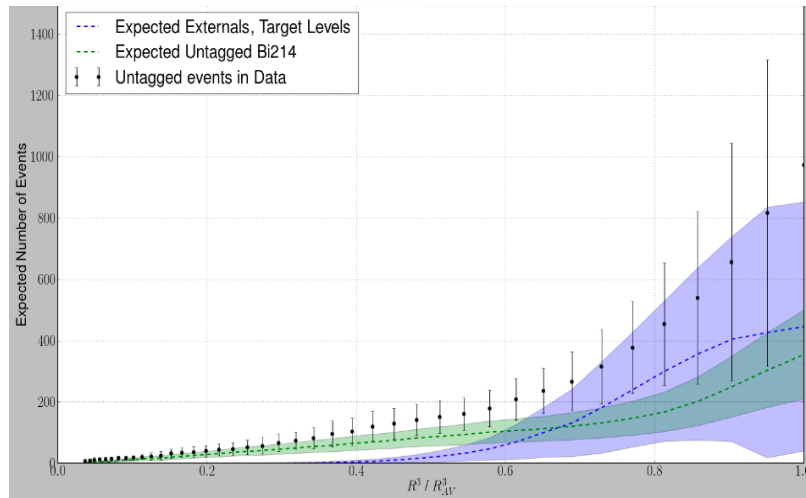
Figure 6.2: Tagged and untagged ^{214}BiPo events as a function of reconstructed radius, along with the expected external γ's, taken from [141].

6.3 ^{214}BiPo Tagging in Scintillator

This section discusses the delayed coincidence analysis of ^{214}BiPo using the partial-fill data and full-fill (scintillator phase) data. Furthermore, the results are presented and discussed.

Partial-Fill

As described in section 2.3, the filling process was interrupted and paused in March 2020 due to COVID-19 pandemic. This period delayed the filling process significantly, however provided about 7 months of stable data with 365 tonnes of liquid scintillator cocktail in the detector. SNO+ took advantage of this stable period to perform a set of calibration using the tagged ^{214}BiPos. The light yield, the reconstruction algorithms, and the scintillation timing are studied in partial-fill using the tagged BiPos [74, 141, 142].

Figure 6.3: Results from tagged ^{214}BiPo in partial-fill; (a) The Nhits distribution of tagged ^{214}BiPo in partial-fill. (b) The time difference (Δt) between the tagged coincident Bi and Po. (c) The difference between the reconstructed positions of the coincident ^{214}BiPos. (d) Reconstructed z vs. reconstructed ρ of the tagged ^{214}Bi in partial-fill.

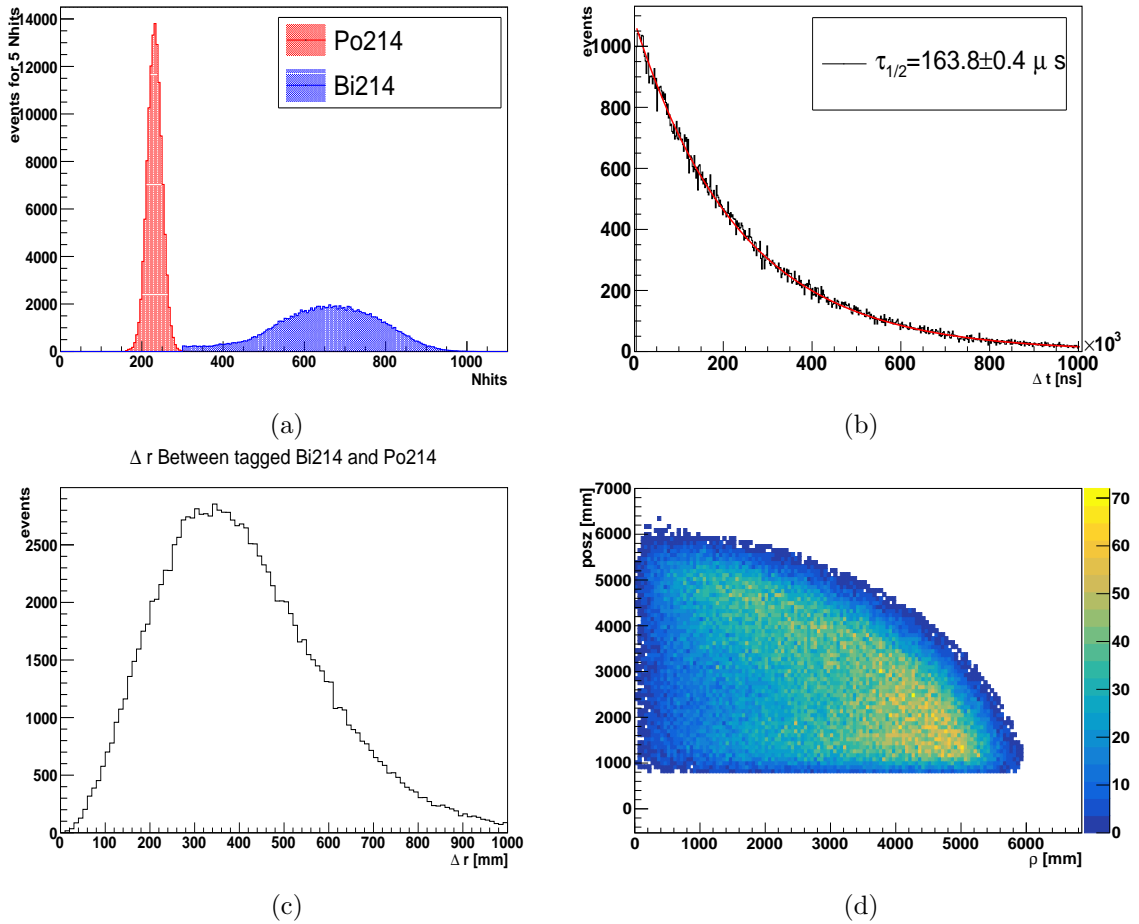The `Nhits` cuts presented in table 6.1 are modified to match the light yield in partial-fill [74]. In addition, a positional cut of $z > 800$mm is applied to select the scintillator events above the LAB/UPW interface. Furthermore, the neck is excluded selecting the events with $R < 6000$mm, and further positional cuts are applied for the delayed events ($z > 1300$mm). Figure 6.3 summarizes the results from tagged ^{214}BiPo events for a month worth of partial-fill data (April 2020). The half-life of ^{214}Po is obtained by fitting the Δt curve, and found to be $\tau_{1/2} = 163.8 \pm 0.4\mu$s, consistent with other measurements [143]. In addition, ΔR distribution from tagged data along with a set of simulated ^{214}BiPo events were used to investigate the position resolution. Moreover, the external 2.6 MeV γ signal from ^{208}Tl was identified and studied in partial-fill after tagging and rejecting BiPo events. This analysis is described in chapter 7.

Scintillator Phase

The pure scintillator phase has started in May 2022, while the detector was filled with $\sim$780 tonnes of scintillator cocktail with the target PPO concentration of 2 g/L. The delayed coincidence tagging has been performed on the full scintillator data, and the tagged ^{214}BiPo events along with the external AmBe source have been used as the primary calibration sources for the time being until the dedicated scintillator calibration sources are ready. The applied cuts are presented in table 6.1. Furthermore, the time residuals of tagged ^{214}Bi events was used to study the emission time, and to determine the scintillation timing constants [69]. The results from the tagging analysis are presented in figure 6.4. The half-life of ^{214}Po is estimated by fitting Δt curve, and found to be $\tau_{1/2} = 162.8 \pm 0.7\mu$s. Furthermore, the reconstructed radius of tagged ^{214}Bi and ^{214}Po are shown in figure 6.4. The radial distribution of the `Nhits` is consistent with the external ^{16}N and the AmBe data, for instance, we can confirm the previously observed light yield suppression at the higher radii in tagged ^{214}BiPo events. However, unlike the external calibration data in which suffers from low statistics at lower radii ($R < 4$m), the tagged BiPo events take place almost everywhere across the detector volume. Therefore a full radial stratification of the

`Nhits` (light yield) is possible using the tagged BiPo pairs. A toy model has been developed that can be used to determine the effective attenuation length by fitting the radial stratification of the mean `Nhits`. The next section describes this model in detail, and presents the analysis result.
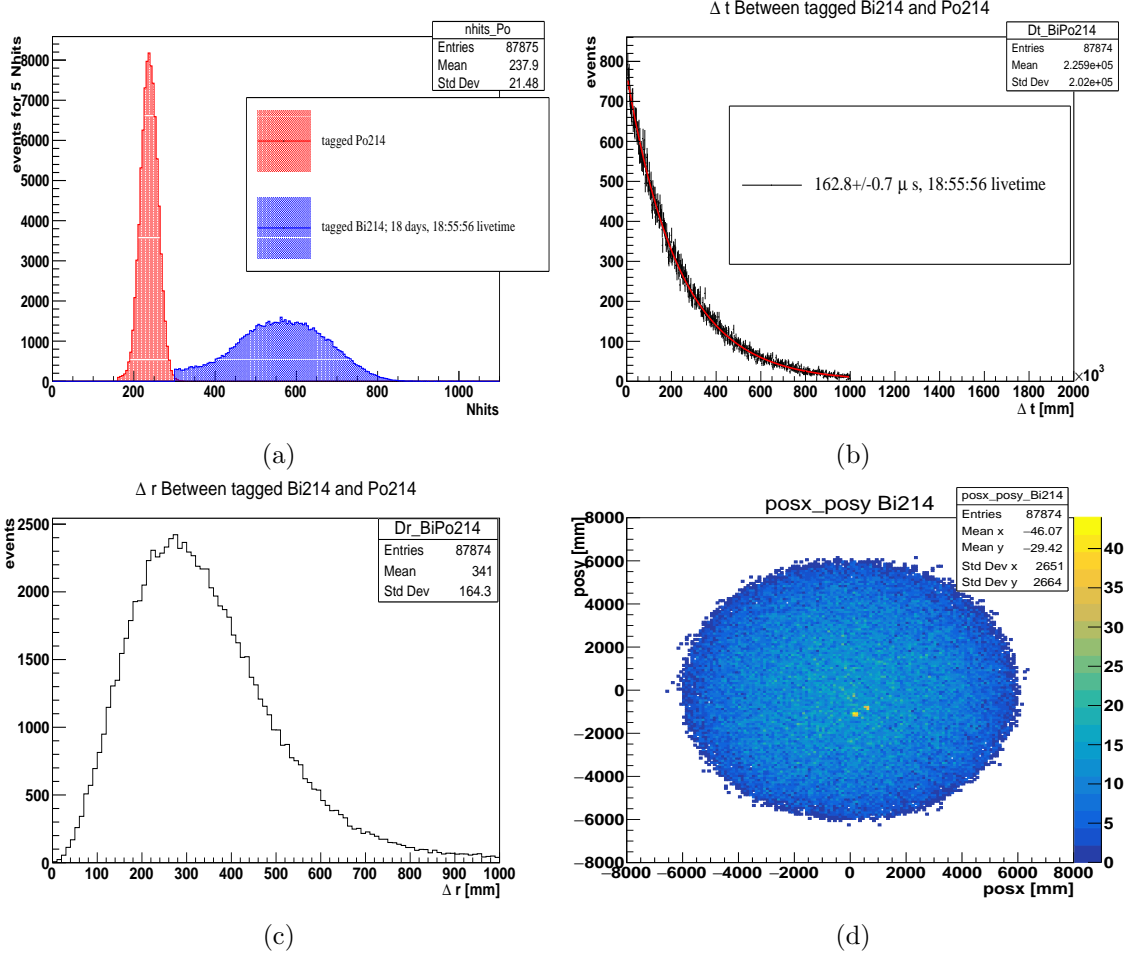
Figure 6.4: Results from tagged ^{214}BiPo in pure scintillator phase using the data from May 2022; (a) The Nhits distribution of tagged ^{214}BiPo in partial-fill. (b) The time difference (Δt) between the tagged coincident Bi and Po. (c) The difference between the reconstructed positions of the coincident ^{214}BiPos. (d) Reconstructed x vs. reconstructed y [mm] of the tagged ^{214}Bi in the full detector.

6.4 Effective Attenuation Length from ^{214}Po

As it can be seen from figure 6.5, the light yield of the tagged bismuth and polonium events increases with radius up to $R \sim 5.2$m which gives the maximum `Nhits`. This

has been observed from other sources such as internal ^{210}Po α decays [134]. This effect is mainly caused by the shorter attenuation for shorter paths.
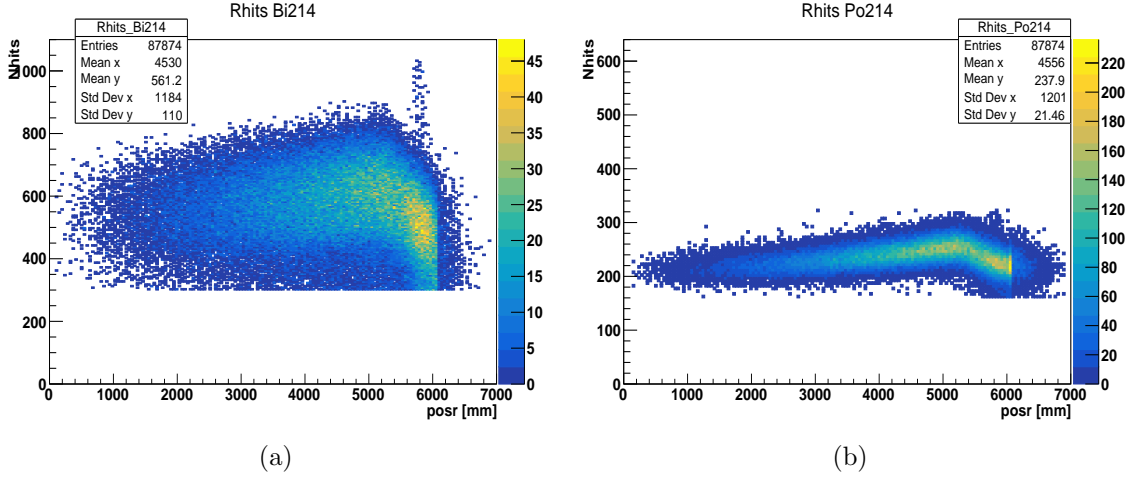
Figure 6.5: Nhits of tagged ^{214}Bi (a), and ^{214}Po (b), vs. the reconstructed radius in scintillator.

The internal reflection takes over passed $R \sim 5.2$m, and the light yield is significantly suppressed. This light yield drop has been observed, and studied using external calibration sources (see section 5.4). The radial distribution of the mean `Nhits` of tagged ^{214}Po is fit by a model to determine the effective attenuation length of the detector in pure scintillator phase. Unlike the β decay spectrum, ^{214}Po α-decay signal is relatively straightforward to characterize, and can adequately fit a Gaussian. Therefore, tagged ^{214}Po Nhits is favored over ^{214}Bi for this analysis. In addition, to avoid the dominant light suppression passed 5.2 m, only ^{214}Po events that are reconstructed within the radius of [0, 5.2]m are selected. The ultimate goal of the model would be to parameterize $Nhits(r)$ as a function of reconstructed radius in the detector. The model is based on a very fundamental assumption; in case of a physics event, the probability of the ith PMT registering a hit can be described as the Poisson distribution of the number of arriving photons (p.e.), which is demonstrated in equation 6.1.

$$P_{hit}^i \sim \text{Poi}(\mu_{\text{i}}) = 1 - \text{e}^{-\mu_{\text{i}}} \tag{6.1}$$

123

where μ_i is the number of p.e. arriving at the ith PMT. The total number of fired PMTs can be expressed in form of a summation over all the working PMTs, and can be written as follows:

$$Nhits = \sum_{PMTs} (1 - e^{\mu_i}) = \int \sigma d\vec{A}(1 - e^{-\mu(\vec{r})}) \tag{6.2}$$

The discrete form of $Nhits$ shown in equation 6.2 can be written in form of an integral over the surface area, where $d\vec{A}$ is the differential surface area, and σ is the surface density of the number of good PMTs, and can be written as:

$$\sigma = \frac{N_{good\ pmts}}{Area} \tag{6.3}$$

Figure 6.6 demonstrates the geometry and the parameters used in this model. In order to simplify the problem we can take advantage of the existing symmetry along the vector pointing to the event vertex, and select the differential surface element $(d\vec{A})$ to be a ring with the width of dl on the surface of the PSUP. The differential surface element is shown with a dashed line in the figure 6.6, and can be expressed as $d\vec{A} = d\gamma 2\pi R^2 \sin(\gamma)$, where R is the radius of PSUP. Therefore the $Nhits(r)$ can be written as:

$$Nhits(\vec{r}) = \int_0^\pi \sigma(r)d\gamma 2\pi R^2 \sin\gamma(1 - e^{-\mu(\vec{r})}) \tag{6.4}$$

The number of photons (μ) arriving at a PMT can be scaled up for a sphere with the radius of the distance that photons travel to reach the PMTs on the ring (r_{pmt}), and can be written as follows:

$$\mu = N_{p.e.}\frac{A_{pmt}}{4\pi r_{pmt}^2}\cos(\phi) \tag{6.5}$$

where $N_{p.e.}$ is the total number of photons passed a sphere with radius of r_{pmt} around the event vertex. In fact, $N_p.e.$ is not quite the same as the total number of generated photons. The generated photons attenuate due to absorption and scattering as they travel in the AV, acrylic, and the external water. Furthermore, the PMT angular response needs to be taken into account in the model. Therefore, the number of

photons ($N_{p.e.}$) at a certain distance r_{pmt} can be included in the model as follows:

$$N_{p.e.} = N_0 e^{-\lambda r_{pmt}} f(\phi) \tag{6.6}$$

where N_0 is the total number of generated photons in a physics event, λ represents the effective attenuation length of the media, and $f(\phi)$ is a function that describes the PMT angular response.
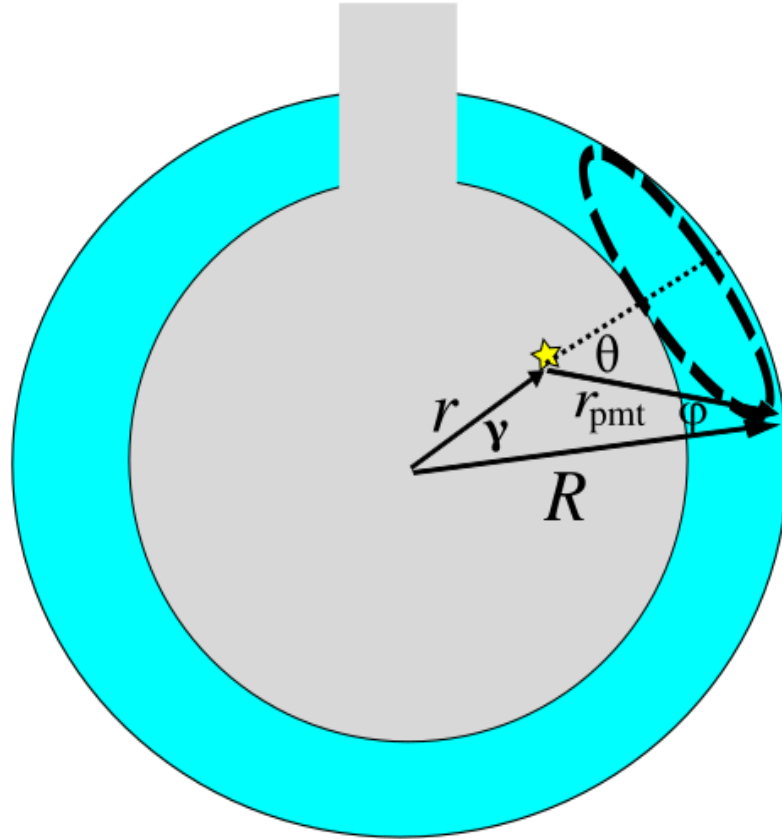
Figure 6.6: The figure demonstrates the parameters used in the toy model to describe Nhits as a function of $\vec{r}$ and γ.

The PMT angular response has been measured for different wavelengths using the laser-ball [76]. Figure 6.7 shows the measured angular response. For the purpose of this analysis, the angular response for $\lambda \sim 420$ nm is selected, $f(\phi)$ is included in form of a table from `RAT-7.0.0`.
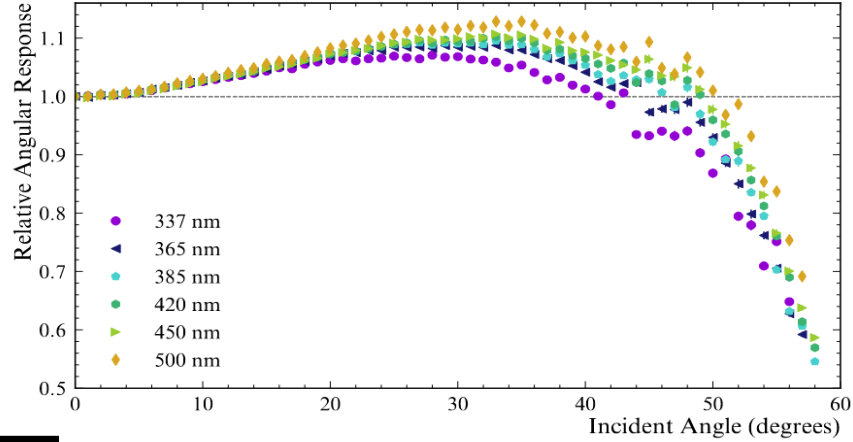
Figure 6.7: The PMT angular response measured during the water phase using laser-ball, taken from [76]

The presented variables r_{pmt} and ϕ need to be written in terms of the reconstructed radius (r) since we are fitting $Nhits(r)$. Using the geometry of the system one can write:

$$r_{pmt} = \sqrt{R^2 + r^2 - 2rR\cos(\gamma)} \tag{6.7}$$

$$\cos(\phi) = \frac{R - r\cos\gamma}{\sqrt{R^2 + r^2 - 2rR\cos\gamma}} \tag{6.8}$$

Using the two equations above, we can re-write equation 6.2 in terms of r. The tagged ^{214}Po from May 2022 is used to fit Nhits(r), and obtain the effective attenuation length (λ). Figure 6.8 shows the mean Nhits from a Gaussian fit using tagged ^{214}Po data versus the mean reconstructed radius. The radial stratification of Nhits is obtained for the intervals of 25cm along the radius. The functional form demonstrated in equation 6.2 is used to fit the data, and the effective attenuation length is estimated. The red line shows the best fit. λ_{eff} is estimated to be 0.0001321 ± 0.0000165 mm^{-1}, and the effective attenuation length is found to be **7547$\pm$928 mm** for the full-fill. Furthermore, Ryan Bayes carried out the same type of analysis using the ^{214}Bi events from May 2022, and determined the effective attenuation length to be 7461 ± 789 mm [144] which is consistent with the obtained value from the ^{214}Po events.
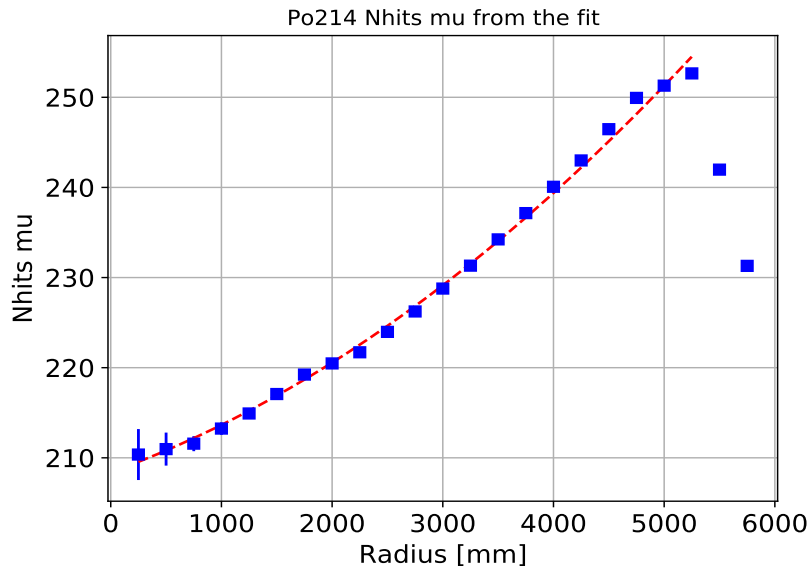
126

Figure 6.8: The mean Nhits from tagged ^{214}Po in vs. the mean reconstructed radius in scintillator. The red line shows the best fit for the functional form of Nhits(r) from the model.

6.5   Summary and the Prospects

The delayed coincidence tagging technique is discussed in section 6.2, and furthermore the performance of this technique for tagging $^{214/212}$BiPo events are demonstrated. This technique was used to tag $^{214/212}$BiPo pairs during the partial-fill and the pure scintillator phase. The results are presented and discussed in section 6.3. The tagged ^{214}BiPo events are used for various purposes such as monitoring ^{222}Rn ingress in the scintillator volume, scintillation timing studies, position reconstruction studies, light yield studies, and optical calibration. I have developed a model that describes the light yield as a functional form of the reconstructed radius. This model is described in detail in section 6.4. The effective attenuation length of the detector is estimated in the full-fill by fitting the Nhits(r) from the tagged ^{214}Po events to the model. The effective attenuation length found to be 7547±928 mm which is consistent with other measurements. In order to find the attenuation length of each medium, more sophisticated analysis can be performed selecting sub-sets of PMTs.

Chapter 7: External Backgrounds in SNO+

7.1 Introduction

The external γ's are coming from the ^{232}Th and ^{238}U decay chains in the acrylic, the rope systems (HD and HU ropes), the external water in the cavity, the AV outer and inner dust, and the PMTs (see section 4.3.2). The most concerning γ emitters are ^{208}Tl and ^{214}Bi produced in thorium and uranium decay chains, respectively. They both undergo β decays, and furthermore produce several γ's with energies up to 2.6 MeV. Figure 7.1 shows the true energy of simulated γ's from external ^{208}Tl and ^{214}Bi in the acrylic. These γ's can be reconstructed at energies within the $0\nu\beta\beta$ energy region and solar neutrino signals, therefore it is crucial to identify and reject them. The primary method to constrain the externals is staying away from the acrylic surface by selecting a spherical region around the center of the AV known as the fiducial volume (FV). Determining the radius of the fiducial volume is a compromise between rejecting the external background and sacrificing the signal [92]. Furthermore, as discussed in section 3.5, a set of timing and topological event classifiers are developed, and optimised for different sources of external γ's versus 0ν signal. This chapter describes the expected signal from external γ's in SNO+. Furthermore, section 7.3 discusses some of the timing and angular classifiers that can be used to identify and reject the externals based on their hit time residuals and their PMT hit patterns. Using a set of MC simulations, the rejection efficiency and the signal sacrifice of the classifiers are investigated for the solar neutrinos within various fiducial volumes. Furthermore, it is demonstrated that the classification performance can be improved utilising supervised

learning methods (TMVA), discussed in section 7.3.1. In addition, a set of analysis was performed on the partial-fill data, and the 2.6 MeV signal from ^{208}Tl was identified, and discussed in section 7.4. Finally, the level of ^{208}Tl γ's from the hold-down ropes is estimated taking advantage of their angular symmetry, discussed in section 7.4.1.

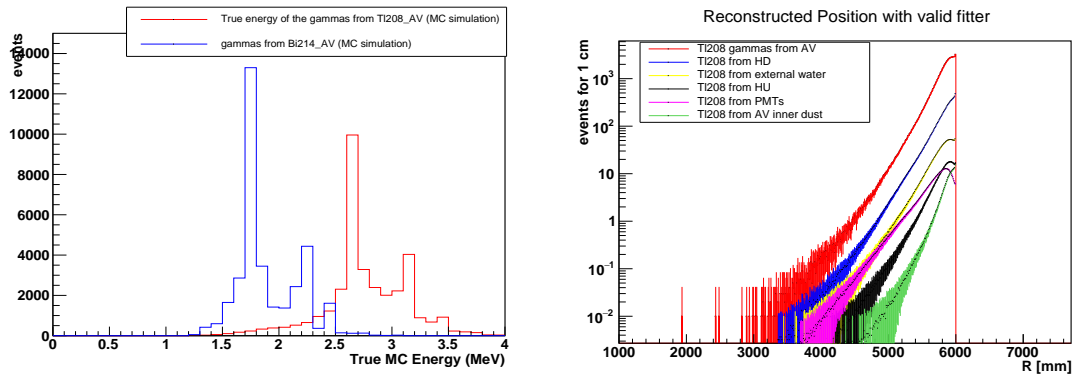## 7.2 External γ's from ^{208}Tl and ^{214}Bi

Figure 7.1: The true energy of external γ's from simulated ^{208}Tl and ^{214}Bi in the acrylic is shown on the left. The reconstructed radius of the external γ's is on the right, simulated using RAT-6.16.8.

Figure 7.1 (right) shows the reconstructed radius of external γ's from various sources of ^{208}Tl simulated using RAT-6.16.6. All the rates are scaled up to match the expected number of events within 1 year of data taking in scintillator [110]. As expected, the number of reconstructed events falls off with the distance from the surface of AV, about 99% of external γ's are expected to be reconstructed further than $R \sim 5.2$ m. This will simply imposes a limit upon the chosen fiducial volume of SNO+. The fiducial volume can be vaguely defined as the region which is not background dominant, in other words, events that are reconstructed outside of this region are statistically likely to be backgrounds. As the first step to study the external γ's, a set of MC simulations was generated for different sources of external ^{208}Tl and ^{214}Bi. Tables 7.1 and 7.2 summarize the simulation statistics as well as the expected number of events within a year of data taking from each source of ^{208}Tl and ^{214}Bi respectively. The ta-

source	expected events/ year	total simulated ev	total recorded events	events with valid fitter	# files	scale factor
Exwater	3.92e+06	1.97861765e+08	1.1615734e+07	4.63769e+06	870	0.0198118
HD ropes	(2.32/1.55)e+6 (full/shell)	7.2171494e+07	4.9259799e+07	2.0789756e+07	2509	0.0214766
HU ropes	(4.78/1.67)e+05 (full/shell)	1.0655959e+07	4.320474e+06	2.21292e+06	180	0.015672
AV outer_dust	4.6e+05	4.599955e+6	3.819951e+06	1.88314e+06	209	0.100001
AV inner_dust	2.48e+04	1.348958e+06	1.24112e+06	6.95507e+05	110	0.0183846
AV_Tl208	1.5e+06	1.4915624e+07	1.3350106e+07	7.57649e+06	887	0.0993309
PMT β γ's	7.18e+04	7.275614e+06	6.149961e+06	5.38575e+06	711	0.009868

Table 7.1: The table shows the MC statistics for external ^{208}Tl. The background rates are taken from [110]

Source	expected events/ year	total simulated ev	total recorded events	first events with valid fitter	# files	scale factor
Exwater	1.32e+08	1.320162393e+09	4.45968e+07	9.07389e+05	2384	0.0999877
HD ropes	2.72e+06	2.49821660e+08	1.14363e+08	5.38897e+05	3169	0.0108878
HU ropes	2.92e+05	4.4983356e+07	1.25045e+07	4.1740e+04	456	0.0064913
AV outer_dust	7.75e+05	1.5512629e+07	8.80361e+06	2.18702e+05	306	0.04996
AV inner_dust	4.15e+04	8.301979e+06	7.37303e+06	2.0731e+04	391	0.00499881
AV_Bi214	1.28e+07	1.28027e+08	8.12944e+07	4.71771e+06	3219	0.0999785

Table 7.2: The table shows MC statistics and the background rates for ^{214}Bi, the background rates are taken from [110]

ble also shows the expected number of events with valid `scintFitter`. The expected number of simulated events with valid `scintFitter` demonstrates that the AV and HD ropes are expected to be the two dominant sources of external backgrounds in scintillator [145]. Therefore, to simplify this analysis, the simulated γ's from the AV was carried out as a reference background signal to obtain the classifiers cuts/decision boundaries, and furthermore, to investigate the rejection efficiency versus the solar ν signals. The next section focuses on the timing and angular classifiers, and discusses their rejection efficiency for different fiducial volumes.

7.3 Timing and Topological Event Classifiers for External ^{208}Tl and ^{214}Bi

As describes in section 3.5, a set of timing and topological classifiers are developed based on the log-likelihood of PMT hit time residuals and hit patterns of the external γ's. Assuming $0\nu\beta\beta$ decay as the desired signal, these classifiers are optimised and weighted for 4 main sources of external γ's, AV, HD ropes, external water, and PMTs.

Overall, there are 16 classifiers; 4 topological, and 12 timing classifiers, 3 different sets that are weighted differently.
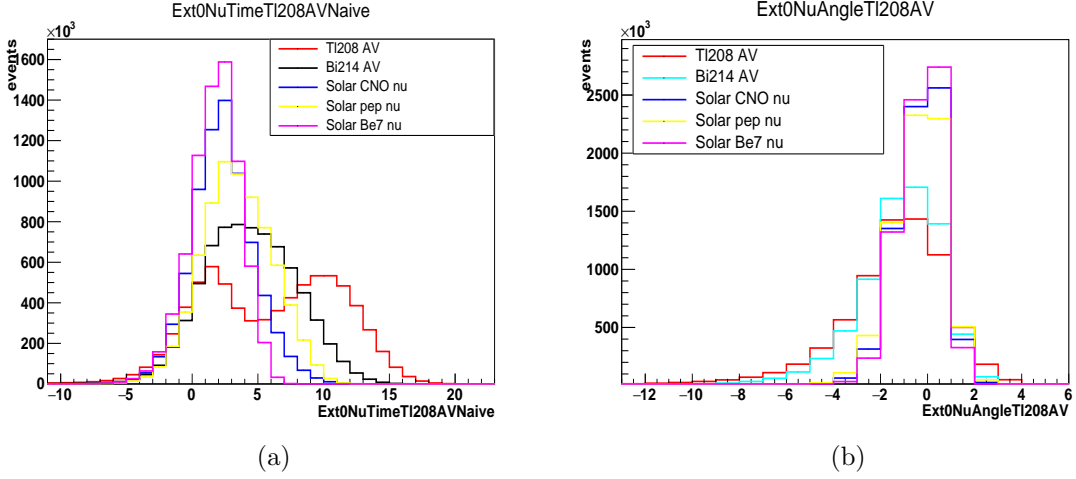

Figure 7.2: The timing classifier (a) and angular classifier (b) (naive weight option) for simulated solar ν, the external ^{214} and ^{208}Tl from the AV.

`ext0NuTimeTl208AVNaive` and `ext0NuAngleTl208AV` are timing and angular classifiers that are developed and optimized to reject the ^{208}Tl γ's from the AV which is the dominant source of external γ's as demonstrated earlier. These two classifiers are frequently used throughout this analysis since they found to be more effective than the other classifiers (e.g. Fisher's weight). The desired physics signal that was carried out in this analysis is a set of simulated solar neutrinos; CNO $\nu_{e/\mu}$s, pep $\nu_{e/\mu}$s, ^{8}B $\nu_{e/\mu}$s, and ^{7}Be $\nu_{e/\mu}$s. Figure 7.2 shows the timing classifier (a) and the angular classifier (b) for the simulated data. Table 7.3 shows certain cuts on these classifiers together with their expected sacrifice levels for the 0ν signal obtained by [146, 100]. As the first step, the simulated external ^{208}Tl and ^{214}Bi data together with the solar ν were used to determine the rejection efficiency and the sacrifice level of the presented cuts on the classifiers. The fiducial volume is set to be $R < 5.5$m. Figure 7.3 shows the reconstructed energy spectrum of the simulated external backgrounds and the solar signal with two different sets of classifier cuts as presented in table 7.3, the 0ν sacrifice of 0.1%(top), and 1% (bottom). The data were scaled to match the expected number of events for 1 year worth of data in scintillator. The sacrifice level and the

rejection of different signals are presented in the legend, and it is verified that the classifiers are effective, and can reject the external γ's up to 78%. However, it can be seen that there is a large sacrifice for lower energy solar ν. This is expected since the classifiers were originally tuned for events with energies about 2.5 MeV 0ν signal. Furthermore, an additional energy cut of 1.5 MeV$< E$ was applied on the data, and the results are presented in figure 7.4. The set of cuts on the classifiers along with the energy cut show about 25% and 54% of rejection for γ's, and sacrifice level of 0.2% and 4% for solar ν signal for two sets of cuts on classifiers, respectively. Even though the presented 0ν cuts seem effective for distinguishing the solar ν signals from the externals, they can be significantly improved. The next section describes some of the techniques that can be used to improve the classification performance.

Classifiers	sacrifice <10%	<1%	<0.1%
ext0NuTimeTl208AVNaive	>13.8	>7.8	>0.6
ext0NuAngleTl208AV	>-3.45	>-6.25	>-19.55

Table 7.3: The timing and angular classifiers for external ^{208}Tl from the AV along with proposed cuts and associated sacrifice for fiducial volume set to be R<5.5 m are shown in this table.

7.3.1 Optimizing Classification using Supervised Learning Methods (*TMVA*)

As it can be seen from figure 7.4, a set of simple cuts on 0ν timing and topological classifiers are found to reject the external γ's effectively. However, the sacrifice level for the lower energy solar ν signal is found to be significantly high, as demonstrated in figure 7.3. Therefore, one can suggest utilizing optimization methods to find a more effective decision boundary rather than a set of cuts which was originally obtained for 0ν signal. In order to find the decision boundary, I have used a supervised learning tool kit known as *TMVA* (Toolkit for Multivariate Data Analysis).
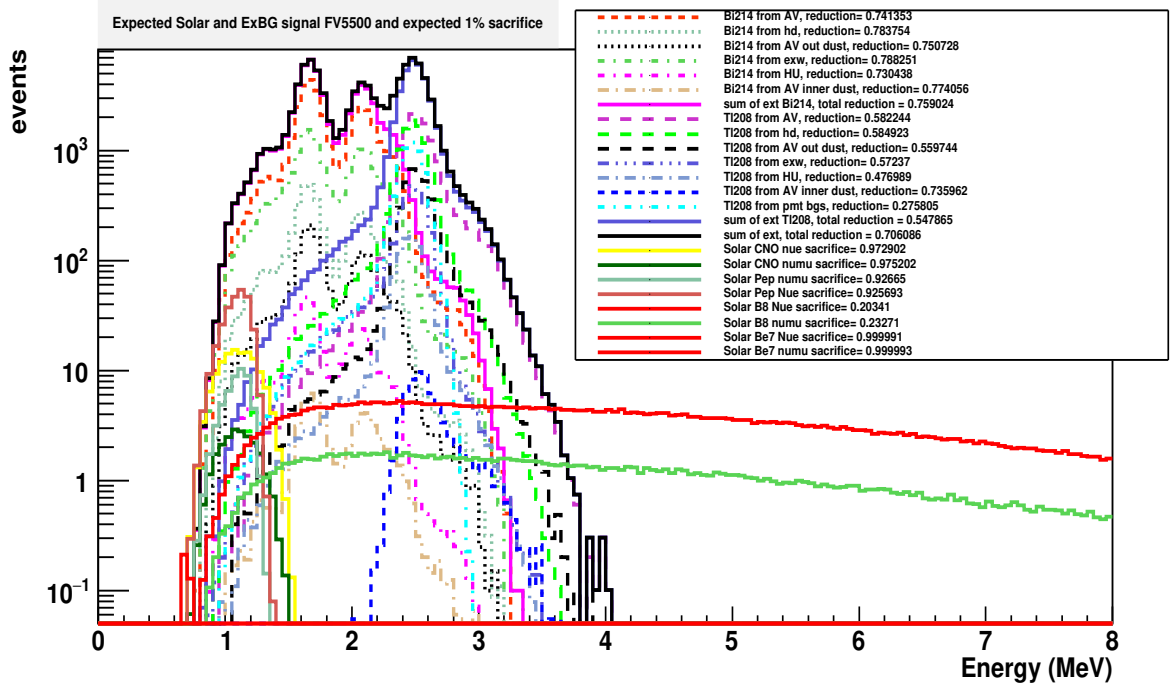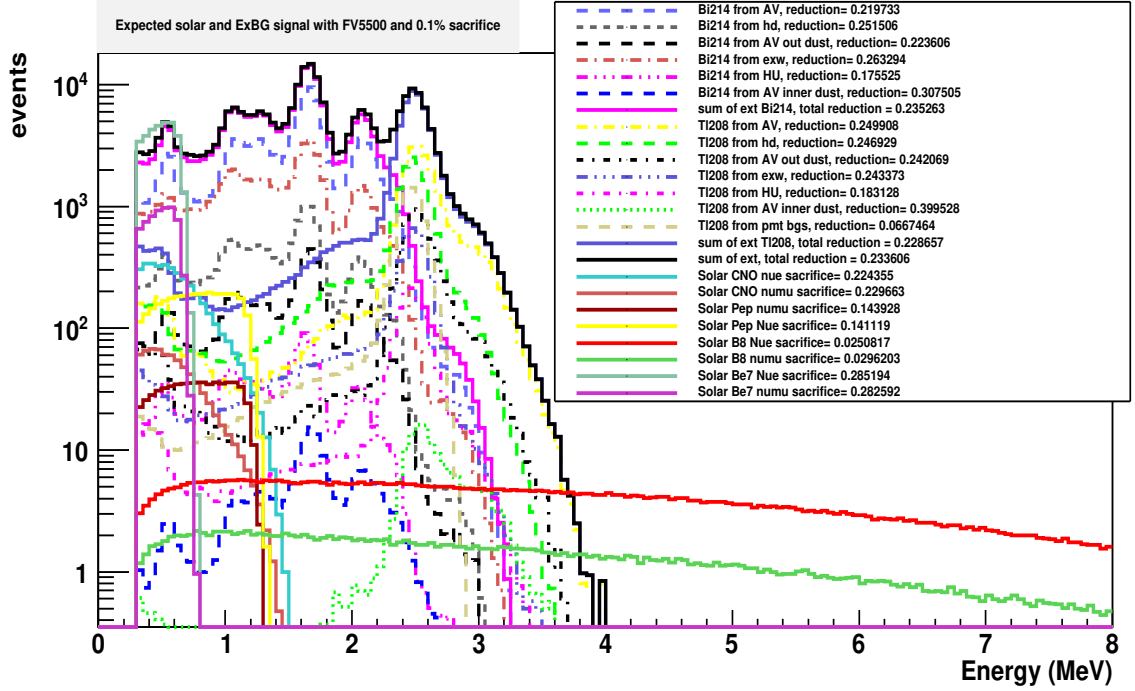
Figure 7.3: The reconstructed energy spectrum of the external gammas as well as solar neutrinos above 0.1 MeV (MC), with the timing/topological classifiers cuts presented in table 7.3. The FV is selected to be $R < 5.5$m. The number of events are scaled up to 1 year worth of data taking. The sacrifice of every signal is presented is shown in the legend.
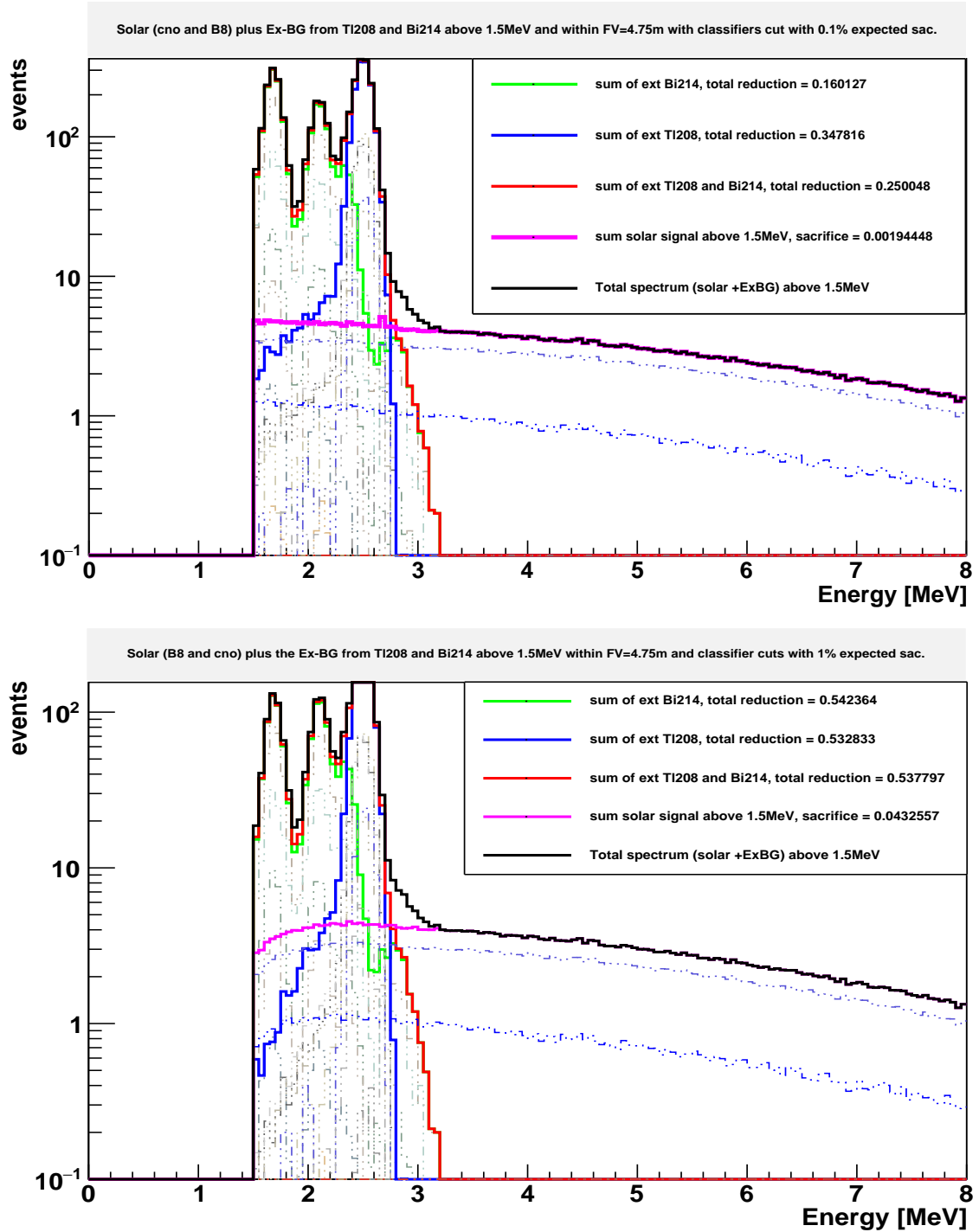
Figure 7.4: The reconstructed energy spectrum of the external γ's as well as solar neutrinos above 1.5 MeV (MC), with the timing/topological classifiers cuts presented in table 7.3. The number of events are scaled up to 1 year worth of data taking. The sacrifice for every signal is shown in the legend.

TMVA is a ROOT-integrated package providing a supervised learning environment for

multivariate analysis such as event classification and regression. `TMVA` utilizes several implemented classification methods such as the decision tree, neural networks, likelihood, the Fisher's linear discriminant, etc. `TMVA` classification consists of two steps: i) the training, where the selected multivariate classification methods are trained, tested, and their performances are evaluated, ii) the application, where the trained classification methods are booked and applied on a data set. The communication between the data set and the `MVA` classification methods is handled through the `Factory` object. The `TMVA::Factory` provides functions to perform the followings: i) to split and specify the training and the test subsets of data, ii) to register the discriminating input variables from data[1], and iii) to book the preferred classification methods [147]. The `TMVA::Factory` performs the training, testing, and the evaluation of the booked methods, and returns the results in form of files consisting "weights" for each classification method. Furthermore, the performance of various methods can be investigated, and the most appropriate method can be selected.
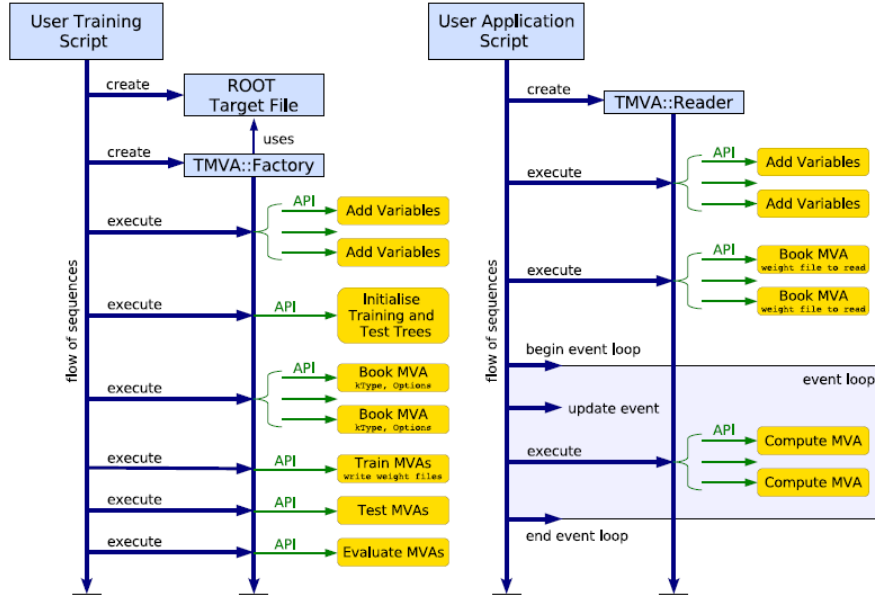

Figure 7.5: Flow of a typical **TMVA** training process (left), and the application process (right), taken from [147].

---

[1]In the case of this analysis, the timing and topological classifiers can be passed as discriminating variables.

In order to apply the trained classifiers, the obtained weights can be used on a data set with unknown composition. The application of the trained classifiers is handled through the `TMVA::Reader` object. Figure 7.5 shows an overview of two phases of `TMVA` classification.

The input data set can be passed to `TMVA::Factory` for training as a `ROOT TTree`, and the signal and background can specified in the same tree or in different trees. Furthermore, overall weights can be assigned to the signal and background[2]. For the purpose of this analysis, a set of simulated external backgrounds and the solar neutrino signal were passed as different the background and signal trees, respectively. Furthermore, the data were split into two subsets, 90% of data were used for training, and 10% is used for testing and the performance evaluation. In addition, 9 variables are registered to be used by the `MVA` classification methods, 4 timing and angular classifiers, `Nhits` and energy, `ITR` , the reconstructed position (R), and the `nearAV` classifier. Figure 7.7 and 7.6 show the correlation matrices of the passed variables for the solar ν signal and the external backgrounds respectively. As expected some of the registered variables are highly correlated such as `Nhits` and the energy.
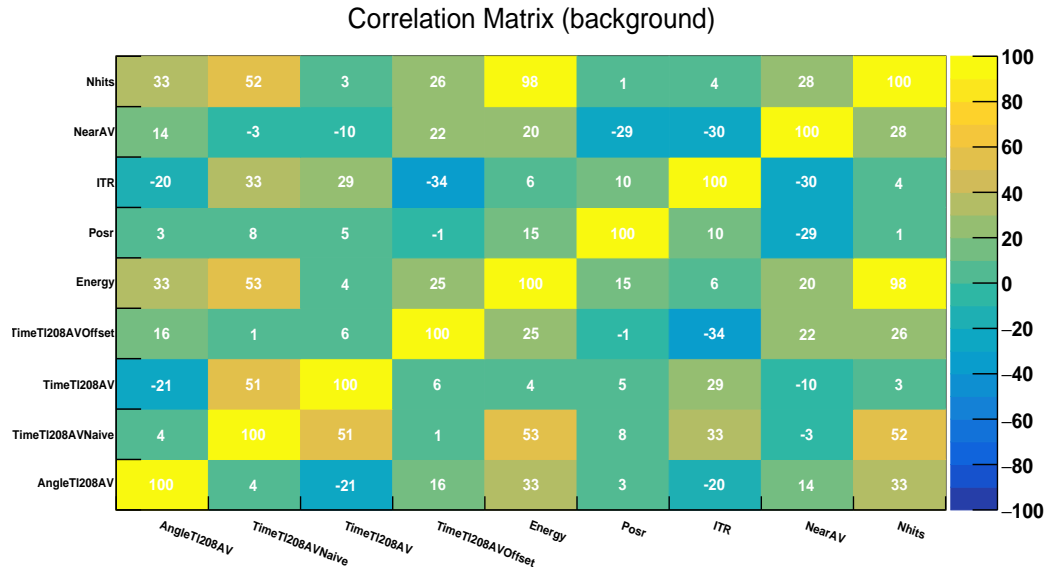

Figure 7.6: The correlation matrix of the registered variables (classifiers) for the background signal.

---

[2]Worth mentioning that event-by-event weights can be assigned to the training data through the Factory, however is beyond the scope of this analysis.
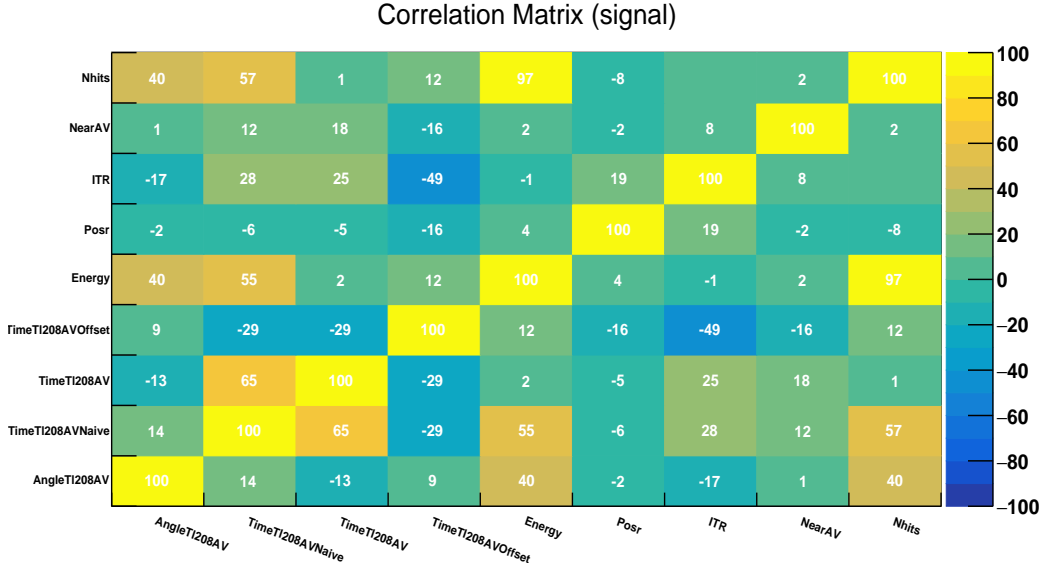
Figure 7.7: The correlation matrix of the registered variables (classifiers) for the solar ν data.

Furthermore, I have booked the "Cuts", Fisher's discriminant, and the Boosted Decision Tree (BDT) as the classification methods. The method "Cuts" essentially consists of a set of cuts on the given variables. Fisher's linear discriminant finds a decision boundary based on the linear combination of variables, for instance the Fisher's decision boundary for 2 given variables (x_1, x_2), would be line on the x_1-x_2 plane that maximises the separation between the background and signal.
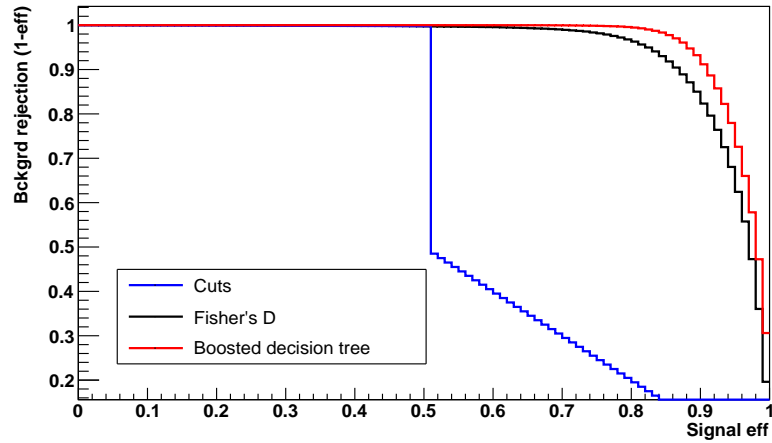

Figure 7.8: The plot shows the ROC curve for three classification methods booked through TMVA. It can be seen that the separation power can be significantly improved using Fisher's Discriminant and Boosted decision tree.

137

The decision tree is a binary tree structured classifier based on partitioning data upon yes/no decisions that are taken on one single variable until a stop criterion is fulfilled. Eventually, the phase space is split into sub-regions that are classified as either signal or background based upon the majority of the training events that end up in the final leaf node. Figure 7.9 gives an overview of decision tree classification. The boosted decision tree essentially extends this concept from one tree to several trees forming a forest [147]. The trees are derived from the same training data set by re-weighting events, and are combined into a single classifier, given by the average of the individual decision trees. Boosting can stabilize the response of the decision trees with respect to fluctuations in the training sample, and is able to considerably enhance the performance. The simulated data were scaled to the expected rates, and
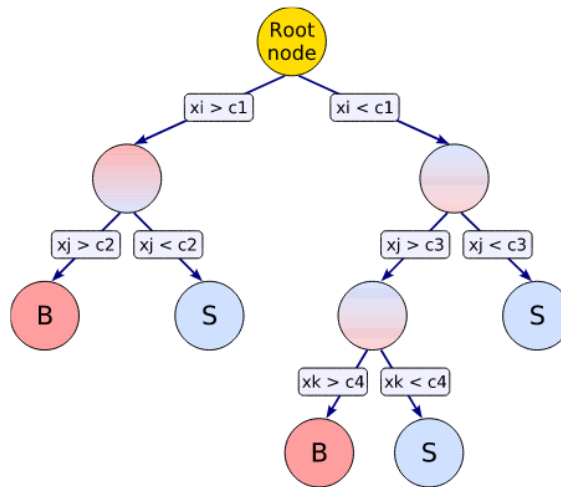

Figure 7.9: Starting from the root node, a sequence of binary splits using the discriminating variables x_i applied to the data. Each split uses the variable that at this node gives the best separation between signal and background. The same variable may thus be used at several nodes, while others might not be used at all. The leaf nodes at the bottom end of the tree are labeled either as signal or background depending on the majority of events that end up in the respective nodes. The schematic is taken from [147].

passed to a ROOT macro file which was modified for this analysis. Figure 7.8 shows the performance of the three booked methods on the training data. As it can be seen, the Fisher's cuts and the boosted decision tree can effectively improve the separation power while having a low sacrifice level for the signal. This is an ongoing study, and

the classification can potentially improve by selecting the registered variables more sophisticatedly.

7.4 Identification of external backgrounds from ^{208}Tl

This section is dedicated to identification of the 2.6 MeV γ peak from external ^{208}Tl. The lower energy external γ peaks from ^{208}Tl are more difficult to identify due the significant rates of other backgrounds such as γ's from ^{40}K and ^{214}Bi. One of the major backgrounds for the 2.6 MeV ^{208}Tl signal comes from ^{214}Bi β-decays inside the scintillator volume. As described previously, ^{214}Bi is a product of ^{222}Rn decays, and undergoes several β and γ-decays with a Q_β-value of 3.27 MeV. Therefore, they can mask the 2.6 MeV γ peak. ^{214}Bi decays into ^{214}Po that subsequently undergoes α decay with half-life of 164μs. As described in detail in chapter 6, SNO+ utilizes the delayed coincidence technique to tag these coincident events. Figure 7.10 (a) shows the Nhits distribution of simulated external γ's from ^{208}Tl (blue), and a set of simulated ^{214}Bi decays in scintillator in partial-fill. The rates are scaled to match the number of tagged ^{214}BiPo events in April 2020 in partial-fill. Furthermore, figure 7.10 (b) shows the Nhits from a set of MC simulations of the most dominant sources of the external γ's; the AV and the HD ropes.
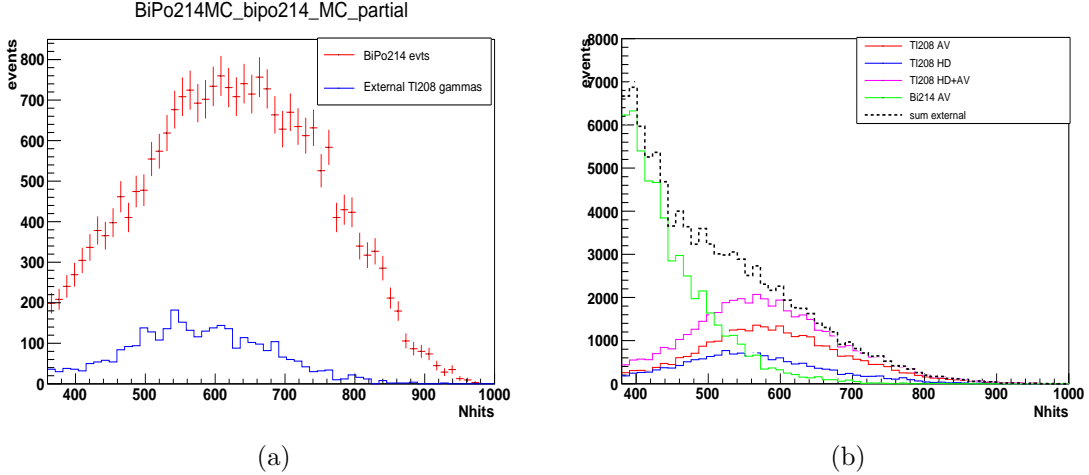
Figure 7.10: (a) Nhits of simulated external ^{208}Tl γ's from the AV, as well as the simulated ^{214}Bi events in the scintillator volume, simulated for the partial-fill geometry. (b) shows the simulated Nhits distribution for dominant sources of external ^{208}Tl and ^{214}Bi γ's.

Figure 7.11 shows the reconstructed radius of simulated external γ's from ^{208}Tl and ^{214}Bi as well as simulated internal ^{214}Bi (pink). It is estimated that more than 99% of the external γ's are being reconstructed at $R > 5$ m, where as only 37% of the total ^{214}Bi events are reconstructed within this region. This can simply impose a radial cut of $R > 5$m on the region of interest for this analysis. In addition, to avoid the hot spot around the PFA tube[1], I have only selected the events with $\rho > 2$m where $\rho = \sqrt{x^2 + y^2}$. Furthermore, an interface cut of $z > 0.8$m was used. As the first step, using the delayed coincidence tagging the ^{214}BiPo events are tagged and removed from the partial-fill data. In order to capture most of BiPos in this analysis, a set of generous `Nhits` cuts are used, `Nhits`$\in$(350, 1000) and (120, 400) for ^{214}Bi and ^{214}Po respectively. The timing and position criteria are the same as the ones described in chapter 6. For the purpose of this analysis, the partial-fill data from stable runs (`Partial Gold`) between April 1$^{\text{st}}$ and July 1$^{\text{st}}$ 2020 are selected. Figure 7.12 (a) shows the time difference between the tagged BiPo coincident events within the region of interest in this time period. The curve matches the half-life of ^{214}Po. In addition, figure 7.12 shows the reconstructed position of the events after removing

---

[1]PFA tube was a temporary tube that was deployed into the AV through the UI, and was used to remove the UPW throughout scintillator filling.
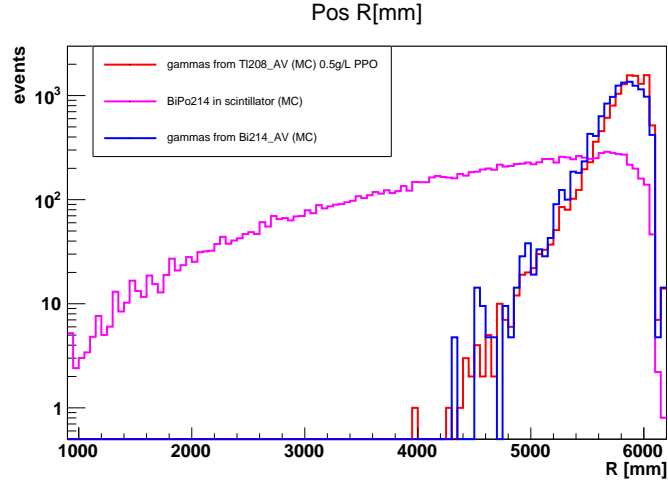
the tagged ^{214}Bis within the region of interest.

Figure 7.11: The reconstructed radius of simulated ^{214}Bi events (pink) as well as the simulated external gammas from ^{208}Tl (red) and ^{214}Bi (blue).
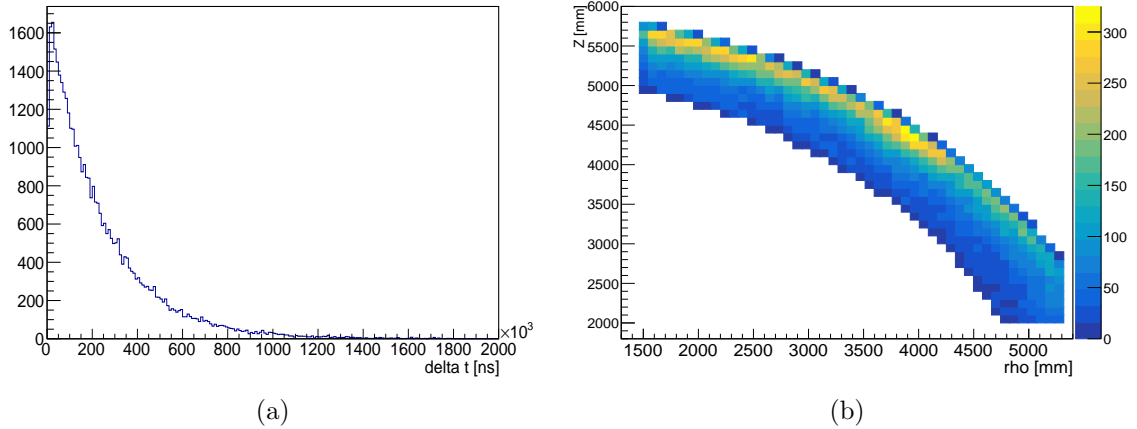

(a)

(b)

Figure 7.12: (a) shows the time difference between the tagged BiPo events for 3 months of partial-fill data. (b) shows the region of interest for 2.6 MeV signal from ^{208}Tl, and the reconstructed position of the events after removing the BiPos.

Figure 7.13 shows the `Nhits` distribution of the events within the region of interest of 2.6 MeV γ peak after removing all the tagged ^{214}BiPo events. The peak is identified in the partial-fill data, and the mean `Nhits` is estimated to be about 756 Nhits ±26 from a Gaussian fit. The identified 2.6 MeV γ peak is consistent with the global calibration curve from partial-fill calibration data shown in figure 7.14 [88]. The 2.6 MeV peak from a set of partial-fill run-by-run MC is found to appear about 580

141

Nhits. This discrepancy is expected and observed from other sources before tuning the partial-fill optics.

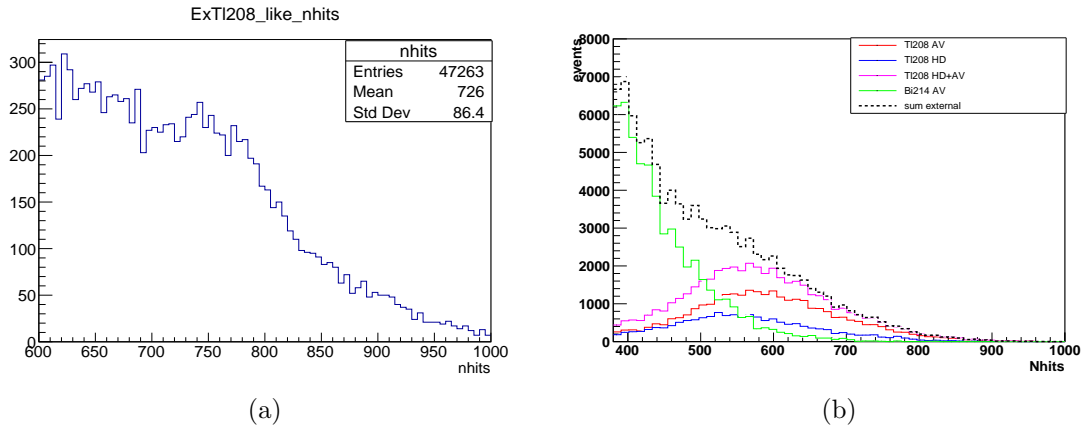(a)   (b)

Figure 7.13: The Nhits distribution in partial-fill (^{208}Tl-like) after removing the BiPo events is shown on the left (a). A Set of MC simulations for the dominant sources of external γ's is shown on the right (b).
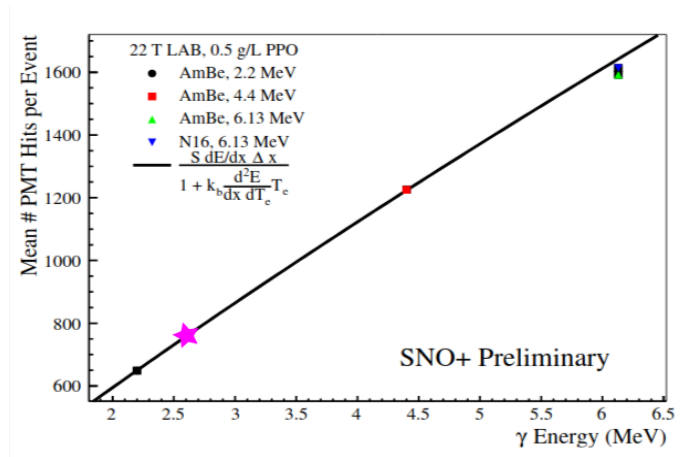
Figure 7.14: The global calibration curve for partial-fill calibration data (^{16}N and AmBe). The pink data point is the fit value from the identified 2.6 MeV ^{208}Tl peak.

7.4.1 ^{208}Tl from Hold Down Ropes

One of the significant sources of external γ's comes from the Hold-down and Hold-up ropes. In addition, these γ's have a higher chance to penetrate deeper into the fiducial volume due to their close proximity. Therefore, it is crucial to study the backgrounds from the ropes, and determine their rates.
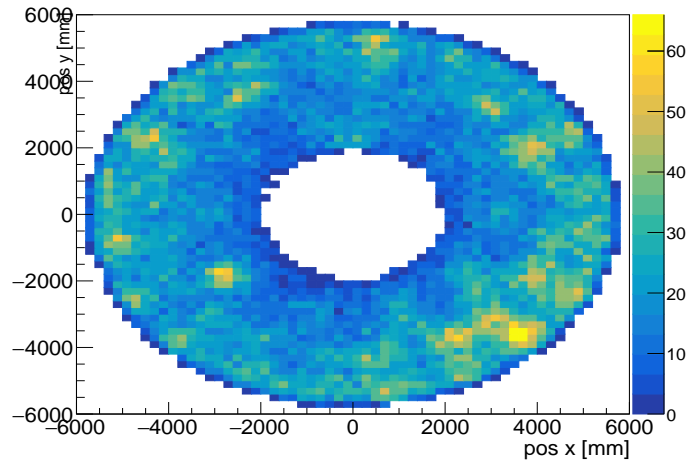
(a)
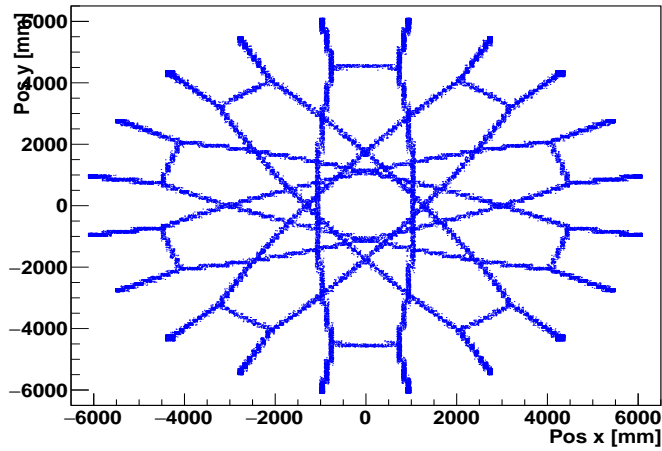
(b)
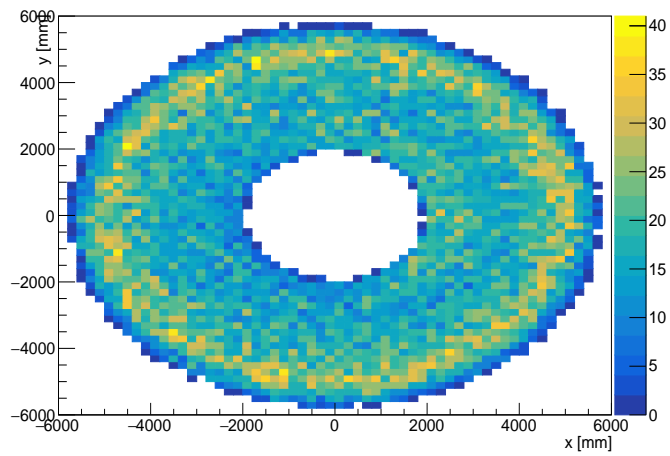
(c)

Figure 7.15: The reconstructed position $(x-y)$ of the events above 600 Nhits after removing the tagged ^{214}BiPo events (a), the true position of the hold-down ropes from MC(b), and the reconstructed position $(x-y)$ of the tagged ^{214}Bi in partial-fill (c).

The γ's from HD ropes are expected to contribute up to about 35% of the external ^{208}Tl signal in scintillator (see table 7.1). The rates of γ's from HU ropes are expected to be an order of magnitude smaller than HD ropes since they are older, and the major portion of their radioactive elements have decayed away. This analysis focuses on determining the level of external ^{208}Tl from HD ropes, and assumes the HU contribution to be negligible. The basic cuts used in this analysis, for both partial-fill data and the generated run-by-run MC, are presented below:

- Energy > 2.6 MeV (MC) (`Nhits`>756 in partial-fill data)

- $R > 5$m

- $0.8 < Z < 3$m

In order to avoid the lower energy γ's from other sources such as ^{40}K, only events with energies greater than 2.6 MeV were selected. Since the ropes are localized sources compared to the other sources such as the AV, they will be more evident in the reconstructed position of the events, for instance figure 7.15 (a) shows the reconstructed position on the $x-y$ plane of the events in partial-fill after removing the tagged ^{214}BiPo. Figure 7.15 (b) shows the true position of the HD down ropes on the $x-y$ plane, and can help identifying the hot spots around the ropes in data. Finally, the reconstructed position of tagged ^{214}Bi is shown in figure 7.15, and as expected they seem to be randomly distributed.

(a)   (b)
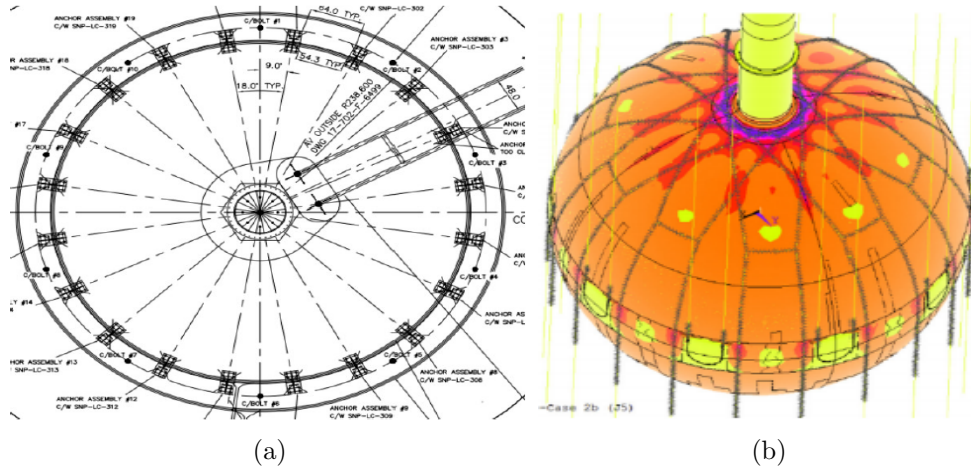
Figure 7.16: (a) shows a top-view drawing of the position of Hold-down ropes, and (b) shows schematics of HD system, taken from [61].

There are 20 HD ropes (10 pairs), and each rope is expected to be separated from the adjacent rope by $18°$ in terms of azimuthal angle ϕ, as demonstrated in figure 7.16. In addition, the angular (ϕ) distribution of the partial-fill data after removing ^{214}BiPo were shown in figure 7.17 (b), in which 20 distinct peaks can be identified. One can suggest a method to isolate the γ's from the ropes from the other events, and furthermore determine their background rates [148], taking advantage of their positional/angular symmetries.

(a)   (b)

Figure 7.17: Azimuthal angle distribution of the tagged ^{214}BiPo (a), and all the events after removing ^{214}Bi (b) where 20 peaks can be identified.

In order to isolate the γ's from the ropes, I have used a method known as *stacking*

145

method. In this method the azimuthal distribution is divided into 18° segments with a rope at the center of the interval (9°). The ev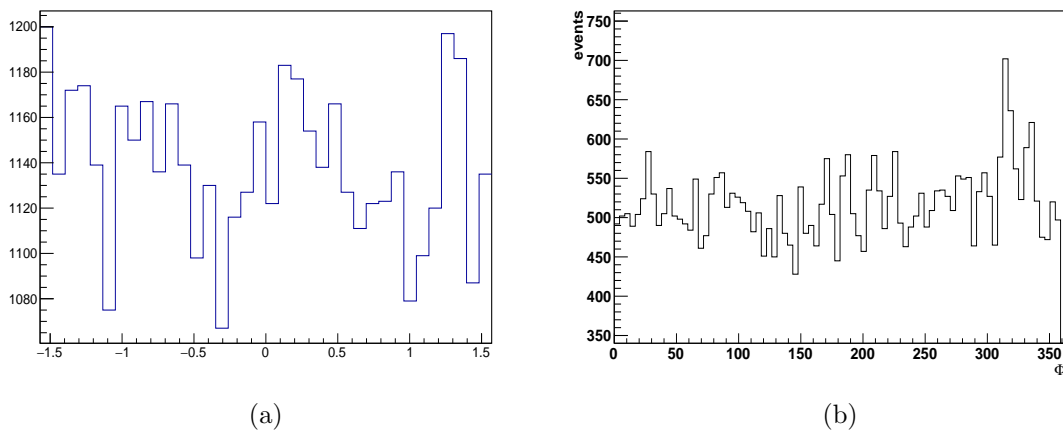ents within the segments can be summed up together and plotted in the range of 0-18° instead of the full azimuthal range (-180°, 180°). Therefore, the γ's from the ropes are expected to form a peak at about 9° in the stacking angular distribution, whereas all the other isotropic sources would make a flat distribution.

(a)   (b)
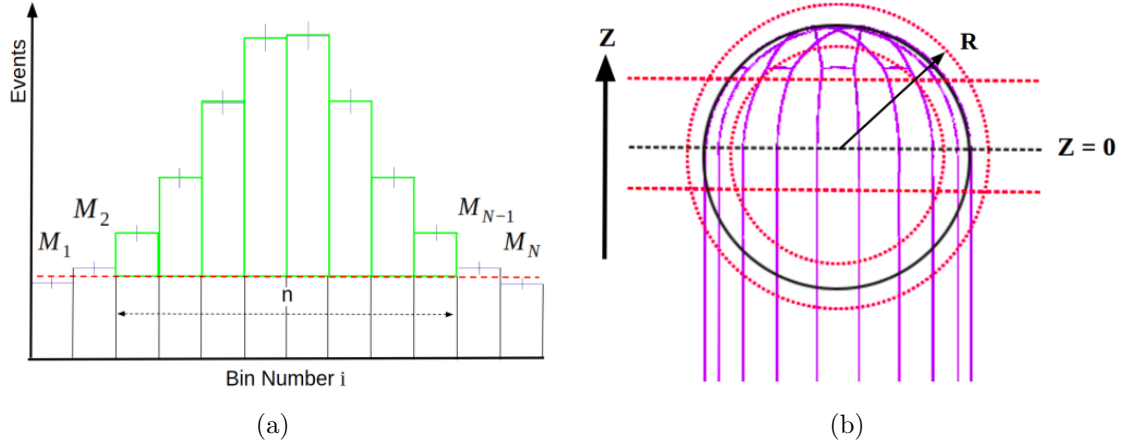
Figure 7.18: Stacked up azimuthal angle distribution of the events (a). The peak integral is shown in green. The selected region of interest for rope analysis is shown in (b), taken from [148].

The peak integral can be calculated by removing the events below the baseline, as demonstrated in figure 7.18. The baseline can be estimated by averaging the bin height of the two minimum bins from both sides. Therefore the peak integral can be calculated as follows:

$$A_{peak} = X - \frac{n}{2}\left(\frac{M_1 + M_2}{2} + \frac{M_{N-1} + M_N}{2}\right) \tag{7.1}$$

where X is the total number events in n bins, n is the number of bins across which the integral is calculated, and N is the total number of bins across ϕ. The peak integral can indicate the relative rate of γ's from the ropes. Assuming that the peak integral is a normal distribution, the standard deviation of A_{peak} can be written as follows:

$$\sigma_A = \sqrt{X - (\frac{n}{2})^2 (\frac{M_1 + M_2}{2^2} + \frac{M_{N-1} + M_N}{2^2})} \qquad (7.2)$$

Figure 7.19 shows the stacked up ϕ distribution of each month during the partial-fill along with their live-times.
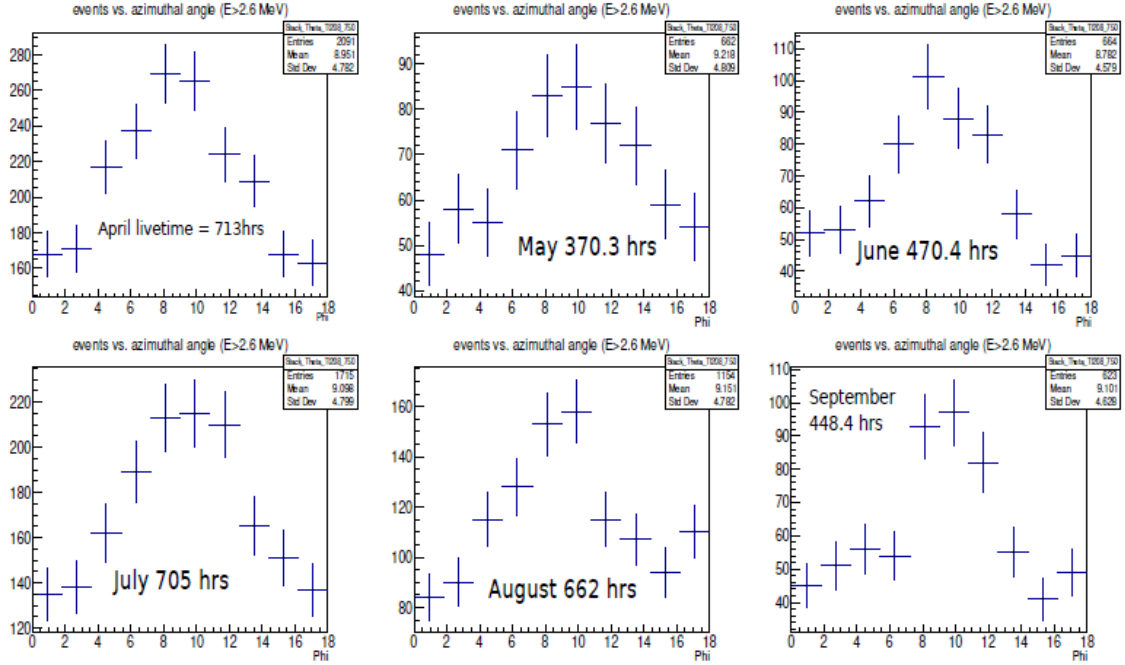
Figure 7.19: Stacked up ϕ distribution of events after removing tagged ^{214}Bi in partial-fill.

Furthermore, a set of run-by-run MC was generated and scaled up to the expected rate of ^{208}Tl from the HD ropes [110]. The peak integral from the MC is calculated, and the ratio between the peak integrals $\frac{A_{data}}{A_{MC}}$ for each month is presented in figure 7.20. The average ratio found to be **0.31±0.05**. Moreover, the level of γ's from the HD ropes has been measured during water phase by Iwan Morton-Blake [148], and the average ratio of peak integrals found to be about 0.29±0.03 which is consistent with the partial-fill measurements. Figure 7.20 (b) shows the measured ratio from the water phase data for various energy regions.
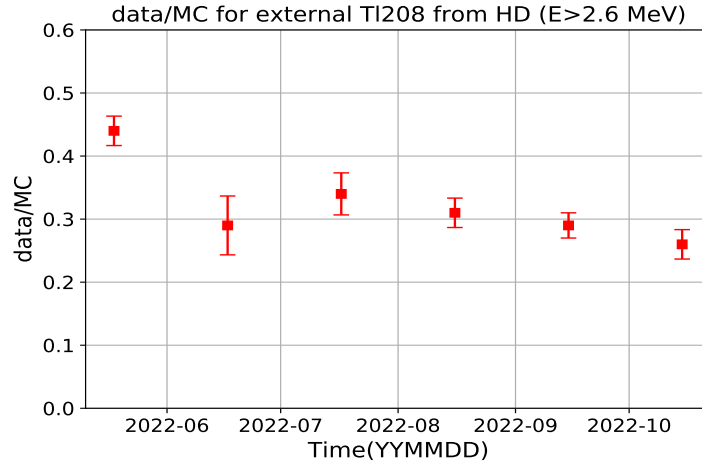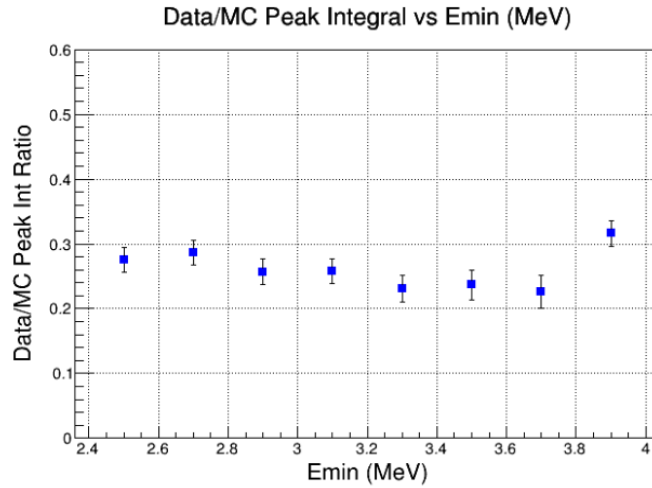
Figure 7.20: (a) The ratio of peak integrals ($\frac{A_{data}}{A_{MC}}$) for 6 months during the partial-fill for events with energies higher than 2.6 MeV. (b) The ratio of peak integrals vs. energy measured during the water phase by [148].

7.5   Summary

The external γ's from ^{208}Tl and ^{214}Bi are discussed in detail, and the performance of 0ν timing and topological classifiers are investigated in section 7.3. Furthermore, it was demonstrated that the supervised learning methods can be utilised to optimize the classification and improve their performance for distinguishing solar ν signal from the external γ's. For this purpose, I have used `ROOT`'s `TMVA` package. Furthermore, the 2.6 MeV γ peak from external ^{208}Tl is identified in partial-fill data. The mean

`Nhits` is estimated to be about 756 ± 26 from a Gaussian fit. Finally, the γ's from HD ropes is isolated using the angular symmetry of the ropes, and the background level is estimated to be 0.31 ± 0.05 of what was originally expected. This result is consistent with a similar type of analysis performed in water phase. This analysis is discussed in section 7.4.1.

Chapter 8: Summary and Conclusions

This thesis has focused on two major research topics carried out by the author: I) chapter 5 is devoted to the detector calibration with the radioactive ^{16}N source, and II) chapter 6 and 7 focus on the background analyses for the SNO+ experiment. Chapter 6 describes a set of analysis to estimate the effective attenuation length of the detector using the tagged ^{214}Po events in scintillator, and chapter 7 focuses on the identification and rejection of the external backgrounds .

SNO+ has used the ^{16}N source as the primary energy calibration source in water phase, see section 5.2. The tagged events from the 6.1 MeV ^{16}N γ's in water, were used to calibrate the event reconstruction model and determine the uncertainties, discussed in section 5.3. The ^{16}N hardware is not designed to be deployed into the scintillator volume since it does not meet the radio-purity requirements. However, the source was deployed externally throughout the filling process. Aside from certain internal background signals such as the ^{210}Po and the tagged coincident ^{214}BiPo which were used for various calibration purposes, the ^{16}N and the AmBe source (see section 2.5.2) were the main two radioactive calibration sources used to calibrate the detector model, while commissioning the scintillator-friendly sources. The ^{16}N scintillator data were used for various analyses. The scintillator light yield was studied using the 6.1 and 7.1 MeV, and 4.4, 2.2 MeV γ's from the ^{16}N and AmBe source respectively, described in section 5.4. Furthermore, the position dependency of the light yield was investigated using the ^{16}N data and a set of run-by-run `RAT` simulated data, described in section 5.4.3. Moreover, the scintillation emission timing is stud-

ied and characterised using the calibration data with different PPO concentrations, discussed in [136]. In addition, the possibility of extracting the Cherenkov signal in scintillator with low PPO concentrations[1] was studied, described in section 5.4.5. I was able to identify the Cherenkov signal and extract the event directionality information through looking at the prompt PMT hit patterns from the tagged γ's.

One of the major backgrounds within the energy region of interest of $0\nu\beta\beta$ signal (~ 2.5 MeV) are the β-γ decays from ^{214}Bi followed by the quenched α-decay signal from ^{214}Po. These coincident ^{214}BiPo events can be tagged with high efficiencies ($\sim99\%$) through the delayed coincidence tagging technique, described in section 6.2. The tagged ^{214}BiPo events were used for several analyses in the scintillator such as the timing studies, the light yield and α-quenching analysis, the reconstructions verification, and the detector's optics analysis. Inspired by the other collaborator's work, I have developed a toy model that was used to fit the tagged ^{214}Po events in full-fill, and estimate the effective attenuation length in scintillator phase. The effective attenuation length found to be 7547±928 [mm], which is consistent with the other measurements [144]. The model and the analysis are described in section 6.4.

Chapter 7 is devoted to the analysis of the external backgrounds in SNO+; the γ's created in ^{208}Tl and ^{214}Bi decays outside of the AV, which can potentially propagate into the scintillator volume, and significantly contribute to the backgrounds for $0\nu\beta\beta$ and the solar neutrinos. In order to distinguish the external γ's from the $0\nu\beta\beta$ signal, a set of timing and topological classifiers is developed. These classifiers are optimised to give the best separation based on the PMT hit patterns and time residuals of the simulated 0ν signal and the external ^{208}Tl γ's, discussed in section 3.5 and section 7.3. The performance of the 0ν-classifiers are investigated for a set of simulated solar neutrino events together with simulated background γ's from ^{214}Bi and ^{208}Tl. As expected, The classifiers found to be effective for energies above 1.5

---

[1] The ^{16}N data for 0.18 g/L and 0.33 g/L PPO+LAB were used for this analysis.

MeV, showing 54% rejection of the externals, and 4% sacrifice level for the solar ν signals. Furthermore, I have demonstrated that the classification performance for solar ν can be improved using supervised learning methods (`TMVA`). The (`TMVA`) was used to optimise the cuts on the 0ν timing and topological classifiers. This analysis is described in section 7.3.1. The second half of this chapter focuses on identifying the external 2.6 MeV γ's from ^{208}Tl, and estimating the level of external ^{208}Tl from hold-down ropes. The 2.6 MeV peak is identified after tagging and removing the ^{214}Bi in partial-fill data. Moreover, the level of external γ's from the HD ropes are estimated in partial-fill taking advantage of their angular symmetry. The result shows about 0.31±0.5 of the expected rate [110], which is consistent with previous measurements in water phase [74].

Appendix A: The Rope System Monitoring and Creep Measurements

A.1 The Hold-down Ropes

SNO+ uses the hold-down rope system to counteract 1.25 MN of buoyant force on the AV due to the lower density of LAB (863.0 kg/m^3) than the surrounding UPW (999.7 kg/m^3). The design of the hold-down rope system is shown in figure A.1 which consists of 20 ropes (10 pairs) forming a net around the neck. The net system consists of 5 sub-nets which are composed of 2 ropes passing on either sides of the neck [61]. All the ropes are anchored to the bottom of the cavity, and every rope has a turnbuckle and an underwater load-cell (see figure A.1). Each load-cell has the measurement capacity of 89kN, and are used to monitor the load on the rope system. Figure A.2 shows the loads on the hold-down and hold-up ropes throughout the scintillator fill. We have observed that filling about 50 tonnes of LAB takes roughly 6800 lbs off the HU ropes. The underwater load-cells are infamous for failure as a few of them have already stopped working, and it is almost impossible to replace them while the cavity is full. However, since each rope has a complimentary partner, the load on the ropes with failed load-cells can be monitored through their complementary partners. Tensylon$^{\text{TM}}$ (a high performance polyethylene fiber) [149] is chosen for the SNO+ rope system, replacing the old Vectran used in SNO. Tensylon has much higher radio-
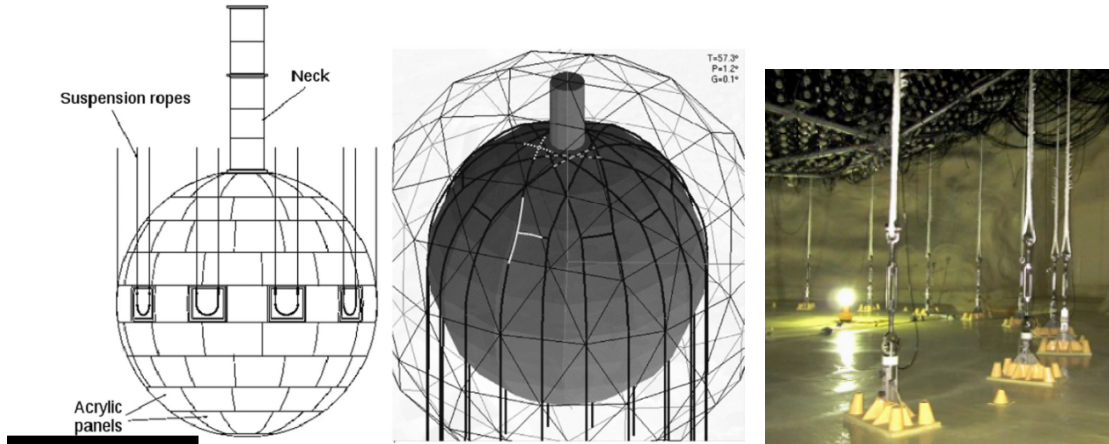
Figure A.1: Schematic of the Hold-up ropes (left) and Hold-down ropes (middle). The Hold-down ropes are anchored to the bottom of the cavity (right).

purity, for instance Tensylon has about two orders of magnitude less ^{40}K compared to Vectran. Furthermore, Tensylon has good mechanical properties such as low creep and good strength [61]. The ropes were fabricated by Yale Cordage in a clean environment. In order to study and monitor the changes in the mechanical properties of the rope, a 45 m long sample of Tensylon fiber kept under a constant load and has been immersed in a tank filled with UPW. Every 6 months a short sample is cut, tested for breaking strength, and compared with a dry fibre sample. This long term break-test is explained in section A.3.

A.2 Creep Measurements using Neck Sense Ropes

Tensylon is a low creep fibre, however not as low as Vectran. Bench-top measurements show about 1% creep per year [150] at 10°C. As it can be seen in figure A.3, half of the elongation takes place within the first few hours (first stage of elongation). Also some company measurements suggest about 0.5% creep per year with 20% of the breaking point load on the rope [149].

Furthermore, the stretch in the upward Tensylon ropes have been measured through *in-situ* measurements in 2012 [149] before filling the cavity. The rope elongation was measured using the equator monitoring system. The equator monitoring system is a
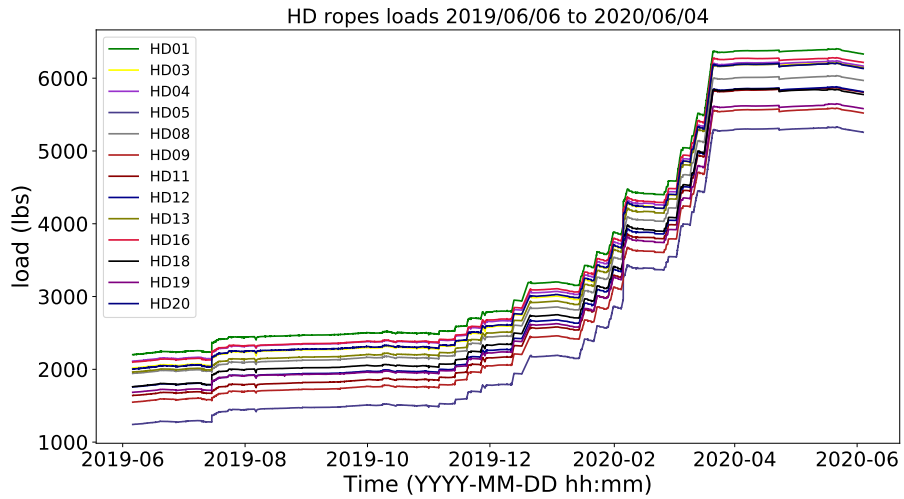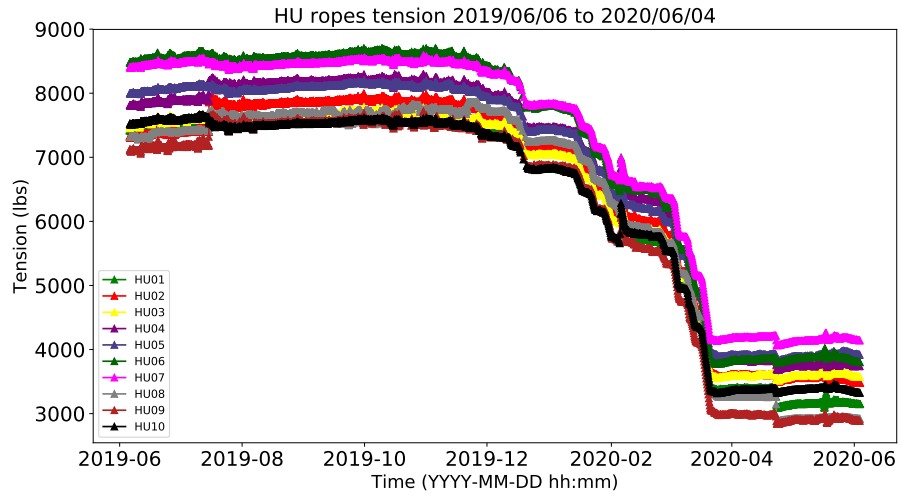
Figure A.2: The load on the HU ropes (top) and the HD ropes (bottom) throughout the scintillator-fill before the partial-fill.

mechanical system that consists of ropes that are attached to the AV equator on one end, and on the other end they run into potentiometer boxes on the deck. The system registers displacements of the AV equator [151] through the potentiometers. Three components of rope elongation; Hook's type stretch, short term creep, and long term creep have been studied and found to be consistent with other external measurements. Furthermore the temperature dependency of the creep rate was investigated [149]. The creep rate for upward Tensylon ropes is estimated for two periods using the equator monitoring data. The precise data for March-May 2012 shows 5.2e-7/hour

Figure A.3: Creep for Dyneema measured at 10°C taken from [150].

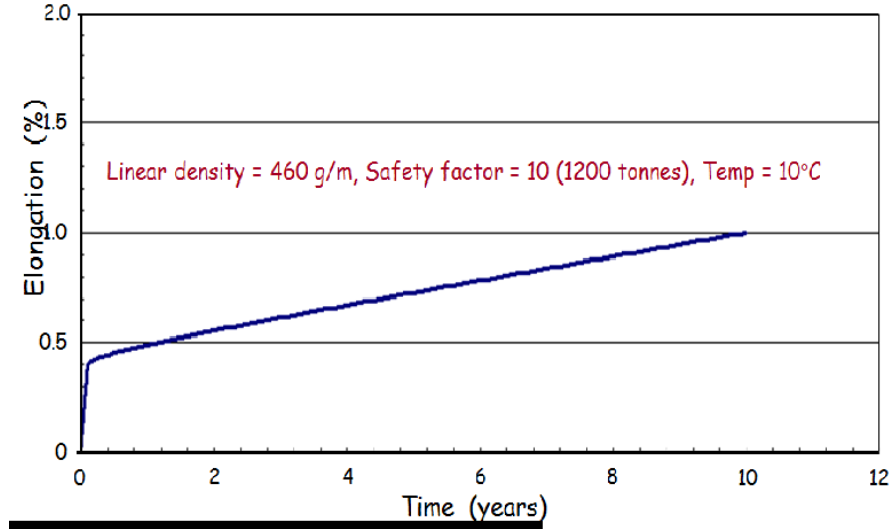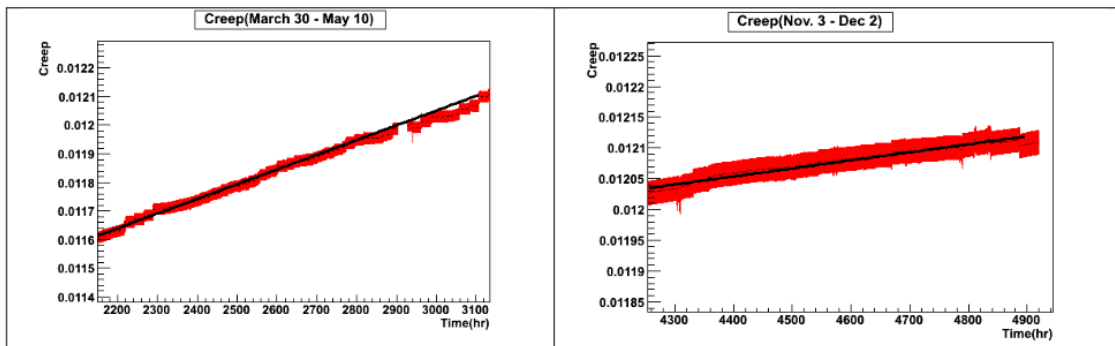Figure A.4: The *in-situ* measurements of Hold-up rope elongations using equator monitor's data in 2012, for the period of March-May (left) and November-October (right) [149]
.

creep rate which translates to 0.45%/year with the average temperature of 22.5°C, consistent with the external measurements. In addition, the creep rate was measured to be 1.31($\pm$0.15)e-7/hour (0.115$\pm$0.013 % /year) for October-November period at 20.4 °C. Figure **??** shows the rope elongations for the two time periods. The models suggest that the temperature difference between two periods can account for about 35%-40% of the creep decrease. Additionally, there is a time-dependent factor to the creep rate that can explain the discrepancy. In order to investigate the temperature dependency of the creep rate, the elongation was studied for a time-period when the chillers were shut down and the temperature had gone up to 31.3°C. The creep rate

was found to be about 3.0e-6/hour or 2.6%/year. Comparing different time-periods shows that the creep rate would increase by a factor of ~ 1.3 for every degree of temperature rise.

A.2.1 Creep measurements during Partial-fill

As mentioned previously, scintillator filling was interrupted for a time period between April and October 2020 due to the pandemic, therefore the load on the rope system remained relatively unchanged. Figure A.6 shows the load on the Hold-up (top), and Hold-down ropes (bottom) within this time period. This period provided a good opportunity to study the long-term creep rate of the ropes using the elongation data. In addition to the equator monitoring system, the vertical displacements of the AV[1]can be monitored through a mechanical system known as the Neck Sense Ropes (NSR), which consists of 7 potentiometers that are attached to the top of the neck [117]. Furthermore, the measurements from a laser level in the DCR have been used to verify the vertical offset from the NSR [151]. Figure A.5 shows the vertical displacements of the AV neck with respect to the center of the PSUP. As mentioned, tempera-
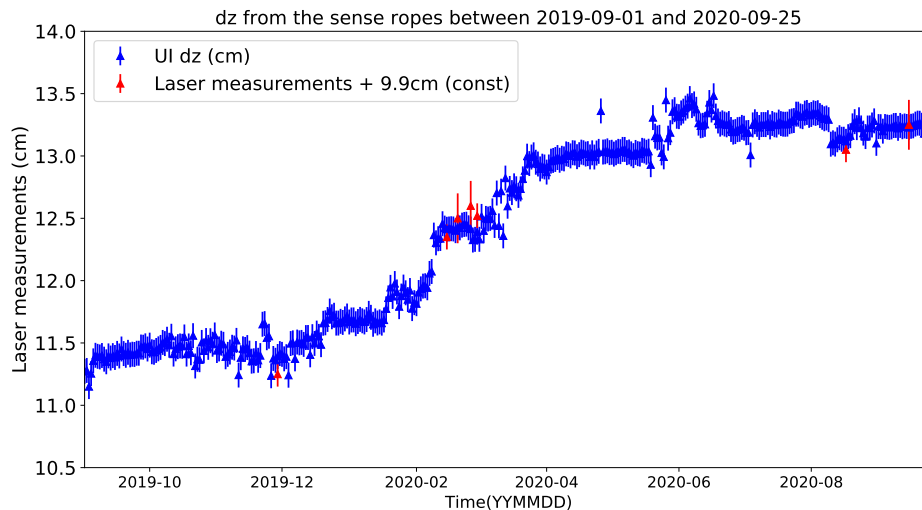

Figure A.5: The AV vertical position (cm) in PSUP coordinates from sense ropes (blue), and the laser level measurements (red). The 0 would be when the center of the AV is at the center of PSUP.

---

[1]Assuming that the AV is a rigid body and its deformation is negligible.
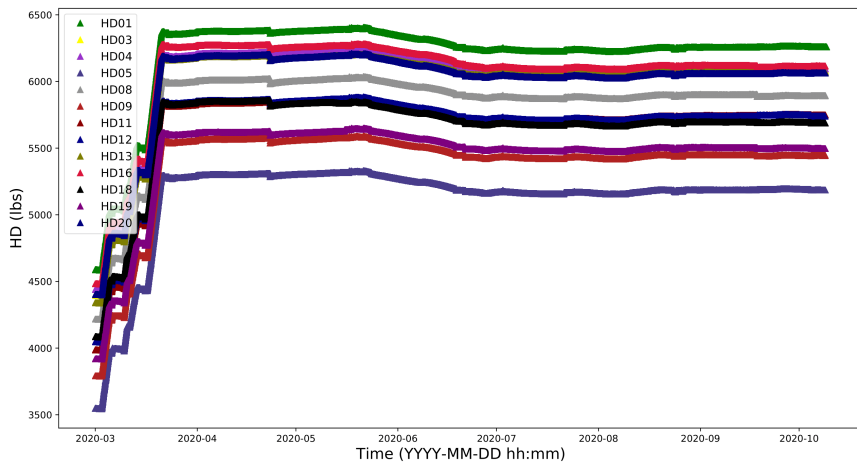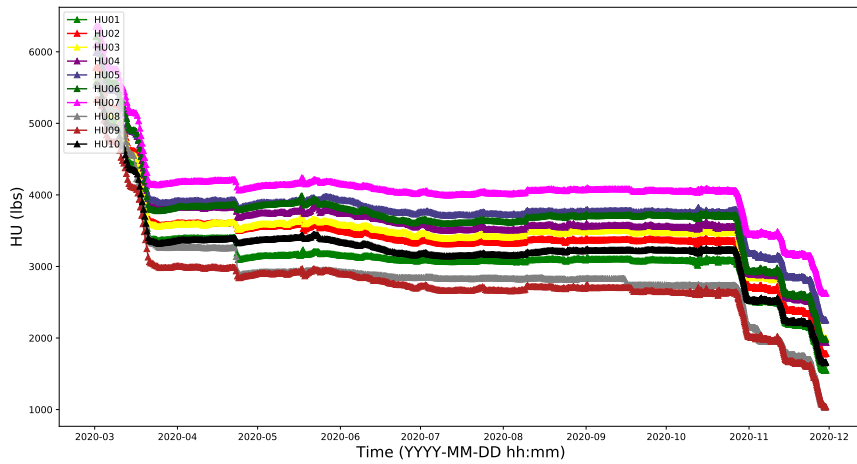
Figure A.6: The load on the HU ropes (top) and the HD ropes (bottom) in partial-fill.

ture has a large effect on the creep rates of Tensylon fibres. It has been observed that the creep would increase by a factor of 1.2 to 2 for every degree Celsius [149]. SNO+ uses 30 under water sensors to monitor the temperature in the cavity. As it can be seen from figure A.7(top) the sensors are positioned in various heights inside the cavity. In addition, figure A.7 (bottom) shows the average temperature of the sensors below the neck for the partial-fill period. In order to minimise the effect of temperature, I have selected the time period between 2020/08/10 and 2020/09/10 in which the temperature has remained relatively constant. Figure A.8 (bottom) shows the elongation within this period, and the creep rate was estimated to be **0.89(±**

0.03)e-7/hour or **2.14e-6/day** (0.078%/year). The average temperature within this period found to be 13.2° C ±0.6 calculated from 14 sensors. Furthermore, the average creep rate was found to be **0.90(±0.03)e-7/hour** or **2.17e-6/day** for the time period of 2020/03/31 − 2020/04/27 in which the average temperature was found to be 13.3°C ± 0.8.
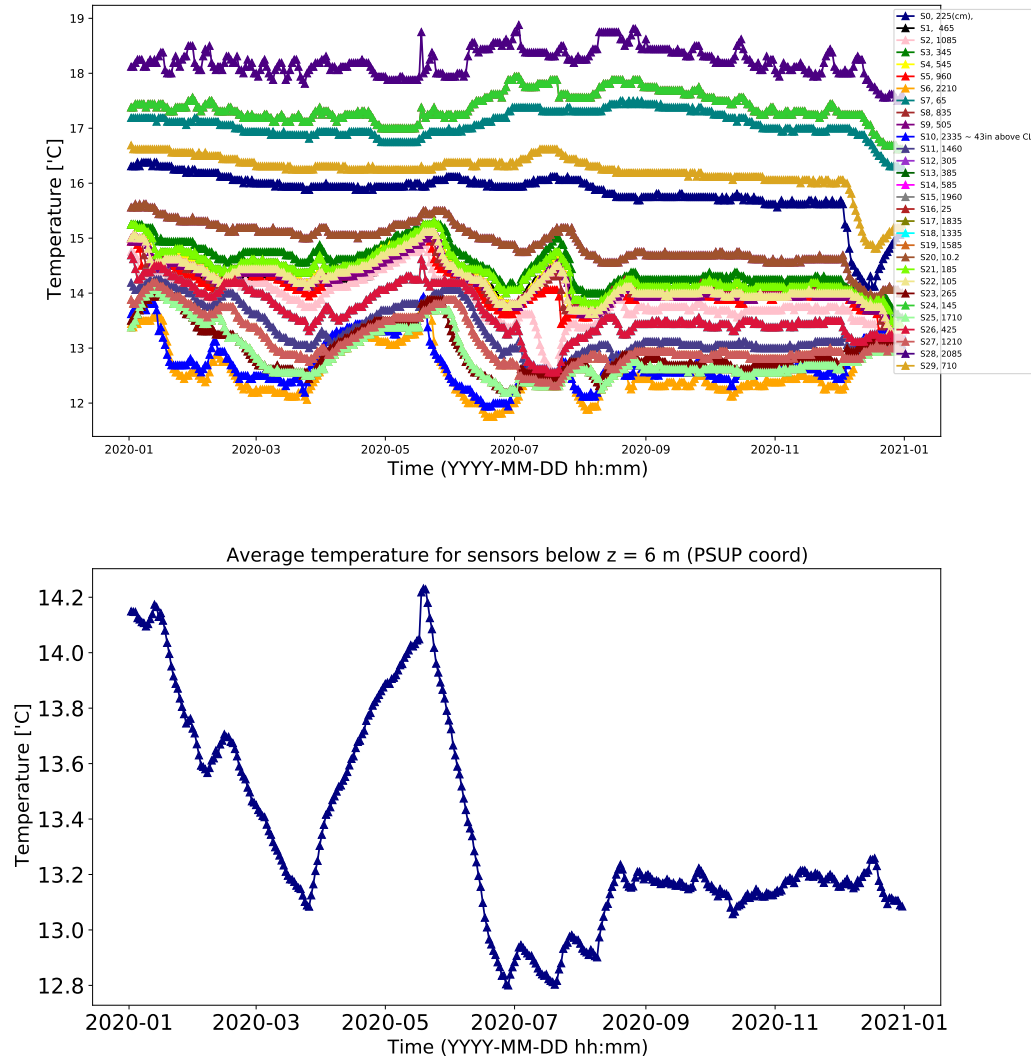
Figure A.7: Cavity temperature from 30 underwater sensors in the cavity (top). The average temperature inside the cavity throughout 2020 (bottom).

As it can be seen there has been a period in May 2020 when the average temperature had risen up to about 14.2°C. The best fit that can be achieved over the elongation

data for this time-period shows the creep rate of **5.2e-7($\pm$1.6)/hour**. Even though the effect of temperature is evident in this case, it is hard to determine the temperature dependency due to the large uncertainties.
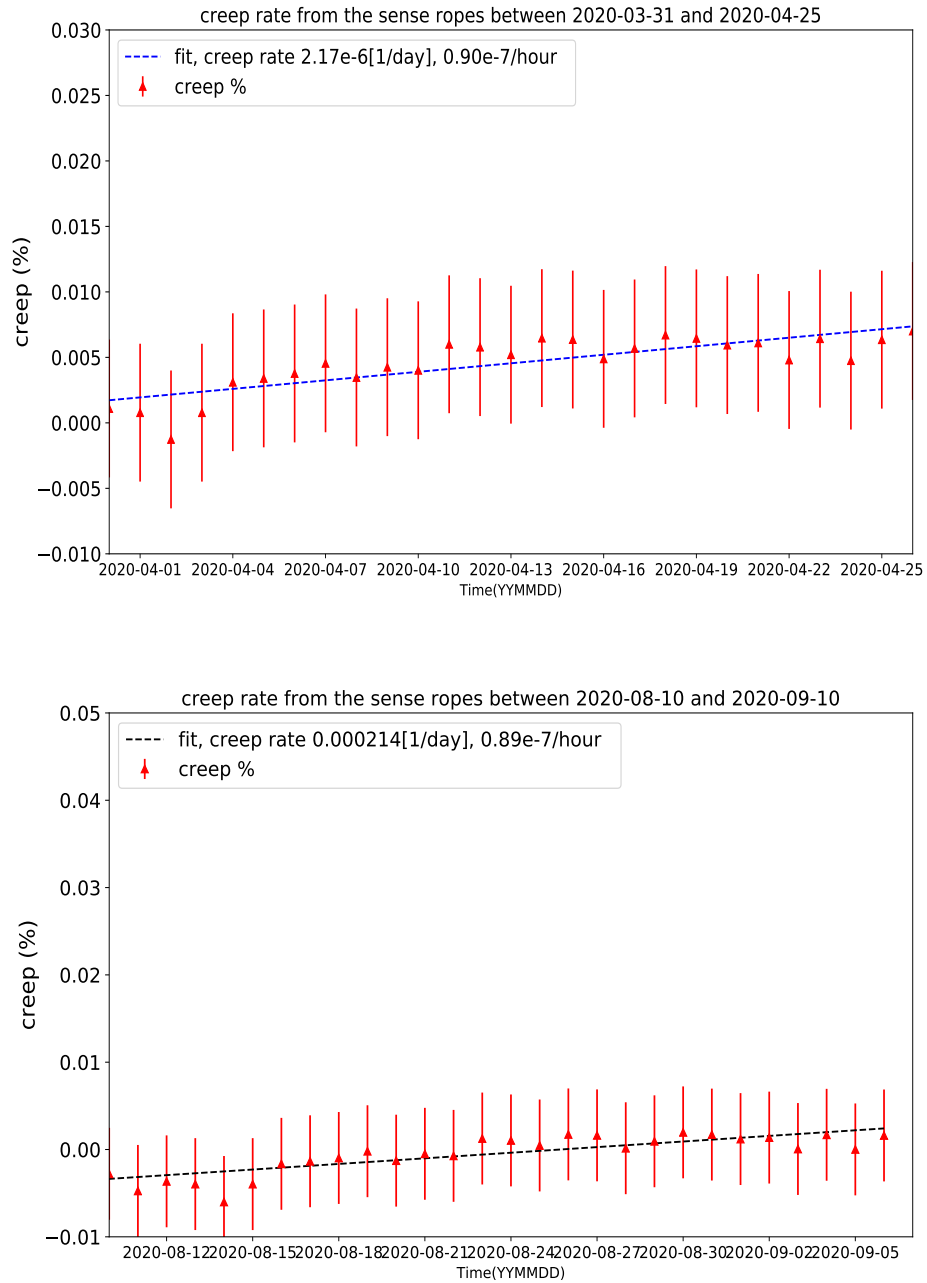
Figure A.8: The elongations from NSR for 2020/04/01 - 2020/04/27 (top), and 2020/08/10-2020/09/10 (bottom).

A.3 Long-Term Test of Tensylon Fibres

Inspection of the ropes, under water load-cells and turnbuckles is not possible while the cavity is full. In order to study the long term effect of UPW, SNO+ has been performing long-term stability tests by keeping the components in a similar working condition inside a UPW tank [152]. This section describes the method that SNO+ uses to frequently test, and monitor the long-term behaviour of Tensylon in UPW. I have been actively involved in this project, performing the long-term tests on Tensylon fibre known as the "break-test".

In order to monitor the effect of UPW on Tensylon, a 45 m long fibre is coiled around a rig (see figure A.9), and kept in a cylindrical soaking tank, shown in figure A.9. The fibre is kept under 7.7 lbs load which is roughly 20% of the breaking point. Every 6 months, up to 3 samples of fibre, known as wet samples, were cut and break-tested using a dedicated jig that was designed in University of Alberta [153]. At the same time, 3 samples of the "dry fibre" are break-tested as well, and the results from the wet and dry samples are compared to determine if the UPW and long-term load had any effect on the properties of the fibre. As it is shown in figure A.10, the test jig consists of an aluminum frame that is designed to allow for changing the distance between the top bar of the frame and the lever which the fibre is spanned. There is a dedicated load-cell (see figure A.10(right)) that records the load on the fibre, and a screw to adjust the load by changing the distance. In addition, a dedicated dial indicator is used to measure the elongation of the fibre throughout the test. There is a FPGA board, and an interface to process and record the data from the load-cell and the dial indicator. The load on the sample is increased by 10 lbs every 1.5 minutes throughout the break test until the fibre breaks. The fibre is expected to break within 30-35 lbs range. Figure A.11 shows the load, and elongation for two samples throughout the test.

The long-term break test has been performed on wet and dry samples every 6 months since 2015. The summary of the results is shown in figure A.12. There is no observable
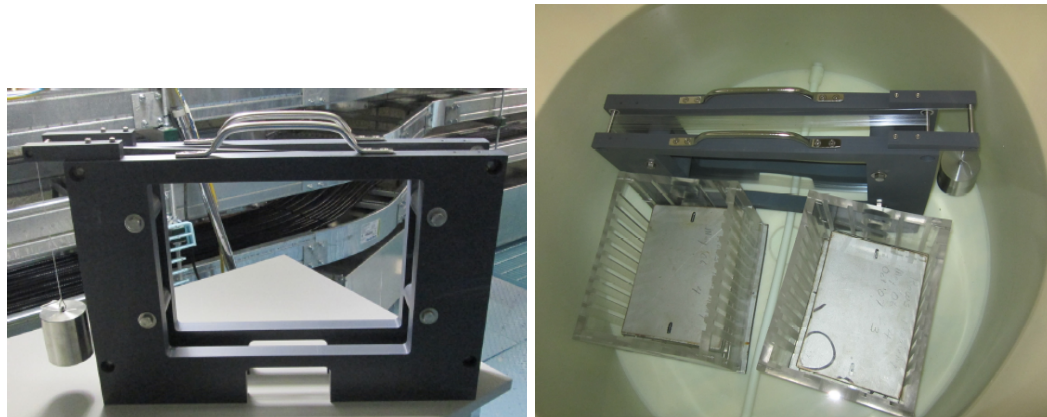
Figure A.9: A 45m long Tensylon fibre is coiled around a rig (left) and kept under a constant load in a soaking tank (right).
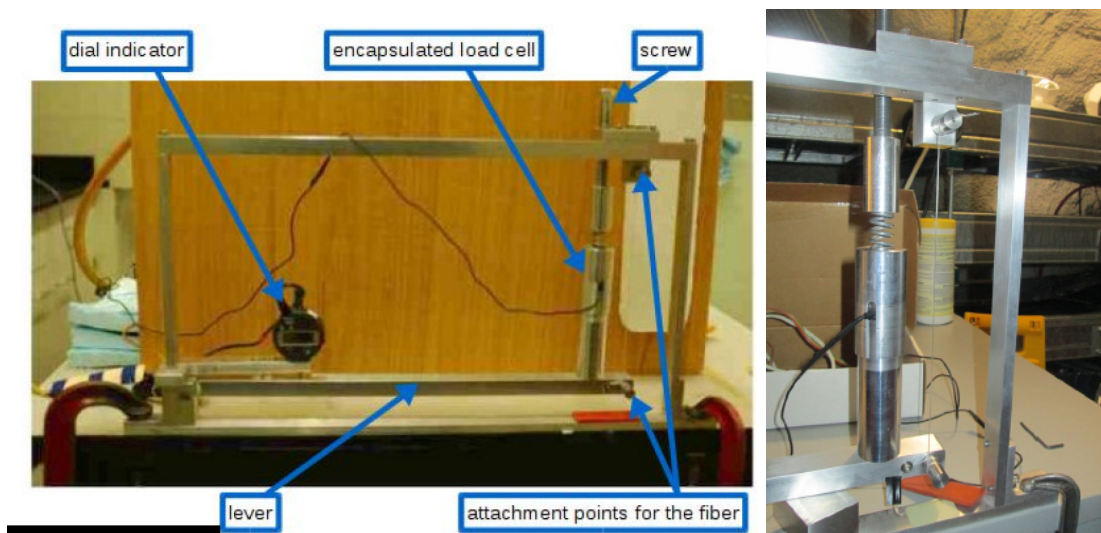
Figure A.10: The test jig used to break-test the Tensylon fibre. The load-cell on the jig is shown on the right.

evidence that fibre's strength has been affected by UPW exposure or the long-term load.
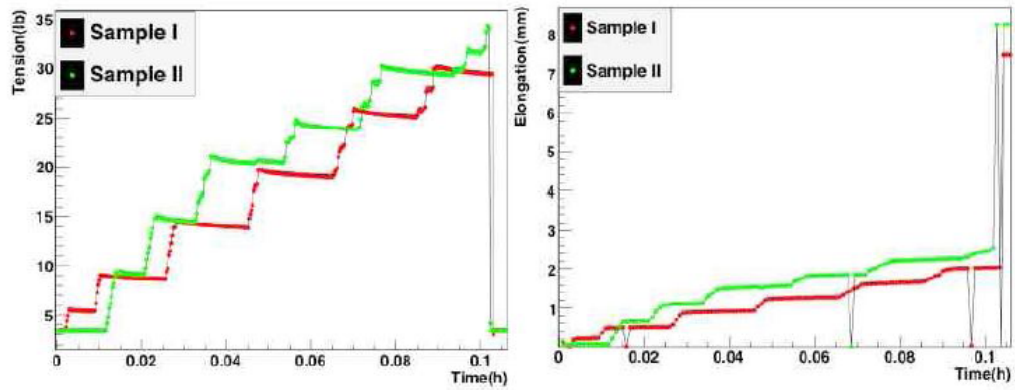
Figure A.11: The load (lbs) on two fibre sample (left), and the elongation (mm) (right).
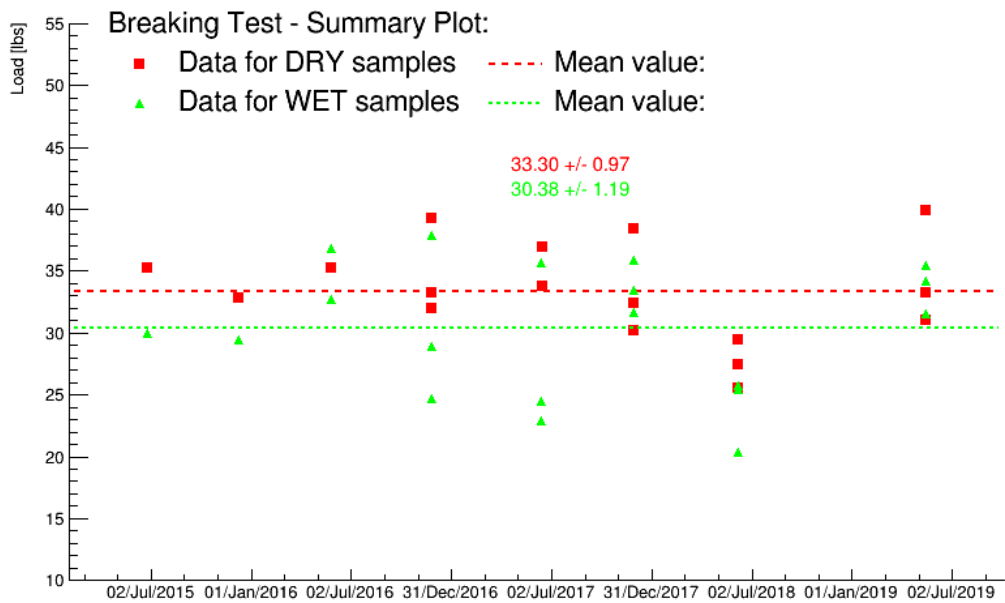
Figure A.12: The maximum applied tension to the samples before the fiber's breaking point for different sets of tests. The results show no effect on the fibre's properties due to UPW exposure.

Appendix B: Leaching Studies of ^{222}Rn Progeny in Scintillator

One problematic class of backgrounds comes from ^{222}Rn daughters diffused into the acrylic surface during the transition time from the SNO experiment when the AV was empty and exposed to the lab air. This class of backgrounds are discussed in section 4.5. ^{222}Rn decays down to ^{210}Pb which has a relatively longer half-life (22.3 years), and therefore would build up on the AV surface. ^{210}Pb decays to ^{210}Bi subsequently. ^{210}Bi with the end point energy of 1.6 MeV can be a direct background for CNO and *pep* solar neutrino measurements. Moreover, ^{210}Bi decays to ^{210}Po which is a source of 5.3 MeV αs. The light yield from α particles is suppressed by about an order of magnitude compared to an electron with the same energy in scintillator [154]. Despite the large quenching of α particles in scintillator, the peak appears to be about 0.4 MeV [134], far above the energy threshold of the experiment. Additionally, the α-particles can go through (α, n) interactions and produce free neutrons that can be captured by atomic nuclei in the detector, and emit 2.2 MeV γs. The 2.2 MeV γs can fall into the energy region of interest for the neutrino-less double beta decay search. These events are discussed in section 4.6. In addition to the surface background events, these isotopes can leach into the scintillator volume and contribute to the internal background.

In order to determine the activity of radon progeny embedded into the acrylic, several *in-situ* measurements have been performed by measuring the radiation on different spots of the acrylic [115, 116], and the average surface activity found to be

$2.4 \pm 0.8\mathrm{Bq/m^2}$ in 2013. In addition, several bench-top measurements have been performed on two spiked acrylic samples to determine the leaching constants of radon daughters into different media, and at different temperatures [155].

As part of my M.Sc. research I have developed a model that can be used to predict the surface activities throughout filling, and furthermore estimate the level of backgrounds from the leaching process [117]. I had the chance to complete the model throughout the first year of my PhD, and also developed a python-based tool that can be used to calculate the level of backgrounds for different filling scenarios, and different temperatures. The model is described in detail in [156]. As the baseline of the leaching calculations, the surface activities of ^{222}Rn daughters is determined as a function of time and position, shown by a density function $\sigma(z, t)$. For instance, figure B.1 shows the surface activities of ^{210}Pb for different segments along the z axis between 2014 and 2020. Every solid line represents the activity of a horizontal ring-shaped strip with $\delta z = 10$cm.
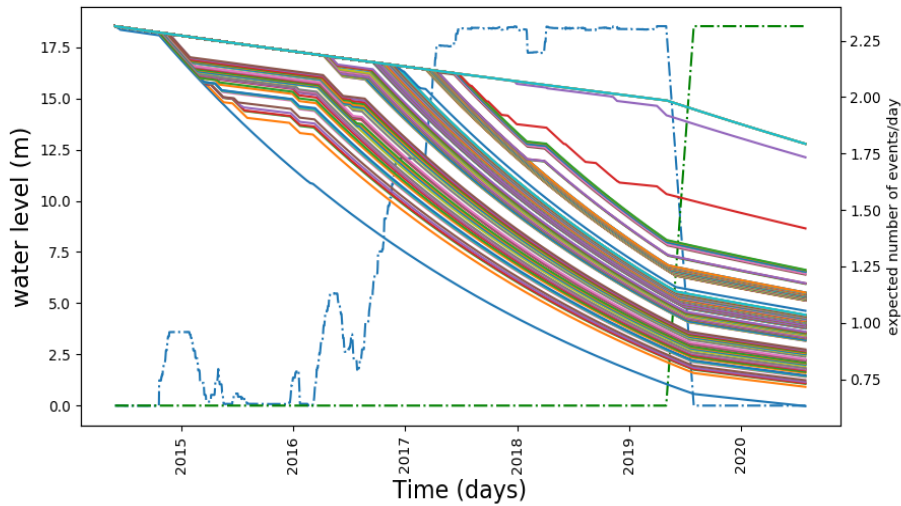
Figure B.1: The surface activities of ^{210}Pb for different levels (solid lines) between 2014 and 2020 is shown in the plot. Every solid line represents the activity of a ring-shaped strip with thickness of 10cm on the acrylic surface. The dashed blue line represents the water levels inside the AV and the green line is the scintillator level. The filling process is assumed to be taking place over a 6 month period with a constant rate.

165

For this example the filling process is assumed to be taking place over a 6 month time-period with a constant rate. Furthermore, the density function can be used to estimate the amount of activities leached into the detection medium. The leaching constants for each isotope were interpolated using the bench-top measurements data points. In addition, several water assays were performed to measure the activity of ^{210}Pb in the UPW [157, 158]. The measured activities are about 20% to 40% higher compared to the activities predicted by the model, however considering the uncertainties the result is consistent with the model within 1 σ. The extra measured activities can be explained by the other sources of ^{222}Rn such as the lab air.

The ^{210}Po signal has been studied by S. Riccetto in partial-fill data and the quenched α peak is identified around 0.4 MeV in electron equivalent energy [114]. The mean `Nhits` value found to be between 100 and 150 depending on the PPO concentrations. This peak is used to monitor the PPO mixing and the light yield throughout the filling and loading process. Stratification analysis of the peak along the radial axis, and also along the z-axis can give insight into the PPO distribution in the AV. For instance, figure B.2 shows the ^{210}Po Nhits distributions versus z for 7 days in a row. The PPO was added in the first day.
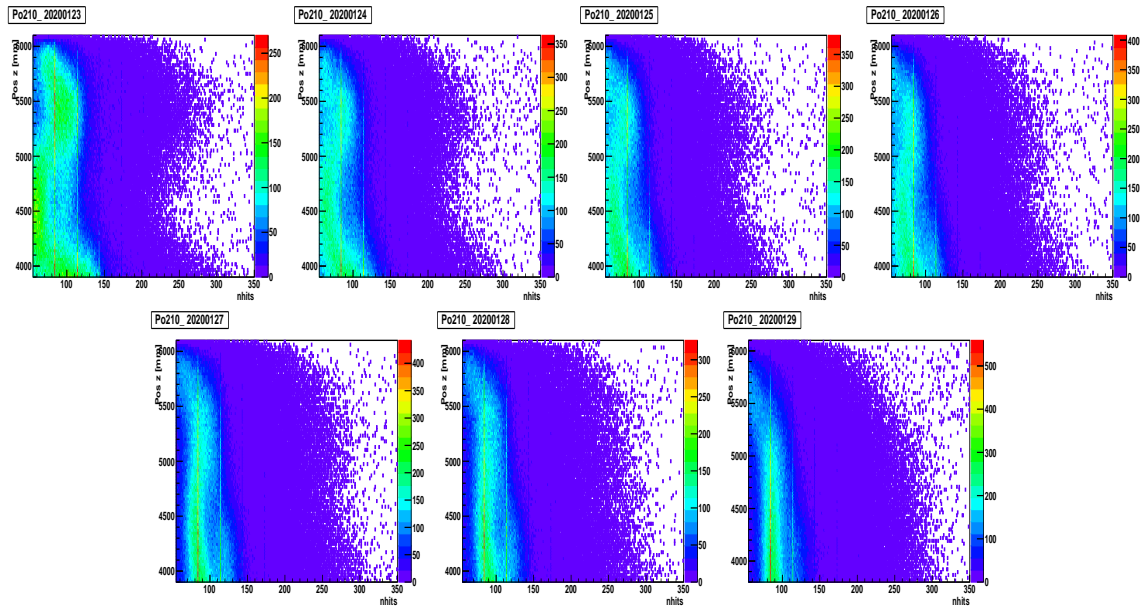
Figure B.2: The ^{210}Pb Nhit distributions along z between April 23rd and the 29th 2019. The PPO was added in the 23rd from the top.

Bibliography

[1] Super-Kamiokande Collaboration. Evidence for oscillation of atmospheric neutrinos. *Phys. Rev. Lett*, 81(1562-1567), 1998.

[2] Q. R. Ahmad et al. Direct evidence for neutrino flavor transformation from Neutral-Current interactions in the Sudbury Neutrino Observatory. *Phys. Rev. Lett. 89, 011301*, 2002.

[3] W. Pauli. Cambridge monogr. part. phys. nucl. phys. cosmol., 14, 122. 2000.

[4] C. Jensen and F. Aaserud. Controversy and consensus: Nuclear beta decay 1911-1934. 2000.

[5] E. Fermi. Versuch einer theorie der β-strahlen. i. *Zeitschrift fur Physik*, 88, 1934.

[6] C. L. Cowan F. Reines. Detection of the free neutrino. *Physical Review, 29: 867*, 1953.

[7] R. Davis. Attempt to detect the antineutrinos from a nuclear reactor by the ^{37}cl$(\bar{\nu}, e^-)$ ^{37}a reaction. *Phys. Rev. Lett.*, 97, 1955.

[8] E. J. Konopinski and H. M. Mahmoud. The universal fermi interaction. *Phys. Rev. Lett.*, 92, 1953.

[9] G. P. S. Occhialini C. M. G. Lattes and C. F. Powell. Observations on the tracks of slow mesons in photographic emulsions. *Nature*, 160, 1947.

[10] K. A. Goulianos L. M. Lederman N. B. Mistry M. Schwartz G. Danby, J. M. Gaillard and J. Steinberger. Observation of high-energy neutrino reactions and the existence of two kinds of neutrinos. *Phys. Rev. Lett.*, 9, 1962.

[11] DONUT collaboration. Observation of tau neutrino interactions. *Phys. Lett. B*, 504, 2001.

[12] C. S. Wu et al. Experimental test of parity conservation in beta decay. *Phys. Rev.*, 105, 1957.

[13] L.M. Lederman R.L. Garwin and M. Weinrich. Observations of the failure of conservation of parity and charge conjugation in meson decays: the magnetic moment of the free muon. *Phys. Rev.*, 105, 1957.

[14] R. P. Feynman and M. Gell-Mann. Theory of the fermi interaction. *Phys. Rev.*, 109, 1958.

[15] S. Weinberg. A model for leptons. *Phys. Rev. Lett.*, 19, 1968.

[16] E. C. G. Sudarshan and R. E. Marshak. Chirality invariance and the universal fermi interaction. *Phys. Rev.*, 109, 1958.

[17] J. J. Sakurai. Mass reversal and weak interactions. (doi:10.1007/BF02781569), 1958.

[18] J. N. Bahcall and R. J. Davis. . solar neutrinos: A scientic puzzle. *Science, 191:264 267*, 1976.

[19] Evelina Arushanova. Development of an 90y calibration source and rejection of pileup backgrounds in the sno+ experiment. *School of Physics and Astronomy Queen Mary University of London*, 2018.

[20] D. S. Harmer R. Davis and K. C. Homan. Search for neutrinos from the sun. *Phys. Rev. Lett.*, 20, 1968.

[21] J. N. Bachall. Solar models: An historical overview. *Int. J. Mod. Phys.*, A. 18, 2003.

[22] Y. Fukuda et al. Solar neutrino data covering solar cycle 22. *Phys. Rev. Lett.*, 77, 1996.

[23] GALLEX collaboration. Results of the whole gallex experiment. *Nuclear Physics B*, 70, 1999.

[24] SAGE collaboration. Solar neutrino flux measurements by the soviet-american gallium experiment (sage) for half the 22 year solar cycle. *J. Exp. Theo. Phys.*, 95, 2002.

[25] Kamiokande collaboration. Observation of a small atmospheric ν_μ/ν_e ratio in kamiokande. *Phys. Lett. B.*, 208, 1992.

[26] R. Becker-Szendy et al. Electron- and muon-neutrino content of the atmospheric flux. *Phys. Rev. D.*, 46, 1992.

[27] Super-Kamiokande collaboration. The super-kamiokande detector. *Nucl. Inst. and Meth.*, 501, 2003.

[28] B. Pontecorvo. Mesonium and anti-mesonium. *Sov. Phys. JETP*, 6, 1957.

[29] B. Pontecorvo. Neutrino experiments and the problem of conservation of leptonic charge. *Sov. Phys. JETP*, 26, 1967.

[30] M. Nakagawa Z. Maki and S. Sakata. Remarks on the unified model of elementary particles. *Progress of Theoretical Physics*, 28, 1962.

[31] A. R. Swift S. Elieze. Experimental consequences of electron neutrino-muon-neutrino mixing in neutrino beams. *Nucl. Phys.*, 105, 1976.

[32] S. P. Mikheev and A. Yu. Smirnov. Resonance amplification of oscillations in matter and spectroscopy of solar neutrinos. *Sov. J. Nucl. Phys.*, 42, 1985.

[33] SNO collaboration. The sudbury neutrino observatory. *Nuclear Instruments and Methods in Physics*, 449, 2000.

[34] GABY RÄDEL and ROLF BEYER. Neutrino electron scattering. *Modern Physics Letters A*, 08, 1993.

[35] P.F.de Salas et. al. Status of neutrino oscillations 2018: 3σ hint for normal mass ordering and improved cp sensitivity. *Phys. Lett. B.*, 782, 2018.

[36] T2K collaboration. Search for cp violation in neutrino and antineutrino oscillations by the t2k experiment with 2.2×10^{21} protons on target. *Phys. Rev. Lett.*, 121, 2018.

[37] KATRIN collaboration. Direct neutrino-mass measurement with sub-electronvolt sensitivity. *Nature Physics*, 18:160–166, 2022.

[38] Abhish Dev Peizhi Du Vivian Poulin Yuhsin Tsai Guillermo F. Abellán, Zackaria Chacko. Improved cosmological constraints on the neutrino mass and lifetime. *JHEP*, 08, 2022.

[39] P. Fayet. Supergauge invariant extension of the higgs mechanism and a model for the electron and its neutrino. *Nuclear Physics B.*, 90, 1975.

[40] MAJORANA collaboration. Final result of the majorana demonstrator's search for neutrino-less double- decay in ^{76}ge. *arXiv:2207.07638v1 [nucl-ex]*, 2022.

[41] M. Goeppert-Mayer. Double beta-disintegration. *Phys. Rev.*, 48, 1935.

[42] Particle Data Group. Review of particle physics. 8, 2022.

[43] Jenni Kotila. Rare weak decays and neutrino mass. *Spring Seminar on Nuclear Physics 2022*, 2022.

[44] J. Engel and J. MenÃlndez. Status and future of nuclear matrix elements for neutrinoless double-beta decay: A review. *Rept. Prog. Phys.*, 80, 2017.

[45] KamLAND-Zen collaboration. Search for majorana neutrinos near the inverted mass hierarchy region with kamland-zen. *Phys. Rev. Lett*, 117, 2017.

[46] P. Di Bari. An introduction to leptogenesis and neutrino properties. *Contemp. Phys.*, 53, 2012.

[47] S. R. Elliott and P. Vogel. Double beta decay. *Ann. Rev. Nucl. Part. Sci. 52*, 115:160–166, 2002.

[48] CUORE collaboration. Search for majorana neutrinos exploiting millikelvin cryogenics with cuore. *Nature*, 604:53–58, 2022.

[49] EXO-200 collaboration. Search for majoron-emitting modes of 136xe double beta decay with the complete exo-200 dataset. *arXiv:2109.01327v2 [hep-ex]*, 2021.

[50] NEMO-3 collaboration. Results of the search for neutrinoless double- decay in 100mo with the nemo-3 experiment. *Phys. Rev. D*, 92, 2015.

[51] NEMO-3 collaboration. Measurement of the 2 decay half-life and search for the 0 decay of 116cd with the nemo-3 detector. *Phys. Rev. D.*, 95, 2017.

[52] NEMO-3 collaboration. Latest results from nemo-3 status of the supernemo experiment. *IOP Conf. Series: Journal of Physics*, 888, 2017.

[53] NEMO-3 collaboration. Measurement of the two neutrino double beta decay halflife of zr-96 with the nemo-3 detector. *Nucl. Phys. A.*, 847, 2010.

[54] NEMO-3 collaboration. Measurement of the double-beta decay half-life and search for the neutrinoless double-beta decay of 48ca with the nemo-3 detector. *Phys. Rev. D.*, 93, 2016.

[55] SNO+ Collaboration. Current status and future prospects of the SNO+ experiment. *Advances in High Energy Physics*, 2016.

[56] S. D. Biller. Probing majorana neutrinos in the regime of the normal mass hierarchy. *Phys. Rev. D.*, 87, 2013.

[57] Snolab user's handbook. *Revision 2*, 2006.

[58] The SNO+ collaboration et al. The sno+ experiment. *Journal of Instrumentation*, 16, 2021.

[59] The Borexino Collaboration et al. The borexino detector at the laboratori nazionali del gran sasso. *Nucl.Instrum.Meth.*, 600:568–593, 2009.

[60] Borexino Collaboration et. al. The liquid handling systems for the borexino solar neutrino detector. *Nuclear Instruments and Methods in Physics Research A*, 609, 2009.

[61] A. Bialek et. al. A rope-net support system for the liquid scintillator detector for the SNO+ experiment. *Nuclear Instruments and Methods in Physics Research A*, (827 152–160), 2016.

[62] I Lawson. Radon levels in the sno+ radon reduction room and acrylic vessel. *SNO+ internal report*, DocDB1453-v7, 2012.

[63] N. Fatemi-Ghomi. Cover gas commissioning report. *operational manual*, SNO+ DocDB-2918-v1.

[64] The SNO Collaboration et al. The sudbury neutrino observatory. *Nucl.Instrum.Meth.*, 449:172–207, 2000.

[65] G. Doucas et al. Light concentrators for the sudbury neutrino observatory. *Nucl. Instrum. Meth.*, A 370(579-596), 1996.

[66] SNO+ Collaboration. Improved search for invisible modes of nucleon decay in water with the sno+ detector. *Phys. Rev. D*, 105(112012), 2022.

[67] M. Anderson et al. Measurement of the ^{8}B solar neutrino flux in with very low backgrounds. *Physical Review D 99 (1), 012012*, 2019.

[68] B. Tam. Partial fill ppo concentration. *SNO+ internal report*, SNO+-doc-7356-v1, 2022.

[69] R. Hunt-Stokes. In-situ α β timing tuning. *SNO+ internal report*, doc-7485-v1, 2022.

[70] Ziyi Guo et. al. Slow liquid scintillator candidates for mev-scale neutrino experiments. *Astroparticle Physics*, 109(33-40), 2019.

[71] John Vernon. Jelley. Cherenkov radiation and its applications. *Book, Pergamon*, 1958, 1987.

[72] M. W. Davidson. Concepts in fluorescence.

[73] SNO+ Collaboration et. al. Development, characterisation, and deployment of the sno+ liquid scintillator. *Journal of Instrumentation*, 16, 2021.

[74] Iwan Morton-Blake. First measurement of reactor antineutrinos in scintillator at sno+ and study of alternative designs for large-scale liquid scintillator detectors. *PhD Thesis*, 2021.

[75] Y. Liu. Attenuation and scattering of tebd the cocktail. *SNO+-docDB 3880.*

[76] J. Sinclair J. Maneira, S. Peeters. Optical calibration of SNO+. *Journal of Physics: Conference Series 598*, 2015.

[77] M. Stringer. Sensitivity of SNO+ to Supernova neutrinos. *PhD Thesis*, University of Sussex, 2018.

[78] R. Stainforth. Characterising the optical response of the sno+ detector. *PhD Thesis*.

[79] Ana Sofia Inacio. Analysis of the july 2018 laserball scan. *SNO+ internal report*, SNO+-doc-5308-v3, 2018.

[80] R. Alves et al. The calibration system for the photomultiplier array of the sno+ experiment. *JINST*, 03, 10, 2015.

[81] M.R. Dragowsky et. al. The ^{16}N calibration source for the sudbury neutrino observatory. *Nucl.Instrum.Meth. A481 284-296*, 2002.

[82] M. Anderson et al. Search for invisible modes of nucleon decay in water with the SNO+ detector. *Physical Review D 99 (3), 032008*, 2019.

[83] L. Lebonowski. SNO+ calibration with the N16 source. *SNO+ internal report*, SNO+-doc-5003-v2, 2018.

[84] M. Stringer. Measurement of the angular response of sno+ using the 16n source. *SNO+ internal report*, SNO+-doc-4632-v1, 2017.

[85] J.C. Loach. Measurement of the flux of 8b solar neutrinos at the sudbury neutrino observatory. *PhD Thesis*, University of Oxford, 2008.

[86] Y. Liu. Neutron measurements and reactor antineutrino search with the sno+ detector in the water phase. *PhD Thesis*, Queen's University, 2020.

[87] SNO+ Collaboration. Measurement of neutron-proton capture in the sno+ water phase. *Physical Review C*, 102, 2020.

[88] R. Bayes. Global calibration in partial-fill. *SNO+ internal report*, SNO+-doc-6283-v1, 2020.

[89] E. Caden. Sliding floor installation plan. *SNO+-doc-2627-v1*, 2013.

[90] Olivier Couet. The root users guide. *CERN*, 2005.

[91] P. G. Jones. Background rejection for the neutrinoless double beta decay experiment sno+. *PhD Thesis*, 2012.

[92] I. Coulter. Modelling and reconstruction of events in sno+ related to future searches for lepton and baryon number violation. *PhD Thesis*, 2013.

[93] Jack Dunger. Topological and time based event classification for neutrino-less double beta decay in liquid scintillator. *Christ Church College, University of Oxford*, 2018.

[94] E. O'Sullivan H. M. O'Keefe and M. C. Chen. Scintillation decay time and pulse shape discrimination in oxygenated and deoxygenated solutions of linear alkylbenzene for the sno+ experiment. *Nucl. Instrum. Meth. A*, 28:119, 2011.

[95] SNO Collaboration. Measurement of the cosmic ray and neutrino-induced muon flux at the sudbury neutrino observatory. *Phys. Rev. D*, 80, 2019.

[96] Josephine L. Paton Steven D. Biller, Edward J. Leming. Slow fluors for effective separation of cherenkov light in liquid scintillators. *Nuclear Inst. and Methods in Physics Research*, A 972, 2020.

[97] M. Yeh J. Caravaca, B. J. Land and G. D. Orebi Gann. Characterization of water-based liquid scintillator for cherenkov and scintillation separation. *The European Physical Journal C*, 80(9), 2020.

[98] Josephine Paton. Directional reconstruction in scintillator. *Reconstruction Workshop, SNO+ CM*, 2022.

[99] P. Khaghani. Partial-fill n16 data and position reconstruction. *SNO+ internal CM*, doc-7079-v1, 2021.

[100] T. Kroupova. External background classifiers for BB production. *SNO+ internal*, SNO+-doc-6432-v1, 2020.

[101] J. A. Dunmore. The separation of cc and nc events in the sudbury neutrino observatory. *Ph.D. Thesis*, 2004.

[102] G. M. Gregor. The measurement of the neutral current interaction at the sudbury neutrino observatory. *PhD Thesis*, Oxford University, 2002.

[103] Adams D.Q. Alduino C. et al. Nutini, I. The cuore detector and results. *J Low Temp Phys*, 199:519–528, 2020.

[104] David J Auty. Rn monitor: Performance and plans. *SNO+ Collaboration Meeting*, SNO+-doc-7309-v1, 2022.

[105] M J Martin. Nuclear data sheets. *Nuclear Data Sheets*, 108(8):1583–1806, 2007.

[106] V Sinev et. al. What can the cno neutrinos flux measurement done by borexino say about 40 k geoneutrino flux? *J. Phys.*, Ser. 1690 012170, 2020.

[107] O. Chkvorets D. Hallman R. Ford, M. Chen and E. Vazquez-Jauregui. A scintillator purification plant and fluid handling system for SNO+. *arXiv:1506.08746 [physics.ins-det]*, 2015.

[108] The Borexino Collaboration. New results on solar neutrino fluxes from 192 days of borexino data. *Phys.Rev.Lett.*, 101:091302, 2008.

[109] K. Majumdar. On the measurement of optical scattering and studies of background rejection in the sno+ detector. *PhD Thesis*, 2015.

[110] H. O'Keeffe M. Chen, V. Lozza. Expected radioactive backgrounds in SNO+. *SNO+ internal report*, SNO+-doc-507-v42, 2019.

[111] S. M. Adil Hussain. Evaluating 238u external background for sno+ experiment using radon assays and 214bi analysis. *MSc Thesis*, 2022.

[112] B. Aharmin et. al. High sensitivity measurement of 224ra and 226ra in water with an improved hydrous titanium oxide technique at the sudbury neutrino observatory. *Nucl. Inst.*, 604(3), 2009.

[113] MS Basunia. Nuclear data sheets for a = 210. *Nuclear Data Sheets - Elsevier*, 121, 2014.

[114] S Riccetto. Partial-fill data 210po updates 2020 - no fill. *SNO+ internal report*, SNO+-doc-6523-v1, 2020.

[115] O. Chkvoret. Leaching studies for SNO+. *SNO+ Collaboration Meeting*, SNO+-doc-2050-v1, 2013.

[116] O Chkvoret. Leaching studies for SNO+ CM. *SNO+ internal report*, SNO+-doc-2050-v1, 2013.

[117] P. Khaghani. Neck Sense Rope System and Leaching Studies for SNO+. M.Sc. Thesis, 2016.

[118] V. Lozza and J. Petzoldt. Cosmogenic activation of a natural tellurium target. *J Astropartphys.*, 61, 2014.

[119] G. Alimonti et al. (Borexino Collaboration). Measurement of the ^{14}c abundance in a low-background liquid scintillator. *Physics Letters B*, 422:349–358, 1998.

[120] R. Bayes. ^{14}c background characterization. *SNO+ internal report*, doc-7519-v1, 2022.

[121] MF Physics Corporation. *Colorado Springs, Colorado, U.S.A.*

[122] G. B. Wilkin. Dt neutron source shielding for the sudbury neutrino. *SNO-STR-95-030*, 1995.

[123] B. Sur A. Hamer. Targets for the n16 calibration source. *SNO-STR-97-033*, 1997.

[124] Z. Barnard. An update to 16n geometry. *SNO+ internal DocDB-4414*, 2017.

[125] Bicron Product. Appendix b, premium plastic scintillators, related materials, figure entitled range of atomic particles in bicron premium plastic scintillators, p. b8.

[126] Electron Tubes Ltd. Electron tubes ltd, middlesex, england.

[127] M. R. Dragowsky. Sudbury neutrino observatory energy calibration using gamma-ray sources. *PhD Thesis-Oregon State University*, 1999.

[128] B. Aharmim et al. (SNO Collaboration). Electron energy spectra, fluxes, and day-night asymmetries of 8b solar neutrinos from measurements with nacl dissolved in the heavy-water detector at the sudbury neutrino observatory. *Physical Review C*, Vol. 72, 2005.

[129] E. Leming. N16 position and direction plots: notes for presenters. *SNO+ internal report*, SNO+-doc-5078-v5, 2018.

[130] Ben Tam. Ben's ppo concentration table. *SNO+*, 2022.

[131] A. Bacon B. Tam. Sno+ scintillator (lab + 2.2 g/l ppo) light yield plot for approval. *SNO+ internal report*, SNO+-doc-7406-v1, 2022.

[132] I S Yeo et al. Measurement of the refractive index of the lab-based liquid scintillator and acrylic at reno. *Phys. Scr.*, 82(065706), 2010.

[133] S. N. Kasarova et al. Analysis of the dispersion of optical plastic materials. *Optical Materials*, 29:1481–1490, 2007.

[134] Serena Riccetto. Fullfill data& mc 210po& 214po nhits radial profile vs. absorption length. *SNO+ internal, SNO+-doc-7185-v3*, 2021.

[135] R. Bayes. Multiple source scintillator calibration. *SNO+ internal report*, SNO+-doc-7227-v3, 2022.

[136] John Betteley Birks. The theory and practice of scintillation counting. *Elsevier*, 27, 2013.

[137] Anthony LaTorre. New measurements for the timing spectrum of electrons and alphas in lab+ppo. *SNO+-docDB-4081*, 2016.

[138] T. Kaptanoglu. Scintillator timing measurement. *SNO+ internal report*, SNO+-doc-5075-v4, 2018.

[139] J. Paton. Cherenkov detection possibilities in sno+. *SNO+ internal report*, SNO+-doc-6331-v1, 2020.

[140] Josh Wang. Bipo background summary. *SNO+ Collaboration Meeting*, docdb-6851, 2021.

[141] Ana-Sofia Inacio. BiPo214 Tagging Efficiency in the 0nuBB ROI. *SNO+ internal report*, SNO+-doc-6050-v7, 2020.

[142] Ana Sofia Inacio. Bipo214 and $0\nu\beta\beta$ roi analysis in the partial-fill. *SNO+ internal*, doc-6823-v5, 2021.

[143] A. M. Gangapshev V. V. Kazalov V. V. Kuzminov S. I. Panasenko S. S. Ratkevich E. N. Alexeyev, Yu. M. Gavrilyuk. Sources of the systematic errors in measurements of ^{214}po decay half-life time variations at the baksan deep underground experiments. *Physics of Particles and Nuclei*, 46, 2015.

[144] R. Bayes. Light yield and quenching measurements from ambe data. *SNO+ Internal*, doc-7486-v1, 2022.

[145] P. Khaghani. The external background from Bi214 and Tl208. *SNO+ internal report*, SNO+-doc-5575-v7, 2019.

[146] T. Kroupova. External background classifiers for BB production. *SNO+ internal*, SNO+-doc-6432-v1, 2020.

[147] J. Stelzer J. Therhaag E. von Toerne H. Voss A. Hoecker, P. Speckmayer. TMVA; Toolkit for Multivariate Data Analysis with ROOT. *arXiv:physics/0703039*, ArXiv e-prints (2009).

[148] Iwan Morton-Blake. Learning the ropes. *SNO+ Internal Report*, doc-4912-v1, 2018.

[149] Aksel Hallin Kalpana Singh, Mohammad Hedayatipoor. The expected performance and motion of the upward and downward ropes in the SNO+ rope net. *SNO+ internal report*, SNO+-doc-1872-v1, 2012.

[150] Jaret Heise. Rope status. *SNO+ internal report*, SNO+-doc-181, 2008.

[151] P Khaghani. Av positioning. (in progress). *SNO+ internal Docdb*, SNO+-doc-3562, 2022.

[152] Kalpana Singh. Long term soak tests for SNO+. *SNO+ internal report*, SNO+-doc-2826-v1, 2014.

[153] A Bialek M Hedayatipoor. Procedure for tensile strength and creep measurements - long term monitoring tests. *SNO+ internal report*, SNO+-doc-2601, 2017.

[154] Belina von Krosigk. Measurement of proton and α-particle quenching in lab based scintillators and determination of spectral sensitivities to supernova neutrinos in the sno+ detector. *PhD Thesis*, 2015.

[155] O Chkvoret. Leaching studies. *SNO+ internal report*, SNO+-doc-2384-v1 and SNO+ doc-507-v31, 2014.

[156] P. Khaghani. leaching doc (in progress). *PhD Thesis*, 2015.

[157] P Khaghani. Leaching studies for SNO+. *SNO+ UniDoc*, 2018.

[158] P Khaghani. Leaching during the water phase. *SNO+ internal report*, SNO+-doc-4917-v1, 2018.